Exploring the edge
Contigiani, O.

Exploring the edge

Proefschrift

ter verkrijging van
de graad van doctor aan de Universiteit Leiden,
op gezag van rector magnificus prof.dr.ir. H. Bijl,
volgens besluit van het college voor promoties
te verdedigen op donderdag 26 januari 2022
klokke 12:30 uur

door

Omar Contigiani
geboren te Montevarchi, Italië in 1992

Contents

Chapter 1

Introduction

1.1 The modern Universe

Humanity's fascination with the cosmos is a pervasive theme of our shared history. The perfect illustration of this is religion, which aims to describe the origin of everything and its relation to our personal experience. In this context, creation myths are the first cosmogonies, i.e. models concerning the origin of the Universe, and most have humanity in a fundamentally privileged role, sometimes as the natural endpoint of cosmic history. In contrast, the development of cosmology, i.e. the scientific study of the origin and evolution of the Universe, has been a process of continuous abstraction from our personal experience and has proved to be a clear rejection of our unique position. What we have designed is an indifferent Universe, where we deliberately do not represent a privileged observer. For the most part, this undertaking has been a humbling and painful process. Consider, for example, Giordano Bruno, who was famously burned at the stake in the year 1600 for claiming that other stars might be other suns and that other worlds orbit around them. Nonetheless, modern cosmology is also a great example of our hubris. We are not concerned with making statements about *us*, *here and now*, but we aspire to explain *everything* that was and will ever be, to derive laws which we can genuinely call Universal.

This outward journey is not only conceptual but also profoundly empirical. Our depiction of the Universe started small, but over time has expanded towards scales that are now barely imaginable. One parsec, originally designed to study the motion of the furthest objects, is now a unit too small for most cosmologists, who are accustomed to units of the order of mega- or giga-parsecs, Mpc and Gpc, respectively. Similarly, it is remarkable that in only one century, we have gone from discussing if there are other galaxies, referred to as island universes (Shapley and Curtis, 1921), to debating if there is a string theory multiverse (Carr and Ellis, 2008). From a purely scientific

perspective, what lead to these developments are two kinds of advancements. The first kind is technological advancements. For example, it is not by chance that Tycho Brahe, Johannes Kepler, and Galileo Galilei were the first to study the Solar System. These people first had the opportunity to look at the sky using large measuring instruments and powerful lenses, able to focus a large amount of light onto their small iris. Without telescopes and sextants to accurately measure the motion of the wandering stars, i.e. planets, we would never know of the Solar System's existence. The second kind is theoretical advancements, and their importance in this process of abstraction cannot be understated. The way we view the world is based on the way we model it. As an example of this, Isaac Newton's law of Universal gravitation, capable of explaining the motion of objects on Earth and in the Solar System alike, now almost sounds like a misnomer. Albert Einstein's theory of general relativity is what we see today as the Universe's law of gravitation because it can describe virtually every phenomenon in its purview. It has been successfully applied to atom interferometry (Rosi et al., 2014), the structure of black holes (Schwarzschild, 1916), and, most notably for this thesis, the evolution of the Universe itself (Friedmann, 1922).

Gravity is the most relevant force on the largest scales because it cannot be screened away, and its range is formally infinite. This fact is astonishing, given its relative weakness. For example, the typical strength of the gravitational pull on an electron, quantified by the gravitational coupling constant $\alpha_G \approx 10^{-45}$, is meager compared to its electromagnetic counterpart, the fine structure constant $\alpha \approx 1/137$. Because of the importance of gravity for cosmological applications, it is not surprising that the leading framework used in the field is based on general relativity. According to the current view, this theory represents the playground hosting a tug of war between two ingredients, dark matter and dark energy. These two components have opposite effects: one enhances structure through gravitational collapse, while the other pushes things apart and destroys structure. The first, dark matter, has dominated the evolution of the Universe for most of its existence thus far, but the second, dark energy, is now winning, and it is expected to eventually lead to the disintegration of all of the Universe's structure. In this process, "normal" matter, i.e. what forms everything we see and touch, is nothing more than a witness. In a humbling twist of fate, these baryons are only $1/6$th of the Universe's matter content according to the latest measurements (Planck Collaboration, 2020), and in our model of the largest scales, they represent a nuisance element with a relatively complex phenomenology. Despite being on the sidelines, the signals emitted by this form of matter act as tracers and provide the primary justification behind the model described above.

1.1.1   General relativity

First proposed in 1915, the theory of general relativity is what is called a metric theory of gravity (Einstein, 1916). It describes spacetime through a dynamical object, the

metric $g_{\mu\nu}$, detailing its curvature. The evolution of this quantity is connected to the energy content of the system, specified by the energy-momentum tensor $T_{\mu\nu}$, and their relationship is formalized by Einstein's field equations:

$$G_{\mu\nu} + \Lambda g_{\mu\nu} = \kappa T_{\mu\nu}. \tag{1.1}$$

In this expression, $G_{\mu\nu}$ is called the Einstein tensor, a quantity derived from the metric itself. In addition to this, notice the presence of two constants: κ, needed to match the units of $G_{\mu\nu}$ and $T_{\mu\nu}$, and Λ. The latter is called the cosmological constant, and it has important implications for cosmology that will be discussed later.

Here, we want to highlight two predictions of general relativity that are particularly relevant. The first is the accurate prediction of the bending of light in the presence of a massive object along the line of sight. Thanks to the first observation of this phenomenon by Arthur Eddington in 1919 (Dyson et al., 1920), gravitational lensing was quickly established as an experimental fact, and, over the years, it became a robust observable that is still used to this day. In this theoretical framework, this unusual behavior has an obvious explanation: because photons are expected to follow the geodesics defined by the metric $g_{\mu\nu}$, the curvature induced by the presence of matter naturally results in a perturbed light path. The second relevant prediction to be highlighted is the existence of gravitational waves. Because the metric is dynamical, perturbations on top of a background profile can propagate after being generated by accelerating compact masses. The measurement of the decaying orbit of a binary pulsar due to the energy deposited in this fashion (Taylor and Weisberg, 1982) represented the first indirect observation of gravitational waves and, similarly to the lensing case, it quickly ushered in the birth of a new field. After a few decades, the interest in this science eventually resulted in the direct detection of these tiny spacetime ripples by the LIGO-Virgo consortium in 2015 (LIGO Scientific Collaboration and Virgo Collaboration, 2016).

When applied to the Universe as a whole, Einstein's field equations are solved under two simple assumptions: the system should have no preferred observer, and it should evolve over time. The first statement is known as the Copernican principle, and it is understood today as an axiom about symmetries. Over large scales, it implies spatial isotropy and homogeneity. In contrast, the second statement is an observational fact about the broken time-symmetry, and it is justified by the early discovery of the Universe's expansion by Edwin Hubble (Hubble, 1929). In practice, the combination of these two assumptions translates into a form for the metric $g_{\mu\nu}$. In terms of the line element ds, we write:

$$ds^2 = g_{\mu\nu}dx^\mu dx^\nu = -dt^2 + a^2(t)\delta_{ij}dx^i dx^j. \tag{1.2}$$

This is known as the Friedmann–Lemaître–Robertson–Walker metric, and it describes spatially flat hypersurfaces parametrized by the coordinates $x^i, i = 1, 2, 3$. The distance between two comoving observers expands over time according to the scale parameter $a(t)$, usually defined such that $a = 1$ is the present-day $t = t_0$ and $a = 0$ represents the

start of the Universe, $t = 0$. An important consequence of the Universe's expansion is the change in the frequency of a monochromatic wave. Its main application is that if the rest-frame wavelength of a light source or spectral feature is known, its shift towards redder frequencies due to cosmic expansion indicates when its light was emitted. This cosmological Doppler shift is a multiplicative factor in wavelength, and it is written in terms of the redshift z. Its connection to the scale factor can be expressed as

$$(1 + z) = \frac{1}{a},\tag{1.3}$$

and represents the main way through which we can map cosmological distances using electromagnetic spectra. A second important consequence of the Universe's finite age and isotropic recession is the existence of a horizon for every observer. Because light travels a finite amount of space in the Universe's lifetime, this naturally determines the size of casually connected patches. In other words, there is a maximum distance that a ray of light could have originated from before reaching said observer. According to the leading model, the value of this horizon is about 14.4 Gpc and can be obtained by integrating the trajectory of a photon moving at the speed of light c in the metric of Equation (1.2):

$$\chi(t = 0) = \int_0^{t_0} \frac{cdt'}{a(t')}.\tag{1.4}$$

By changing the integration limits, the expression above can also define a measure of distance between two arbitrary instants in cosmic time. If evaluated between today and an arbitrary time t, it is called comoving distance, but in an expanding Universe, this definition of distance to the past is not unique. Two other definitions are commonly used in cosmology, the luminosity distance D_L and the angular diameter distance D_A. Historically, the first is defined based on the energy flux of photons, and the second is based on the angular size of objects in the sky. In the first case, the additional energy change due to cosmological redshift must be accounted for, resulting in $D_L(t) = \chi(t)/a(t)$. In the second case, the angular diameter distance is different from the comoving distance because of the evolution of the comoving grid defined by the metric in Equation (1.2). An object of fixed physical size is measured differently by comoving grids at different times and, because of this, the angular distance is defined as $D_A(t) = a(t)\chi(t)$.

1.1.2   Dark energy

In the late 1990s, the discovery of the Universe's accelerated expansion proved the existence of an additional component besides matter and radiation (Riess et al., 1998; Perlmutter et al., 1999). This discovery came initially as a surprise, as such acceleration is possible only in a Universe dominated by an exotic constituent with negative effective pressure. Over time, however, what we now call dark energy quickly became accepted

as an observational fact thanks to numerous supporting observations. Broadly speaking, the evidence can be divided into two groups: one related to its role in shaping the expansion of the Universe, that led to its discovery, and the other pertaining to its part in shaping the distribution of structure in the Universe, that appeared only a few years later (Springel et al., 2005; Eisenstein et al., 2005). Despite the general belief in its existence, however, very little has been discovered about dark energy apart from the fact that it accounts for about 70 percent of the Universe's present-day energy content.

Cosmological constant

In the context of general relativity, the simplest explanation for dark energy is the cosmological constant appearing on the left-hand side of Equation (1.1). When moved to the right-hand side, Λ can be interpreted as a zero-point energy in addition to the energy-momentum content described by $T_{\mu\nu}$. If we assume that this constant is the sole cause of the accelerated expansion, then its value in terms of the Planck length l_P is measured to be

$$\Lambda = 2.89 \times 10^{-122} \, l_P^2, \tag{1.5}$$

with an uncertainty of a few percentage points. In general, an accelerated expansion causes the energy density of matter and radiation to quickly dilute over time and eventually results in a Universe completely dominated by the cosmological constant. Asymptotically, this leads to a de-Sitter Universe where the scale factor can be written as:

$$a(t) \propto \exp\left(\sqrt{\frac{\Lambda c^2}{3}}t\right). \tag{1.6}$$

Under such exponential expansion, all structures made of matter are eventually pulled apart until nothing remains. Despite this bleak outlook, it is important to stress that this explanation for dark energy appears at first glance to be perfectly satisfactory: it is a minimal solution, and it is consistent with data. Nevertheless, it would be deceiving not to mention that it is also associated with two main theoretical concerns. The first is due to its vacuum energy interpretation. In this case, the value of the cosmological constant is expected to be connected to micro-physics. However, the extremely low Λ needed to account for cosmic acceleration is so far removed from the scales associated with known forces that the fine-tuning required for such cancellations casts significant doubts on this interpretation. Currently, developments aimed at addressing this question and quantifying its discrepancy are limited by our inability to frame gravity within a quantum physics framework. The second issue linked to Λ is the suspicious timing of the emergence of dark energy. The exact value of this constant determines when this component becomes dominant in the history of time, and, in our Universe, it corresponds to the moment when dark matter begins to form complex structures through gravitational collapse. If the value of Λ is arbitrary and not connected to cosmology, it

seems quite coincidental that dark energy is only now taking over the Universe, after the interplay of matter and radiation led to the variety of structures that we observe today.

Both of these points can be addressed if one posits the existence of a multiverse. According to the anthropic principle, if multiple realizations of the Universe with different fundamental constants are possible, only those where humanity can emerge should be considered valid since we are, in fact, observing the Universe. This is a relatively new and powerful idea, but it has not been thoroughly tested yet. From a practical perspective, it is unclear how such a theory could be falsifiable or, more simply, how to compute the likelihood of humanity's existence in the large parameter space of the Universe's constants. On a more fundamental level, what is troubling about this solution is that it might take us back to when our models assumed that the cosmos was explicitly designed to host humanity. This is a profoundly unsettling notion, especially for a science that has been fighting this urge for most of its history.

Dynamical dark energy and modified gravity

In light of these concerns, it is not surprising that the attempts to address the nature of dark energy as something beyond the cosmological constant have attracted great interest. These efforts can be divided into two camps. On one side, the introduction of a fluid with its energy density $T_{\mu\nu}^{DE}$ capable of mimicking the effects of Λ. This component is named *dynamical* dark energy, and its most straightforward realization is quintessence, a scalar field with negative pressure (Caldwell et al., 1998). Models of quintessence are noteworthy because they can address the coincidence problem in a general way through so-called tracker solutions, where a scalar field follows the formation of cosmic structure and its emergence today is guaranteed for a variety of initial conditions (Zlatev et al., 1999). On the other side, the second set of widespread attempts is based on modifying Einstein's field equations. Because general relativity is the only healthy metric theory of gravity describing a spin-2 massless field in four dimensions, there are only a handful of ways it can be generalized. Of these ways, a class of models that has been investigated extensively is the addition of an extra scalar force carrier. The archetypal example of this class of solution is Brans-Dicke gravity, where the inverse of the gravitational constant κ appearing in Equation (1.1) is upgraded to a dynamical degree of freedom (Brans and Dicke, 1961). This thesis discusses this and related generalizations and, for the purposes of this work, the main feature of these models is a non-zero derivative of the Planck mass M_P; usually a constant that is a function of κ.

The most generic version of such scalar-tensor theories was already written down by Gregory Horndeski in 1974 (Horndeski, 1974). This feat was possible thanks to the requirement that the equations of motion should not contain derivatives of order higher than second. Theories that do not respect this condition describe ghosts, i.e. fields with Hamiltonian unbounded from below and, in general, any field interacting with a ghost has an infinite decay rate as a consequence. Technically, this condition can be circum-

vented by exploiting some caveats, but the freedom is still limited (Gleyzes et al., 2015). From a practical point of view, the main constraints on scalar-field theories come from the prediction of an extra force associated with the new degree of freedom, a.k.a. a fifth force. Because no departure from general relativity has been detected at both laboratory and solar-system scales (Will, 1993), a method to avoid these constraints must be devised. These are called screening mechanisms and aim at reducing the impact of the fifth force in regions of high density while keeping the effects of the extra degree of freedom visible at cosmological scales. Screening in a dense environment is achieved dynamically either by limiting the range of propagation of the force in these regions (Vainshtein and chameleon mechanisms, Vainshtein, 1972; Khoury and Weltman, 2004), or by reducing the coupling of matter to this extra force carrier (symmetron mechanism, Hinterbichler et al., 2011).

1.1.3 Dark matter

The second puzzle of modern cosmology is the nature of dark matter. Similar to its dark energy counterpart, the presence of this component is necessary to explain a plethora of observations, but the details of its nature are still unknown. As opposed to dark energy, it should be noted that the existence of invisible material capable of interacting only gravitationally has never been a controversial statement. For most of the history of modern cosmology, however, it was assumed that this invisible material was simply extinguished stars, cool dim gas or microscopic bodies akin to asteroids. Only in the 1990s, with the advent of early Universe observations, it became apparent that the fraction of traditional matter formed in the primordial Universe was insufficient, and a new, unfamiliar kind was needed.

Before the era of precision gravitational lensing, the existence of dark matter could only be inferred through the motion of luminous matter in its gravitational potentials. Pioneering observations of these phenomena, performed by Fritz Zwicky (Zwicky, 1933), Vera Rubin (Rubin and Ford, 1970) and many others, eventually became the primary justification behind the present-day paradigm of dark matter. Its fundamental principles are simple: dark matter should be cold and non-interacting. These two properties are required to reproduce the observed distribution of structure in the Universe and match simulated data. In this context, cold represents the opposite of relativistic. Examples of relativistic species in the Universe are radiation and neutrinos, for which the majority of the energy is in the form of momentum instead of rest mass. This results in high velocities that help relativistic particles stream away from gravitational potentials and makes them unable to form small structures. In the case of dark matter, this suppression is not observed. The second property is connected to the fact that dark matter appears to interact only through gravitational forces. The argument behind this principle is also linked to the distribution of matter in the Universe. The existence of additional interactions would lead to more compact structures since kinetic energy

would be dissipated into random motion more efficiently than through gravitational interactions alone. Once again, this phenomenon is not observed in the real Universe.

Finally, the non-interacting property of dark matter refers also to its inability to interact with baryons. Because the standard model of particle physics is equipped with weakly interacting particles, the idea that dark matter might actually be coupled to the standard model with low interaction cross-sections is now the leading hypothesis (Steigman and Turner, 1985). From a scientific point of view, models based on these standard model extensions have proved to be easily falsifiable thanks to their precise predictions. The methods used to test these predictions can be divided into three detection channels. The first channel is related to dark matter production. Particle colliders could produce dark matter by annihilating standard model particles and then detect the missing mass. The second channel is the reverse of this process, i.e. when dark matter particles annihilate with themselves and result in standard model particle-antiparticle pairs. Finally, the last channel is called direct detection. It is based on the ability of dark matter to scatter off of an extensive reservoir of baryons and deposit energy into the system. So far, multiple efforts to detect dark matter through all three of these methods have been attempted with no success (Schumann, 2019) and the region of parameter space allowed for these models has shrunk considerably. As a result, alternatives to this mainstream approach have now begun to attract the community's attention. Exotic theories such as primordial black holes or light bosonic fields such as axions appear promising. Still, the parameter spaces of these theories are also heavily constrained by observations, and the predictive power of the remaining freedom is still under scrutiny.

1.2 The large-scale structure of the Universe

1.2.1 Linear perturbations

In cosmology, the distribution of matter takes the form of what is called the large-scale structure of the Universe. Its emergence is a complex phenomenon, and it is studied in multiple separate regimes using different techniques.

At the linear level, the matter density ρ is treated as a dimensionless perturbation δ on top of a fluid of spatially constant density $\bar{\rho}(t)$, such that $\delta = \rho/\bar{\rho} - 1$. This treatment can also be extended to the other ingredients of our models: the background metric in Equation (1.2) is perturbed by the gravitational potentials induced by this matter distribution, and the dark energy fluid, if it exists, can also be described with its own perturbations. These perturbed quantities are Fourier transformed both to investigate the dynamics as a function of spatial scale and because, at linear level, different Fourier modes labeled by their Fourier vector $\boldsymbol{k}$ are independent. Furthermore, for an isotropic Gaussian field, the distribution of these perturbed quantities can be described by a single function, the power spectrum. For example, the Fourier transformed matter density contrast $\delta_{\boldsymbol{k}}$ is described by the matter power spectrum $P(k)$, defined as an

average over Fourier space:

$$\langle \delta_{\boldsymbol{k}} \delta_{\boldsymbol{k'}} \rangle = (2\pi)^3 P(k) \delta^3(\boldsymbol{k} - \boldsymbol{k'}), \tag{1.7}$$

where $\delta^3(\boldsymbol{k})$ is the three-dimensional Dirac delta function. If we assume isotropy, it is common to drop the vector index and simply refer to these modes as δ_k.

A simple and instructive example of how these perturbations can be studied is the equation governing the evolution of cold dark matter perturbations in a Universe dominated by this component. If we consider scales below the size of the horizon, we are able to recover the Newtonian dynamics limit and write down the evolution of perturbations as:

$$\delta_k'' + \mathcal{H}\delta_k' = 4\pi G a^2 \bar{\rho} \delta_k, \tag{1.8}$$

where $\mathcal{H} = a'/a$ is named the Hubble parameter, and the prime symbol indicates a derivative with respect to conformal time τ such that $dt = a(\tau)d\tau$. In this equation, the right-hand side represents the mechanism through which gravity enhances overdensities. The second term on the left side, on the other hand, is a friction term and shows how the expansion of the Universe can affect the growth of structures. For example, a matter-dominated Universe implies $\delta \propto a$, while in a de-Sitter Universe, the growth is slowed to a halt. In a complete framework, the presence of nonlinearities and multiple interacting components, e.g. dark matter and baryonic matter, need, of course, to be considered. To make the importance of this first point clear, note that Equation (1.8) is valid only in the limit $\delta \ll 1$, where terms of the order δ^2 or higher are ignored. Outside of this linear regime, the growth of these massive perturbations cannot be tracked with this equation. In terms of the wavelength k, this breakdown roughly corresponds today to a scale of $0.1\,\mathrm{Mpc}^{-1}$, and it is said that such overdensities have decoupled from the so-called Hubble flow. This gravitational collapse can happen in three spatial directions and, depending on how many directions have been affected, the resulting structures are referred to as walls, filaments, or nodes. This process is still ongoing, and the combination of these formations creates the so-called cosmic web.

A crucial nonlinear aspect determining the Universe's large-scale structure is the fact that fully collapsed overdensities, known as halos, can also interact with each other. In fact, today's structures grow mainly through mergers, and smaller structures assemble into larger ones. This process of hierarchical structure formation was first investigated by William Press and Paul Schechter (Press and Schechter, 1974) and this research direction has led to a widely used semi-analytical formalism still in use today to study smaller scales. In simple terms, such halo models describe the Universe's structure as a superposition of collapsed spherical objects characterized only by their mass. This approach has been highly successful thus far and has allowed us to predict the average clustering of visible matter based on the statistical properties of dark matter. However, as we push to smaller scales and larger samples, its limited ability to model the connection to visible matter and the additional properties that might affect its spatial distribution have begun to show.

1.2.2   Spherical collapse and the edge of halos

Today, knowledge of physics below the 10 Mpc scale is predominantly extracted from numerical simulations, and the resulting computer-assisted studies can be used to describe the interaction of baryons with dark matter in a wide range of scales. Despite this, semi-analytical and purpose-built models to study these same scales are still relatively widespread. In this context, the objective is not to obtain accurate predictions but to quickly gain insight into the mechanism behind the observable.

In the case of gravitational collapse, the seminal work of James Gunn and Richard Gott, Gunn and Gott (1972), represents the first glimpse into the effects of self-gravity in an expanding Universe. Like many subsequent models, this one is based on the evolution of spherical shells of matter around a central overdensity. The setup is straightforward: the presence of an initial overdensity causes matter to move towards it and eventually decouple from the Universe's expansion, with the closest material collapsing first. After this moment, the individual shells are stuck in a periodic motion of constant expansion followed by re-collapse and, because multiple shells undergo this process at different times, bubbles with opposite velocities continuously intersect each other. In the real Universe, this simple picture is complicated by the existence of angular momentum. In this case, the virial theorem can account for the inherent instability of the spherical solutions and quantify the size of the collapsed region.

Contrary to the basic assumption of most halo models, non-fully virialized halos undergoing this process still exist today. Around such massive objects, we can identify a multi-stream region dominated by orbiting material surrounded by a single-stream region dominated by infalling material. The mass profile in the first zone is a collisionless equilibrium profile common to all collapsed structures, while the profile in the second zone can be quickly derived from first principles. If we assume a time-independent profile, the continuity equation of the collapsing material can be written in terms of the density ρ_s and velocity vector $\boldsymbol{v}$:

$$\nabla(\rho_s \boldsymbol{v}) = 0, \tag{1.9}$$

where the radial component of the velocity vector for an asymptotically unbound stream is fixed by conservation of energy:

$$v_r^2 = \frac{2GM(<r)}{r}, \tag{1.10}$$

where $M(<r)$ is the mass contained within each shell at radius r. In the proximity of the halo, this quantity is dominated by the mass of the collapsed object. Hence, we can consider it constant and neglect the self-gravity of the stream. Under this assumption, these two equations combined imply $\rho_s \propto r^{-3/2}$.

Even though numerical simulations corroborate this result, the simple derivation above has an evident shortcoming: it does not depend on nor predicts the amount

of mass deposited on the halo since the incoming mass was neglected entirely. To extend this simple calculation, semi-analytical shell models can characterize this phenomenon and explore how the mass accretion rate shapes the transition between the single-stream and multi-stream regions. The sudden drop in density associated with the piling up of orbiting material leads to the formation of a constantly expanding, ever-present halo edge. This feature is a general prediction of spherical collapse, but its potential to study the physics of accretion has only been recently recognized (Diemer and Kravtsov, 2014).

The splashback feature, as it is now called (More et al., 2015), has been the subject of multiple theoretical studies in the last few years. Two factors can explain the popularity of this research line: its existence highlights a limitation of the halo model, and its phenomenology can be easily captured. This ability to truly describe nonlinear behavior instead of just reading it off of numerical simulations is particularly appealing in the context of the modeling complexities associated with small scales. Finally, what is perhaps more important is the fact that this interest has not been purely theoretical. This field thrived in the past few years thanks to wide galaxy surveys, capable of accessing a sizable fraction of the visible Universe, and the precision of present-day lensing measurements used to estimate the mass profile of halos.

1.3   Observations

1.3.1   Galaxies and baryons

Based on the conservation of entropy, we can retrace the expansion of the Universe to a denser and hotter infant state (Lemaître, 1931; Gamow, 1946). In this epoch, the baryonic matter was completely ionized and coupled to photons. Due to the resulting radiation pressure, the baryons could not collapse onto the primordial dark matter overdensities and moved instead in periodic motions called baryonic acoustic oscillations. As the Universe expanded, electrons and nuclei recombined, and baryons decoupled from radiation. At this point, these two components were free to evolve independently: baryons started collapsing onto the primordial dark matter overdensities, and light started streaming across the Universe, forming a cosmic relic we can still see today, the cosmic microwave background. Although they might appear related, gravitational collapse for baryons is not akin to its dark matter counterpart due to cooling, i.e. the ability to transform gravitational potential energy in forms of energy other than kinetic. For baryons, collapse assumes the form of a slow accretion process, and the end product is the collection of dense gas at the center of dark matter overdensities. Eventually, this gas fragments and stars are ignited, resulting in the birth of galaxies.

Because the dynamics of dark and baryonic matter are so intimately connected, the distribution of galaxies in the Universe acts as a probe of the total matter distribution. This is a powerful idea, but despite what might transpire from the initial description, the

relationship between the two components is not purely one-directional. Feedback, i.e. the backreaction of baryonic dynamics on the distribution and motion of dark matter, is an important phenomenon, and nowadays, its effects are studied through hydro-dynamical simulations capable of tracking both gravitational dynamics and baryonic microphysics. To provide an example of this relationship, consider the fact that lumi-nous matter can release a large amount of energy through, e.g. supernovae explosions or the bright accretion disks of supermassive black holes. The energy deposited in this fashion can then reshape the host dark matter halos and impact the relationship between the luminosity of a galaxy and the mass of its host halo. When combined, cooling and feedback are perfect examples of how cosmology can connect micro and macro-scales: physics set by quantum mechanical interactions dictates the appearance of our Universe on the largest scales.

Naturally, galaxies also follow the process of hierarchical structure formation, and, in the case of the largest conglomerates, they assemble in so-called galaxy clusters or groups. These objects inhabit the heaviest dark matter halos and can be detected in the late Universe as overdensities of galaxies in the sky. The brightest one is usually associated with the heaviest halo and is commonly referred to as the central galaxy. Fainter galaxies, stuck in orbits surrounding it, are called satellite galaxies. For this thesis, it should be mentioned that a diffuse hot ionized gas is also present in galaxy clusters. This results in two main observables used to detect galaxy clusters: the X-ray signal emitted through cooling and the signal generated by the cosmic microwave background scattering off the ions, known as the Sunyaev-Zeldovich effect.

1.3.2   Gravitational lensing

The deflection of light paths in the presence of mass along the line of sight is the only observable capable of providing a direct snapshot of the dark matter distribution of cosmic structures. This thesis makes wide use of this technique and focuses exclusively on weak-lensing. In this regime, the shape of distant objects is distorted by the presence of matter, e.g. a cluster, and detecting this distortion corresponds to a direct measure of the mass profile. The linearized lensing equation governing this phenomenon is:

$$\delta\boldsymbol{\beta} = \mathcal{A}\delta\boldsymbol{\theta}, \tag{1.11}$$

where $\boldsymbol{\theta}+\delta\boldsymbol{\theta}$ is the perturbed location in the image plane of the point located at $\boldsymbol{\beta}+\delta\boldsymbol{\beta}$ in the source plane, i.e. the plane that would be observed in the absence of lensing. The Jacobian matrix $\mathcal{A}$ connects the two and it is derived from the so-called lensing po-tential, an integral of the gravitational potential along the light-path. If $\mathcal{A}$ is constant in the region surrounding $\boldsymbol{\theta}$, then it can be generically split into two constant quan-tities: a spin two-field $\boldsymbol{\gamma} = \gamma_1 + i\gamma_2$, called shear, and a scalar component κ. At first order, the scalar component quantifies magnification, i.e. the isotropic change in size of an infinitesimal area, while the shear quantifies deformations. These effects can be

seen if we consider a circle centered on $\boldsymbol{\theta}$. This shape is deformed into an ellipse with imaginary ellipticity equal to

$$\epsilon = \frac{\gamma}{1-\kappa} \approx \boldsymbol{\gamma}, \tag{1.12}$$

and its area is multiplied by a magnification factor

$$\mu = \frac{1}{\det \mathcal{A}} = \frac{1}{(1-\kappa)^2 - |\gamma|^2} \approx 1 + 2\kappa. \tag{1.13}$$

Because the absence of lensing corresponds to a value of 0 for both shear and convergence, we have Taylor expanded around this value to obtain the approximate equations. Notice that outside of this weak-lensing limit, e.g., if $|\gamma|, |\kappa| \sim 1$, the matrix $\mathcal{A}$ can be singular. Points where this happens are called critical points, and in their vicinity, we approach the strong lensing regime where multiple images are formed. The most famous example of this arises when a source, lens, and observer are collinear. In this case, distant sources deformed into arcs, called Einstein rings, surrounding the central mass.

In practice, galaxies are not simple circles, and shear in the weak lensing regime is obtained by measuring the shapes of a large number of distant galaxies. This is a sophisticated procedure since the image visible in the reduced data is a convolution of the intrinsic galaxy ellipticity, the lensing effect, and a point-spread function, i.e. the impact of the atmosphere and telescope optics. While the first represents an intrinsic source of scatter and can only be defeated by averaging multiple galaxies, instruments and observing conditions need to be optimized in order to minimize the unpredictability of the last. The best results, for example, are obtained using space telescopes, for which the effect of atmospheric diffraction is obviously not present.

1.4   This thesis

In studying the largest scales, the boundaries of collapsed structures offer a laboratory to examine the relationship between structure formation, cosmology, and galaxy formation. Theoretical and technological advancements have allowed us to test our hypotheses directly, but the field is still in its infancy, and additional knowledge is required before its true potential can be unleashed. In this thesis, we present four papers aimed at transforming this field into a mature probe and showcasing how the dynamical nature of the large-scale structure can be modeled and measured.

Chapter 2 presents the first constraints on the splashback feature around massive galaxy clusters. This result is unique because the targeted lensing measurements considered here explore a mass range otherwise inaccessible. Chapter 3 presents the first quantitative predictions of how the edge of halos is affected in the presence of modifications of gravity. A straightforward but not simplistic semi-analytical model is used

to get a handle on the most critical parameters and connect this feature to the coincidence problem. Chapter 4 brings forward two new splashback observables. The first one is related to the correlation between a cluster splashback signal and the orientation of its central galaxy. The second is a mass-size relation for dark matter halos accessible thanks to the combination of lensing and galaxy profile measurements. By comparing hydrodynamical simulations to their dark-matter-only counterpart, this chapter also shows that the presence of baryons does not affect this feature. Chapter 5 is the culmination of the previous two and presents a concrete measurement of the mass-size relation used to constrain gravity models. Particularly noteworthy is the fact that this measurement is based only on photometric data. Finally, Chapter 6 presents three unrelated projects performed during the writing of this thesis. The focus is the intersection between gravitational-wave physics and the study of the large-scale structure of the Universe. We explore how this new class of signals is affected by gravitational lensing and cosmic expansion. Thanks to the direct connection to the metric, gravitational waves can be used to test a new sector of alternative theories of gravity that would be otherwise hard to constrain.

Bibliography

C. Brans and R. H. Dicke. Mach's Principle and a Relativistic Theory of Gravitation. *Physical Review*, 124(3):925–935, November 1961. doi: 10.1103/PhysRev.124.925.

R. R. Caldwell, Rahul Dave, and Paul J. Steinhardt. Cosmological Imprint of an Energy Component with General Equation of State. Phys. Rev. Lett., 80(8):1582–1585, February 1998. doi: 10.1103/PhysRevLett.80.1582.

Bernard Carr and George Ellis. Universe or multiverse? *Astronomy & Geophysics*, 49 (2):2.29–2.33, 04 2008. ISSN 1366-8781. doi: 10.1111/j.1468-4004.2008.49229.x.

Benedikt Diemer and Andrey V. Kravtsov. Dependence of the Outer Density Profiles of Halos on Their Mass Accretion Rate. ApJ, 789(1):1, July 2014. doi: 10.1088/0004-637X/789/1/1.

F. W. Dyson, A. S. Eddington, and C. Davidson. A Determination of the Deflection of Light by the Sun's Gravitational Field, from Observations Made at the Total Eclipse of May 29, 1919. *Philosophical Transactions of the Royal Society of London Series A*, 220:291–333, January 1920. doi: 10.1098/rsta.1920.0009.

Albert Einstein. Näherungsweise Integration der Feldgleichungen der Gravitation. *Sitzungsberichte der Königlich Preußischen Akademie der Wissenschaften (Berlin)*, pages 688–696, Jan 1916.

Daniel J. Eisenstein, Idit Zehavi, David W. Hogg, Roman Scoccimarro, Michael R. Blanton, Robert C. Nichol, Ryan Scranton, Hee-Jong Seo, Max Tegmark, Zheng Zheng, Scott F. Anderson, Jim Annis, Neta Bahcall, Jon Brinkmann, Scott Burles, Francisco J. Castander, Andrew Connolly, Istvan Csabai, Mamoru Doi, Masataka Fukugita, Joshua A. Frieman, Karl Glazebrook, James E. Gunn, John S. Hendry, Gregory Hennessy, Zeljko Ivezić, Stephen Kent, Gillian R. Knapp, Huan Lin, Yeong-Shang Loh, Robert H. Lupton, Bruce Margon, Timothy A. McKay, Avery Meiksin, Jeffery A. Munn, Adrian Pope, Michael W. Richmond, David Schlegel, Donald P. Schneider, Kazuhiro Shimasaku, Christopher Stoughton, Michael A. Strauss, Mark

SubbaRao, Alexander S. Szalay, István Szapudi, Douglas L. Tucker, Brian Yanny, and Donald G. York. Detection of the Baryon Acoustic Peak in the Large-Scale Correlation Function of SDSS Luminous Red Galaxies. ApJ, 633(2):560–574, November 2005. doi: 10.1086/466512.

A. Friedmann. Über die Krümmung des Raumes. *Zeitschrift fur Physik*, 10:377–386, January 1922. doi: 10.1007/BF01332580.

G. Gamow. Expanding Universe and the Origin of Elements. *Physical Review*, 70(7-8): 572–573, October 1946. doi: 10.1103/PhysRev.70.572.2.

Jérôme Gleyzes, David Langlois, Federico Piazza, and Filippo Vernizzi. New Class of Consistent Scalar-Tensor Theories. Phys. Rev. Lett., 114(21):211101, May 2015. doi: 10.1103/PhysRevLett.114.211101.

James E. Gunn and III Gott, J. Richard. On the Infall of Matter Into Clusters of Galaxies and Some Effects on Their Evolution. ApJ, 176:1, August 1972. doi: 10.1086/151605.

Kurt Hinterbichler, Justin Khoury, Aaron Levy, and Andrew Matas. Symmetron cosmology. Phys. Rev. D, 84(10):103521, November 2011. doi: 10.1103/PhysRevD.84. 103521.

Gregory Walter Horndeski. Second-Order Scalar-Tensor Field Equations in a Four-Dimensional Space. *International Journal of Theoretical Physics*, 10(6):363–384, September 1974. doi: 10.1007/BF01807638.

Edwin Hubble. A Relation between Distance and Radial Velocity among Extra-Galactic Nebulae. *Proceedings of the National Academy of Science*, 15(3):168–173, March 1929. doi: 10.1073/pnas.15.3.168.

Justin Khoury and Amanda Weltman. Chameleon cosmology. Phys. Rev. D, 69(4): 044026, February 2004. doi: 10.1103/PhysRevD.69.044026.

G. Lemaître. The Beginning of the World from the Point of View of Quantum Theory. Nature, 127(3210):706, May 1931. doi: 10.1038/127706b0.

LIGO Scientific Collaboration and Virgo Collaboration. Observation of Gravitational Waves from a Binary Black Hole Merger. Phys. Rev. Lett., 116(6):061102, February 2016. doi: 10.1103/PhysRevLett.116.061102.

Surhud More, Benedikt Diemer, and Andrey V. Kravtsov. The splashback radius as a physical halo boundary and the growth of halo mass. *The Astrophysical Journal*, 810 (1):36, Aug 2015. ISSN 1538-4357. doi: 10.1088/0004-637x/810/1/36.

S. Perlmutter, G. Aldering, G. Goldhaber, R. A. Knop, P. Nugent, P. G. Castro, S. Deustua, S. Fabbro, A. Goobar, D. E. Groom, I. M. Hook, A. G. Kim, M. Y. Kim, J. C. Lee, N. J. Nunes, R. Pain, C. R. Pennypacker, R. Quimby, C. Lidman, R. S. Ellis, M. Irwin, R. G. McMahon, P. Ruiz-Lapuente, N. Walton, B. Schaefer, B. J. Boyle, A. V. Filippenko, T. Matheson, A. S. Fruchter, N. Panagia, H. J. M. Newberg, W. J. Couch, and The Supernova Cosmology Project. Measurements of Ω and Λ from 42 High-Redshift Supernovae. ApJ, 517(2):565–586, June 1999. doi: 10.1086/307221.

Planck Collaboration. Planck 2018 results. I. Overview and the cosmological legacy of Planck. A&A, 641:A1, September 2020. doi: 10.1051/0004-6361/201833880.

William H. Press and Paul Schechter. Formation of Galaxies and Clusters of Galaxies by Self-Similar Gravitational Condensation. ApJ, 187:425–438, February 1974. doi: 10.1086/152650.

Adam G. Riess, Alexei V. Filippenko, Peter Challis, Alejandro Clocchiatti, Alan Diercks, Peter M. Garnavich, Ron L. Gilliland, Craig J. Hogan, Saurabh Jha, Robert P. Kirshner, B. Leibundgut, M. M. Phillips, David Reiss, Brian P. Schmidt, Robert A. Schommer, R. Chris Smith, J. Spyromilio, Christopher Stubbs, Nicholas B. Suntzeff, and John Tonry. Observational Evidence from Supernovae for an Accelerating Universe and a Cosmological Constant. AJ, 116(3):1009–1038, September 1998. doi: 10.1086/300499.

G. Rosi, F. Sorrentino, L. Cacciapuoti, M. Prevedelli, and G. M. Tino. Precision measurement of the Newtonian gravitational constant using cold atoms. Nature, 510(7506): 518–521, June 2014. doi: 10.1038/nature13433.

Vera C. Rubin and Jr. Ford, W. Kent. Rotation of the Andromeda Nebula from a Spectroscopic Survey of Emission Regions. ApJ, 159:379, February 1970. doi: 10.1086/150317.

Marc Schumann. Direct detection of WIMP dark matter: concepts and status. *Journal of Physics G Nuclear Physics*, 46(10):103003, October 2019. doi: 10.1088/1361-6471/ab2ea5.

Karl Schwarzschild. On the gravitational field of a mass point according to Einstein's theory. *Sitzungsber. Preuss. Akad. Wiss. Berlin (Math. Phys.)*, 1916:189–196, 1916.

Harlow Shapley and Heber D. Curtis. The Scale of the Universe. *Bulletin of the National Research Council*, 2(11):171–217, May 1921.

Volker Springel, Simon D. M. White, Adrian Jenkins, Carlos S. Frenk, Naoki Yoshida, Liang Gao, Julio Navarro, Robert Thacker, Darren Croton, John Helly, John A. Peacock, Shaun Cole, Peter Thomas, Hugh Couchman, August Evrard, Jörg Colberg, and Frazer Pearce. Simulations of the formation, evolution and clustering of galaxies and quasars. Nature, 435(7042):629–636, June 2005. doi: 10.1038/nature03597.

Gary Steigman and Michael S. Turner. Cosmological constraints on the properties of weakly interacting massive particles. *Nuclear Physics B*, 253:375–386, January 1985. doi: 10.1016/0550-3213(85)90537-1.

J. H. Taylor and J. M. Weisberg. A new test of general relativity - Gravitational radiation and the binary pulsar PSR 1913+16. ApJ, 253:908–920, February 1982. doi: 10.1086/159690.

A. I. Vainshtein. To the problem of nonvanishing gravitation mass. *Physics Letters B*, 39(3):393–394, May 1972. doi: 10.1016/0370-2693(72)90147-5.

Clifford M. Will. *Theory and Experiment in Gravitational Physics*. 1993.

Ivaylo Zlatev, Limin Wang, and Paul J. Steinhardt. Quintessence, Cosmic Coincidence, and the Cosmological Constant. Phys. Rev. Lett., 82(5):896–899, February 1999. doi: 10.1103/PhysRevLett.82.896.

F. Zwicky. Die Rotverschiebung von extragalaktischen Nebeln. *Helvetica Physica Acta*, 6:110–127, January 1933.

Chapter 2

Weak-lensing constraints on splashback around massive clusters

The splashback radius r_{sp} separates the physical regimes of collapsed and infalling material around massive dark matter halos. In cosmological simulations, this location is associated with a steepening of the spherically averaged density profile $\rho(r)$. In this work, we measure the splashback feature in the stacked weak gravitational lensing signal of 27 massive clusters from the Cluster Canadian Comparison Project with careful control of residual systematics effects. We find that the shear introduced by the presence of additional structure along the line of sight significantly affects the noise at large clustercentric distances. Although we do not detect a significant steepening, the use of a simple parametric model enables us to measure both $r_{sp} = 3.5^{+1.1}_{-0.7}$ comoving Mpc and the value of the logarithmic slope $\gamma = \log \rho / \log r$ at this point, $\gamma(r_{sp}) = -4.3^{+1.0}_{-1.5}$.

2.1   Introduction

In the concordance lambda cold dark matter (ΛCDM) model, collisionless dark matter acts as the building block of cosmic structure, contributing about 25 percent of the total energy density in the Universe and the majority of the total mass (Planck Collaboration, 2016). In this framework, gravity is the primary force behind the growth of structure in the matter field and is able to form the present-day cosmic web from an almost homogeneous initial state. Fully collapsed structures, known as halos, are thought to grow both through mergers of smaller ones (hierarchical clustering) and continuous infall of ambient dark matter (smooth accretion).

An intuitive understanding of this second mechanism is given by the study of spherical collapse in an expanding Universe (see Gunn and Gott, 1972; Fillmore and Goldreich, 1984, for some historic landmark results). Shells of material surrounding an overdensity eventually decouple from the Hubble flow and start collapsing toward it. As more shells orbit the halo, the wrapping in phase space of different streams results in caustics visible in the density profile. Of particular interest is the region around the outermost caustic, where the physical regimes of accreting and collapsed material meet.

More recently, Diemer and Kravtsov (2014, DK14 from now on) studied the spherically averaged density profile $\rho(r)$ of these regions in dark matter only simulations and have reported a change in slope compared to the collisionless equilibrium profile (Einasto or NFW, Einasto, 1965; Navarro et al., 1997). More et al. (2015) argued that the splashback radius r_{sp}, corresponding to the minimum logarithmic slope $\gamma(r) = \log \rho(r) / \log r$, could function as a physically motivated definition for the boundary of dark matter halos. This role is usually assumed by proxies for the virial radius such as r_{200m}, defined as the radius inside which the average halo density is 200 times the average matter density of the Universe ρ_m. While this radius has a clear definition based on analytical solutions of idealized virialization scenarios, the mass contained within it, known as M_{200m}, is an imperfect measure of the halo mass. This is because it is subject to a pseudo-evolution caused by the redshift dependence of ρ_m (Diemer et al., 2013). In contrast, because the caustic associated with splashback is connected to the apocenter of recently accreted material, all the material within r_{sp} is necessarily collapsed material and should rightfully contribute to the halo mass.

At larger distances, the presence of correlated structure surrounding the halo is expected to shape the density profile. Using the language of the halo model (see e.g. Cooray and Sheth, 2002, for a review), this is a transition region from the 1-halo term to the 2-halo term. DK14 have however reported that in the outermost regions ($r \lesssim 9 r_{200m}$), the 2-halo term based on the matter correlation function provides a worse fit to simulations compared to a simple power law.

Because the slope of the density profile at r_{sp} is found to be, on average, a decreasing function of the halo mass, DK14 first pointed out that large overdensities are the

ideal target for the detection of this feature – i.e. measuring a significant departure from the equilibrium profile. This makes galaxy clusters the ideal candidates since they correspond to the most massive halos in the Universe. For this mass range, r_{sp} is expected to be located around r_{200m}, at a cluster-centric distance of the order of a few Mpc.

The splashback feature should also be present in the radial distribution of galaxies. This was first detected by More et al. (2016) using the large sample of redMaPPer clusters from Rykoff et al. (2014), and studied further in Baxter et al. (2017). However, these studies find a discrepancy between the inferred splashback radius and the expected distribution of subhalos based on dark matter only simulations. Known physical processes (e.g. tidal disruption and dynamical friction) are not expected to induce a mismatch between the galaxy and subhalo distributions at splashback scales and this deviation is still unexplained. In particular, while the results have been shown to depend on the details of the cluster finding algorithm (Zu et al., 2017; Busch and White, 2017), it is still uncertain if this can fully explain the discrepancy (Chang et al., 2018).

Chang et al. (2018) studied a sample of redMaPPer clusters selected in Dark Energy Survey year 1 data. For this large sample, they detected a splashback feature in the galaxy distribution *and* from weak lensing measurements. The latter has the advantage that the lensing signal probes the matter distribution directly (see e.g. Hoekstra et al., 2013, for a review). The first attempt to detect the splashback feature using weak gravitational lensing was presented in Umetsu and Diemer (2017), who used a sample of 16 high-mass clusters in the Cluster Lensing and Supernova survey with Hubble (CLASH). Unfortunately, the limited field of view (foV) of Suprime-Cam prevented precise measurements in the outer regions, and as a result, Umetsu and Diemer (2017) could only provide a lower limit on the splashback radius.

In this work, we provide a measurement[1] of splashback using weak lensing observations for a sample of 27 massive clusters of galaxies that were observed as part of the Canadian Cluster Comparison Project (CCCP; Hoekstra et al., 2012). Hence our strategy is similar to that employed by Umetsu and Diemer (2017), but we take advantage of the fact that the CCCP observations were obtained using MegaCam, which has a foV of 1 deg^2, and enables us to measure the lensing signal beyond the splashback radius. The chaper is organized as follows: in Sec. 2.2 we present our dataset and describe our lensing analysis, in Sec. 2.3 we show the results of our fit and the implications for splashback, and in Sec. 2.4 we draw our conclusions. Throughout the chapter we employ a flat ΛCDM cosmology with $H_0 = 70 \ \mathrm{km \ s^{-1} \ Mpc^{-1}}$, $\Omega_m = 0.3$, $\Omega_c = 0.25$ and $\sigma_8 = 0.80$.

---

[1]In the interest of reproducibility we make our splashback code publicly available at https://github.com/contigiani/splash/.

Table 2.1: The full cluster sample, 'CCCP all', used in this chapter. RA and Dec. are the sky position of the cluster center (brightest cluster galaxy, or X-ray peak for coordinates marked with §), z is the cluster redshift, $\langle\beta\rangle$ is the average value of D_{LS}/D_S (see Sec. 2.2.2), M_g is the gas mass within r_{500c}, defined as the radius of the sphere inside which the mean halo density is 500 times the critical density of the Universe at redshift z and M_{200m} is the mass enclosed within r_{200m}. These values are recovered from the NFW fit performed in H15. The values for M_g are taken from the X-ray analysis of M13 or, for values marked with †, they are defined using the scaling relations found in the same paper. Clusters listed below the horizontal line belong to the high-mass subsample.

Name	RA (J2000)	Dec. (J2000)	z	$\langle\beta\rangle$	M_g [10^{13} M$_\odot$]	M_{200m} [10^{14} M$_\odot$]
MS 0440.5+0204	$04^h43^m09.0^s$	$+02°10'19''$	0.19	0.656	2.4	3.8
Abell 1234	$11^h22^m30.0^s$	$+21°24'22''$	0.163	0.699	3.8†	8.3
RX J1524.6+0957	$15^h24^m38.3^s$	$+09°57'43''$	0.516	0.329	4.1	6.5
Abell 1942	$14^h38^m21.9^s$	$+03°40'13''$	0.224	0.621	4.4	14.6
Abell 2259	$17^h20^m09.7^s$	$+27°40'08''$	0.164	0.697	5.0	8.6
MACS J0913.7+4056	$09^h13^m45.5^s$	$+40°56'29''$	0.442	0.396	5.3	6.8
Abell 1246	$11^h23^m58.5^s$	$+21°28'50''$	0.19	0.661	5.6†	9.5
MS 1008.1-1224	$10^h10^m32.3^s$	$-12°39'53''$	0.301	0.526	5.8	17.4
3C295	$14^h11^m20.6^s$	$+52°12'10''$	0.46	0.374	6.2	12.6
Abell 586	$07^h32^m20.3^s$	$+31°38'01''$	0.171	0.674	6.5	5.0
Abell 611	$08^h00^m56.8^s$	$+36°03'24''$	0.288	0.533	6.6	10.0
Abell 2104	$15^h40^m07.9^s$	$-03°18'16''$	0.153	0.712	6.8	17.2
Abell 2111	$15^h39^m40.5^s$	$+34°25'40.5''$	0.229	0.614	7.4	10.2
Abell 959	$10^h17^m36.0^s$	$+59°34'02''$	0.286	0.549	7.5	21.1
Abell 520	$04^h54^m10.1^s$§	$+02°55'18''$§	0.199	0.654	8.5	16.6

Abell 2537	$23^{\rm h}08^{\rm m}22.2^{\rm s}$	$-02°11′32″$	0.295	0.532	8.6	22.4
Abell 851	$09^{\rm h}42^{\rm m}57.5^{\rm s§}$	$+46°58′50″^§$	0.407	0.421	9.7	22.6
Abell 1914	$14^{\rm h}26^{\rm m}02.8^{\rm s§}$	$+37°49′28″^§$	0.171	0.693	9.9	14.7
MS 0451.6–0305	$04^{\rm h}54^{\rm m}10.8^{\rm s}$	$-03°00′51″$	0.54	0.315	10.3	18.0
Abell 521	$04^{\rm h}54^{\rm m}06.9^{\rm s}$	$-10°13′25″$	0.253	0.577	10.6	11.5
Abell 2204	$16^{\rm h}32^{\rm m}47.0^{\rm s}$	$+05°34′33″$	0.152	0.714	11.6	21.8
Abell 1835	$14^{\rm h}01^{\rm m}02.1^{\rm s}$	$+02°52′43″$	0.253	0.58	12.1	21.5
Abell 2261	$17^{\rm h}22^{\rm m}27.2^{\rm s}$	$+32°07′58″$	0.224	0.621	14.6	26.4
CIZA J1938+54	$19^{\rm h}38^{\rm m}18.1^{\rm s}$	$+54°09′40″$	0.26	0.569	15.6[†]	18.6
Abell 697	$08^{\rm h}42^{\rm m}57.6^{\rm s}$	$+36°21′59″$	0.282	0.552	15.6	15.1
RX J1347.5–1145	$13^{\rm h}47^{\rm m}30.1^{\rm s}$	$-11°45′09″$	0.451	0.377	16.3	20.9
Abell 2163	$16^{\rm h}15^{\rm m}49.0^{\rm s}$	$-06°08′41″$	0.203	0.63	23.3	18.9

2.2   Cluster lensing

In this section, we discuss how the sheared images of distant galaxies can be used to constrain the matter distribution of clusters along the line of sight. After introducing our cluster sample, we present the weak lensing measurements and explain our methodology, with a particular focus on systematic effects and noise estimation.

2.2.1   Sample characterization

Our dataset is based on CCCP, a survey targeting X-ray selected massive clusters at $z \lesssim 0.5$ introduced for the first time in Hoekstra et al. (2012) and re-analyzed in Hoekstra et al. (2015, H15 from now on). The starting points of our analysis are the r-band images of 27 clusters captured by MegaCam at the Canada–France–Hawaii Telescope (CHFT). We exclude from the original CCCP images those corresponding to ongoing mergers: Abell 115, Abell 222/3, Abell 1758, and MACS J0717.5+3745 because these systems display a visible double peaked matter distribution for which two splashback surfaces might intersect each other.

The objects are characterized by masses $3.8 < M_{200m}/(10^{14}\ \mathrm{M_\odot}) < 26.4$ and cover a redshift range $0.15 < z < 0.55$, with only six of them located at $z > 0.3$. Table 2.1 reviews the sample and presents the quantities relevant for this work. For more details about the cluster sample we refer the reader to Hoekstra et al. (2012), H15 for a description of the weak lensing analysis, and the companion paper Mahdavi et al. (2013) for the analysis of X-ray observations.

In simulations, DK14 found a correlation between the splashback feature and the halo mass. We, therefore, define a high-mass subsample of our clusters, containing the 13 most massive objects. The average M_{200m} of the sample and the subsample, weighted by the signal-to-noise ratio (SNR), equal 1.7 and $2.0 \times 10^{15}\ \mathrm{M_\odot}$, respectively. We choose to employ the gas mass M_g within r_{500c} reported by Mahdavi et al. (2013) to define our high-mass threshold. This is because this value is found to be a robust estimator of the weak lensing mass and its measurement is mostly independent of it since it is based on a different physical mechanism. A weak dependence between the two is left due to the lensing-based definition of r_{500c}.

Targeted observations such as the ones discussed in this work currently represent the most efficient approach to study clusters of virial mass around $10^{15}\ \mathrm{M_\odot}$. In particular, such a sample cannot be obtained by present-day or near-future wide surveys, e.g. DES (DES Collaboration, 2017) or the Kilo-Degree Survey (KiDS collaboration, 2017), because massive halos are rare (i.e. $\ll 1$ per FoV) and targeted deep data result in a higher SNR compared to wide surveys. For these reasons, the SDSS and DES studies of More et al. (2016), Baxter et al. (2017) and Chang et al. (2018) are based instead on large samples of low-mass clusters: 8649 clusters with $\langle M_{200m} \rangle = 2.7 \times 10^{14}\ \mathrm{M_\odot}$ for SDSS (Miyatake et al., 2016) and 3684 clusters with $\langle M_{200m} \rangle = 3.6 \times 10^{14}\ \mathrm{M_\odot}$ for DES Y1. In contrast, our dataset is much closer in nature to the CLASH sample used in Umetsu

and Diemer (2017), also based on targeted observations. In particular, the mass of their stacked ensemble, $M_{200m} = 1.9 \times 10^{15}$ M$_\odot$, matches ours. Nevertheless, we want to mention one feature unique to CCCP: the FoV of MegaCam (1×1 deg) is significantly larger than that of Suprime-Cam (34×27 arcmin), the instrument used for the CLASH profile reconstruction at large scales (Umetsu et al., 2016). This is particularly suited for our purposes since it allows us to better cover cluster-centric distances where the splashback radius is located.

2.2.2   Tangential shear

In the weak lensing regime, the shear field is found by averaging the PSF-corrected ellipticities of a sample of background sources. We follow H15 and use sources in the magnitude range $22 < m_r < 25$. The lower limit reduces the presence of foreground objects such as bright galaxies belonging to the clusters, which are abundant in the central regions and are not sheared by the cluster's mass distribution. Because this operation is unable to completely remove cluster members, we chose to model the residual contamination statistically, as explained in Sec. 2.2.3.

Shapes are measured using an improved KSB method (Kaiser et al., 1995; Luppino and Kaiser, 1997; Hoekstra et al., 1998). The quadrupole moments of the galaxy images are used to construct a polarization tensor e, which is then corrected for the point spread function (PSF) of the observing instrument. In Sec. 2.2.3 we address this step in more detail and mention the improvements we have implemented since H15. The shear polarizability $\tilde{P}^\gamma$ quantifies how the observed polarization of an individual galaxy is related to the gravitational shear. For an ensemble of sources the shear components are hence measured as a noise-weighted average, $\langle e_i/\tilde{P}^\gamma \rangle$, where the individual weights are written as (Hoekstra et al., 2000)

$$w = \frac{1}{\langle \epsilon^2 \rangle + \left(\sigma_e/\tilde{P}^\gamma \right)^2}. \tag{2.1}$$

In this expression two sources of noise are included: the scatter introduced by the intrinsic variance of galaxy ellipticities $\langle \epsilon^2 \rangle$ and the uncertainty in the measured polarization σ_e due to noise in the imaging data. Following Hoekstra et al. (2000) we use $\langle \epsilon^2 \rangle^{1/2} = 0.25$.

For an isolated circular overdensity, the induced shear is purely tangential, i.e. the deformation is parallel to the radial direction. In general, this shear component is related to the projected mass surface density $\Sigma(R)$ as a function of the radial coordinate
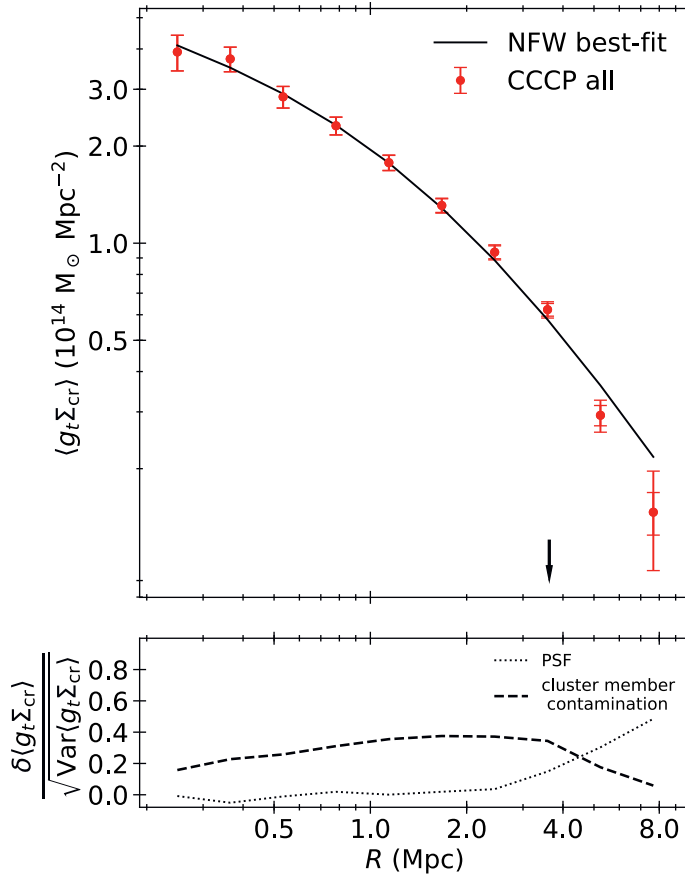
Figure 2.1: Lensing signal. The top panel shows the noise-weighted stacked signal of the 27 clusters in our sample as a function of comoving clustercentric distance, together with a best-fitting NFW profile to the first five data points (see Sec. 2.2.2 for more information). The arrow points to the inferred location of r_{200m}; in simulated galaxy clusters the splashback feature is located around this position. The larger error bars are the full 1σ errors for the data points, while the inner error bars account only for statistical uncertainty. The difference between the two is apparent only in the last few data points. The bottom panel shows an estimate of the expected residual systematics left after the corrections discussed in Sec. 2.2.3 are applied, expressed as a fraction of the total uncertainty. These effects are found to be consistent with the error bars.

R:

$$\gamma_{\mathrm{t}}(R) = \frac{\overline{\Sigma}(< R) - \Sigma(R)}{\Sigma_{\mathrm{cr}}} = \frac{\Delta\Sigma(R)}{\Sigma_{\mathrm{cr}}}, \qquad (2.2)$$

$$\Sigma_{\mathrm{cr}} = \frac{c^2}{4\pi G} \frac{1}{\langle\beta\rangle} \frac{1}{D_{\mathrm{L}}}. \qquad (2.3)$$

In these expressions, the profile $\Delta\Sigma(R)$ is called excess surface density and the critical density Σ_{cr} is a geometrical factor quantifying the lensing efficiency as a function of the relative position of source and lens. The definition above applies for a lens at distance D_{L} shearing an ensemble of sources. $\langle\beta\rangle$ is the average of the quantity $\max[0, D_{\mathrm{LS}}/D_{\mathrm{S}}]$ for each source, with D_{LS} being the individual lens-to-source distance[2] and D_{S} the distance to the source.

Because we work with single-band observations, we are unable to derive individual photometric redshifts. Fortunately, a representative photometric redshift distribution is sufficient to estimate β. This distribution is obtained for all clusters by magnitude-matching the most recent COSMOS photometric catalog (COSMOS2015, Laigle et al., 2016) to our source r-band magnitude range.

We point out that the measured average ellipticity is an estimator of the reduced shear

$$g_i = \frac{\gamma_i(R)}{1 - \Sigma(R)/\Sigma_{\mathrm{crit}}}. \qquad (2.4)$$

However, because we are interested in constraining a feature located in a low-density region, for our main analysis we will assume the first-order approximation $g_i \simeq \gamma_i$ when fitting a model. From our source catalogs we extract the tangential component $g_{\mathrm{t}}(\theta_j)$ in radial bins and estimate for each cluster the data covariance matrix as the sum of two terms: the first accounts for statistical noise in the average ellipticity and the second one takes into account the presence of additional shear introduced by uncorrelated structure along the line of sight. More details about the evaluation are presented in Appendix 2A.

The top panel of Figure 2.1 presents the average noise-weighted signal of the full cluster sample. The double error bars in the figure illustrate how the inclusion of the second source of noise has an impact on the uncertainties at large scales. An indicative NFW fit, obtained using the virial overdensity from Bryan and Norman (1998) at an assumed redshift $z = 0.25$, is also shown. The position of r_{200m} for the best-fit model is also indicated in the same figure.

---

[2]Note that D_{LS} is negative for foreground sources.
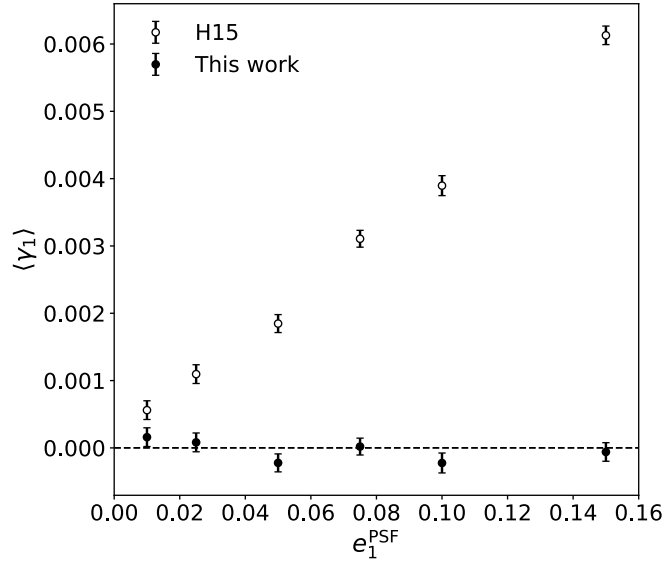
Figure 2.2: PSF correction improvements. Image simulations are used to quantify the residual additive bias not captured by the correction obtained in H15. The circles show how residual additive bias in the average shear $\langle \gamma_1 \rangle$ was present in the presence of simulated PSF anisotropy ($e_1^{\mathrm{PSF}} \neq 0$). In this work (filled points) we are able to nullify this effect by boosting the KSB smear polarizability P^{sm}. See Sec. 2.2.3 for more details.

2.2.3   Residual systematics

In this section, we address the effects of the corrections we have implemented to tackle two systematic effects that are particularly important for our analysis: PSF anisotropy and cluster member contamination. In particular, we estimate the amplitude of any residual systematic effects as plotted in the bottom panel of Figure 2.1.

In the KSB method, the observed galaxy polarizations are corrected for PSF anisotropy using

$$e_i \rightarrow e_i - \sum_j P_{ij}^{\mathrm{sm}} p_j^*, \tag{2.5}$$

where the smear polarizability P^{sm} quantifies how susceptible a source is to PSF distortions and p_j is the PSF anisotropy measured using point-like sources (see e.g. Hoekstra et al., 1998).

The observed polarizations and polarizabilities are, however, biased because of noise in the images. If unaccounted for, this leads to biased cluster masses. For the shear, these corrections can be expressed in terms of a multiplicative and additive bias, μ and b:

$$\gamma_i \rightarrow (1 + \mu)\gamma_i + b. \tag{2.6}$$

To ensure accurate mass estimates, H15 focused on the impact of multiplicative bias. To do so, they used image simulations with a circular PSF to calibrate the bias as a function of source SNR and size. However, the actual PSF is not round and H15, therefore, quantified the impact of an anisotropic PSF on the multiplicative bias correction. The details of these simulations, based on `galsim` (Rowe et al., 2015), can be found in section 2.2 and appendix A of H15. The galaxy properties are based on HST observations, resulting in images that match the cluster data. The PSF is modeled as a Moffat profile, which is a good representation of ground-based data. Appendix A in H15 examines the impact of PSF anisotropy and revealed that about 4 percent of this source of bias remains after correction (see their fig. A1). While the impact of this residual bias is negligible, further study revealed that it can be reduced by empirically correcting the smear polarizability for noise bias. We have increased P^{sm} by a factor of 1.065, such that no residual additive bias remains visible, see Figure 2.2. We also verified that this latest correction does not introduce significant trends with source characteristics. We use the difference between the ensemble lensing signal measured before and after this improvement as a (conservative) estimate of any unknown systematics affecting the shape measurement method.

The second effect we account for is the presence of cluster members in our source catalogs. Note that in this case, we have not updated the methodology from H15, but we still report it here for completeness. If we assume that cluster members are randomly oriented, as found by Sifón et al. (2015), their inclusion among our sources has the effect

of diluting the measured shear. To correct for this, we multiply $\gamma_t(R)$ by a boost factor $B(R)$ defined as a function of the projected comoving distance R:

$$B(R) = 1 + f_{\text{cont}}(R)/f_{\text{obs}}(R). \tag{2.7}$$

The contamination term f_{cont} accounts for the decrease of the ellipticity average due to the presence unsheared sources and, by comparison with blank fields, it is found to be (1) a decreasing function of distance from the cluster center and (2) negligible beyond a distance r_{max}. An extra factor f_{obs} is also introduced to model the reduced background galaxy counts due to obscuration by cluster members. This factor is computed by stacking the cluster images with simulated blank fields and measuring how many simulated sources are obscured.

The functions appearing in the boost factor are written empirically as

$$\frac{1}{f_{\text{obs}}(R)} = 1 + \frac{0.021}{0.14 + (R/r_{500})^2} \text{ and} \tag{2.8}$$

$$f_{\text{cont}}(R) = n_0 \left(\frac{1}{R + R_c} - \frac{1}{r_{\text{max}} + R_c} \right); \tag{2.9}$$

where n_0 and R_c are fitted independently for each cluster and $B(R) = 0$ for $R > r_{\text{max}} \equiv 4(1 + z)$ Mpc.

To quantify the amplitude of residual systematics for this second correction, we refer to H15, where a residual scatter of about 2 percent around the ensemble correction was reported.

2.3   Splashback

In this main part of the chapter, we fit the observed weak lensing signal using the spherical density profile presented in DK14. This profile is designed to reproduce the expected flattening of the density profile at large radii due to the presence of infalling material, as seen in numerical simulations.

2.3.1   Fitting procedure

The projected surface density profile $\Sigma(R)$ for a spherical lens with matter density $\rho(r)$ is:

$$\Sigma(R) = 2 \int_0^\infty dr' \, \rho \left(\sqrt{r'^2 + R^2} \right), \tag{2.10}$$

where we limit the integration range of the line of sight variable r' to $[0, 40]$ Mpc for our numerical calculations. We also verify that the chosen upper limit has no effect on our results by repeating the analysis with a wider range $[0, 80]$ Mpc. For cosmological

overdensities, this profile can be connected to the lensing signal through Eqs. 2.2 and 2.4.

In this section we use a model for $\rho(r)$ first introduced by DK14 with the following components: an Einasto profile ρ_{Ein} (Einasto, 1965) to model the inner dark matter halo, a transition term $f_{\text{trans}}(r)$ to capture a steepening effect at the halo edge and a power-law $\rho_{\text{out}}(r)$ to model the distribution of infalling material in the outer regions. The mathematical expressions are the following:

$$\rho(r) = \rho_{\text{Ein}}(r) f_{\text{trans}}(r) + \rho_{\text{out}}(r); \tag{2.11}$$

$$\rho_{\text{Ein}}(r) = \rho_{\text{s}} \exp\left(-\frac{2}{\alpha}\left[\left(\frac{r}{r_{\text{s}}}\right)^{\alpha} - 1\right]\right), \tag{2.12}$$

$$f_{\text{trans}}(r) = \left[1 + \left(\frac{r}{r_{\text{t}}}\right)^{\beta}\right]^{-\gamma/\beta}, \tag{2.13}$$

$$\rho_{\text{out}} = \rho_0 \left(\frac{r}{r_0}\right)^{-s_e}. \tag{2.14}$$

In DK14 the infalling term includes an offset corresponding to the average matter density, but this is not present in our fitting function because the tangential shear in Equation (2.2) is completely insensitive to it.

In its general form, this model depends on a large number of parameters. In order to reduce its degrees of freedom we, therefore, choose to set strong priors on a few parameters. As done in Baxter et al. (2017) and Chang et al. (2018) we do not fit both ρ_0 and r_0, but choose to fix one of them, as they are degenerate. We impose Gaussian priors $\log(0.2) \pm 0.1$, $\log(6) \pm 0.2$ and $\log(4) \pm 0.2$ on the logarithms of the exponents $\log\alpha$, $\log\beta$, and $\log\gamma$, respectively. The loose prior on the Einasto shape parameter α is motivated by dark matter only simulations and its 1σ interval covers the expected scatter due to the redshift and mass distribution of our sample (Gao et al., 2008; Dutton and Macciò, 2014), while for the exponents in the transition term the stringent priors are centered on the values suggested by DK14. We also set a Gaussian prior on the truncation radius r_t, 4 ± 2, based on the same results. The location of the median is based on the r_{200m} inferred from our NFW fit and the selected standard deviation covers the expected range due to the mass distribution of our sample. Finally, based on previous measurements, we also set a minimum value of 1 for the outer slope s_e and a physically motivated minimum value of 0 for the density parameters ρ_s and ρ_0.

A rescaling of the radial coordinate with an overdensity radius (e.g. r_{200m}) is often employed when fitting the profile described above. We also attempt to rescale our coordinates with either r_{500c} or r_{200m}, but due to the uncertainties on the individual cluster profiles, no rescaling results in the splashback feature being constrained with

higher precision. Despite this, we still attempt to remove the redshift dependence of the average matter density of the Universe by using comoving coordinates.

We follow Umetsu and Diemer (2017) and do not include a miscentering term in our tangential shear model. In general, a shift in position of the cluster centres reported in Table 2.1 would cause a smoothing of the lensing profile in the central region. An estimate of the area affected by such an effect can be obtained by considering the difference between two independent estimators of the halo centre: the position of the brightest cluster galaxy or the X-ray luminosity peak. Our sample is found to be well centered (see M13) with the root mean square of the offset between the two $\sigma_{\mathrm{off}} = 33$ kpc. For the scales plotted in Figure 2.3 we therefore do not expect our data to be affected by miscentering.

A fit to input data $\gamma_t(R)$ with the covariance matrix defined in Sec. 2.2 is performed by sampling the posterior distribution of the parameters $[\rho_s, r_s, \log \alpha, r_t, \log \beta, \log \gamma, \rho_0, s_e]$ using the Markov Chain Monte Carlo ensemble sampler emcee[3] (Foreman-Mackey et al. 2013, based on Goodman and Weare 2010).

2.3.2 Interpretation

Figure 2.3 visually presents our results. The left-hand panel shows the best-fitting model to the lensing signal, while the right-hand panel shows the posterior distribution of the inferred profile. To better highlight the splashback feature we choose to focus on the dimensionless logarithmic slope $\gamma = d \log \rho / d \log r = r/\rho \; d\rho/dr$ when plotting the posterior of our model.

For both CCCP samples considered a minimum of the slope is identified. At larger distances, the results are the least interesting. In these regions, the power-law term becomes dominant and the value of the slope is set exclusively by the exponent s_e. In particular, its lower limit is artificially imposed by our prior.

What is more relevant to our study is the minimum value of the slope $\gamma(r)$ and its location, i.e. the splashback radius r_{sp}. The 68 percent credible intervals of both quantities are indicated as shaded sections of the vertical and horizontal histograms. Our measured 99.7 percent confidence interval of $\gamma(r_{\mathrm{sp}})$ for the full sample is $[-10.9, -2.3]$, meaning that we are unable to measure a significant departure from the slope expected for an NFW profile (about -2.5). Despite this, we are still able to constrain the value of both the splashback radius and the logarithmic slope at this point, $r_{\mathrm{sp}} = 3.5^{+1.1}_{-0.7}$ Mpc and $\gamma(r_{\mathrm{sp}}) = -4.3^{+1.0}_{-1.5}$. We also highlight that the high-mass sample returns similar constraints with only half the sample size, $r_{\mathrm{sp}} = 3.5^{+1.3}_{-0.8}$ and $\gamma(r_{\mathrm{sp}}) = -3.7^{+0.9}_{-1.6}$.

As a point of reference, we also show the expected profiles from a suite of zoom-in hydrodynamical simulations of massive clusters (Hydrangea, Bahé et al., 2017). From the full Hydrangea sample, we have selected the eight most massive clusters for this comparison in order to obtain a sample with an average value of $\langle M_{200m} \rangle = 1.7 \times 10^{15}$

---

[3]https://emcee.readthedocs.io/
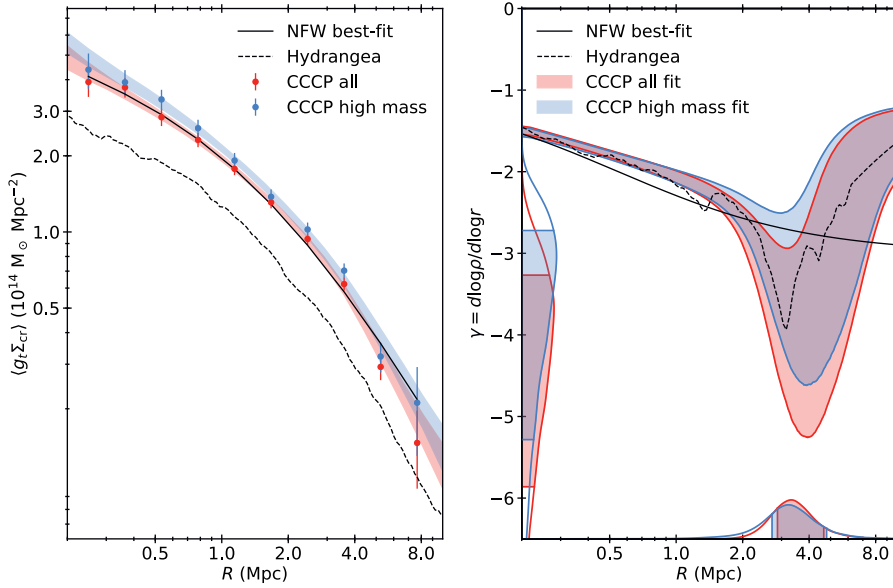
Figure 2.3: Splashback measurement. The left-hand panel shows the measured lensing signal for our full sample and a subsample of the 13 most massive clusters as a function of comoving clustercentric distance, together with the 68 percent confidence intervals from the DK14 fit. The right-hand panel shows the posterior of the three-dimensional logarithmic slope for the same model. The histograms on the horizontal axis are the distributions of the inferred position for the minimum of γ (i.e. the splashback radius r_{sp}), while the histograms on the vertical axis are the distributions of $\gamma(r_{sp})$. The solid black lines refer to the NFW fit shown in Figure 2.1, while the dashed lines correspond to predictions from hydrodynamical simulations of massive clusters (Hydrangea). The amplitude of the Hydrangea and CCCP signals are different because we match the virial mass of our observed sample at $z \gtrsim 0.2$ with simulated clusters at $z = 0$.

$M_\odot$, similar to our dataset, but evaluated at $z = 0$ instead of $z = 0.2$. Note that the amplitude of the signal plotted in Figure 2.3 is lower than the observed sample due the evolution of the average matter density of the Universe. Our slope measurements are found to be agreement with what is seen in simulations.

As done in Umetsu and Diemer (2017), we study the impact of the model parameters on the predictions for r_{sp} and $\gamma(r_{sp})$ to verify that our dataset is informative and we are not simply sampling our model priors. Of crucial importance is the truncation radius r_t, which, in the original definition of the DK14 profile, explicitly sets the position of the splashback feature.

Similarly to Umetsu and Diemer (2017), we also find that we are unable to fully constrain this parameter. This can be seen in Figure 2.4, where we plot the posteriors of three relevant parameters for two different choices of the r_t prior: the Gaussian assumed in our main study and a flat prior in the range $[0, 20]$ Mpc. While the posterior for $\gamma(r_{sp})$ (middle row) is mostly unaffected by this choice, we obtain a looser upper limit on the splashback radius (top panel) in the second case: $r_{sp} = 3.9^{+2.4}_{-0.9}$. As visible in the bottom-left panel, this is due to a clear correlation with r_t.

We find no correlation between r_{sp} and r_t for $r_t \gtrsim 10$ Mpc. In this regime, the location of the minimum of $\gamma(r)$ is controlled by the presence of the infalling term $\rho_{in}(r) \propto r^{-s_e}$. Because the slope s_e is relatively gentle, if r_t is large enough the truncation happens in a region dominated by the infalling material and cannot be constrained. Because the truncation is expected to be visible in the transition regime, our Gaussian prior on r_t effectively forces it to a physically motivated position and, from the figure, we confirm that it does not introduce a biased posterior peak.

2.4   Conclusions

We have shown in this work that targeted weak lensing observations of massive clusters can be used to measure the splashback feature and that particular care is required when correcting for residual PSF contaminations, which should be well understood, and estimating the data covariance matrix, which should take into account the presence of additional structure along the line of sight. Using a stack of 27 massive clusters from CCCP we have fully constrained for the first time the splashback radius around massive clusters, $r_{sp} = 3.6^{+1.2}_{-0.7}$, and similar precision has also been achieved with as little as 13 objects. We stress that, because of the purely gravitational nature of weak lensing, minimal assumptions are required to interpret our signal.

In the last few years, the study of the physics of accretion at the outskirts of massive dark matter halos has become observationally viable. Splashback offers a unique view into the phase-space configuration of halos, which has not yet been explored in observations. In particular, the physics behind it appears to be remarkably uncomplicated and semianalytical models of spherical collapse for cold dark matter are able to reproduce the expectations from N-body simulations (e.g. Adhikari et al., 2014; Shi, 2016).
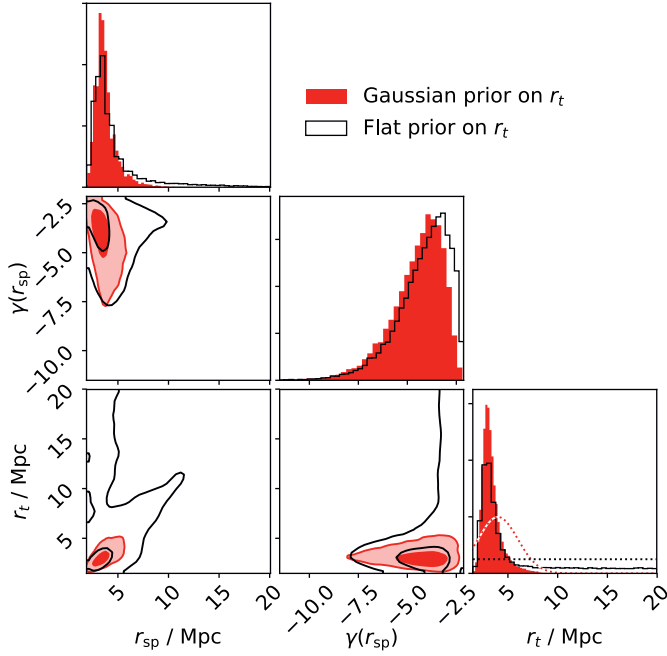
Figure 2.4: Impact of the prior on the truncation radius r_t on our results. The corner plot presents the two-dimensional and marginalized posterior distributions for the DK14 parameter r_t, the inferred splashback position r_{sp}, and logarithmic slope $\gamma(r_{sp})$. If, instead of a Gaussian prior (dashed red line), a flat prior is assumed (dashed black line), the parameter r_t has no upper bound. This translates into weaker constraints on r_{sp}.

The fact that these results are based only on the dynamics of collapsing dark matter in an expanding Universe makes splashback a remarkable prediction of general relativity and dark matter. More generally, its connection to the growth of cosmological structures makes it a test for ΛCDM. As an example, it has also been shown recently that modifications of gravity have a significant impact on this feature (Adhikari et al., 2018). As the first results are starting to appear in the literature, we argue that splashback solicits further investigation exactly because it is a falsifiable prediction of the current paradigm.

We found that at the relevant scales a significant contribution to the lensing signal is cosmic noise. In the near future, this term can be reduced significantly with larger cluster samples. Looking further ahead, deep wide-area surveys such as *Euclid* (Laureijs et al., 2011) and LSST (LSST Science Collaboration et al., 2009) will provide unprecedented depth and survey area, and thus deliver the data required to study splashback over a wider mass and redshift range.

Appendix

2A   Noise covariance matrix

For each cluster we model the noise covariance matrix for the lensing signal as the sum of two components:

$$\boldsymbol{C} = \boldsymbol{C}^{\text{stat}} + \boldsymbol{C}^{\text{lss}}. \tag{2.15}$$

The first is a diagonal matrix accounting for the statistical error on the weighted average of the measured ellipticities and the second quantifies the additional shear variance caused by the presence of cosmic structure between viewer and source (Hoekstra, 2003; Umetsu et al., 2011)

$$\boldsymbol{C}^{\text{lss}}_{i,j} = 2\pi \int_0^\infty d\ell\; \ell P_\kappa(\ell) g(\ell, \theta_i) g(\ell, \theta_j), \tag{2.16}$$

where $P_\kappa(\ell)$ represents the projected convergence power spectrum for the multipole number ℓ. For an angular bin θ extending from θ_- to θ_+, $g(l, \theta)$ is defined using the Bessel functions of the first kind of order zero and one, J_0 and J_1:

$$
\begin{aligned}
g(\ell, \theta) = {} & \left[\frac{1 - 2\ln\theta_-}{\pi(\theta_+^2 - \theta_-^2)}\right] \frac{\theta_- J_1(\ell\theta_-)}{\ell} - \left[\frac{1 - 2\ln\theta_+}{\pi(\theta_+^2 - \theta_-^2)}\right] \frac{\theta_+ J_1(\ell\theta_+)}{\ell} \\
& - \frac{2}{\pi(\theta_+^2 - \theta_-^2)} \int_{\theta_1}^{\theta_2} d\phi\; \phi \log\phi J_0(l\phi).
\end{aligned}
\tag{2.17}
$$
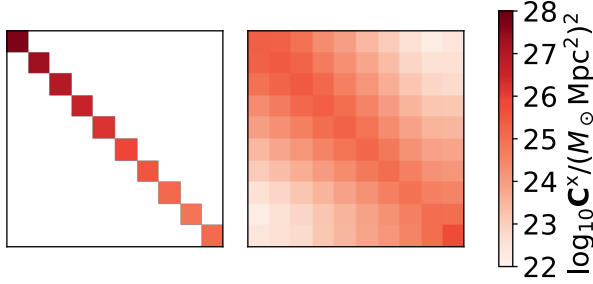
Figure 2.5: Covariance matrix. Visualization of the two components of the covariance matrix $C = C^{\text{stat}} + C^{\text{lss}}$ for the data points plotted in Figure 2.1. The diagonal matrix (left) is the statistical error C^{stat}, the second one (right) is the component due to uncorrelated structure along the line of sight, C^{lss}. The top-left corner corresponds to the first data point.

For a given cosmology, $P_\kappa(\ell)$ can be evaluated using the Limber projection starting from a source redshift distribution and a model for the nonlinear matter power-spectrum (Kilbinger, 2015). For this work, this is done using CAMB[4] (Lewis, 2013) and HALOFIT (Takahashi et al., 2012). As an example, the resulting covariance matrices for the average signal in Fig. 1 are presented in Figure 2.5.

A third term accounting for the intrinsic variance in a particular realization of galaxy clusters should be added to the matrix in Equation (2.15). For massive clusters in the considered redshift range, this term is found to be dominated by Poissonian scatter in the number of halos contained within the correlated neighborhood (Gruen et al., 2015). We neglect this term because in similar lensing analyses (e.g. Umetsu et al., 2016; Miyatake et al., 2018) it is always found to be sub-dominant to statistical and large-scale structure noise, especially on the scales of interest for this work.

---

[4]https://camb.info/

Bibliography

Susmita Adhikari, Neal Dalal, and Robert T Chamberlain. Splashback in accreting dark matter halos. *Journal of Cosmology and Astroparticle Physics*, 2014(11):019–019, November 2014. ISSN 1475-7516. doi: 10.1088/1475-7516/2014/11/019.

Susmita Adhikari, Jeremy Sakstein, Bhuvnesh Jain, Neal Dalal, and Baojiu Li. Splashback in galaxy clusters as a probe of cosmic expansion and gravity. J. Cosmology Astropart. Phys., 2018(11):033, November 2018. doi: 10.1088/1475-7516/2018/11/033.

Yannick M. Bahé, David J. Barnes, Claudio Dalla Vecchia, Scott T. Kay, Simon D. M. White, Ian G. McCarthy, Joop Schaye, Richard G. Bower, Robert A. Crain, Tom Theuns, Adrian Jenkins, Sean L. McGee, Matthieu Schaller, Peter A. Thomas, and James W. Trayford. The Hydrangea simulations: galaxy formation in and around massive clusters. *Monthly Notices of the Royal Astronomical Society*, 470(4):4186–4208, October 2017. ISSN 0035-8711. doi: 10.1093/mnras/stx1403.

Eric Baxter, Chihway Chang, Bhuvnesh Jain, Susmita Adhikari, Neal Dalal, Andrey Kravtsov, Surhud More, Eduardo Rozo, Eli Rykoff, and Ravi K Sheth. The Halo Boundary of Galaxy Clusters in the SDSS. *The Astrophysical Journal*, 841(1):18, May 2017. ISSN 1538-4357. doi: 10.3847/1538-4357/aa6ff0.

Greg L. Bryan and Michael L. Norman. Statistical Properties of X-Ray Clusters: Analytic and Numerical Comparisons. *The Astrophysical Journal*, 495(1):80–99, March 1998. ISSN 0004-637X. doi: 10.1086/305262.

Philipp Busch and Simon D. M. White. Assembly bias and splashback in galaxy clusters. *Monthly Notices of the Royal Astronomical Society*, 470(4):4767–4781, October 2017. ISSN 0035-8711. doi: 10.1093/mnras/stx1584.

C. Chang, E. Baxter, B. Jain, C. Sánchez, S. Adhikari, T. N. Varga, Y. Fang, E. Rozo, E. S. Rykoff, A. Kravtsov, D. Gruen, W. Hartley, E. M. Huff, M. Jarvis, A. G. Kim, J. Prat, N. MacCrann, T. McClintock, A. Palmese, D. Rapetti, R. P. Rollins, S. Samuroff, E. Sheldon, M. A. Troxel, R. H. Wechsler, Y. Zhang, J. Zuntz, T. M. C. Abbott, F. B.

Abdalla, S. Allam, J. Annis, K. Bechtol, A. Benoit-Lévy, G. M. Bernstein, D. Brooks, E. Buckley-Geer, A. Carnero Rosell, M. Carrasco Kind, J. Carretero, C. B. D'Andrea, L. N. da Costa, C. Davis, S. Desai, H. T. Diehl, J. P. Dietrich, A. Drlica-Wagner, T. F. Eifler, B. Flaugher, P. Fosalba, J. Frieman, J. García-Bellido, E. Gaztanaga, D. W. Gerdes, R. A. Gruendl, J. Gschwend, G. Gutierrez, K. Honscheid, D. J. James, T. Jeltema, E. Krause, K. Kuehn, O. Lahav, M. Lima, M. March, J. L. Marshall, P. Martini, P. Melchior, F. Menanteau, R. Miquel, J. J. Mohr, B. Nord, R. L. C. Ogando, A. A. Plazas, E. Sanchez, V. Scarpine, R. Schindler, M. Schubnell, I. Sevilla-Noarbe, M. Smith, R. C. Smith, M. Soares-Santos, F. Sobreira, E. Suchyta, M. E. C. Swanson, G. Tarle, J. Weller, and DES Collaboration. The Splashback Feature around DES Galaxy Clusters: Galaxy Density and Weak Lensing Profiles. ApJ, 864:83, September 2018. doi: 10.3847/1538-4357/aad5e7.

A Cooray and R Sheth. Halo models of large scale structure. *Physics Reports*, 372(1): 1–129, December 2002. ISSN 03701573. doi: 10.1016/S0370-1573(02)00276-4.

DES Collaboration. Dark Energy Survey Year 1 Results: Cosmological Constraints from Galaxy Clustering and Weak Lensing. August 2017.

Benedikt Diemer and Andrey V. Kravtsov. Dependence of the outer density profiles of halos on their mass accretion rate. *The Astrophysical Journal*, 789(1):1, June 2014. ISSN 0004-637X. doi: 10.1088/0004-637X/789/1/1.

Benedikt Diemer, Surhud More, and Andrey V. Kravtsov. The pseudo-evolution of halo mass. *The Astrophysical Journal*, 766(1):25, March 2013. ISSN 0004-637X. doi: 10.1088/0004-637X/766/1/25.

Aaron A. Dutton and Andrea V. Macciò. Cold dark matter haloes in the Planck era: evolution of structural parameters for Einasto and NFW profiles. *Monthly Notices of the Royal Astronomical Society*, 441(4):3359–3374, July 2014. ISSN 1365-2966. doi: 10.1093/mnras/stu742.

J Einasto. On the Construction of a Composite Model for the Galaxy and on the Determination of the System of Galactic Parameters. *Trudy Astrofizicheskogo Instituta Alma-Ata*, 5:87−100, 1965.

James A Fillmore and Peter Goldreich. Self-similar gravitational collapse in an expanding universe. *The Astrophysical Journal*, 281:1, 1984. ISSN 0004-637X. doi: 10.1086/162070.

Daniel Foreman-Mackey, David W. Hogg, Dustin Lang, and Jonathan Goodman. emcee: The MCMC Hammer. *Publications of the Astronomical Society of the Pacific*, 125(925): 306−312, March 2013. ISSN 00046280. doi: 10.1086/670067.

Liang Gao, Julio F. Navarro, Shaun Cole, Carlos S. Frenk, Simon D. M. White, Volker Springel, Adrian Jenkins, and Angelo F. Neto. The redshift dependence of the structure of massive Λ cold dark matter haloes. *Monthly Notices of the Royal Astronomical Society*, 387(2):536–544, June 2008. ISSN 0035-8711. doi: 10.1111/j.1365-2966.2008.13277.x.

Jonathan Goodman and Jonathan Weare. Ensemble samplers with affine invariance. *Communications in Applied Mathematics and Computational Science*, 5(1):65–80, January 2010. ISSN 2157-5452. doi: 10.2140/camcos.2010.5.65.

D. Gruen, S. Seitz, M. R. Becker, O. Friedrich, and A. Mana. Cosmic variance of the galaxy cluster weak lensing signal. *Monthly Notices of the Royal Astronomical Society*, 449(4):4264–4276, April 2015. ISSN 0035-8711. doi: 10.1093/mnras/stv532.

James E. Gunn and J. Richard III Gott. On the Infall of Matter Into Clusters of Galaxies and Some Effects on Their Evolution. *The Astrophysical Journal*, 176:1, August 1972. ISSN 0004-637X. doi: 10.1086/151605.

H. Hoekstra, M. Franx, and K. Kuijken. Hubble Space Telescope Weak-Lensing Study of the z =0.83 Cluster MS 1054-03. *The Astrophysical Journal*, 532(1):88–108, March 2000. ISSN 0004-637X. doi: 10.1086/308556.

Henk Hoekstra. How well can we determine cluster mass profiles from weak lensing? *Monthly Notices of the Royal Astronomical Society*, 339(4):1155–1162, March 2003. ISSN 0035-8711. doi: 10.1046/j.1365-8711.2003.06264.x.

Henk Hoekstra, Marijn Franx, Konrad Kuijken, and Gordon Squires. Weak Lensing Analysis of Cl 1358+62 Using Hubble Space Telescope Observations. *The Astrophysical Journal*, 504(2):636–660, September 1998. ISSN 0004-637X. doi: 10.1086/306102.

Henk Hoekstra, Andisheh Mahdavi, Arif Babul, and Chris Bildfell. The Canadian Cluster Comparison Project: weak lensing masses and SZ scaling relations. *Monthly Notices of the Royal Astronomical Society*, 427(2):1298–1311, December 2012. ISSN 00358711. doi: 10.1111/j.1365-2966.2012.22072.x.

Henk Hoekstra, Matthias Bartelmann, Håkon Dahle, Holger Israel, Marceau Limousin, and Massimo Meneghetti. Masses of Galaxy Clusters from Gravitational Lensing. *Space Science Reviews*, 177(1-4):75–118, August 2013. ISSN 0038-6308. doi: 10.1007/s11214-013-9978-5.

Henk Hoekstra, Ricardo Herbonnet, Adam Muzzin, Arif Babul, Andisheh Mahdavi, Massimo Viola, and Marcello Cacciato. The Canadian Cluster Comparison Project: detailed study of systematics and updated weak lensing masses. *Monthly Notices of the Royal Astronomical Society*, 449(1):685–714, May 2015. ISSN 1365-2966. doi: 10.1093/mnras/stv275.

Nick Kaiser, Gordon Squires, and Tom Broadhurst. A Method for Weak Lensing Observations. *The Astrophysical Journal*, 449:460, August 1995. ISSN 0004-637X. doi: 10.1086/176071.

KiDS collaboration. The third data release of the Kilo-Degree Survey and associated data products. *Astronomy & Astrophysics*, 604:A134, August 2017. ISSN 0004-6361. doi: 10.1051/0004-6361/201730747.

Martin Kilbinger. Cosmology with cosmic shear observations: a review. *Reports on Progress in Physics*, 78(8):086901, July 2015. ISSN 0034-4885. doi: 10.1088/0034-4885/78/8/086901.

C. Laigle, H. J. McCracken, O. Ilbert, B. C. Hsieh, I. Davidzon, P. Capak, G. Hasinger, J. D. Silverman, C. Pichon, J. Coupon, H. Aussel, D. Le Borgne, K. Caputi, P. Cassata, Y.-Y. Chang, F. Civano, J. Dunlop, J. Fynbo, J. S. Kartaltepe, A. Koekemoer, O. Le Fèvre, E. Le Floc'h, A. Leauthaud, S. Lilly, L. Lin, S. Marchesi, B. Milvang-Jensen, M. Salvato, D. B. Sanders, N. Scoville, V. Smolcic, M. Stockmann, Y. Taniguchi, L. Tasca, S. Toft, Mattia Vaccari, and J. Zabl. The cosmos2015 catalog: Exploring the $1 < z < 6$ universe with half a million galaxies. *The Astrophysical Journal Supplement Series*, 224(2):24, June 2016. ISSN 1538-4365. doi: 10.3847/0067-0049/224/2/24.

R. Laureijs, J. Amiaux, S. Arduini, J. . Auguères, J. Brinchmann, R. Cole, M. Cropper, C. Dabin, L. Duvet, A. Ealet, and et al. Euclid Definition Study Report. *ArXiv e-prints*, October 2011.

Antony Lewis. Efficient sampling of fast and slow cosmological parameters. *Physical Review D*, 87(10):103529, May 2013. ISSN 1550-7998. doi: 10.1103/PhysRevD.87.103529.

LSST Science Collaboration, P. A. Abell, J. Allison, S. F. Anderson, J. R. Andrew, J. R. P. Angel, L. Armus, D. Arnett, S. J. Asztalos, T. S. Axelrod, and et al. LSST Science Book, Version 2.0. *ArXiv e-prints*, December 2009.

G. A. Luppino and Nick Kaiser. Detection of Weak Lensing by a Cluster of Galaxies at z = 0.83. *The Astrophysical Journal*, 475(1):20–28, January 1997. ISSN 0004-637X. doi: 10.1086/303508.

Andisheh Mahdavi, Henk Hoekstra, Arif Babul, Chris Bildfell, Tesla Jeltema, and J. Patrick Henry. JOINT ANALYSIS OF CLUSTER OBSERVATIONS. II. CHANDRA / XMM-NEWTON X-RAY AND WEAK LENSING SCALING RELATIONS FOR A SAMPLE OF 50 RICH CLUSTERS OF GALAXIES. *The Astrophysical Journal*, 767(2):116, April 2013. ISSN 0004-637X. doi: 10.1088/0004-637X/767/2/116.

Hironao Miyatake, Surhud More, Masahiro Takada, David N. Spergel, Rachel Mandelbaum, Eli S. Rykoff, and Eduardo Rozo. Evidence of Halo Assembly Bias in Massive

Clusters. *Physical Review Letters*, 116(4):041301, January 2016. ISSN 0031-9007. doi: 10.1103/PhysRevLett.116.041301.

Hironao Miyatake, Nicholas Battaglia, Matt Hilton, Elinor Medezinski, Atsushi J Nishizawa, Surhud More, Simone Aiola, Neta Bahcall, J Richard Bond, Erminia Calabrese, Steve K Choi, Mark J Devlin, Joanna Dunkley, Rolando Dunner, Brittany Fuzia, Patricio Gallardo, Megan Gralla, Matthew Hasselfield, Mark Halpern, Chiaki Hikage, J. Colin Hill, Adam D. Hincks, Renée Hložek, Kevin Huffenberger, John P. Hughes, Brian Koopman, Arthur Kosowsky, Thibaut Louis, Mathew S. Madhavacheril, Jeff McMahon, Rachel Mandelbaum, Tobias A. Marriage, Loïc Maurin, Satoshi Miyazaki, Kavilan Moodley, Ryoma Murata, Sigurd Naess, Laura Newburgh, Michael D. Niemack, Takahiro Nishimichi, Nobuhiro Okabe, Masamune Oguri, Ken Osato, Lyman Page, Bruce Partridge, Naomi Robertson, Neelima Sehgal, Masato Shirasaki, Jonathan Sievers, Cristóbal Sifón, Sara Simon, Blake Sherwin, David N Spergel, Suzanne T Staggs, George Stein, Masahiro Takada, Hy Trac, Keiichi Umetsu, Alex van Engelen, and Edward J Wollack. Weak-Lensing Mass Calibration of ACTPol Sunyaev-Zel'dovich Clusters with the Hyper Suprime-Cam Survey. April 2018.

Surhud More, Benedikt Diemer, and Andrey V. Kravtsov. The splashback radius as a physical halo boundary and the growth of halo mass. *The Astrophysical Journal*, 810 (1):36, August 2015. ISSN 1538-4357. doi: 10.1088/0004-637X/810/1/36.

Surhud More, Hironao Miyatake, Masahiro Takada, Benedikt Diemer, Andrey V. Kravtsov, Neal K. Dalal, Anupreeta More, Ryoma Murata, Rachel Mandelbaum, Eduardo Rozo, Eli S. Rykoff, Masamune Oguri, and David N. Spergel. Detection of the splashback radius and halo assembly bias of massive galaxy clusters. *The Astrophysical Journal*, 825(1):39, June 2016. ISSN 1538-4357. doi: 10.3847/0004-637X/825/1/39.

Julio F. Navarro, Carlos S. Frenk, and Simon D. M. White. A Universal Density Profile from Hierarchical Clustering. *The Astrophysical Journal*, 490(2):493–508, December 1997. ISSN 0004-637X. doi: 10.1086/304888.

Planck Collaboration. Planck 2015 results. *Astronomy & Astrophysics*, 594:A13, October 2016. ISSN 0004-6361. doi: 10.1051/0004-6361/201525830.

B. T. P. Rowe, M. Jarvis, R. Mandelbaum, G. M. Bernstein, J. Bosch, M. Simet, J. E. Meyers, T. Kacprzak, R. Nakajima, J. Zuntz, H. Miyatake, J. P. Dietrich, R. Armstrong, P. Melchior, and M. S. S. Gill. GALSIM: The modular galaxy image simulation toolkit. *Astronomy and Computing*, 10:121–150, April 2015. doi: 10.1016/j.ascom.2015.02.002.

E. S. Rykoff, E. Rozo, M. T. Busha, C. E. Cunha, A. Finoguenov, A. Evrard, J. Hao, B. P. Koester, A. Leauthaud, B. Nord, M. Pierre, R. Reddick, T. Sadibekova, E. S. Sheldon, and R. H. Wechsler. redmapper. i. algorithm and sdss dr8 catalog. *The Astrophysical Journal*, 785(2):104, April 2014. ISSN 0004-637X. doi: 10.1088/0004-637X/785/2/104.

Xun Shi. The outer profile of dark matter haloes: an analytical approach. *Monthly Notices of the Royal Astronomical Society*, 459(4):3711–3720, July 2016. ISSN 0035-8711. doi: 10.1093/mnras/stw925.

Cristóbal Sifón, Henk Hoekstra, Marcello Cacciato, Massimo Viola, Fabian Köhlinger, Remco F. J. van der Burg, David J. Sand, and Melissa L. Graham. Constraints on the alignment of galaxies in galaxy clusters from ~14000 spectroscopic members. *Astronomy & Astrophysics*, 575:A48, March 2015. ISSN 0004-6361. doi: 10.1051/0004-6361/201424435.

Ryuichi Takahashi, Masanori Sato, Takahiro Nishimichi, Atsushi Taruya, and Masamune Oguri. Revising the halofit model for the nonlinear matter power spectrum. *The Astrophysical Journal*, 761(2):152, December 2012. ISSN 0004-637X. doi: 10.1088/0004-637X/761/2/152.

Keiichi Umetsu and Benedikt Diemer. Lensing Constraints on the Mass Profile Shape and the Splashback Radius of Galaxy Clusters. *The Astrophysical Journal*, 836(2):231, April 2017. ISSN 1538-4357. doi: 10.3847/1538-4357/aa5c90.

Keiichi Umetsu, Tom Broadhurst, Adi Zitrin, Elinor Medezinski, Dan Coe, and Marc Postman. A precise cluster mass profile averaged from the highest-quality lensing data. *The Astrophysical Journal*, 738(1):41, September 2011. ISSN 0004-637X. doi: 10.1088/0004-637X/738/1/41.

Keiichi Umetsu, Adi Zitrin, Daniel Gruen, Julian Merten, Megan Donahue, and Marc Postman. Clash: Joint analysis of strong-lensing, weak-lensing shear, and magnification data for 20 galaxy clusters. *The Astrophysical Journal*, 821(2):116, April 2016. ISSN 1538-4357. doi: 10.3847/0004-637X/821/2/116.

Ying Zu, Rachel Mandelbaum, Melanie Simet, Eduardo Rozo, and Eli S. Rykoff. On the level of cluster assembly bias in SDSS. *Monthly Notices of the Royal Astronomical Society*, 470(1):551–560, September 2017. ISSN 0035-8711. doi: 10.1093/mnras/stx1264.

Chapter 3

Splashback in symmetron gravity

The splashback radius $r_{\rm sp}$ has been identified in cosmological N-body simulations as an important scale associated with gravitational collapse and the phase-space distribution of recently accreted material. We employ a semianalytical approach to study the spherical collapse of dark matter halos in symmetron gravity and provide, for the first time, insights into how the phenomenology of splashback is affected by modified gravity. The symmetron is a scalar-tensor theory which exhibits a screening mechanism whereby higher-density regions are screened from the effects of a fifth force. In this model, we find that, as over-densities grow over cosmic time, the inner region becomes heavily screened. In particular, we identify a sector of the parameter space for which material currently sitting at $r_{\rm sp}$ has followed, during the collapse, the formation of this screened region. As a result, we find that for this part of the parameter space the splashback radius is maximally affected by the symmetron force, and we predict changes in $r_{\rm sp}$ up to around 10% compared to its general relativity value. Because this margin is within the precision of present splashback experiments, we expect this feature to soon provide constraints for symmetron gravity on previously unexplored scales.

3.1 Introduction

Gravity, one of the fundamental forces of nature, plays a crucial role in inferring our model of the cosmos as well as all the precision constraints placed on fundamental physics through cosmology. The theory of general relativity (GR), introduced by Einstein a century ago (Einstein, 1916), provided a coherent theoretical framework within which to study all gravitational phenomena. While it is arguably one of the most successful theories of modern physics, having passed a host of empirical phenomena, there remain regimes of curvature and scale where GR has yet to be accurately tested. Its theoretical and phenomenological limitations are being fully explored, with an endeavor which is carried out at virtually all energy scales, ranging from the ultraviolet properties of the theory, down to the energy scale of H_0, associated to the present-day expansion rate of the Universe (Riess et al., 1998).

Upcoming large-scale structure (LSS) surveys will provide unprecedented constraints on gravity on cosmological scales, allowing one to discriminate among many theories alternative to GR. The phenomenology of theories of modified gravity (MG) on linear cosmological scales is fairly well understood, and it is commonly characterized in terms of modifications in the relation between matter density contrast and gravitational potentials (Zhao et al., 2010; collaboration, 2016; Pogosian and Silvestri, 2016). On the other hand, it is well known that non-linear mechanisms in MG theories "screen away" the effects of additional degrees of freedom in high-density regions. This ensures that any fifth force is suppressed and MG reduces to GR in regions where it has been tested with remarkable accuracy (Will, 1993).

A natural regime of interest is the intermediate range, between the screened and unscreened regimes, e.g. the regions of space at the boundaries of dark matter halos. To this extent, a feature that is gaining prominence is the so-called *splashback*, which corresponds to an observable steepening of the dark matter halo density profile close to the boundary (Diemer and Kravtsov, 2014). Locally, the position of this steepening contains interesting information about the clustering of dark matter shells, and it can be understood as the dividing radius of single-stream and multi-stream sectors of the dark matter phase space. This feature has already been noticed in the self-similar spherical collapse framework developed and studied in Fillmore and Goldreich (1984) and Bertschinger (1985), and generalized to three-dimensional collapse in Lithwick and Dalal (2011). Self-similarity, however, is fully operational in a universe without a characteristic scale, such as the Einstein-de Sitter (EdS) universe with $\Omega_m = 1$. Even though realistic applications of the same principle to a ΛCDM universe are possible (Shi, 2016), in this chapter, we will focus on the collapse in the EdS scenario and will leave more realistic scenarios for future work.

The profiles of the largest dark matter halos in the Universe, where galaxy clusters reside, can be mapped by measuring the deformation of background sources (Kaiser and Squires, 1993; Umetsu et al., 2011). This technique, known as lensing, has been

used to measure the splashback feature around clusters (Umetsu and Diemer, 2017; Contigiani et al., 2019). It should be noted, however, that the most stringent constraints are obtained using the distribution of subhalos traced by the cluster galaxy members (More et al., 2016; Baxter et al., 2017; Chang et al., 2018; Shin et al., 2018). In this case, the interpretation is nevertheless not straightforward and an accurate comparison with N-body ΛCDM simulations is required.

In this chapter, we consider the splashback radius in MG scenarios, investigating the microscopic effects of alternative theories of gravity on the dark matter shells accreting into the halo. Since we aim to gain insight on the physical details, we do not resort to numerical simulations but rather employ a semianalytical method based on the framework of self-similar spherical collapse of Fillmore and Goldreich (1984). We focus on the class of theories of gravity that display the symmetron screening mechanism (Hinterbichler and Khoury, 2010). While we present an overview of the symmetron gravity in the main text, let us mention here that our analysis can be easily extended to other types of screening mechanisms, e.g. to Chameleon screening exhibited by $f(R)$ models (Capozziello et al., 2003; Carroll et al., 2004), in which the density dependence is explicitly in the scalar field mass, rather than the field couplings.

We have organized our presentation as follows. In Sec. 3.2 we introduce the self-similar density profile and present the relevant equations of motion for the collapsing shells. In Sec. 3.3 we discuss the basics of symmetron gravity. In Sec. 3.4 we present our numerical methods and demonstrate the effect of the symmetron force on the phase space of the dark matter halo and the shift in the splashback radius.[1] Finally, we discuss the implications of our findings and suggest potential further studies in Sec. 3.5.

3.2 Density profile

In order to study the motion of accreting material onto an overdensity, we first need to specify a matter density profile. In this work, we employ the so-called self-similar approximation in the problem of spherical collapse. In this context, the idea of self-similarity was introduced for the first time by Fillmore and Goldreich (1984), in which it was shown that around EdS backgrounds, where the scale factor scales as a power law of cosmic time, $a(t) \propto t^{2/3}$, the spherical collapse equations admit self-similar and self-consistent solutions.

The material surrounding a scale-free perturbation initially coupled to the Hubble flow eventually reaches turnaround and collapses onto a central overdensity. We denote by $R(t)$ and $M(r, t)$ the position of the turnaround radius at a time t and the mass contained within the radius r, respectively. The mass within the turnaround radius can

---

[1]In the interest of reproducibility we make our numerical codes available at http://github.com/contigiani/sym-splash.

be written as a function of scale radius as:

$$M(R,t) \propto a(t)^s, \tag{3.1}$$

where the parameter s is referred to as the *accretion rate*. In this model, $M(R,t)$ and $R(t)$ are related to each other through

$$\frac{4\pi}{3} R(t)^3 \rho_b(t) = \left(\frac{4}{3\pi}\right)^2 M(R,t), \tag{3.2}$$

where $\rho_b(t)$ is the EdS background density at time t. This additionally implies that the position R as a function of time also depends on s:

$$R(t) \propto a(t)^{1+s/3}. \tag{3.3}$$

Notice that s and the mass of the present-day perturbation are the only free parameters of this model. In this work, we choose a fixed value of $s = 1.5$ for the accretion rate, known to be representative for the low-redshift Universe in numerical simulations (Correa et al., 2015; Diemer and Kravtsov, 2014).

During spherical collapse, Gauss's law ensures that the trajectory for each shell of material is influenced only by the mass contained within it. The equation of motion for each shell can be written as

$$\frac{d^2 r}{dt^2} = -\frac{GM(r,t)}{r^2}, \tag{3.4}$$

where the left-hand side is the Newtonian force $F_N(r)$ proportional to Newton's gravitational constant G.

While before turnaround the mass within a shell is manifestly constant, afterward, this is not true; as multiple shells start orbiting the halo, their trajectories start intersecting. This phenomenon is known as shell crossing, and it is the principal reason why integrating Equation (3.4) is not straightforward.

If we label each shell of material by its turnaround time t_* and radius r_*, such that $R(t_*) = r_*$, the trajectory for each shell is found to be independent of these quantities when self-similarity is satisfied. This can be verified by rewriting the equation of motion for the given shell in terms of the rescaled variables

$$\xi = \frac{r}{r_*}, \quad \tau = \frac{t}{t_*}; \tag{3.5}$$

and by enforcing the mass profile $M(r)$ to be of the form:

$$M(r,t) = M(R,t)\mathcal{M}(r/R). \tag{3.6}$$

Notice that, from Equation (3.3) it follows that the rescaling of the local turnaround radius $\Xi = \frac{R(t)}{r_*}$ can be also written as a function of τ alone:

$$\Xi(\tau) = \tau^{2/3+2s/9}. \tag{3.7}$$

The system is then evolved through the following self-similarity equations for $\xi(\tau)$ and $\mathcal{M}(\xi/\Xi)$:

$$\frac{d^2\xi}{d\tau^2} = -\frac{\pi^2}{8}\frac{\tau^{2s/3}}{\xi^2}\mathcal{M}\left(\frac{\xi}{\Xi(\tau)}\right), \tag{3.8}$$

$$\mathcal{M}(y) = \frac{2s}{3}\int_1^\infty \frac{d\tau}{\tau^{1+2s/3}}H\left(y - \frac{\xi(\tau)}{\Xi(\tau)}\right), \tag{3.9}$$

where $H(\dots)$ is the Heaviside step function, and the turnaround initial conditions for $\xi(\tau)$ are $\xi(\tau = 1) = 1$, $d\xi/d\tau(\tau = 1) = 0$. Notice that, because these two equations are coupled to each other, they should be solved jointly to obtain self-consistent solutions for the orbits and the mass profile. This is done by starting from an initial guess for $\mathcal{M}(y)$ and then evaluating numerically the trajectories $\xi(\tau)$ using Equation (3.8). The corresponding $\mathcal{M}(y)$, evaluated using Equation (3.9), is then taken as an initial guess for the next iteration. This is repeated until convergence is reached and a final result for $M(r, t)$ is obtained. The corresponding density profile is then simply

$$\rho(r,t) = \frac{1}{4\pi r^2}\frac{dM}{dr}(r,t), \tag{3.10}$$

and it is shown in Figure 3.1. Notice in particular that its time-dependence is completely described by $\rho_b(t)$ and $R(t)$.

3.3   Symmetron gravity

In this section, we provide a brief overview of symmetron gravity and introduce the framework needed to study its effects on spherical collapse.

We consider a scalar-tensor theory of the form

$$S = S_\varphi + S_M\left(\tilde{g}_{\mu\nu}, \Psi\right), \tag{3.11}$$

with

$$S_\varphi = \int \sqrt{-g}\,d^4x\left[\frac{M_p^2}{2}R - \frac{1}{2}\nabla^\mu\varphi\nabla_\mu\varphi - V(\varphi)\right], \tag{3.12}$$

M_p being the Planck mass, and S_{M} being the action for matter fields. The scalar field φ couples to the Einstein frame metric $g_{\mu\nu}$ with Ricci scalar R, while matter fields
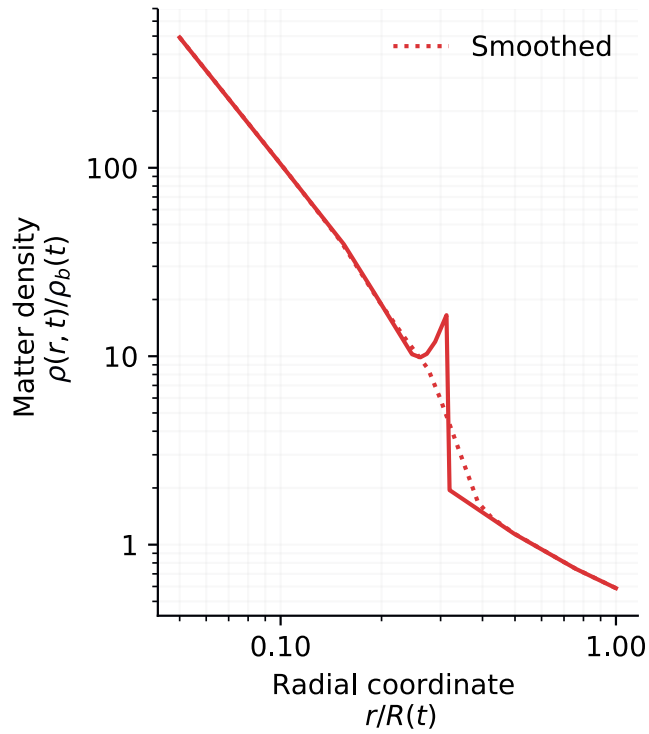
Figure 3.1: Prescription for the spherical halo density profile. The red dotted line is a smoothed version of the self-consistent profile which removes the non-physical sharp caustic.

(collectively represented by Ψ) couple to the Jordan frame metric $\tilde{g}_{\mu\nu}$. The two metrics are assumed to be related by the transformation

$$\tilde{g}_{\mu\nu} = A^2(\varphi)g_{\mu\nu}. \tag{3.13}$$

Notice that such model is fully specified by the functions $A(\varphi)$ and $V(\varphi)$. Varying the action with respect to φ gives us the equation of motion,

$$\Box\varphi = V_{,\varphi} - A^3(\varphi)A_{,\varphi}(\varphi)\rho \equiv \tilde{V}_{,\varphi}(\varphi), \tag{3.14}$$

where ρ is the trace of the matter stress-energy tensor, equal to the local matter density, and $\tilde{V}(\varphi)$ is an effective potential. The fifth force per unit mass exerted by the field φ and experienced by a matter test particle can then be written as

$$F_\varphi = -\nabla \log A(\varphi). \tag{3.15}$$

In this chapter, we will focus on a realization of such a theory, namely the symmetron model specified by the functions

$$V(\varphi) = -\frac{1}{2}\mu\varphi^2 + \frac{1}{4}\lambda\varphi^4, \tag{3.16}$$

$$A(\varphi) = 1 + \frac{1}{2}\frac{\varphi^2}{M^2}, \tag{3.17}$$

and effective potential:

$$\tilde{V}(\varphi) = \frac{1}{2}\left(\frac{\rho}{M^2} - \mu^2\right)\varphi^2 + \frac{1}{4}\lambda\varphi^4. \tag{3.18}$$

In this parametrization, the symmetron naturally assumes the form of an effective field theory with $\varphi \to -\varphi$ symmetry.

In high-density regions, where the condition

$$\rho > \rho_{ssb} \equiv M^2\mu^2 \tag{3.19}$$

is satisfied, the effective potential $\tilde{V}(\varphi)$ has only one minimum in $\varphi = 0$ and the field is driven toward it, resulting in a null fifth force. In other words, high-density regions are screened. In low-density environments, on the other hand, the minimum is not located at zero. For example, for $\rho = 0$ the vacuum expectation value is $\varphi_0 = \mu/\sqrt{\lambda}$.

The fifth force can be constrained by local tests of gravity; to see in detail how local limits translate into bounds on the mass scale M and the Mexican hat parameters μ, λ we refer the reader to Hinterbichler and Khoury (2010), for a general overview, and to the introduction of O'Hare and Burrage (2018), for a more recent analysis.

In an EdS background, the average matter density as a function of redshift z is

$$\rho_b = \frac{1}{6\pi G t^2} \propto (1+z)^3. \tag{3.20}$$

As the Universe expands, the symmetron can undergo spontaneous symmetry breaking (SSB) when $\rho_b(z_{\mathrm{ssb}}) = \rho_{\mathrm{ssb}}$. For more details about the cosmological evolution of the symmetron field and the allowed expansion histories, we refer the reader to Hinterbichler et al. (2011) and Bamba et al. (2013). Let us stress, however, that we are not interested in the possibility of using the field φ to drive the late-time expansion of the Universe, but we are only interested in the additional fifth force and its effects on spherical collapse.

In this chapter, we will work in terms of the dimensionless field $\chi = \varphi/\varphi_0$ and symmetron parameters composed by the average matter density at symmetry breaking ρ_{ssb}, the vacuum Compton wavelength

$$\lambda_0 = \frac{1}{\sqrt{2}\mu}, \tag{3.21}$$

and the dimensionless coupling

$$\beta = \frac{\varphi_0 M_p}{M^2}. \tag{3.22}$$

Using these parameters, the fifth force sourced by the symmetron field can be written as

$$F_\varphi = -16\pi G \beta^2 \lambda_0^2 \rho_{ssb} \, \chi \nabla \chi. \tag{3.23}$$

3.4 Spherical collapse with the symmetron

Having introduced the symmetron, let us now go back to the original goal of this chapter, i.e. to study spherical collapse in symmetron gravity with a particular focus on splashback.

The splashback radius is commonly defined as the point where the density profile $\rho(r)$ is at its steepest. While this steepening is noteworthy because it can be detected as a departure from an equilibrium profile, this definition is clearly not suited for our study, in which we assume a predefined density profile. Fortunately, the splashback radius is also known to be connected to the apocenter of recently accreted material and the location of the latest caustic visible in the density profile. Here we study the effects of the symmetron force on splashback by using this latter definition.

Our simulation is based on a system of equations that includes the spherical collapse equations, as discussed in Sec. 3.2, coupled to the equation for the field profile of the symmetron field, discussed in Sec. 3.3. We start by presenting our numerical method to

compute both the symmetron field profile and the additional fifth force for the assumed density profile. We then proceed to integrate the shell equation to predict the fractional change in the splashback position in the presence of the symmetron force.

3.4.1   Field profile

Assuming the temporal evolution of the field to be very fast compared to the other timescales of the problem, i.e. the Hubble timescale and that of the clustering of matter, the dimensionless field profile $\chi(r)$ sourced by a density profile $\rho(r, t)$ satisfies the following equation:

$$\frac{d^2\chi}{dr^2} + \frac{2}{r}\frac{d\chi}{dr} = \frac{1}{2\lambda_0^2}\left[\left(\frac{\rho(r,t)}{\rho_{ssb}} - 1\right)\chi + \chi^3\right]. \tag{3.24}$$

This quasistatic approximation is common in the literature (Davis et al., 2012; Clampitt et al., 2012; Brax et al., 2012) and has been tested in the context of N-body simulations (Llinares and Mota, 2014; Noller et al., 2014). In order to provide a rough, order of magnitude justification for this assumption, let us just mention that the timescale associated with the field dynamics in vacuum is given by $\sim \lambda_0/c$. It is clear that in order for the symmetron field to be relevant for the dynamics of the spherical collapse this λ_0 should be of the same order of magnitude as the scale of the cluster itself. The latter, of course, is several orders of magnitude smaller than c/H_0.

The *static* symmetron equation of motion (3.24) is a nonlinear elliptical boundary value problem, for which we set the standard boundary conditions of vanishing spatial gradient of the field at $r = 0$ and $r \to \infty$. We use a one-dimensional version of the Newton-Gauss-Seidel relaxation method for the numerical integration of the equation. This is a standard method used for obtaining the scalar field profiles in N-body simulations with modifications of gravity mentioned above.

In practice, we discretize our one-dimensional static symmetron equation of motion on a regular grid of size h and use a second order discretization scheme for all the derivatives.[2] The resulting equation takes the form

$$\mathcal{L}[\chi_{i+1}, \chi_{i-1}; \chi_i] = 0, \tag{3.25}$$

where

$$\mathcal{L}[\chi_{i+1}, \chi_{i-1}; \chi_i] \equiv \mathcal{D}_K[\chi_{i+1}, \chi_{i-1}; \chi_i] - \mathcal{D}_P[\chi_i, \rho_i] \tag{3.26}$$

contains the discretization of the Laplace operator

$$\mathcal{D}_K \equiv \frac{\chi_{i+1} + \chi_{i-1} - 2\chi_i}{h^2} + \frac{2}{r_i}\frac{\chi_{i+1} - \chi_{i-1}}{2h} \tag{3.27}$$

---

[2]We have tested some outputs of our integrator against the results of the version in which higher order discretization schemes are employed. For our particular problem, we did not encounter significant differences in performance of the integrator and performed the main analysis with the version which employs the second order scheme.

and effective potential:

$$\mathcal{D}_{\mathrm{P}} = \frac{1}{\lambda_0^2} \left(\left(\frac{\rho_i}{\rho_{\mathrm{ssb}}} - 1 \right) \chi_i + \chi_i^3 \right). \tag{3.28}$$

The basic idea of the relaxation methods is to find a field profile from this equation which is closer to the real solution than a randomly chosen initial guess. This step is iterated over multiple (improved) guesses labeled $\chi_n(i)$ until convergence is reached.

At a given step, we define an improved (new) field profile:

$$\chi^{\mathrm{new}}(i) = \chi_n(i) - \left. \frac{\mathcal{L}(\chi(i))}{\partial \mathcal{L}(\chi(i))/\partial \chi(i)} \right|_{\chi(i)=\chi_n(i)}. \tag{3.29}$$

Then, we use a part of this *new* χ as the field profile for our next relaxation iteration,

$$\chi_{n+1}(i) = \omega \chi^{\mathrm{new}} + (1 - \omega)\chi_n, \tag{3.30}$$

where $0 < \omega \leqslant 1$ is a weight parameter with, in principle, a problem-dependent optimal value.

We employ two intuitive convergence diagnostics, in which at each step we terminate the iteration if a certain parameter is within a predefined threshold. The first parameter is the residual function,

$$\mathcal{R}_1 \equiv \sqrt{\sum_i \mathcal{L}[\chi(i+1), \chi(i-1); \chi(i)]^2}, \tag{3.31}$$

and the second one is the all-mesh average of the fractional change in the field profile

$$\mathcal{R}_2 \equiv \sqrt{\sum_i (\chi^{\mathrm{new}}(i) - \chi^{\mathrm{old}}(i))^2}. \tag{3.32}$$

To validate our integrator and convergence thresholds, we compare the numerical solution to a known analytic solution. In our case, this known solution is an exact $\tanh(r)$ field profile, for which the corresponding density profile was recovered using Equation (3.24).

When solving for the density profiles plotted in Figure 3.1, we numerically evaluate the equation of motion in the range $[0, 2]$ for $r/R(t)$, where the density profile for $r \geq R(t)$ is assumed to be constant. We make sure that the arbitrary choice of the upper limit has no effect on our results by testing larger values.
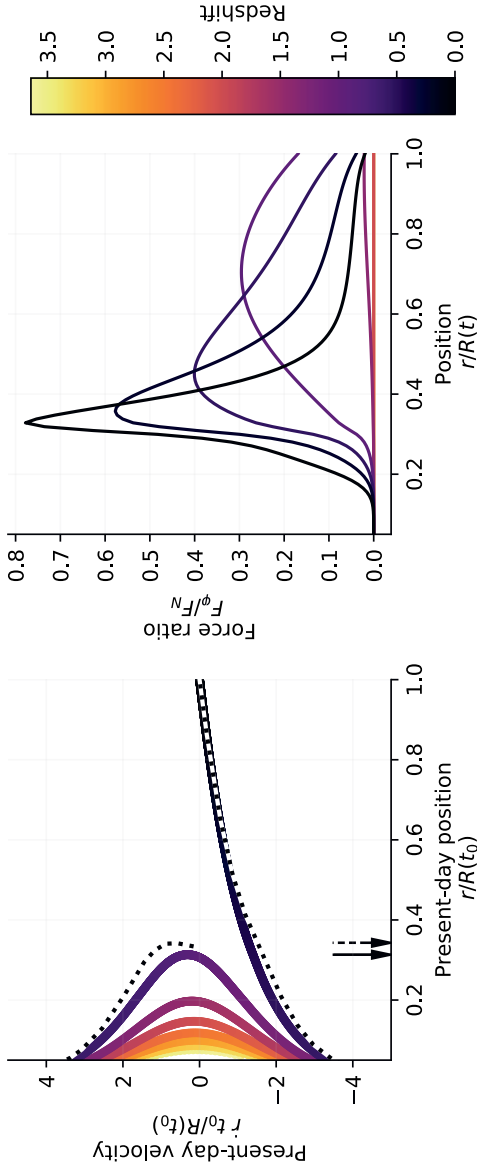
Figure 3.2: Effects of the symmetron force on the splashback location for $\beta = 3$, $z_{\mathrm{ssb}} = 2$, $\lambda_0/R(t_0) = 0.05$. On the left side, we show the phase-space distribution of shells around a spherically symmetric halo, where the shells are color coded by their turnaround redshift. The dotted line shows how this distribution is affected by the presence of the symmetron force. The arrows on the bottom point to the inferred splashback radius in the two cases. On the right side, we display the ratio between the symmetron and the Newtonian force profiles, $\frac{F_S}{F_N}$, for different instants in time. At high redshift, when the innermost material is accreted, the symmetron force is ten times smaller than its peak value today.

3.4.2 Splashback

Once the symmetron field is found as a function of time, the present-day phase-space distribution of recently accreted material can be obtained by integrating numerically the equation of motion (3.4) with added fifth force (3.23) for different collapse times.

We find that after imposing self-similarity the collapse equations can be written only as a function of three dimensionless symmetron parameters: the redshift of symmetry breaking z_{ssb}, the dimensionless coupling β, and the ratio $\lambda_0/R(t_0)$ between the vacuum Compton wavelength λ_0 and the present-day turnaround radius $R(t_0)$. An important combination of these parameters is

$$f = (1 + z_{\text{ssb}})^3 \beta^2 \frac{\lambda_0^2}{R^2(t_0)}, \tag{3.33}$$

which explicitly sets the strength of the symmetron force according to Equation (3.15).

From our testing, we found that values $\lambda_0/R(t_0) \in [0.02, 0.1]$ offer nontrivial cases. For $\lambda \sim R(t_0)$ we always obtain *thin-shell*-like solutions, while for $\lambda \ll R(t_0)$ the field is heavy and simply relaxes onto the minimum of the potential $\tilde{V}(\chi)$ in Equation (3.18).

In Figure 3.2 we illustrate our method and show how the symmetron force modifies the phase-space configuration of the latest accreted orbits (left-side plot). We find that the splashback position is significantly affected for parameter values $f \sim 1$, $z_{\text{ssb}} \sim 2$ and $\lambda_0/R(t_0) \sim 0.1$. These values imply $M \lesssim 10^{-3} M_p$, which is in agreement with local tests of gravity (Hinterbichler and Khoury, 2010).

From the same figure (right-side plot), it is clear that the innermost regions of the overdensity are screened from the effects of the fifth force at all times, and this becomes relevant in the outer regions only for $z \ll z_{\text{ssb}}$. Past this point, the force profile slowly transitions from a *thick-shell-* to a *thin-shell*-like behavior, in which the force gets progressively concentrated around the surface of the screened region (Taddei et al., 2014). Due to the sudden drop in density associated with splashback, this surface is delimited by the splashback radius.

A systematic exploration of the symmetron effects on this feature as a function of all parameters is presented in Figure 3.3, which represents our main result.

A clear trend with z_{ssb} is visible. Notice that the fractional change on the splashback position has an optimal peak as a function of z_{ssb} that is independent of f. If we call z_{sp} the accretion redshift of the shell currently sitting at the splashback position after its first pericenter, i.e. the *splashback shell*, we see that the effect is maximized when $z_{\text{sp}} \simeq z_{\text{ssb}}$. This is easily explained by studying the profile of the fifth force over time. For $z_{\text{sp}} \gg z_{\text{ssb}}$, the selected shell collapses when the symmetron is in its symmetric phase and the material spends the rest of its trajectory in a screened region, away from the effects of the fifth force; for $z_{\text{sp}} \ll z_{\text{ssb}}$, the thin shell has had time to form before z_{sp}, and the shell feels the effects of the fifth force only during a small fraction of its trajectory. Between these two limiting cases, there is an efficient z_{ssb} for which the

splashback shell has time to follow the formation of the thin shell, and it is optimally positioned near the peak of the force profile for most of its trajectory. In our figure, we show how this peak still has a dependence on λ_0, introduced by the presence of this factor on the symmetron equation of motion (3.24).

To conclude this section, we point out that the smoothness of the density profile as plotted in Figure 3.1 has little impact on our results and no impact on the trends discussed above. Differences between the two prescriptions exist only for $\lambda_0 \ll R(t_0)$, when the field profile becomes susceptible to the small-scale features of the profile. However, since we expect the sharp caustic to be smoothed by gravitational instabilities, for the main results, we chose not to use the discontinuous profile and assumed instead its smoothed version. Notice also that considering such high-resolution scenarios would introduce additional caveats (e.g. the presence of substructure) that are not the focus of this work.
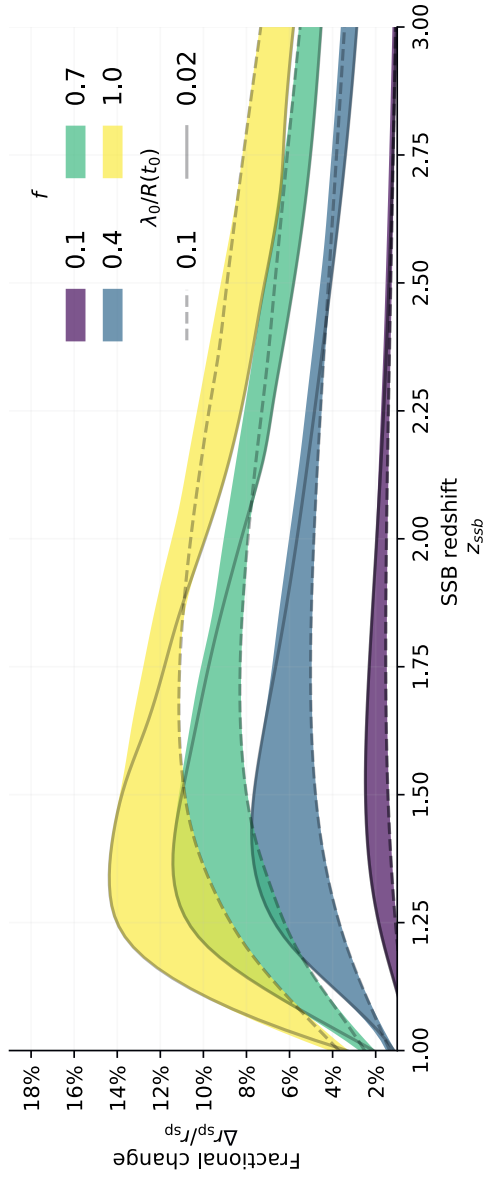
Figure 3.3: Percentage change in the splashback position in symmetron gravity as a function of symmetron parameters: the dimensionless force strength f and the SSB redshift z_{ssb}. The spread of the different curves is given by variations of the third parameter, the vacuum Compton wavelength of the field λ_0. We emphasize in particular the cases $\lambda_0/R(t_0) = 0.1$ (dashed line) and $\lambda_0/R(t_0) = 0.02$ (solid line), in which $R(t_0)$ is the present-day turnaround radius.

3.5 Discussion and conclusion

In this chapter, we have explored how symmetron gravity affects the splashback feature at the edges of cosmological halos. In our approach, we assume a self-similar mass distribution motivated by spherical collapse in an EdS Universe, where the shape of the spherically symmetric matter distribution is assumed to be only a function of $r/R(t)$. This allows us to easily solve for the corresponding symmetron fifth force and estimate its effects on the splashback feature by studying the changed phase-space distribution of recently accreted shells.

The main limitation of our study is the lack of a fully consistent framework in which the density profile, the turnaround physics, and the phase-space distribution are solved for in conjunction with the newly introduced symmetron equation of motion. For example, we would expect a consistent framework to take into account the back-reaction of the scalar field on the density profile.

While deriving self-consistent solutions is outside the scope of this chapter and more suited to N-body simulation studies, we find it useful to discuss the impact of our assumptions on the results. Changes to the turnaround physics are commonly studied through the use of different approximations, like a scale-dependent Newton's constant (Schaefer and Koyama, 2008; Brax et al., 2010; Hu et al., 2018; Nojiri et al., 2018; Lopes et al., 2018). In our case, if we maintain the assumptions of self-similarity and power-law accretion in Equation (3.1), the main change to our formalism will come in the form of upgrading the numerical constant appearing in Equation (3.2) to a function of the perturbation scale and cosmic time.

Previous works have estimated these corrections to be of the order of a few percentage points at $z \simeq 0$; see (Taddei et al., 2014) for results in symmetron gravity and (Lopes et al., 2018) for similar results in $f(R)$ theory. In particular, we expect our assumption to first break at a redshift z such that the condition $F_\varphi(r) \sim F_N(r)$ is satisfied at the turnaround radius $r = R(t)$. In our analysis, however, we have seen that the effects on splashback are maximized when the collapse redshift of the splashback shell $z_{\rm sp}$ is equivalent to this transition redshift. After this point, the splashback shell is confined in the inner region, and we expect its trajectory to be unaffected by the turnaround physics. Therefore, we consider our results around the peak of Figure 3.3 to be robust against this assumption. For the same reason, however, we expect to lose predictability for higher values of $z_{\rm ssb}$, since the initial condition of the splashback shell will differ from what we have assumed.

Notice that the argument presented above also implies that our results can be extended to a standard ΛCDM scenario. The present-day splashback shell is expected to have collapsed in the matter-dominated era and to have followed a trajectory mostly unaffected by the late-time expansion, especially for low values of the accretion rate s like the one considered here (Shi, 2016).

Effects of modified gravity on the structure of dark matter halos are usually pre-

sented in the form of changes in the small-scale power spectra (Cui et al., 2010; Davis et al., 2012; Li et al., 2013; Brax et al., 2012) and two-point correlation functions (Lombriser et al., 2012) or the whole phase-space distribution (Zu et al., 2014; Lam et al., 2012). In this analysis, we focused instead on a particular scale, the splashback radius, and showed that up to a 10% change can be induced (Figure 3.3). It should be pointed out that Adhikari et al. (2018) was the first work to explore how modified gravity affects the splashback position. We stress, however, that our work differs from that of its authors in three major aspects. First, here, we focus on symmetron gravity which displays a different screening mechanism from the chameleon or k-mouflage explored in (Adhikari et al., 2018) . Second, while their results based on N-body simulations represent more realistic predictions, they do not allow for a simple exploration of the theory parameter space. Third, with our semianalytical approach, we are able to gain insight by obtaining quantitative results as a function of multiple theory parameters and provide an explanation for the visible trends. All this said, it also should be mentioned that the quantitative estimation of the modeling uncertainties will still resort on N-body simulations. This is an interesting aspect, and we leave its systematic investigation to a future work.

Observationally, splashback can be measured predominantly around galaxy clusters,å for which the present-day turnaround radius $R(t_0)$ is of the order of a few Mpc. Our results, therefore, imply that this feature can be used to constrain fifth forces with vacuum Compton wavelength λ_0 just below the Mpc scale. Because measurements of splashback in the galaxy distribution around clusters have already achieved a precision below the size of our predicted effect (More et al., 2016; Baxter et al., 2017; Chang et al., 2018; Shin et al., 2018), we expect to soon be able to constrain not only the symmetron, but other fifth force models on similar scales.

Note in particular that, while other works have explored the possibility of constraining symmetron gravity on Mpc scales (Hammami and Mota, 2017; Gronke et al., 2015), the range considered here for λ_0 is unconstrained for this model. Thus, we expect a measurement based on splashback to naturally complement other results based on laboratory experiments (Burrage et al., 2016; Brax et al., 2018), stellar and compact astrophysical objects (Jain et al., 2013; Brax et al., 2014) or galactic disks and stellar clusters (O'Hare and Burrage, 2018; Llinares, 2018; Desmond et al., 2018).

As the physics of splashback matures into a new cosmological observable, we expect it to play a powerful role in testing modifications of gravity, complementary to already established techniques such as those for large-scale structure.

Bibliography

Susmita Adhikari, Jeremy Sakstein, Bhuvnesh Jain, Neal Dalal, and Baojiu Li. Splashback in galaxy clusters as a probe of cosmic expansion and gravity. *JCAP*, 1811(11): 033, 2018. doi: 10.1088/1475-7516/2018/11/033.

K. Bamba, R. Gannouji, M. Kamijo, S. Nojiri, and M. Sami. Spontaneous symmetry breaking in cosmos: The hybrid symmetron as a dark energy switching device. *JCAP*, 1307:017, 2013. doi: 10.1088/1475-7516/2013/07/017.

Eric Baxter, Chihway Chang, Bhuvnesh Jain, Susmita Adhikari, Neal Dalal, Andrey Kravtsov, Surhud More, Eduardo Rozo, Eli Rykoff, and Ravi K. Sheth. The Halo Boundary of Galaxy Clusters in the SDSS. *Astrophys. J.*, 841(1):18, 2017. doi: 10. 3847/1538-4357/aa6ff0.

E. Bertschinger. Self - similar secondary infall and accretion in an Einstein-de Sitter universe. *Astrophys. J. Suppl.*, 58:39, 1985. doi: 10.1086/191028.

Ph. Brax, R. Rosenfeld, and D. A. Steer. Spherical Collapse in Chameleon Models. *JCAP*, 1008:033, 2010. doi: 10.1088/1475-7516/2010/08/033.

Philippe Brax, Anne-Christine Davis, Baojiu Li, Hans A. Winther, and Gong-Bo Zhao. Systematic Simulations of Modified Gravity: Symmetron and Dilaton Models. *JCAP*, 1210:002, 2012. doi: 10.1088/1475-7516/2012/10/002.

Philippe Brax, Anne-Christine Davis, and Jeremy Sakstein. Pulsar Constraints on Screened Modified Gravity. *Class. Quant. Grav.*, 31:225001, 2014. doi: 10.1088/ 0264-9381/31/22/225001.

Philippe Brax, Anne-Christine Davis, Benjamin Elder, and Leong Khim Wong. Constraining screened fifth forces with the electron magnetic moment. *Phys. Rev.*, D97 (8):084050, 2018. doi: 10.1103/PhysRevD.97.084050.

Clare Burrage, Andrew Kuribayashi-Coleman, James Stevenson, and Ben Thrussell. Constraining symmetron fields with atom interferometry. *JCAP*, 1612:041, 2016. doi: 10.1088/1475-7516/2016/12/041.

Salvatore Capozziello, Sante Carloni, and Antonio Troisi. Quintessence without scalar fields. *Recent Res. Dev. Astron. Astrophys.*, 1:625, 2003.

Sean M. Carroll, Vikram Duvvuri, Mark Trodden, and Michael S. Turner. Is cosmic speed - up due to new gravitational physics? *Phys. Rev.*, D70:043528, 2004. doi: 10.1103/PhysRevD.70.043528.

Chihway Chang et al. The Splashback Feature around DES Galaxy Clusters: Galaxy Density and Weak Lensing Profiles. *Astrophys. J.*, 864(1):83, 2018. doi: 10.3847/1538-4357/aad5e7.

Joseph Clampitt, Bhuvnesh Jain, and Justin Khoury. Halo Scale Predictions of Symmetron Modified Gravity. *JCAP*, 1201:030, 2012. doi: 10.1088/1475-7516/2012/01/030.

Planck collaboration. Planck 2015 results. XIV. Dark energy and modified gravity. *Astron. Astrophys.*, 594:A14, 2016. doi: 10.1051/0004-6361/201525814.

O. Contigiani, H. Hoekstra, and Y. M. Bahé. Weak lensing constraints on splashback around massive clusters. MNRAS, 485(1):408–415, May 2019. doi: 10.1093/mnras/stz404.

Camila A. Correa, J. Stuart B. Wyithe, Joop Schaye, and Alan R. Duffy. The accretion history of dark matter haloes – II. The connections with the mass power spectrum and the density profile. *Mon. Not. Roy. Astron. Soc.*, 450(2):1521–1537, 2015. doi: 10.1093/mnras/stv697.

Weiguang Cui, Pengjie Zhang, and Xiaohu Yang. Nonlinearities in modified gravity cosmology I: signatures of modified gravity in the nonlinear matter power spectrum. *Phys. Rev.*, D81:103528, 2010. doi: 10.1103/PhysRevD.81.103528.

Anne-Christine Davis, Baojiu Li, David F. Mota, and Hans A. Winther. Structure Formation in the Symmetron Model. *Astrophys. J.*, 748:61, 2012. doi: 10.1088/0004-637X/748/1/61.

Harry Desmond, Pedro G. Ferreira, Guilhem Lavaux, and Jens Jasche. The Fifth Force in the Local Cosmic Web. MNRAS, 2018. doi: 10.1093/mnrasl/sly221.

Benedikt Diemer and Andrey V. Kravtsov. Dependence of the outer density profiles of halos on their mass accretion rate. *Astrophys. J.*, 789:1, 2014. doi: 10.1088/0004-637X/789/1/1.

Albert Einstein. The Foundation of the General Theory of Relativity. *Annalen Phys.*, 49(7):769–822, 1916. doi: 10.1002/andp.200590044,10.1002/andp.19163540702.

J. A. Fillmore and P. Goldreich. Self-similar gravitational collapse in an expanding universe. ApJ, 281:1–8, 1984. doi: 10.1086/162070.

Max Gronke, David F. Mota, and Hans A. Winther. Universal predictions of screened modified gravity on cluster scales. *Astron. Astrophys.*, 583:A123, 2015. doi: 10.1051/0004-6361/201526611.

Amir Hammami and David F. Mota. Probing modified gravity via the mass-temperature relation of galaxy clusters. *Astron. Astrophys.*, 598:A132, 2017. doi: 10.1051/0004-6361/201629003.

Kurt Hinterbichler and Justin Khoury. Symmetron Fields: Screening Long-Range Forces Through Local Symmetry Restoration. *Phys. Rev. Lett.*, 104:231301, 2010. doi: 10.1103/PhysRevLett.104.231301.

Kurt Hinterbichler, Justin Khoury, Aaron Levy, and Andrew Matas. Symmetron Cosmology. *Phys. Rev.*, D84:103521, 2011. doi: 10.1103/PhysRevD.84.103521.

Bin Hu, Xue-Wen Liu, and Rong-Gen Cai. CHAM: a fast algorithm of modelling nonlinear matter power spectrum in the sCreened HAlo Model. *Mon. Not. Roy. Astron. Soc.*, 476(1):L65–L68, 2018. doi: 10.1093/mnrasl/sly032.

Bhuvnesh Jain, Vinu Vikram, and Jeremy Sakstein. Astrophysical Tests of Modified Gravity: Constraints from Distance Indicators in the Nearby Universe. *Astrophys. J.*, 779:39, 2013. doi: 10.1088/0004-637X/779/1/39.

Nick Kaiser and Gordon Squires. Mapping the dark matter with weak gravitational lensing. *Astrophys. J.*, 404:441–450, 1993. doi: 10.1086/172297.

Tsz Yan Lam, Takahiro Nishimichi, Fabian Schmidt, and Masahiro Takada. Testing Gravity with the Stacked Phase Space around Galaxy Clusters. *Phys. Rev. Lett.*, 109:051301, 2012. doi: 10.1103/PhysRevLett.109.051301.

Baojiu Li, Wojciech A. Hellwing, Kazuya Koyama, Gong-Bo Zhao, Elise Jennings, and Carlton M. Baugh. The nonlinear matter and velocity power spectra in f(R) gravity. *Mon. Not. Roy. Astron. Soc.*, 428:743–755, 2013. doi: 10.1093/mnras/sts072.

Yoram Lithwick and Neal Dalal. Self-Similar Solutions of Triaxial Dark Matter Halos. *Astrophys. J.*, 734:100, 2011. doi: 10.1088/0004-637X/734/2/100.

Claudio Llinares. Testing modified gravity with globular clusters: the case of NGC 2419. *Mon. Not. Roy. Astron. Soc.*, 476(1):L29–L33, 2018. doi: 10.1093/mnrasl/sly021.

Claudio Llinares and David F. Mota. Cosmological simulations of screened modified gravity out of the static approximation: effects on matter distribution. *Phys. Rev.*, D89(8):084023, 2014. doi: 10.1103/PhysRevD.89.084023.

Lucas Lombriser, Fabian Schmidt, Tobias Baldauf, Rachel Mandelbaum, Uros Seljak, and Robert E. Smith. Cluster Density Profiles as a Test of Modified Gravity. *Phys. Rev.*, D85:102001, 2012. doi: 10.1103/PhysRevD.85.102001.

Rafael C. C. Lopes, Rodrigo Voivodic, Luis Raul Abramo, and Laerte Sodré, Jr. Turnaround radius in $f(R)$ model. *JCAP*, 1809(09):010, 2018. doi: 10.1088/1475-7516/2018/09/010.

Surhud More et al. Detection of the Splashback Radius and Halo Assembly bias of Massive Galaxy Clusters. *Astrophys. J.*, 825(1):39, 2016. doi: 10.3847/0004-637X/825/1/39.

Shin'ichi Nojiri, Sergei D. Odintsov, and Valerio Faraoni. Effects of modified gravity on the turnaround radius in cosmology. *Phys. Rev.*, D98(2):024005, 2018. doi: 10.1103/PhysRevD.98.024005.

Johannes Noller, Francesca von Braun-Bates, and Pedro G. Ferreira. Relativistic scalar fields and the quasistatic approximation in theories of modified gravity. *Phys. Rev.*, D89(2):023521, 2014. doi: 10.1103/PhysRevD.89.023521.

Ciaran A.J. O'Hare and Clare Burrage. Stellar kinematics from the symmetron fifth force in the Milky Way dxisk. *Phys. Rev.*, D98(6):064019, 2018. doi: 10.1103/PhysRevD.98.064019.

Levon Pogosian and Alessandra Silvestri. What can cosmology tell us about gravity? Constraining Horndeski gravity with Σ and μ. *Phys. Rev.*, D94(10):104014, 2016. doi: 10.1103/PhysRevD.94.104014.

Adam G. Riess et al. Observational evidence from supernovae for an accelerating universe and a cosmological constant. *Astron. J.*, 116:1009–1038, 1998. doi: 10.1086/300499.

Bjoern Malte Schaefer and Kazuya Koyama. Spherical collapse in modified gravity with the Birkhoff-theorem. *Mon. Not. Roy. Astron. Soc.*, 385:411–422, 2008. doi: 10.1111/j.1365-2966.2008.12841.x.

Xun Shi. The outer profile of dark matter haloes: an analytical approach. *Mon. Not. Roy. Astron. Soc.*, 459(4):3711–3720, 2016. doi: 10.1093/mnras/stw925.

T. Shin et al. Measurement of the Splashback Feature around SZ-selected Galaxy Clusters with DES, SPT and ACT. 2018.

Laura Taddei, Riccardo Catena, and Massimo Pietroni. Spherical collapse and halo mass function in the symmetron model. *Phys. Rev.*, D89(2):023523, 2014. doi: 10.1103/PhysRevD.89.023523.

Keiichi Umetsu and Benedikt Diemer. Lensing Constraints on the Mass Profile Shape and the Splashback Radius of Galaxy Clusters. *Astrophys. J.*, 836(2):231, 2017. doi: 10.3847/1538-4357/aa5c90.

Keiichi Umetsu, Tom Broadhurst, Adi Zitrin, Elinor Medezinski, Dan Coe, and Marc Postman. A Precise Cluster Mass Profile Averaged from the Highest-Quality Lensing Data. *Astrophys. J.*, 738:41, 2011. doi: 10.1088/0004-637X/738/1/41.

C. M. Will. *Theory and experiment in gravitational physics.* 1993. ISBN 9780521439732.

Gong-Bo Zhao, Tommaso Giannantonio, Levon Pogosian, Alessandra Silvestri, David J. Bacon, Kazuya Koyama, Robert C. Nichol, and Yong-Seon Song. Probing modifications of General Relativity using current cosmological observations. *Phys. Rev.*, D81: 103510, 2010. doi: 10.1103/PhysRevD.81.103510.

Ying Zu, D. H. Weinberg, Elise Jennings, Baojiu Li, and Mark Wyman. Galaxy Infall Kinematics as a Test of Modified Gravity. *Mon. Not. Roy. Astron. Soc.*, 445(2):1885–1897, 2014. doi: 10.1093/mnras/stu1739.

Chapter 4

The mass–size relation of galaxy clusters

The outskirts of accreting dark matter halos exhibit a sudden drop in density delimiting their multi-stream region. Due to the dynamics of accretion, the location of this physically motivated edge strongly correlates with the halo growth rate. Using hydrodynamical zoom-in simulations of high-mass clusters, we explore this definition in realistic simulations and find an explicit connection between this feature in the dark matter and galaxy profiles. We also show that the depth of the splashback feature correlates well with the direction of filaments and, surprisingly, the orientation of the brightest cluster galaxy. Our findings suggest that galaxy profiles and weak-lensing masses can define an observationally viable mass–size scaling relation for galaxy clusters, which can be used to extract cosmological information.

4.1   Introduction

In the ΛCDM paradigm, structure in the Universe arises from the initial density perturbations of an (almost) homogeneous dark matter distribution. Due to gravitational evolution, this leads to the appearance of collapsed structures, i.e. dark matter halos. Some of the baryonic matter, following this process, cools down and settles at the centers of the gravitational potentials where it forms galaxies.

This mechanism has been studied through models of so-called spherical collapse (Gunn and Gott, 1972; Bertschinger, 1985), whose main prediction is the existence of a radius within which the material orbiting the halo is completely virialized. In general, this virial radius depends on cosmology and redshift, but both in numerical simulations and observations, fixed overdensity radii are widely used as proxies for this quantity. An example of this is r_{200m}, defined as the radius within which the average density is 200 times the average matter density of the Universe, ρ_m. The corresponding enclosed mass is known as M_{200m}.

Halo mass functions constructed with these idealized definitions can capture the effects of cosmology (Press and Schechter, 1974), the nature of dark matter (Angulo et al., 2013), and dark energy (Mead et al., 2016) on the growth of structure. In the real Universe, however, this picture is complicated by the triaxiality of halos (Dubinski and Carlberg, 1991; Monaco, 1995) and the existence of clumpy (baryonic) substructure (Bocquet et al., 2015).

Because the process of structure formation is hierarchical, massive halos contain subhalos, some of which host galaxies themselves. The resulting clusters of galaxies are the focus of this work. What makes these objects particularly unique is the fact that they are not fully virialized yet. To this day, they are still accreting both ambient material and subhalos through filamentary structures surrounding them (Bond et al., 1996). Because of their definition, however, traditional overdensity definitions of mass are not only affected by halo growth, but also by a pseudo-evolution due to the redshift dependence of ρ_m (Diemer et al., 2013).

Diemer and Kravtsov (2014) and More et al. (2015) were the first to note that this growth process leads to the formation of a sharp feature in the density profile that separates collapsed and infalling material. This feature therefore defines a natural boundary of the halo. The location of this edge, i.e. the splashback radius r_sp, has an obvious primary dependence on halo mass, but also a secondary dependence on accretion rate. While this behavior can be qualitatively explained using simple semi-analytical models of spherical collapse, none of the analytical models currently proposed (Adhikari et al., 2014; Shi, 2016) can fully describe its dependency on mass and accretion rate (Diemer et al., 2017). Despite this, the corresponding definition of halo mass is particularly suited to define a universal mass function valid for a wide range of cosmologies (Diemer, 2020a).

In this chapter, we try to bridge the gap between the theoretical understanding of

the splashback feature and observational results, both past and future. The outer edge of clusters has already been extensively measured through different tracers: the radial distribution of galaxies from wide surveys (More et al., 2016; Baxter et al., 2017; Chang et al., 2018), but also their velocity distribution (Tomooka et al., 2020; Fong and Han, 2021), and in the weak-lensing signal of massive clusters (Umetsu and Diemer, 2017; Chang et al., 2018; Contigiani et al., 2019a). Furthermore, forecasts have already set expectations for what will be obtainable from near-future experiments (Fong et al., 2018; Xhakaj et al., 2019; Wagoner et al., 2020). Despite the wealth of data and studies, however, not many *splashback observables* have been proposed. The only robust application of this feature found in the literature is related to the study of quenching for newly accreted galaxies (Adhikari et al., 2020).

To achieve our goal, we make use of hydrodynamical simulations of massive galaxy clusters, which we introduce in Section 4.2. We focus mainly on $z = 0$, but also make use of snapshots at redshifts $z = 0.474$ and $z = 1.017$. In Section 4.3, we start our discussion by introducing the physical interpretation of splashback and consider the connection between the galaxy and dark matter distributions. We then continue in Sections 4.4 and 4.5, where we explain how galaxy profiles and weak-lensing mass measurements can be combined to construct a mass–size relationship for galaxy clusters. Finally, we summarize our conclusions and suggest future developments in Section 4.6.

4.2 Hydrangea

The Hydrangea simulations are a suite of 24 zoom-in hydrodynamical simulations of massive galaxy clusters ($\log_{10} M_{200m}/M_\odot$ between 14 and 15.5 at redshift $z = 0$) designed to study the relationship between galaxy formation and cluster environment (Bahé et al., 2017). They are part of the Cluster-EAGLE project (Bahé et al., 2017; Barnes et al., 2017) and have been run using the EAGLE galaxy formation model (Schaye et al., 2015), which is known to reproduce galaxy observables such as color distribution and star formation rates. To better reproduce the observed hot gas fractions in galaxy groups, the AGNdT9 variant of this model was used (Schaye et al., 2015).

The zoom-in regions stretch to between 10 and 30 Mpc from the cluster center, roughly corresponding to $\lesssim 10r_{200m}$. For the definition of the cluster center, in this work, we choose the minimum of the gravitational potential. We note, however, that this choice will not impact our conclusions since we will focus on locations around r_{200m}. The particle mass of $m \sim 10^6$ M$_\odot$ for baryons and $m \sim 10^7$ M$_\odot$ for dark matter allows us to resolve galaxy positions down to stellar masses $M_* \geq 10^8$ M$_\odot$ and total masses $M_{sub} \geq 10^9$ M$_\odot$, respectively.

In Figure 4.1 we show the log-derivative of the stacked subhalo density $n_s(r)$ at large scales. This is the result of a fit obtained using the model of Diemer and Kravtsov (2014), and we refer the reader to the aforementioned paper and Chapter 2 of this thesis for a detailed explanation of the model and its components. The choice to employ this
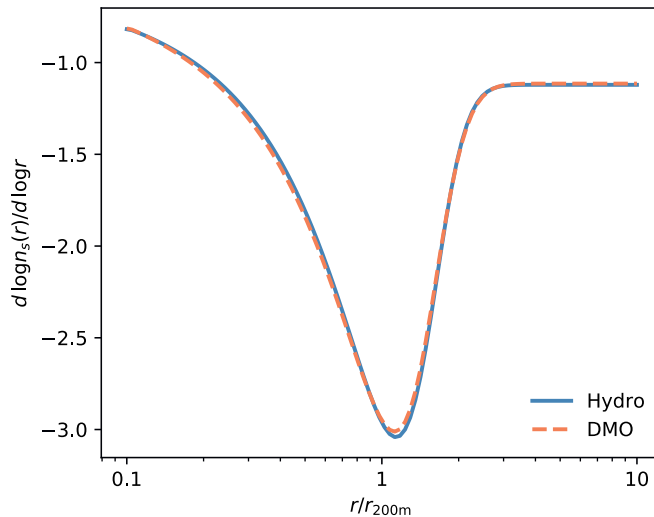
Figure 4.1: The splashback feature visible in the average subhalo distribution of simulated high-mass clusters. We extract the logarithmic slope by fitting a smooth profile to the mean of the Hydrangea profiles rescaled by $r_{200\mathrm{m}}$. We perform this operation both on the hydrodynamical simulations (Hydro) and their dark matter only counterparts (DMO). The minimum around r_{200m} marks the halo boundary, and this figure highlights the lack of baryonic effects on the location or depth of this feature. The two logarithmic slope profiles are consistent with each other at the 1 percent level.

profile is based on its ability to capture the sharp feature visible around $r_{200\mathrm{m}}$, which is the focus of this work. We optimally sample its eight-dimensional parameter space using an ensemble sampler (Foreman-Mackey et al., 2013).

In the same plot, we also include the stacked subhalo profile of the accompanying dark matter only (DMO) simulations, initialized with matching initial conditions. The two profiles match almost exactly, suggesting that baryonic effects do not alter this feature to a significant extent (see also O'Neil et al., 2020). While not shown, we report that the same conclusion can be reached by looking at the full matter distribution $\rho(r)$ in the two sets of simulations. Similarly, this feature is also visible in the number density of galaxies, $n_g(r)$. Due to our focus on all three of these profiles, we choose not to work with background subtracted quantities.

For reference, we present a full list of the simulated clusters used in this chapter and their relevant properties, some of them defined in the following sections, in Table 4.1.

Table 4.1: The Hydrangea clusters used in this chapter and their $z = 0$ properties. $\Gamma_{0.3}$ is the accretion rate measured between $z = 0$ and $z = 0.297$. The three splashback radii $r_{\rm sp}$, $r_{\rm sp}^{\rm g}$, $r_{\rm sp}^{\rm s}$ refer to the splashback radius measured, respectively, in the dark matter, galaxy, and subhalo distributions (see Section 4.3). For two clusters, CE-28 and CE-18, the radius $r_{\rm sp}$ is not used in this work because the dark matter distribution displays a featureless profile at large scales. All quantities are in physical units.

Name	$\Gamma_{0.3}$	$M_{\rm 200m}$ $[10^{14}\ M_\odot]$	$r_{\rm 200m}$ [Mpc]	$r_{\rm sp}$ [Mpc]	$r_{\rm sp}^{\rm g}$ [Mpc]	$r_{\rm sp}^{\rm sub}$ [Mpc]
CE-0	0.8	1.74	1.74	2.98	2.72	2.60
CE-1	2.0	1.41	1.63	1.71	1.56	1.79
CE-2	0.5	1.41	1.63	2.36	3.27	2.36
CE-3	0.8	2.04	1.84	2.60	2.72	2.72
CE-4	2.8	2.19	1.89	1.63	1.87	1.79
CE-5	2.0	2.24	1.90	2.36	2.60	2.48
CE-6	1.1	3.31	2.16	2.60	2.48	2.60
CE-7	1.2	3.39	2.17	3.13	2.60	2.85
CE-8	1.8	3.09	2.12	2.26	2.48	2.06
CE-9	1.1	4.27	2.36	3.76	3.76	3.27
CE-10	0.8	3.55	2.21	3.13	3.13	2.98
CE-11	1.4	4.27	2.34	3.13	2.85	2.72
CE-12	0.1	5.13	2.49	3.43	3.76	4.13
CE-13	1.5	5.25	2.52	2.26	3.13	2.72
CE-14	2.1	6.17	2.66	2.60	2.72	2.48
CE-15	4.2	6.76	2.73	1.96	2.26	2.48
CE-16	2.7	7.59	2.84	1.42	4.13	3.43
CE-18	1.1	9.12	3.03	-	3.76	3.76
CE-21	3.7	12.30	3.34	2.36	2.85	2.60
CE-22	1.5	16.98	3.72	4.53	4.53	4.33
CE-24	1.5	15.49	3.61	3.27	3.27	4.33
CE-25	3.4	19.05	3.87	3.43	3.43	3.43
CE-28	1.9	21.88	4.06	-	3.94	3.27
CE-29	3.5	32.36	4.61	3.94	4.13	3.94

4.3   Splashback

4.3.1   Definition

For halos that continuously amass matter, material close to its first apocenter piles up next to the edge of the multi-stream region, where collapsed and infalling material meets (Adhikari et al., 2014). A sudden drop in density, i.e. the feature visible in the profiles of Figure 4.1, is associated with this process.

This intuitive picture leads to three characterizations of the splashback radius, depending on the approach used to measure or model it:

1. The location of the outermost phase-space caustic.

2. The point of steepest slope in the density profile.

3. The apocenter of recently accreted material.

While these definitions have all been previously hinted at in the introduction, in this section, we explicitly present them and discuss the connections existing between them. This also justifies our adopted definition, based on the density profile.

The first definition is clearly motivated in the spherical case but fails once it is applied to realistic halos. The presence of angular momentum and tidal streams from disrupted subhalos (see e.g. Vogelsberger and White, 2011), smooth out this feature and make its description murky. The second definition was the first suggested in the literature. Introduced by Diemer and Kravtsov (2014), it is based on the study of dark matter profiles in N-body simulations and has been linked to the first, more dynamical, definition (Adhikari et al., 2014; Shi, 2016). The third was first suggested by Diemer (2017), who showed that this location can be calibrated to the second one (Diemer et al., 2017) by choosing specific percentiles of the apocenter distribution.

To clarify the relationship between the outermost caustic and apocenter, it is educational to use a self-similar toy model based on Adhikari et al. (2014) to show the phase-space distribution of a constantly accreting halo with an NFW-like mass profile (Navarro et al., 1997).

In the absence of dark energy, we follow the radial motion of particles,

$$\ddot{r} = \frac{GM(<r,t)}{r^2}, \tag{4.1}$$

between their first and second turnaround in the mass profile:

$$M(r,t) = M(R,t)\,\frac{f_{\mathrm{NFW}}(r/r_{\mathrm{s}})}{f_{\mathrm{NFW}}(R/r_s)}. \tag{4.2}$$

We impose that the total mass evolves as $M(R,t) \propto t^{2\Gamma/3}$, $R \propto t^{2(1+\Gamma/3)/3}$, and the dimensionless NFW profile is defined as: $f(x) = \log(1+x) - x/(1+x)$. In this set of

equations, Γ is the dimensionless accretion rate, R represents the turnaround radius, and the scale parameter r_s is defined by the infall boundary condition

$$\frac{d\log M}{d\log r}(R) = \frac{3\Gamma}{3+\Gamma}. \tag{4.3}$$

This condition, combined with the turnaround dynamics, imposes that $M(R,t) \propto (1+z)^{-\Gamma}$ (Fillmore and Goldreich, 1984).

We point out that the dependence on the time-sensitive turnaround properties $M(R,t), R(t)$ can be factored out from the equations above, meaning that the entire phase-space at all times can be obtained with a single numerical integration.

In Figure 4.2 we show the result of this calculation, denoting the location of the outermost caustic as $r_{\rm sp}^c$. The caustic is formed by the outermost radius at which shells at different velocities meet ($r/r_{\rm sp}^c = 1$ in the plot) and the location of shells at apocenter is defined by the intersection between the zero-velocity line and the phase-space distributions. From the figure, two things are noticeable: material at $r_{\rm sp}^c$ has not reached its apocenter yet, and the ratio between these two locations depends on the accretion rate.

It is beyond the scope of this work to quantify this dependence since it depends heavily on the mass profile inside $r_{\rm sp}^c$. Qualitatively, however, the difference between caustic and apocenter is easy to understand once the dynamical nature of this feature is considered: the halo is growing in size, and while some material is now reaching its apocenter, mass accreted more recently has the chance to overshoot it and form the actual caustic. In a static picture, this would not be the case.

In realistic halos, this dependence on accretion rate is only one of many factors that biases and adds scatter to the relationship between the halo boundary and apocenters. Other factors include, e.g. nonspherical orbits and the presence of multiple accretion streams. Despite this, Diemer (2017) has shown that there is a clear link between the apocenter distribution and splashback. The percentile definition introduced there is particularly suited to theoretical investigations, but its usefulness in the very low-Γ regime is still uncertain (Mansfield et al., 2017; Xhakaj et al., 2019), and it has not been explored in the presence of modifications of gravity (Adhikari et al., 2018; Contigiani et al., 2019).

For this work, we define the splashback radius as the location of the steepest slope as defined by a profile fit. In Table 4.1 we report, for each cluster, this radius measured in the distribution of galaxies, subhalos, and total matter ($r_{\rm sp}^g, r_{\rm sp}^s, r_{\rm sp}$). The model is a modified Einasto profile (Einasto, 1965) with the addition of a power-law to take into account infalling material (Diemer and Kravtsov, 2014). Regarding the goodness of fit, we find that up to and around r_{200m} the standard deviation of the residuals is of order 10 percent. On the other hand, the presence of substructure superimposed on a shallow density profile results in normalized residuals of order 50 percent in the outer regions.

To further justify our approach, we show in Figure 4.3 how this simple definition of
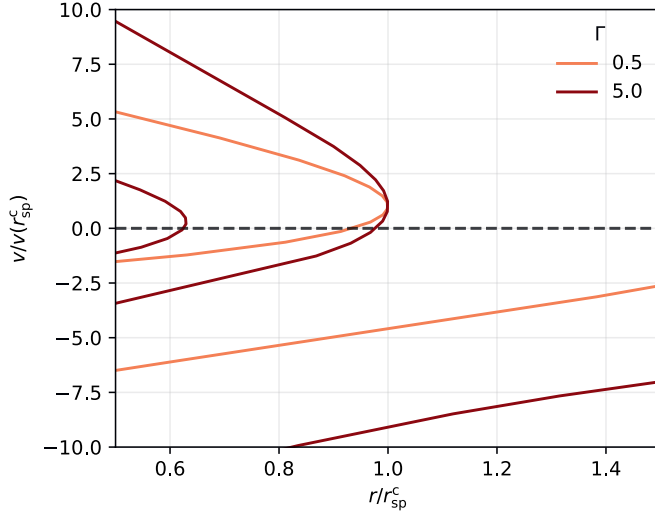
Figure 4.2: The phase-space structure of accreting dark matter halos depends on the accretion rate Γ. We employ a toy model of spherical collapse to describe the multi-stream region of NFW-like halos. The figure shows that the material at the outermost caustic, r_{sp}^c, is not necessarily at apocenter (where $v = 0$) and that the ratio of these two radii is a function of accretion rate. For ease of readability, we have rescaled the coordinates by r_{sp}^c, and the velocity of collapsed material at this point.

splashback radius is able to capture the phase-space boundary of different halos, even when a sudden drop in density is absent. The main benefit of this definition is that it avoids the arbitrariness of the apocenter definition, or the bias induced by multiple caustics in the minimum slope definition (Mansfield et al., 2017). Its main caveats, however, are that (1) it is computationally expensive since it requires high-resolution simulations and a multi-parameter fit procedure, and (2) it might not apply to low-mass clusters and galaxy groups. We leave this last question open for future investigations.

We wrap this subsection up by stressing that this definition of 'the' splashback radius is, like any other, useful only to study its correlation with other properties, or quantify the impact of different physical processes. While the flexibility of the chosen model is not surprising given the number of free parameters, the clear connection between the phase-space and the log-derivative in individual halos is a powerful and seemingly general result. Ultimately, however, the observational results focus on stacked projected density profiles, and so should the predictions.

4.3.2 Accretion

It is well established (Diemer and Kravtsov, 2014; More et al., 2015; Mansfield et al., 2017; Diemer, 2020) that the location of the halo boundary correlates with the accretion rate

$$\Gamma_{0.3} = \frac{\Delta \log M_{200\text{m}}}{\Delta \log(1+z)}. \tag{4.4}$$

In this work, this ratio is calculated in the redshift range $z = 0$ to $z = 0.293$, since this time interval roughly corresponds to one crossing time for all clusters considered here, i.e. how long ago the material currently at splashback has been accreted (Diemer, 2017). Although this choice is partially arbitrary, we have investigated the dependence of our results on the redshift upper limit and we have verified that our main conclusions are not affected.

The archetypical relation demonstrating this idea is plotted in Figure 4.4, where we have also included the relations found in More et al. (2015), Diemer et al. (2017), and Diemer (2020), to provide additional context. We find good agreement, even though a perfect match is not necessarily expected. The Hydrangea clusters represent a biased sample, selected to be mostly isolated at low redshift (Bahé et al., 2017). While the effect of this selection on the accretion rate distribution is not fully known, we show below that a connection between cluster environment and this quantity exists, and the presence of mergers might therefore influence it. This is not surprising since a connection between accretion and large-scale bias is already known (e.g. Fakhouri and Ma, 2010).

We show this relationship explicitly in Figure 4.5 by using one of the parameters of the profile model. As visible in the figure, the power-law index of material outside of splashback correlates with the accretion rate. We find that this is true for both subhalos and galaxies and that the difference between the two is consistent with sample variance.
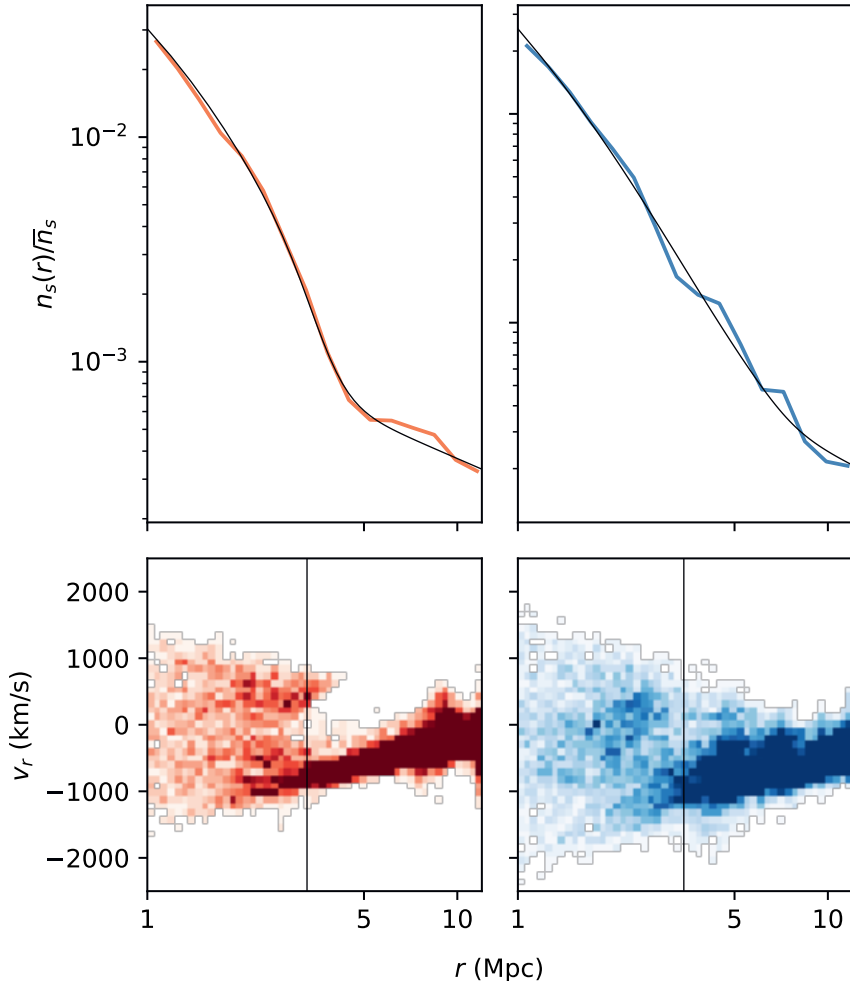
Figure 4.3: Fitting simulated subhalo profiles with a smooth model. In the top panels, we show the radial subhalo distributions of two clusters (CE-16, left and CE-9, right), together with the best-fit profiles used to reconstruct the log-derivative. In the bottom panels, we show how the inferred location of the log-derivative minimum (vertical line) identifies the phase-space edge of relaxed (left) and perturbed (right) galaxy clusters. In the phase-space plots, the cluster on the left is formed by collapsed particles, while the stream visible on the lower right is infalling material. The right panels demonstrate how our approach is effective even in the presence of an ongoing merger when the splashback feature is not visible as a sharp transition in the density profile.
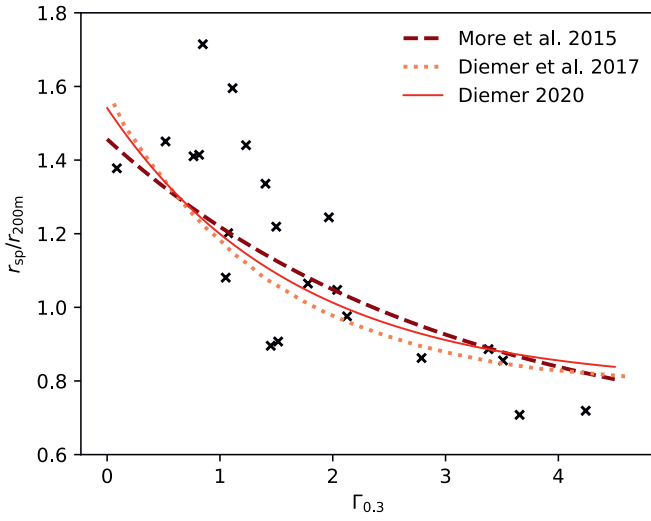
Figure 4.4: The splashback radius and its correlation with the accretion rate. The ratio between the splashback radius and the 200m overdensity radius correlates with the accretion rate. We show that this correlation exists for the clusters studied in this work and compare it to the relations obtained in three other studies (see text for references).

To try and explain this behavior, we use a fully consistent model of spherical collapse introduced by Bertschinger (1985), which was also used in Contigiani et al. (2019). The setup of this toy model is the same as what is shown in Equation (4.1), but with a mass profile that also needs to be solved for. Starting from an initial guess for $M(r,t) = \mathcal{M}(r/R(t))$, orbits are integrated and their mass distribution is calculated. Iterating this process multiple times returns a self-similar density profile and orbits consistent with each other.

The result of this calculation is also shown in Figure 4.5. Because the mass-profile prediction is not a power law, we plot a filled line displaying the range of logarithmic slopes allowed between r_{sp}^{c} and $2r_{sp}^{c}$. The fact that this prediction is not a function of accretion rate implies that the correlation between the slope and the accretion rate seen in the simulations is not purely dynamical, and suggests a connection between the cluster environment and accretion rate.

We stress here that previous splashback works have mostly focused on stacked halo profiles, for which the expectation of the spherically symmetric calculation shown above is roughly verified, even in the presence of dark energy (Shi, 2016). We also recover this result for our sample (see the star symbol in Figure 4.5), but we point out that this is a simple conclusion. Because Newtonian gravity is additive, stacking enough clusters should always recover the spherically symmetric result. Despite this, we also note that results from the literature do not always agree with this prediction. However, we do not linger on these discrepancies since (1) this was never the focus of previous articles, and (2) different methods to extract the power law have been employed.

4.3.3   Anisotropy

This departure from the spherical case implies that anisotropies play a role in shaping the accretion rate Γ. To study the impact of accretion flows on the cluster boundary, we study 72 sky projections of the Hydrangea clusters (3 each, perpendicular to the x, y, and z axes of the simulation boxes) and rotate them to align the preferred accretion axes in these planes. For each projection, we define this direction $\theta \in (-\pi/2, \pi/2)$ in two ways: (1) to capture the filamentary structure around the cluster between r_{200m} and $5r_{200m}$, we divide the subhalo distribution in 20 azimuthal bins and mark the direction of the most populated one, and (2) to capture the major axis of the BCG, we use unweighted quadrupole moments of the central galaxy's stellar profile within 10 kpc from its center. The mean projected distributions according to these two methods are presented in the left and right top panels of Figure 4.6, respectively.

Looking at the top-left panel of the figure, it is not surprising that filamentary structures of the cosmic web are visible around the central cluster – this is by construction. Because of the higher contrast between outside and inside regions, the subhalo distribution exhibits a sharper feature in the directions pointing toward voids (see central panel of Figure 4.6). More surprisingly, however, these same traits are also noticeable in
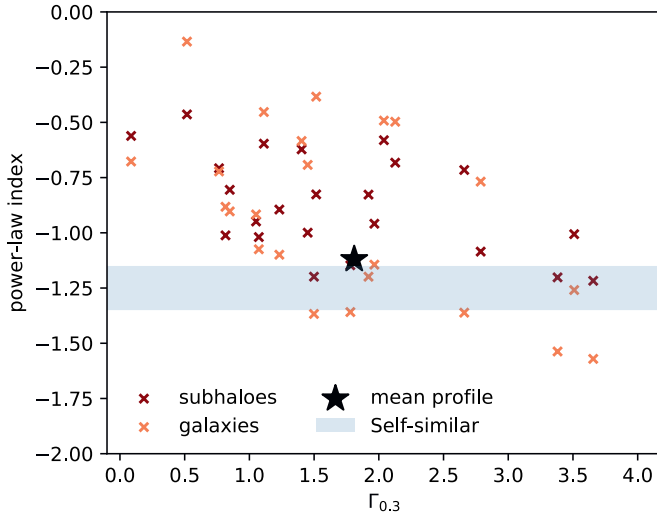
Figure 4.5: The distribution of subhalos and galaxies outside the cluster edge as a function of accretion rate. Faster growing halos display a more concentrated distribution of satellites outside of their boundary. This behavior seen in individual clusters is not explained by simple models of spherical collapse (blue shaded area), but the average profile (marked by a star) matches the expectation. This suggests that non-isotropic processes shape this relation.
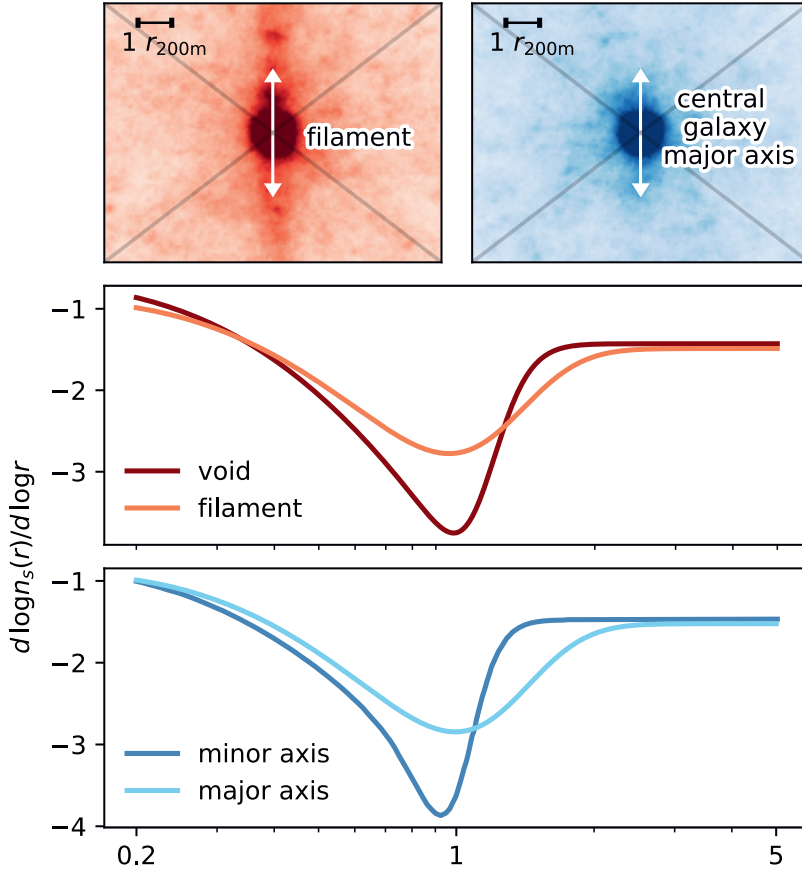
Figure 4.6: The impact of filaments and accretion flows on the cluster's edge. We rotate the two-dimensional subhalo distributions of different clusters to align their accretion axes. The top panels show the resulting mean distributions in a square region of size $5r_{200m}$ obtained with two definitions of this direction: one based on the presence of filaments outside r_{200m} (left), and one based on the central galaxy's major axis (right). The first one better identifies the filamentary structures around the clusters, but the second one is closer to what can be observed. In the bottom panels, we show how the inferred 3-dimensional logarithmic slope inside the quadrants aligned with the accretion direction (darker shade) differs from the profile outside (lighter shade). The results from the bottom panel imply that the central galaxy's major axis traces the direction of infalling material.

the mean distributions aligned according to the central galaxy's axis (see lower panel).

This result implies that the distribution of stellar mass within the central 10 kpc of the cluster contains information about the distribution of matter at radii which are a factor 10^2 larger. In fact, the connection between the shape of the dark matter halo and the ellipticity of the brightest cluster galaxy (BCG, which is also the central galaxy for massive galaxy clusters) is known (Okumura et al., 2009; Herbonnet et al., 2019; Ragone-Figueroa et al., 2020). And, similarly to other results (Conroy et al., 2007; De Lucia and Blaizot, 2007), the Hydrangea simulations predict that the stellar-mass buildup of the BCG is driven by the stripping of a few massive satellites after their first few pericenter passages (Bahé et al., in preparation). Because these galaxies quickly sink to the center, the material they leave behind is therefore a tracer of their infalling direction.

4.4   The mass–size relation

In our sample, we find that the splashback feature seen in the galaxy, subhalo, and total matter profiles are all at the same location. The mean fractional difference between any two of $r_{\mathrm{sp}}^g, r_{\mathrm{sp}}^s$, or r_{sp} is consistent with zero, with a mean standard deviation of 3 percent. We also verified that this statement is unaffected by cuts in subhalo mass or galaxy stellar mass. Due to the limited size of our sample, the effects of dynamical friction on the distribution of high-mass subhalos are not visible (Adhikari et al., 2016).

We emphasize, however that this does not mean that galaxy selection effects have no impact on these quantities. For example, it is an established result, both in the Hydrangea simulations (Oman et al., 2020) and in observations (Adhikari et al., 2020), that the location of a galaxy in projected phase-space correlates with its color and star-formation rate. This is because a red color preferentially selects quenched galaxies that have been orbiting the halo for a longer time.

Until their first apocenter after turnaround, galaxies act as test particles orbiting the overdensity as the halo grows in mass. In the standard cold dark matter paradigm, based on a non-interacting particle, it is not surprising then that the edge formed in their distribution is identical to the one seen in the dark matter profile. It should be noted, however, that this is not necessarily true in extended models in which dark matter does not act as a collisionless fluid. Due to their infalling trajectories, the distribution of galaxies will always display a splashback feature, even if the dark matter profile does not exhibit one.

In the cold dark matter scenario, our result implies that galaxies can be used to trace the edge of clusters. We note, in particular, that this measurement has already been performed several times using photometric surveys (Baxter et al., 2017; Nishizawa et al., 2017; Chang et al., 2018; Zürcher and More, 2019; Shin et al., 2019). Furthermore, due to the large number of objects detected, galaxy distributions obtained through this method offer the most precise measurements of splashback. The accuracy of the results, however, depends heavily on the details of the cluster finding algorithm (Busch and

White, 2017; Shin et al., 2019).

With this in mind, we build an observational mass–size relation between the location of this feature in the galaxy distribution (r_{sp}^g) and the mass enclosed within it (M_{sp}^g). In Figure 4.7 we present the correlation between the two for the Hydrangea clusters. Because the splashback radius is roughly located at $r_{200\mathrm{m}}$ (see Figure 4.4), this relationship can be understood as a generalization of the virial mass-radius relation, where we have introduced a dependence on accretion rate. Surprisingly, we find that the dependence on $\Gamma_{0.3}$ is well captured by a simple form:

$$\frac{M_{\mathrm{sp}}}{r_{\mathrm{sp}}^3} \propto (1 + \Gamma_{0.3})^\beta. \tag{4.5}$$

While we do not constrain β precisely, we find that $\beta = 1.5$ provides an adequate fit by reducing the total scatter from 0.25 dex to about half of this value. This choice of exponent and functional form is supported by the model of self-similar collapse used for Figure 4.5, where we find that a power-law $\beta = 1.45$ fits this relationship with the same precision as the exponential functions calibrated to numerical simulations shown in Figure 4.4. For a more extensive comparison with these predictions, we refer the reader to Section 4.6.

The virial relation is a trivial connection between the mass and size of halos based on an overdensity factor, but its observational power is limited by the fact that these masses are usually extracted from parametric fits to weak-lensing profiles that do not extend to the respective overdensity radii. Because of this, the overdensity masses have a strong dependence on the assumed mass-concentration relation (see e.g. Umetsu et al., 2020). The splashback feature, on the other hand, naturally predicts a mass–size relation for galaxy clusters and does so without the need for external calibrations.

In Figure 4.7 we also plot the expected change in this relation to due modifications of gravity. We use the symmetron gravity model of Contigiani et al. (2019) with parameters $f = 1$ and $z_{\mathrm{ssb}} = 1.5$, and assume that the change affects only the splashback radius and not the mass contained within it. The exact result depends on the theory parameters, but the expected change in this relation is around 0.15 dex.

Experimentally, we argue that this relation can be probed using a combination of galaxy density profiles (to extract r_{sp}^g) and weak lensing measurements. Aperture masses (Clowe et al., 2000), in particular, can be used to extract in a model-independent fashion the average projected mass within a large enough radius. If necessary, the aperture mass can also be deprojected to obtain a low-bias estimate (Herbonnet et al., 2020).

4.5   Redshift evolution

So far, we have only considered the simulation predictions at $z = 0$. In this section, we extend our analysis to higher redshifts by exploring two other snapshots of the Hydrangea simulations at $z = 0.474$ and $z = 1.017$.
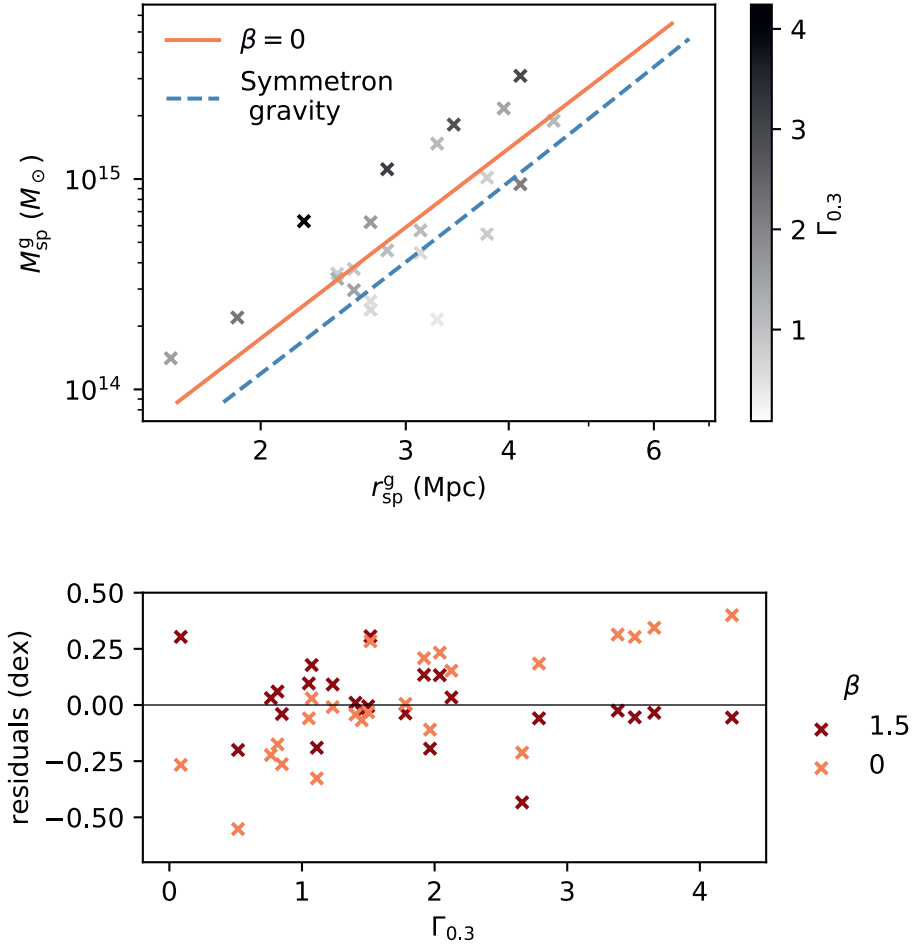
Figure 4.7: The mass–size relation of galaxy clusters. In the top panel, we show how the size of the cluster boundary seen in the galaxy distribution, r_{sp}^g, scales with its enclosed mass, M_{sp}^g. In the same panel we also show the median relation in Equation (4.5) obtained for $\beta = 0$ and how modifications of gravity are expected to affect this relation (blue dashed line, see text for more details). In this relation, a secondary dependence on the accretion rate $\Gamma_{0.3}$ is a source of scatter that can be captured if $\beta \neq 0$. As visible in the residuals in the bottom panel, a simple power-law form well reproduces this dependence. In the considered sample, we find that half of the total scatter (0.25 dex) is due to the mass accretion rate distribution.

At these higher redshifts, we find that the scatter in the splashback relation for individual halos is large. This is visible in Figure 4.8, where we plot the equivalent of Figure 4.4 for these two snapshots. We recover the general result of Diemer (2020) that the average values of $r_{\mathrm{sp}}/r_{\mathrm{200m}}$ and Γ should be higher at early times, but the correlation between the two is completely washed out by $z = 1$. We connect this to three causes: (1) The fixed time interval between the snapshots does not allow us to reliably estimate Γ at higher redshift when the crossing times are smaller. (2) The lower number of resolved galaxies and subhalos means that the residuals of the individual profile fits are larger around the virial radius. And finally, (3) the higher frequency of mergers at high redshift means that the number of halos with profiles not displaying a clear splashback feature increases.

We find that Equation (4.5) is still valid, even if our ability to constrain the scatter at high redshift is impeded by the sample variance. Furthermore, we report that the splashback overdensity $M_{\mathrm{sp}}/r_{\mathrm{sp}}^3$ has a redshift dependence. Or, in other words, that the logarithmic zero-point that was not specified in Equation (4.5) is a function of redshift. Not accounting for the Γ dependence, our best fit values for the logarithm of the average overdensity $\log_{10}(M_{\mathrm{sp}}/\mathrm{M}_\odot) - 3\log_{10}(r_{\mathrm{sp}}/\mathrm{Mpc})$ are $[13.3, 13.8, 14.1] \pm 0.3$ at redshifts $[0, 0.5, 1]$.

Regarding the anisotropy in the splashback feature due to filamentary structures, we report that this phenomenon exists also at high redshift. In Figure 4.9, we compare the sky-projected subhalo profiles $\Sigma_s(R)$ toward different directions, similarly to what we have done for Figure 4.6. In this case, however, we explicitly discuss the connection with observations by plotting directly the ratio of the density profiles inside quadrants oriented toward and perpendicular to the two accretion directions, instead of focusing on the result of the profile fits. The mean and variance of these ratios are calculated assuming that the different projections are independent. We find that the orientation of the major axis of the brightest cluster galaxy does not correlate with a splashback anisotropy at $z = 1$. This is because, in most cases, the identification of a central, brightest galaxy is not straightforward at this redshift. At early times, the future central galaxy is still in the process of being created from the mergers of multiple bright satellites located close to the cluster's center of potential.

To conclude this section, we point out that in the region around r_{200m}, the difference between the profiles perpendicular and parallel to the central galaxy's major axis is about 10 percent at redshift $z \lesssim 0.5$. This departure is well within the precision of galaxy profiles extracted from large surveys (e.g. Adhikari et al., 2020). Therefore, this measurement might already be possible using such catalogs.

4.6   Discussion and conclusions

On its largest scales, the cosmic web of the Universe is not formed by isolated objects, but by continuously flowing matter distributed in sheets, filaments, and nodes. For
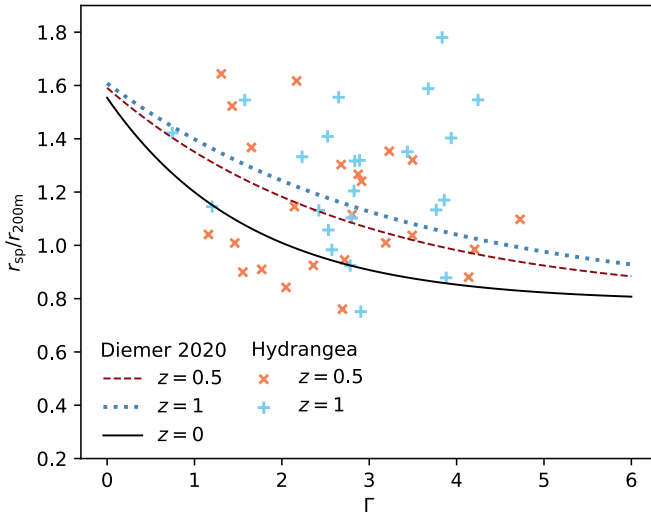
Figure 4.8: The splashback radius and its correlation with the accretion rate as a function of redshift. This plot is an extension of Figure 4.4 for redshifts $z = 0.474$ (orange crosses) and $z = 1.017$ (light blue plus symbols). The ratio between the splashback radius and the 200m overdensity radius should correlate with the accretion rate Γ, but for the Hydrangea snapshot at $z = 1.017$ the large sample variance washes out this correlation. Despite this, we still recover the expectation of previous results (plotted lines), a larger average $r_{\rm sp}/r_{\rm 200m}$ at higher redshift.
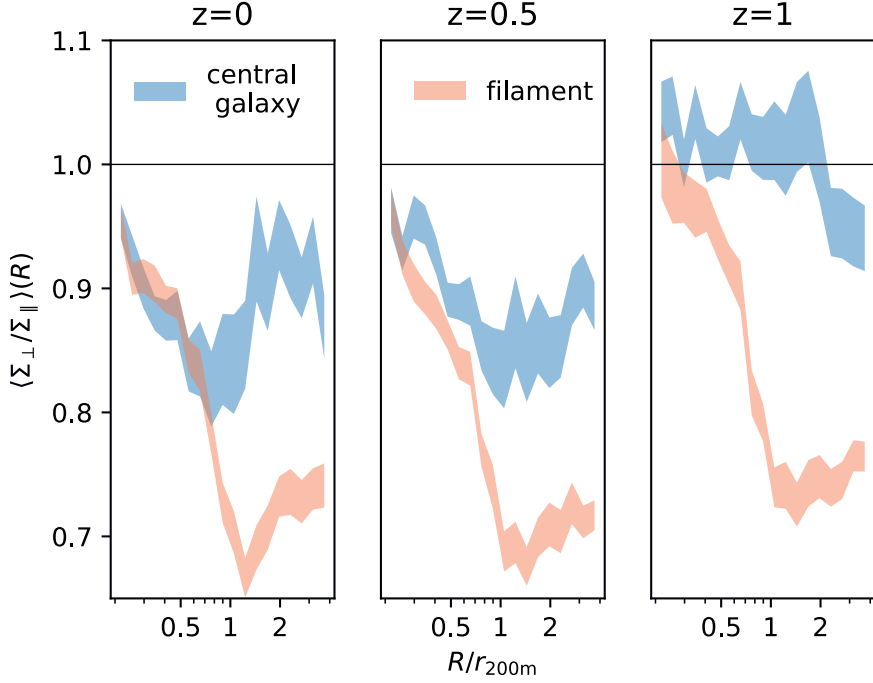
Figure 4.9: The impact of filaments and accretion flows on the outer density profile of massive halos as a function of redshift. We plot the mean value and variance of the ratio between the two-dimensional subhalo distributions in quadrants perpendicular ($\Sigma_\perp$) and parallel ($\Sigma_\parallel$) to the accretion direction defined through two tracers. This ratio is closely related to what can be measured in observations. While the difference in profile toward and away from filamentary structures is visible at all redshifts, the orientation of the central galaxy is not a good tracer of the splashback anisotropy at high redshift. This is because the central BCG is still forming and its orientation is not yet finalized.

accreting (and hence non-virialized) structures such as galaxy clusters, the splashback radius r_{sp} represents a physical boundary motivated by their phase-space distributions. To exploit the information content of this feature, in this chapter we have introduced and studied two observable quantities related to it.

First, we have shown that the full galaxy profile can be used to define a cluster mass, i.e. the mass within r_{sp}. This is an extension of the traditional approach of using richness as mass proxy (see e.g. Simet et al., 2016). Because of the dynamical nature of the equivalent feature in the dark matter profile, we conclude that, observationally, the splashback feature in the galaxy profile *defines* the physical halo mass. Moreover, we have shown here that the natural relation between the mass and size of halos according to this definition (see Figure 4.7) can be used to constrain new physics at cluster scales. Because this boundary is delimited by recently accreted material, we found that a majority of the scatter in this mass–size relation can be explained through a secondary dependence on accretion rate Γ.

Secondly, we have explored how this connection to the accretion rate might be interpreted as a connection between the geometry of the cosmic web and how clusters are embedded in it. The relation between the two is made explicit in Figures 4.5, Figure 4.6, and Figure 4.9. In these figures, we have investigated how the cluster environment affects both the halo growth and the stellar distribution of the central galaxy. This information, combined with the scatter of the mass–size relation, can therefore be used as a consistency check for any property that claims to select for accretion rate.

4.6.1   The role of simulations

In the last few years, the study of the splashback feature has evolved into a mature field both observationally and theoretically. We use this section to discuss explicitly the connection between the two, in light of this work and its connection to previous endeavors.

In the context of splashback, simulations have guided the formulation of theoretical principles and hypotheses. However, as more measurements become viable, it becomes necessary to provide clear and powerful observables. Following this spirit, we used high-resolution hydrodynamical simulations to explore directly the connection between measurements based on sky-projected galaxy distributions and theoretical predictions.

Our conclusions regarding the mass–size relation and its redshift evolution are similar to the results of Diemer et al. (2017) and Diemer (2020), which are based on more extensive N-body simulations. For the sake of completeness, it important to note that, in the same papers, it was also found that the splashback overdensity is not universal, but has both a mild dependency on M_{200m} and a strong dependency on cosmology, especially at low redshift ($z \approx 0.2$). Due to our limited sample, we are clearly unable to model these effects in this work. Nonetheless, we point out that our goal here is to

construct a pure splashback scaling-relation based on galaxy profiles and weak lensing mass measurements. Every other dependency, if present, should be captured either as additional scatter or through different parameter values.

We also point out that these previous works are based on the apocenter definition of splashback (see Section 4.3). In contrast, we defined the splashback radius as the point of steepest slope according to a model fit to the density profiles of galaxy clusters. While we do not necessarily expect the two definitions to differ, our choice is based on its connection to observations, and the desire to highlight the fact that the splashback radius is not only some abstract halo property but can be defined as a characteristic of individual profiles, such as, e.g., the concentration parameter (Navarro et al., 1997).

An alternative method employed by other studies (Diemer and Kravtsov, 2014; Mansfield et al., 2017; Xhakaj et al., 2019) to obtain a measure of r_{sp} makes use of the minimum of the logarithmic slope in smoothed profiles. While this approach is much faster than profile fitting when only r_{sp} is of interest, it does not describe the full shape visible in Figure 4.1. In particular, a model that captures the width of this feature is necessary to define the slope of the outer region without an arbitrary choice of which radial scales to consider. Because the model used here contains an asymptotic outer slope, this definition is unique.

Our decision has, of course, its drawbacks. The versatility of the fitted model is necessary to capture the variance of the individual profiles, but the resulting intrinsic scatter is large and not the best suited to study tight splashback correlations (such as Figure 4.4). At the same time, the large parameter space might also be seen by some as a chance to study a multitude of correlations between different model parameters. However, we resist this temptation, as inferences based on such correlations might say more about the particular model employed than provide any physical information.

A subtler difference between our method to characterize splashback and other ones present in the literature is related to the definition of spherical density profiles. Mansfield et al. (2017) and Deason et al. (2020) found that the most successful method to achieve a clear splashback feature for individual halos is to measure the median profile along multiple angular directions. In light of the results of Figure 4.6, we argue that the distribution of splashback as a function of direction is skewed by the presence of a few dense filaments and hence the difference between a median and mean splashback can be substantial. Therefore, we stress that future works should exercise caution when employing such methods. The use of median profiles smooths substructure by focusing on the halo boundary in the proximity of voids, but because this process is itself correlated with the halo growth rates (see Figure 4.5), the connection with observations is not as simple as one might expect.

4.6.2   Next steps

Because in this work we have focused only on high-mass objects ($M \sim 10^{14.5} M_\odot$), a natural future step is to investigate if the results apply also in other regimes. For example, a larger sample over a wide range of masses and redshifts is required to confirm the simple form of Equation (4.5) and verify if it applies to lower mass groups ($M \sim 10^{13.5} M_\odot$).

Exploring a wider range in mass, both in observations and simulations, can also be used to confirm a key prediction: because the median accretion rate is expected to be a function of mass and redshift (More et al., 2015), we expect the mass–size relation for an observed halo sample to not necessarily follow a simple form.

Finally, we point out that our results encourage a concentrated effort toward understanding the relationship between cluster environment and splashback. What is discussed in Figures 4.5, 4.6 and 4.9 suggests that the connection between accretion-flows, filaments, and cluster boundary is not a simple one. To better understand this process, it will become necessary to complement the usual *inside-out* theoretical approaches to splashback, that look at halos to define their boundaries, with *outside-in* approaches, that connect the cosmic web to its nodes. In this context, the amount of splashback data gathered by projects such as the Kilo Degree Survey (de Jong et al., 2013), Dark Energy Survey (DES Collaboration, 2005), and, in the future, LSST (LSST Science Collaboration et al., 2009) and *Euclid* (Laureijs et al., 2011) will provide a powerful probe for the study of structure formation.

Bibliography

Susmita Adhikari, Neal Dalal, and Robert T. Chamberlain. Splashback in accreting dark matter halos. *Journal of Cosmology and Astroparticle Physics*, 2014(11):019–019, November 2014. ISSN 1475-7516. doi: 10.1088/1475-7516/2014/11/019.

Susmita Adhikari, Neal Dalal, and Joseph Clampitt. Observing dynamical friction in galaxy clusters. J. Cosmology Astropart. Phys., 2016(7):022, July 2016. doi: 10.1088/1475-7516/2016/07/022.

Susmita Adhikari, Jeremy Sakstein, Bhuvnesh Jain, Neal Dalal, and Baojiu Li. Splashback in galaxy clusters as a probe of cosmic expansion and gravity. *Journal of Cosmology and Astroparticle Physics*, 2018(11):033–033, November 2018. ISSN 1475-7516. doi: 10.1088/1475-7516/2018/11/033.

Susmita Adhikari, Tae-hyeon Shin, Bhuvnesh Jain, Matt Hilton, Eric Baxter, Chihway Chang, Risa H. Wechsler, Nick Battaglia, J. Richard Bond, Sebastian Bocquet, Joseph DeRose, Steve K. Choi, Mark Devlin, Jo Dunkley, August E. Evrard, Simone Ferraro, J. Colin Hill, John P. Hughes, Patricio A. Gallardo, Martine Lokken, Amanda MacInnis, Jeffrey McMahon, Mathew S. Madhavacheril, Frederico Nati, Laura B. Newburgh, Michael D. Niemack, Lyman A. Page, Antonella Palmese, Bruce Partridge, Eduardo Rozo, Eli Rykoff, Maria Salatino, Alessandro Schillaci, Neelima Sehgal, Cristóbal Sifón, Chun-Hao To, Ed Wollack, Hao-Yi Wu, Zhilei Xu, Michel Aguena, Sahar Allam, Alexandra Amon, James Annis, Santiago Avila, David Bacon, Emmanuel Bertin, Sunayana Bhargava, David Brooks, David L. Burke, Aurelio C. Rosell, Matias Carrasco Kind, Jorge Carretero, Francisco Javier Castander, Ami Choi, Matteo Costanzi, Luiz N. da Costa, Juan De Vicente, Shantanu Desai, Thomas H. Diehl, Peter Doel, Spencer Everett, Ismael Ferrero, Agnès Ferté, Brenna Flaugher, Pablo Fosalba, Josh Frieman, Juan García-Bellido, Enrique Gaztanaga, Daniel Gruen, Robert A. Gruendl, Julia Gschwend, Gaston Gutierrez, Will G. Hartley, Samuel R. Hinton, Devon L. Hollowood, Klaus Honscheid, David J. James, Tesla Jeltema, Kyler Kuehn, Nikolay Kuropatkin, Ofer Lahav, Marcos Lima, Marcio A. G. Maia, Jennifer L. Marshall, Paul Martini, Peter Melchior, Felipe Menanteau, Ramon Miquel, Robert Morgan, Ricardo

L. C. Ogando, Francisco Paz-Chinchón, Andrés Plazas Malagón, Eusebio Sanchez, Basilio Santiago, Vic Scarpine, Santiago Serrano, Ignacio Sevilla-Noarbe, Mathew Smith, Marcelle Soares-Santos, Eric Suchyta, Molly E. C. Swanson, Tamas N. Varga, Reese D. Wilkinson, Yuanyuan Zhang, Jason E. Austermann, James A. Beall, Daniel T. Becker, Edward V. Denison, Shannon M. Duff, Gene C. Hilton, Johannes Hubmayr, Joel N. Ullom, Jeff Van Lanen, Leila R. Vale, DES Collaboration, and ACT Collaboration. Probing galaxy evolution in massive clusters using ACT and DES: splashback as a cosmic clock. *arXiv e-prints*, art. arXiv:2008.11663, August 2020.

Raul E. Angulo, Oliver Hahn, and Tom Abel. The warm dark matter halo mass function below the cut-off scale. MNRAS, 434(4):3337–3347, October 2013. doi: 10.1093/mnras/stt1246.

Yannick M. Bahé, David J. Barnes, Claudio Dalla Vecchia, Scott T. Kay, Simon D. M. White, Ian G. McCarthy, Joop Schaye, Richard G. Bower, Robert A. Crain, Tom Theuns, Adrian Jenkins, Sean L. McGee, Matthieu Schaller, Peter A. Thomas, and James W. Trayford. The Hydrangea simulations: galaxy formation in and around massive clusters. *Monthly Notices of the Royal Astronomical Society*, 470(4):4186–4208, October 2017. ISSN 0035-8711. doi: 10.1093/mnras/stx1403. URL http://arxiv.org/abs/1703.10610http://dx.doi.org/10.1093/mnras/stx1403https://academic.oup.com/mnras/article/470/4/4186/3868206.

David J. Barnes, Scott T. Kay, Yannick M. Bahé, Claudio Dalla Vecchia, Ian G. McCarthy, Joop Schaye, Richard G. Bower, Adrian Jenkins, Peter A. Thomas, Matthieu Schaller, and et al. The cluster-eagle project: global properties of simulated clusters with resolved galaxies. *Monthly Notices of the Royal Astronomical Society*, 471(1):1088–1106, June 2017. ISSN 1365-2966. doi: 10.1093/mnras/stx1647.

Eric Baxter, Chihway Chang, Bhuvnesh Jain, Susmita Adhikari, Neal Dalal, Andrey Kravtsov, Surhud More, Eduardo Rozo, Eli Rykoff, and Ravi K. Sheth. The halo boundary of galaxy clusters in the sdss. *The Astrophysical Journal*, 841(1):18, May 2017. ISSN 1538-4357. doi: 10.3847/1538-4357/aa6ff0.

E. Bertschinger. Self-similar secondary infall and accretion in an Einstein-de Sitter universe. ApJS, 58:39–65, May 1985. doi: 10.1086/191028.

Sebastian Bocquet, Alex Saro, Klaus Dolag, and Joseph J. Mohr. Halo mass function: baryon impact, fitting formulae, and implications for cluster cosmology. *Monthly Notices of the Royal Astronomical Society*, 456(3):2361–2373, December 2015. ISSN 1365-2966. doi: 10.1093/mnras/stv2657.

J. Richard Bond, Lev Kofman, and Dmitry Pogosyan. How filaments of galaxies are woven into the cosmic web. *Nature*, 380(6575):603–606, April 1996. ISSN 1476-4687. doi: 10.1038/380603a0.

Philipp Busch and Simon D. M. White. Assembly bias and splashback in galaxy clusters. *Monthly Notices of the Royal Astronomical Society*, 470(4):4767–4781, June 2017. ISSN 1365-2966. doi: 10.1093/mnras/stx1584.

C. Chang, E. Baxter, B. Jain, C. Sánchez, S. Adhikari, T. N. Varga, Y. Fang, E. Rozo, E. S. Rykoff, A. Kravtsov, and et al. The splashback feature around des galaxy clusters: Galaxy density and weak lensing profiles. *The Astrophysical Journal*, 864(1):83, August 2018. ISSN 1538-4357. doi: 10.3847/1538-4357/aad5e7.

D. Clowe, G. A. Luppino, N. Kaiser, and I. M. Gioia. Weak Lensing by High-Redshift Clusters of Galaxies. I. Cluster Mass Reconstruction. ApJ, 539(2):540–560, August 2000. doi: 10.1086/309242.

Charlie Conroy, Risa H. Wechsler, and Andrey V. Kravtsov. The hierarchical build-up of massive galaxies and the intracluster light sincez= 1. *The Astrophysical Journal*, 668(2):826–838, October 2007. ISSN 1538-4357. doi: 10.1086/521425.

Omar Contigiani, Henk Hoekstra, and Yannick M Bahé. Weak lensing constraints on splashback around massive clusters. *Monthly Notices of the Royal Astronomical Society*, 485(1):408–415, February 2019a. ISSN 1365-2966. doi: 10.1093/mnras/stz404.

Omar Contigiani, Valeri Vardanyan, and Alessandra Silvestri. Splashback radius in symmetron gravity. *Physical Review D*, 99(6), March 2019b. ISSN 2470-0029. doi: 10.1103/physrevd.99.064030.

Jelte T. A. de Jong, Gijs A. Verdoes Kleijn, Konrad H. Kuijken, and Edwin A. Valentijn. The Kilo-Degree Survey. *Experimental Astronomy*, 35(1-2):25–44, January 2013. doi: 10.1007/s10686-012-9306-1.

Gabriella De Lucia and Jérémy Blaizot. The hierarchical formation of the brightest cluster galaxies. MNRAS, 375(1):2–14, February 2007. doi: 10.1111/j.1365-2966.2006.11287.x.

Alis J. Deason, Kyle A. Oman, Azadeh Fattahi, Matthieu Schaller, Mathilde Jauzac, Yuanyuan Zhang, Mireia Montes, Yannick M. Bahé, Claudio Dalla Vecchia, Scott T. Kay, and Tilly A. Evans. Stellar splashback: the edge of the intracluster light. MNRAS, November 2020. doi: 10.1093/mnras/staa3590.

DES Collaboration. The Dark Energy Survey. *arXiv e-prints*, art. astro-ph/0510346, October 2005.

Benedikt Diemer. The splashback radius of halos from particle dynamics. i. the sparta algorithm. *The Astrophysical Journal Supplement Series*, 231(1):5, July 2017. ISSN 1538-4365. doi: 10.3847/1538-4365/aa799c.

Benedikt Diemer. The splashback radius of halos from particle dynamics: III. Halo catalogs, merger trees, and host-subhalo relations. *arXiv e-prints*, 2020.

Benedikt Diemer. Universal at last? the splashback mass function of dark matter halos, 2020a.

Benedikt Diemer and Andrey V. Kravtsov. Dependence of the outer density profiles of halos on their mass accretion rate. *The Astrophysical Journal*, 789(1):1, June 2014. ISSN 1538-4357. doi: 10.1088/0004-637x/789/1/1.

Benedikt Diemer, Surhud More, and Andrey V. Kravtsov. The Pseudo-evolution of Halo Mass. ApJ, 766(1):25, March 2013. doi: 10.1088/0004-637X/766/1/25.

Benedikt Diemer, Philip Mansfield, Andrey V. Kravtsov, and Surhud More. The splash-back radius of halos from particle dynamics. ii. dependence on mass, accretion rate, redshift, and cosmology. *The Astrophysical Journal*, 843(2):140, July 2017. ISSN 1538-4357. doi: 10.3847/1538-4357/aa79ab.

John Dubinski and R. G. Carlberg. The Structure of Cold Dark Matter Halos. ApJ, 378:496, September 1991. doi: 10.1086/170451.

J Einasto. On the Construction of a Composite Model for the Galaxy and on the De-termination of the System of Galactic Parameters. *Trudy Astrofizicheskogo Instituta Alma-Ata*, 5:87−100, 1965.

R. Laureijs et al. Euclid definition study report, 2011.

Onsi Fakhouri and Chung-Pei Ma. Dark matter halo growth - II. Diffuse accretion and its environmental dependence. MNRAS, 401(4):2245−2256, February 2010. doi: 10.1111/j.1365-2966.2009.15844.x.

J. A. Fillmore and P. Goldreich. Self-similar gravitational collapse in an expanding universe. ApJ, 281:1−8, June 1984. doi: 10.1086/162070.

M. Fong, R. Bowyer, A. Whitehead, B. Lee, L. King, D. Applegate, and I. McCarthy. Prospects for determining the mass distributions of galaxy clusters on large scales using weak gravitational lensing. *Monthly Notices of the Royal Astronomical Society*, May 2018. ISSN 1365-2966. doi: 10.1093/mnras/sty1339.

Matthew Fong and Jiaxin Han. A natural boundary of dark matter haloes revealed around the minimum bias and maximum infall locations. MNRAS, 503(3):4250−4263, May 2021. doi: 10.1093/mnras/stab259.

Daniel Foreman-Mackey, David W. Hogg, Dustin Lang, and Jonathan Goodman. emcee: The MCMC Hammer. *Publications of the Astronomical Society of the Pacific*, 125(925): 306−312, March 2013. ISSN 00046280. doi: 10.1086/670067. URL http://iopscience.iop.org/article/10.1086/670067.

James E. Gunn and J. Richard III Gott. On the Infall of Matter Into Clusters of Galaxies and Some Effects on Their Evolution. *The Astrophysical Journal*, 176:1, August 1972. ISSN 0004-637X. doi: 10.1086/151605. URL http://adsabs.harvard.edu/doi/10.1086/151605.

Ricardo Herbonnet, Anja von der Linden, Steven W Allen, Adam B Mantz, Pranati Modumudi, R Glenn Morris, and Patrick L Kelly. Ellipticity of brightest cluster galaxies as tracer of halo orientation and weak-lensing mass bias. *Monthly Notices of the Royal Astronomical Society*, 490(4):4889–4897, Nov 2019. ISSN 1365-2966. doi: 10.1093/mnras/stz2913.

Ricardo Herbonnet, Cristóbal Sifón, Henk Hoekstra, Yannick Bahé, Remco F J van der Burg, Jean-Baptiste Melin, Anja von der Linden, David Sand, Scott Kay, and David Barnes. CCCP and MENeaCS: (updated) weak-lensing masses for 100 galaxy clusters. *Monthly Notices of the Royal Astronomical Society*, 497(4):4684–4703, August 2020. ISSN 1365-2966. doi: 10.1093/mnras/staa2303.

LSST Science Collaboration, Paul A. Abell, Julius Allison, Scott F. Anderson, John R. Andrew, J. Roger P. Angel, Lee Armus, David Arnett, S. J. Asztalos, Tim S. Axelrod, and et al. LSST Science Book, Version 2.0. *arXiv e-prints*, art. arXiv:0912.0201, December 2009.

Philip Mansfield, Andrey V. Kravtsov, and Benedikt Diemer. Splashback shells of cold dark matter halos. *The Astrophysical Journal*, 841(1):34, May 2017. ISSN 1538-4357. doi: 10.3847/1538-4357/aa7047.

A. J. Mead, C. Heymans, L. Lombriser, J. A. Peacock, O. I. Steele, and H. A. Winther. Accurate halo-model matter power spectra with dark energy, massive neutrinos and modified gravitational forces. *Monthly Notices of the Royal Astronomical Society*, 459 (2):1468–1488, March 2016. ISSN 1365-2966. doi: 10.1093/mnras/stw681.

Pierluigi Monaco. The mass function of cosmic structures with nonspherical collapse. *The Astrophysical Journal*, 447:23, July 1995. ISSN 1538-4357. doi: 10.1086/175853.

Surhud More, Benedikt Diemer, and Andrey V. Kravtsov. The splashback radius as a physical halo boundary and the growth of halo mass. *The Astrophysical Journal*, 810 (1):36, August 2015. ISSN 1538-4357. doi: 10.1088/0004-637x/810/1/36.

Surhud More, Hironao Miyatake, Masahiro Takada, Benedikt Diemer, Andrey V. Kravtsov, Neal K. Dalal, Anupreeta More, Ryoma Murata, Rachel Mandelbaum, Eduardo Rozo, Eli S. Rykoff, Masamune Oguri, and David N. Spergel. Detection of the Splashback Radius and Halo Assembly Bias of Massive Galaxy Clusters. ApJ, 825(1): 39, July 2016. doi: 10.3847/0004-637X/825/1/39.

Julio F. Navarro, Carlos S. Frenk, and Simon D. M. White. A universal density profile from hierarchical clustering. *The Astrophysical Journal*, 490(2):493–508, December 1997. ISSN 1538-4357. doi: 10.1086/304888.

Atsushi J Nishizawa, Masamune Oguri, Taira Oogi, Surhud More, Takahiro Nishimichi, Masahiro Nagashima, Yen-Ting Lin, Rachel Mandelbaum, Masahiro Takada, Neta Bahcall, and et al. First results on the cluster galaxy population from the subaru hyper suprime-cam survey. ii. faint end color–magnitude diagrams and radial profiles of red and blue galaxies at 0.1 ¡ z ¡ 1.1. *Publications of the Astronomical Society of Japan*, 70 (SP1), October 2017. ISSN 2053-051X. doi: 10.1093/pasj/psx106.

Teppei Okumura, Y. P. Jing, and Cheng Li. Intrinsic ellipticity correlation of sdss luminous red galaxies and misalignment with their host dark matter halos. *The Astrophysical Journal*, 694(1):214–221, March 2009. ISSN 1538-4357. doi: 10.1088/0004-637x/694/1/214.

Kyle A. Oman, Yannick M. Bahé, Julia Healy, Kelley M. Hess, Michael J. Hudson, and Marc A. W. Verheijen. A homogeneous measurement of the delay between the onsets of gas stripping and star formation quenching in satellite galaxies of groups and clusters, 2020.

Stephanie O'Neil, David J. Barnes, Mark Vogelsberger, and Benedikt Diemer. The splashback boundary of haloes in hydrodynamic simulations. *arXiv e-prints*, art. arXiv:2012.00025, November 2020.

William H. Press and Paul Schechter. Formation of Galaxies and Clusters of Galaxies by Self-Similar Gravitational Condensation. ApJ, 187:425–438, February 1974. doi: 10.1086/152650.

C. Ragone-Figueroa, G. L. Granato, S. Borgani, R. De Propris, D. García Lambas, G. Murante, E. Rasia, and M. West. Evolution and role of mergers in the BCG-cluster alignment. A view from cosmological hydrosimulations. MNRAS, 495(2):2436–2445, June 2020. doi: 10.1093/mnras/staa1389.

Joop Schaye, Robert A. Crain, Richard G. Bower, Michelle Furlong, Matthieu Schaller, Tom Theuns, Claudio Dalla Vecchia, Carlos S. Frenk, I. G. McCarthy, John C. Helly, and et al. The eagle project: simulating the evolution and assembly of galaxies and their environments. *Monthly Notices of the Royal Astronomical Society*, 446(1): 521–554, January 2015. ISSN 0035-8711. doi: 10.1093/mnras/stu2058.

Xun Shi. The outer profile of dark matter haloes: an analytical approach. *Monthly Notices of the Royal Astronomical Society*, 459(4):3711–3720, July 2016. ISSN 0035-8711. doi: 10.1093/mnras/stw925. URL https://arxiv.org/pdf/1603.01742.pdfhttps://academic.oup.com/mnras/article-lookup/doi/10.1093/mnras/stw925.

T Shin, S Adhikari, E J Baxter, C Chang, B Jain, N Battaglia, L Bleem, S Bocquet, J DeRose, D Gruen, and et al. Measurement of the splashback feature around sz-selected galaxy clusters with des, spt, and act. *Monthly Notices of the Royal Astronomical Society*, 487(2):2900–2918, May 2019. ISSN 1365-2966. doi: 10.1093/mnras/stz1434.

Melanie Simet, Tom McClintock, Rachel Mandelbaum, Eduardo Rozo, Eli Rykoff, Erin Sheldon, and Risa H. Wechsler. Weak lensing measurement of the mass–richness relation of sdss redmapper clusters. *Monthly Notices of the Royal Astronomical Society*, 466(3):3103–3118, December 2016. ISSN 1365-2966. doi: 10.1093/mnras/stw3250.

Paxton Tomooka, Eduardo Rozo, Erika L. Wagoner, Han Aung, Daisuke Nagai, and Sasha Safonova. Clusters have edges: The projected phase spacestructure of sdss redmapper clusters, 2020.

Keiichi Umetsu and Benedikt Diemer. Lensing constraints on the mass profile shape and the splashback radius of galaxy clusters. *The Astrophysical Journal*, 836(2):231, April 2017. ISSN 1538-4357. doi: 10.3847/1538-4357/aa5c90.

Keiichi Umetsu, Mauro Sereno, Maggie Lieu, Hironao Miyatake, Elinor Medezinski, At-sushi J. Nishizawa, Paul Giles, Fabio Gastaldello, Ian G. McCarthy, Martin Kilbinger, and et al. Weak-lensing analysis of x-ray-selected xxl galaxy groups and clusters with subaru hsc data. *The Astrophysical Journal*, 890(2):148, February 2020. ISSN 1538-4357. doi: 10.3847/1538-4357/ab6bca.

Mark Vogelsberger and Simon D. M. White. Streams and caustics: the fine-grained structure of Λ cold dark matter haloes. MNRAS, 413(2):1419–1438, May 2011. doi: 10.1111/j.1365-2966.2011.18224.x.

Erika L. Wagoner, Eduardo Rozo, Han Aung, and Daisuke Nagai. Measuring Cosmological Distances Using Cluster Edges as a Standard Ruler. *arXiv e-prints*, art. arXiv:2010.11324, October 2020.

Enia Xhakaj, Benedikt Diemer, Alexie Leauthaud, Asher Wasserman, Song Huang, Yifei Luo, Susmita Adhikari, and Sukhdeep Singh. How accurately can we detect the splashback radius of dark matter halos and its correlation with accretion rate?, 2019.

Dominik Zürcher and Surhud More. The splashback radius of planck sz clusters. *The Astrophysical Journal*, 874(2):184, April 2019. ISSN 1538-4357. doi: 10.3847/1538-4357/ab08e8.

Chapter 5

Dynamical cluster masses from photometric surveys

Traditionally, the masses of galaxy clusters are measured using wide photometric surveys in one of two ways: directly from the amplitude of the weak lensing signal or, indirectly, through the use of scaling relations calibrated using binned lensing measurements. Here, we build on a recently proposed idea and implement an alternative method based on the radial profile of the satellite distribution. This technique relies on splashback, a feature associated with the apocenter of recently accreted galaxies that offers a clear window into the phase-space structure of clusters without the use of velocity information. We carry out this measurement in the stacked satellite distribution around a sample of luminous red galaxies in the fourth data release of the Kilo-Degree Survey and validate our results using abundance-matching masses. To illustrate the power of this measurement, we combine this dynamical mass measurement with lensing mass estimates to robustly constrain scalar-tensor theories of gravity at cluster scales. Our results exclude departures from General Relativity of order unity. Finally, we conclude by rescaling our results and discussing how stage-IV photometric surveys will use splashback to provide percentage level cluster masses at high redshifts.

5.1   Introduction

Today the majority of ordinary matter, a.k.a. baryonic matter, is trapped inside the potential wells of the large-scale structure of the Universe. The main constituent of this invisible scaffolding is dark matter, and most of the mass in the Universe is concentrated in its fully collapsed overdensities, known as halos. At first order, the relationship between dark matter structures and galaxies is simple, and the result of their joint evolution is a tight relationship between the luminosity of a galaxy and the mass of the dark matter halo it inhabits. Because halos are perturbations on top of a background of constant density, their size is usually quantified in terms of overdensity masses. For example, $M_{200\mathrm{m}}$ is defined as the mass contained within a sphere of radius $r_{200\mathrm{m}}$ such that the average density within it is 200 times the average matter density of the Universe $\rho_{\mathrm{m}}(z)$,

$$M_{200\mathrm{m}} = 200 \times \frac{4\pi}{3}\rho_{\mathrm{m}}(z)r_{200\mathrm{m}}^3. \tag{5.1}$$

Dark matter structures are not isolated, however, and the process of structure formation is known to be hierarchical (Press and Schechter, 1974). This means that smaller halos collapsed first and became subhalos once they were accreted onto larger structures. Unsurprisingly, baryonic matter also followed this process, which resulted in today's clusters of galaxies. These represent the largest halos in the Universe and they are still accreting matter from the surrounding environment, i.e. they are not fully virialized yet.

Observationally, the distribution of galaxies in the sky is divided into two populations: red and blue (Strateva et al., 2001). Red galaxies derive their color from their aging stellar population, whereas blue galaxies display active star formation, and young stars dominate their light. The exact mechanism behind quenching, i.e. the transition from star-forming to "red and dead", is still not fully understood (see e.g. Schaye et al., 2010; Trayford et al., 2015), but it is known to be connected to both baryonic feedback (see e.g. Somerville et al., 2008; Schaye et al., 2010) and interactions inside the dense cluster environment (see e.g. Larson et al., 1980; Moore et al., 1996; van den Bosch et al., 2008). An important consequence of this environmental dependence is the formation of a red sequence, i.e. a close relationship between the color and magnitude of red galaxies in clusters. By calibrating this red sequence as a function of redshift, it is possible to identify clusters in photometric surveys, even in the absence of precise spectroscopic redshifts (Gladders and Yee, 2000).

In recent years, splashback has been recognized as a feature located at the edge of galaxy clusters. The radius of this boundary, r_{sp}, is close to the apocenter of recently accreted material (see e.g. Adhikari et al., 2014; Diemer, 2017; Diemer et al., 2017) and it is associated with a sudden drop in density. This is because it naturally separates the single and multi-stream regions of galaxy clusters: orbiting material piles up inside this radius, while collapsing material located outside it is entering the cluster for

the first time. In simulations and observations, the distribution of red satellite galaxies and dark matter seem to trace this feature in the same fashion (Contigiani et al., 2021; O'Neil et al., 2021), but a possible dependence on satellite properties is still mostly unexplored (Shin et al., 2021). Nonetheless, the existence and detectability of this physical feature have theoretical and observational implications for the study of the large-scale structure of the Universe.

From a theory perspective, the splashback radius defines an accurate cluster mass and sidesteps the issue of pseudo evolution due to an evolving $\rho_{\mathrm{m}}(z)$ as a function of redshift z (Diemer et al., 2013; More et al., 2015). Thanks to this property, this definition can be used to create a universal mass function that is valid for a variety of cosmologies (Diemer, 2020a). Moreover, the shape of the matter profile around this feature can also be used to learn about structure formation, the nature of dark matter (Banerjee et al., 2020) and dark energy (Contigiani et al., 2019).

Observationally, one of the most noteworthy applications of splashback is the study of quenching through the measurement of the spatial distribution of galaxy populations with different colors (Adhikari et al., 2020). While notable, this was not the first result, and many other measurements preceded it. Published works can be divided into three groups: those based on targeted weak lensing observations of X-ray selected clusters (Umetsu and Diemer, 2017; Contigiani et al., 2019), those based on the lensing signal and satellite distributions around SZ-selected clusters (see e.g. Shin et al., 2019), and those based on samples constructed with the help of cluster-finding algorithms applied to photometric surveys (see e.g. More et al., 2016; Collaboration, 2018). However, we note that in the case of the last group, the results are difficult to interpret because the splashback signal correlates with the parameters of the cluster detection method (Busch and White, 2017).

In this work, we implement an application of this feature based on Contigiani et al. (2021). The location of the splashback radius is connected to halo mass, and its measurement from the distribution of cluster members can therefore lead to a mass estimate. Because this distribution can be measured without spectroscopy, this means that we can extract a dynamical mass purely from photometric data. In this chapter, we apply this technique to a present-day photometric survey (see Section 5.2), but we also discuss future prospects. To avoid issues related to cluster-finding algorithms, we studied the average distribution of faint galaxies around luminous red galaxies (LRGs) instead of the targets identified through overdensities of red galaxies. If we consider only passive evolution, the observed magnitude of the LRGs can be corrected to construct a sample with constant comoving density (Rozo et al., 2016; Vakili et al., 2019), and, by selecting the brightest among them, we expect to choose the central galaxies of groups and clusters.

We present our analysis in Section 5.3 and produce two estimates of the masses of the halos hosting the LRGs in Section 5.4. The first is based on the splashback feature measured in the distribution of faint galaxies, while the second is based on weak

lensing measurements. After validating these results with two alternative methods in Section 5.5, we conclude our analysis by discussing our measurements in the context of modified models of gravity. We limit ourselves to redshifts $z < 0.55$ here, but the sample constructed in this manner also has implications for the higher redshift range probed by future stage-IV photometric surveys (Albrecht et al., 2006) such as *Euclid* (Laureijs et al., 2011) and the Legacy Survey of Space and Time (LSST, LSST Science Collaboration et al., 2009). This is because at $z \sim 1$, central galaxies are still assembling, and therefore, their identification can be uncertain. Section 5.5.2 discusses these complications in more detail and explores how this method can be used to complement the use of lensing to extract the masses of X-ray (Contigiani et al., 2019) or SZ selected clusters (Shin et al., 2019).

Unless stated otherwise, we assume a cosmology based on the 2015 Planck data release (Collaboration, 2016). For cosmological calculations, we use the Python packages ASTROPY (Price-Whelan et al., 2018) and COLOSSUS (Diemer, 2018). The symbols R and $r_{\rm sp}$ always refer to a comoving projected distance and a comoving splashback radius.

5.2   Data

This section introduces both the Kilo-Degree Survey (KiDS, de Jong et al., 2013) and its infrared companion, the VISTA Kilo-degree INfrared Galaxy survey (VIKING, Edge et al., 2013). Their combined photometric catalog and the sample of LRGs extracted from it (Vakili et al., 2020) are the essential building blocks of this chapter.

5.2.1   KiDS

KiDs is a multi-band imaging survey in four filters ($ugri$) covering 1350 deg^2. Its fourth data release (DR4, Kuijken et al., 2019) is the basis of this chapter and has a footprint of 1006 deg^2 split between two regions located in the north and south Galactic caps (770 deg^2 after masking). The 5σ mean limiting magnitudes in the $ugri$ bands are, respectively, 24.23, 25.12, 25.02, and 23.68. The mean seeing for the r-band data used both as a detection band and for the weak lensing measurements is 0.7″. VIKING covers the same footprint in five infrared bands, $ZYJHK_s$.

The raw data have been reduced with two separate pipelines, THELI (Erben et al., 2005) for a lensing-optimized reduction of the r-band data, and AstroWISE (McFarland et al., 2013), used to create photometric catalogs of extinction corrected magnitudes. The source catalog for weak lensing analyses was produced from the THELI images and lensfit (Miller et al., 2013; Fenech Conti et al., 2017; Kannawadi et al., 2019) was used to extract the galaxy shapes.

5.2.2 LRGs

The LRG sample presented in Vakili et al. (2020) is based on KiDS DR4. There, the red sequence up to redshift $z = 0.8$ was obtained by combining spectroscopic data with the $griZ$ photometric information provided by the two surveys mentioned above. Furthermore, using the near-infrared K_s band from VIKING allowed for a clean separation of stellar objects and considerably lowered the stellar contamination of the sample.

The color-magnitude relation that applies to red galaxies allows the redshifts of LRGs to be calibrated to a precision higher than generic photometric redshifts (photo-zs) resulting in redshift errors for each galaxy below $\sigma_z \lesssim 0.02$. For more details on how the total LRG sample is defined and its broad properties, we direct the interested reader to Vakili et al. (2020), or Vakili et al. (2019), a similar work based on a previous KiDS data release.

Fortuna et al. (2021) further analyzed this same catalog and calculated absolute magnitudes for all LRGs using LePHARE (Arnouts and Ilbert, 2011) and EZGAL (Mancone and Gonzalez, 2012). The first code corrects for the redshift of the rest-frame spectrum in the different passbands (k-correction), while the second corrects for the passive evolution of the stellar population (e-correction). For this work, we used these (k+e)-corrected luminosities as a tracer of total mass since the two are known to be highly correlated (see e.g. Mandelbaum et al., 2006; van Uitert et al., 2015). Based on this, we then defined two samples with different absolute r-band magnitude cuts, $M_r < -22.8$ and $M_r < -23$, that we refer to as *all* and *high-mass* samples. These are the 10 and 5 percentile of the absolute magnitude distribution of the *luminous* sample studied in Fortuna et al. (2021), and the two samples contain 5524 and 2850 objects each.

Because the (k+e)-correction presented above is designed to create a redshift independent sample, the expected redshift distribution of the LRGs should correspond to a constant comoving density. However, when studying our samples (see Figure 5.1), it is clear that this assumption holds only until $z = 0.55$. This suggests that the empirical corrections applied to the observed magnitudes are not optimal. We stress that this discrepancy was not recognized before because our selection amplifies it: we considered the tail of a much larger sample ($N \sim 10^5$) with a steep magnitude distribution, for which a small error in the lower limit induced a large mismatch at the high-luminosity end. We discard all LRGs above $z = 0.55$ and after fitting the distributions in Figure 5.1, we obtained comoving densities $n = 7.5 \times 10^{-6}$ Mpc^{-3} and $n = 4.0 \times 10^{-6}$ Mpc^{-3} for the full and the high-mass samples respectively.
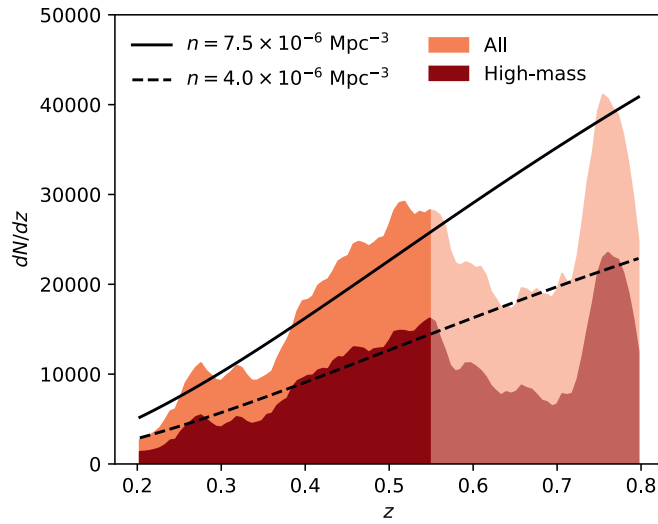
Figure 5.1: The redshift distributions of the LRG samples studied in this chapter. As visible in the figure, the distributions are consistent with the assumption of a constant comoving density up to redshift $z = 0.55$, the maximum considered here. The empirical selection criteria were explicitly designed to select for constant comoving density fail for higher redshifts.
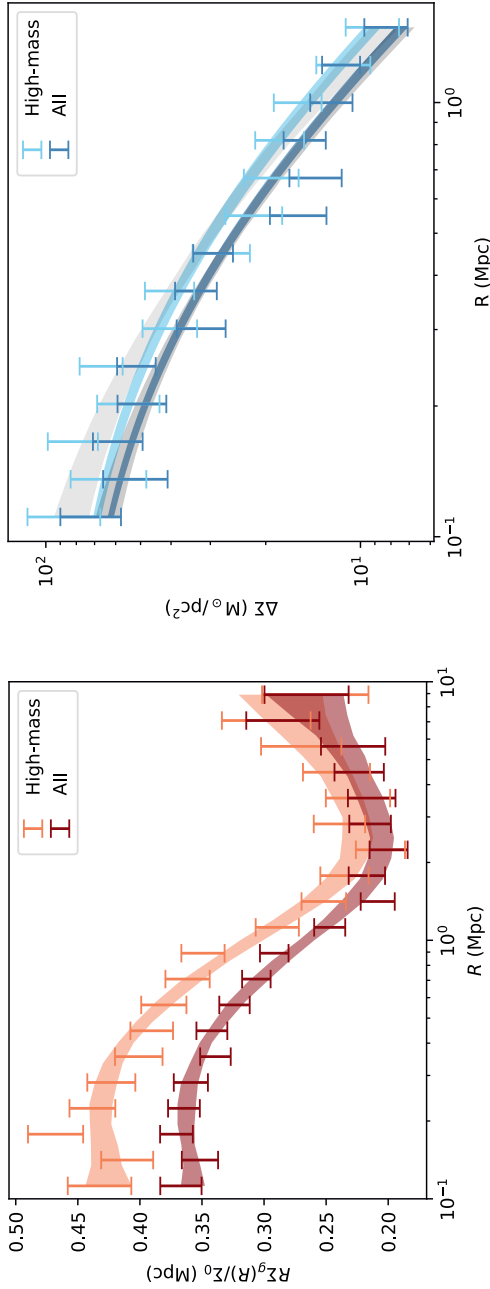
Figure 5.2: The signals studied in this chapter. We measure the number density of faint red galaxies (left panel) and the lensing signal (right panel) around the LRGs in our sample (*all*) and its high-luminosity subsample (*high-mass*). Both measurements are based on the KiDS photometric catalog. The steep drop around 1 Mpc visible in the left panel is the splashback feature, and it is connected to the total mass of the LRG halos. Similarly, the amplitude of the lensing signal on the right is also a measure of the same mass. In addition to the data and the 1σ error bars, we also display the 68 percent contours of a profile fit performed to extract the mass measurements. The fit on the right is performed either by varying only the amplitude of the signal (thinner contours) or by varying its amplitude and concentration (wider contours). See text for more details. Section 5.2 presents the data and the two samples, Section 5.3 discusses how the profiles are measured, and Section 5.4 discusses the fitting procedure.

5.3   Profiles

In this section, we discuss how we used the data introduced in the previous section to produce two stacked signals measured around the LRGs: the galaxy profile, capturing the distribution of faint red galaxies, and the weak lensing profile, a measure of the projected mass distribution extracted from the distorted shapes of background galaxies. We present these two profiles and the 68 percent contours of two separate parametric fits in Figure 5.2. The details of the fitting procedure are explained in Section 5.4.

5.3.1   Galaxy profile

We expect bright LRGs to be surrounded by fainter satellites, i.e. we expect them to be the central galaxies of galaxy groups or clusters. We focused in particular on the distribution of red satellites as this is the most abundant population in galaxy clusters and, due to their repeated orbits, they are known to trace dynamical features such as splashback better (see e.g. Baxter et al., 2017). To obtain the projected number density profile of these surrounding galaxies, we split the LRG samples in 7 redshift bins of size $\delta_z = 0.05$ in the range $z \in [0.2, 0.55]$. We then defined a corresponding KiDS galaxy catalog for each redshift bin, obtained the background-subtracted distribution of these galaxies around the LRGs, and finally stacked these distributions using the weights w_i defined below.

The KiDS catalogs used in this process were based on two redshift-dependent selections: in magnitude and color. The reason behind the first selection is simple: compared to a flat signal-to-noise (SNR) threshold, a redshift-dependent magnitude limit does not mix populations with different intrinsic magnitudes as a function of redshift (as suggested by More et al., 2016). On the other hand, the color cut is more physical since we are only interested in the distribution of red galaxies. Combining a color cut and a magnitude cut means choosing a similar population across redshifts, even in the absence of k-corrected magnitudes for the KiDS galaxies. Finally, we point out that we did not select the photo-zs of the KiDS galaxies as this is unnecessary.

For the highest redshift considered here, z_{max}, we limited ourselves to observed magnitudes $m_r < 23$, equivalent to a 10σ SNR cut. We then extrapolated this limit to other redshift bins by imposing

$$m_r < 23 - 5 \log \left(\frac{d_L(z_{\mathrm{max}})}{d_L(z_i)} \right), \tag{5.2}$$

where z_i is the upper edge of the redshift bin considered, and $d_L(z)$ is the luminosity distance as a function of redshift. Afterward, we divided the galaxy catalogs into two-color populations by following the method of Adhikari et al. (2020). Compared to random points in the sky, the color distribution of KiDS galaxies around LRGs contains two features: an overdensity of "red" objects and a deficit of "blue" objects. Based on

the red-sequence calibration of Vakili et al. (2020) and the location of the 4000 Å break, we identified the $(g-r)-(r-i)$ plane as the most optimal color space to separate these two population at redshifts $z \leq 0.55$. The two classes can then be separated by the line perpendicular to the segment connecting these two loci and passing through its midpoint. We note that the $(i\text{-}Z)\text{-}(r\text{-}i)$ plane would be better suited for higher redshifts.

We used TREECORR (Jarvis et al., 2004; Jarvis, 2015) to extract the correlation functions from the catalogs defined above

$$\xi_i = \frac{DD_i}{DR_i} - 1, \tag{5.3}$$

where DD and DR are the numbers of LRG-galaxy pairs calculated using the KiDS catalogs or the random catalogs, respectively. These randoms are composed of points uniformly distributed in the KiDS footprint. We then produced covariance matrices by dividing our survey area into 50 equal-areal jackknife regions to provide an error on the binned radial signal. Because the signal is statistics limited, we can ignore the negligible off-diagonal terms of this matrix. To support this statement, we point out that due to the low number density of the sample (see Figure 5.1), the clusters do not overlap in real space.

Formally, the correlation function written above is related to the surface overdensity of galaxies:

$$\Sigma_i(R) = \xi_i(R)\Sigma_{0,i}, \tag{5.4}$$

where $\Sigma_{0,i}$ is the average surface density of KiDS galaxies in the i-th redshift bin. However, since we are interested in the shape of the profile and not its amplitude, we did not take this into account when stacking the correlation functions ξ_i. To optimize the measurement, we use as weights w_i the inverse variance of our measurement. This corresponds to an SNR weighted average, where the SNR is, in our case, dominated by the statistical error of the DD counts. Formally:

$$\frac{\Sigma_{\mathrm{g}}(R)}{\Sigma_0} = \frac{\sum_i w_i \xi_i(R)}{\sum_i w_i}, \tag{5.5}$$

where Σ_0 is a constant needed to transform the dimensionless correlation function into the projected mass density. Because we decided to fit the combination $\Sigma_{\mathrm{g}}(R)/\Sigma_0$ directly, the value of this constant is unimportant.

The left side of Figure 5.2 presents our measurement of the galaxy profile around the LRGs. As expected, the high-mass subsample has a higher amplitude compared to the entire sample.

5.3.2 Weak lensing profile

The shapes of background sources are deformed, i.e. lensed, by the presence of matter along the line of sight. In the weak lensing regime, this results in the observed ellipticity

ϵ of a galaxy being a combination of its intrinsic ellipticity and a lensing shear. If we assume that the intrinsic shapes of galaxies are randomly oriented, we can then measure a coherent shear in a region of the sky by computing the mean of the ellipticity distribution.

Consider a circularly symmetric matter distribution acting as a lens. In this case, the shear is only tangential, i.e. the shapes of background galaxies are deformed only in the direction parallel and perpendicular to the line in the sky connecting the source to the center of the lens. Therefore, we can define the lensing signal in an annulus of radius R as the average value of the tangential components of the ellipticities $\epsilon^{(t)}$. Below, we describe the exact procedure we followed to measure this signal for the LRGs samples using the KiDS source catalog extending up to redshift $z = 1.2$ (see also, Viola et al., 2015; Dvornik et al., 2017).

Based on the *lensfit* weights w_s associated with each source, we defined *lensing* weights for every lens-source combination,

$$w_{l,s} = w_s \left(\Sigma^{-1}_{\text{crit, l}} \right)^2,$$ (5.6)

where the two indices l and s are used to indicate multiple lens-source pairs if more than one lens is considered. The second factor in the product above represents a lensing efficiency contribution and, in our formalism, this quantity does not depend on the source. It is calculated instead as an average over the entire source redshift distribution $n(z_s)$:

$$\Sigma^{-1}_{\text{crit, l}} = \frac{4\pi G}{c^2} \frac{d_A(z_l)}{(1 + z_l)^2} \int_{z_l + \delta}^{\infty} dz_s \frac{d_A(z_l, z_s)}{d_A(0, z_s)} n(z_s),$$ (5.7)

where $d_A(z_1, z_2)$ is the angular diameter distance between the redshifts z_1 and z_2 in the chosen cosmology. Sources that belong to the correlated structure surrounding the lens might scatter behind it due to the uncertainty of photo-zs. The gap between the lens plane and the source plane in the expression above ($\delta = 0.2$) is there to make sure our signal is not diluted by this effect (see appendix A4 of Dvornik et al., 2017). The additional factor $(1+z_l)$ in this expression is there because we are working in comoving coordinates. Once all of the ingredients are computed, an estimate of the measured lensing signal is given by:

$$\Delta\Sigma(R) = \frac{\sum_{l,s} \epsilon^{(t)}_{l,s} w_{l,s} \Sigma_{\text{crit, l}}}{\sum_{l,s} w_{l,s}} \frac{1}{1 + m},$$ (5.8)

where the sums are calculated over every source-lens pair, and m is a residual multiplicative bias of order 0.014 calibrated using image simulations (Fenech Conti et al., 2017; Kannawadi et al., 2019). This signal is connected to the mass surface density $\Sigma_m(R)$ and its average value within that radius, $\overline{\Sigma}_m(< R)$.

$$\Delta\Sigma(R) = \overline{\Sigma}_m(< R) - \Sigma_m(R).$$ (5.9)

The covariance matrix of this average lensing signal was extracted through bootstrapping, i.e. by resampling 10^5 times the 1006 1×1 deg^2 KiDS tiles used in the analysis. This signal, like the galaxy profile before, is also statistics limited. Therefore we have not included the negligible off-diagonal terms of the covariance matrix in our analysis.

Finally, we note that we have thoroughly tested the consistency of our lensing measurement. The average cross-component lensing signal is expected to be zero. To confirm that this is true for our results, we computed the expression in Equation (5.8) using the cross-component $\epsilon^{(\times)}$ instead of the tangential $\epsilon^{(t)}$ and verified that its value was consistent with zero. Similarly, we also confirmed that the measurement was not affected by additive bias by measuring the lensing signal evaluated around random points.

5.4 Four ways to measure cluster masses

This section discusses how we have obtained two independent measures of the total mass contained in the LRG halos by fitting parametric profiles to the signals extracted in the previous section. We measured two quantities: a dynamical mass and a lensing mass. The first is connected to the splashback feature seen in the distribution of satellite galaxies, while the second one is connected to the amplitude of the lensing signal (see Figure 5.2).

5.4.1 Splashback mass

By fitting the galaxy distribution with a flexible model, it is possible to estimate the total halo mass. The essential feature that such a three-dimensional profile, $\rho(r)$, must capture is a sudden drop in density around r_{200m} and its most important parameter is the point of steepest slope, also known as the splashback radius r_{sp}. Equivalently, this can be defined as the radius where the function $d\log\rho/d\log r$ reaches its minimum.

In general, the average projected correlation function can be written in terms of the average three-dimensional mass density profile as:

$$\frac{\Sigma_g(R)}{\Sigma_0} = \frac{2}{\Sigma_0} \int_0^\infty d\Delta\, \rho\left(\sqrt{\Delta^2 + R^2}\right), \qquad (5.10)$$

In practice, we evaluated this integral in the range [0, 40] Mpc, but we have also confirmed that our results are not sensitive to the exact value of the upper integration limit.

The specific density profile that we used is based on Diemer and Kravtsov (2014),

Parameter	Prior
α	$\mathcal{N}(0.2, 2)$
g	$\mathcal{N}(4, 0.2)$
β	$\mathcal{N}(6, 0.2)$
$r_t/(1 \text{ Mpc})$	$\mathcal{N}(1, 4)$
s_e	$[0.1, 2]$

Table 5.1: The priors used in the fitting procedure of Section 5.4. When fitting the data in the left panel of Figure 5.2, we employ the model in Equation (5.11) with the priors presented above. For some parameters, we impose flat priors in a range, e.g. $[a, b]$, while for others we impose a Gaussian prior $\mathcal{N}(m, \sigma)$ with mean m and standard deviation σ. We do not restrict the prior range of the two degenerate parameters $\bar{\rho}$ and r_0.

and it has the following form:

$$\rho(r) = \rho_{\text{Ein}}(r) f_{\text{trans}}(r) + \rho_{\text{out}}(r), \tag{5.11}$$

$$\rho_{\text{Ein}}(r) = \rho_s \exp\left(-\frac{2}{\alpha}\left[\left(\frac{r}{r_s}\right)^{\alpha} - 1\right]\right), \tag{5.12}$$

$$f_{\text{trans}}(r) = \left[1 + \left(\frac{r}{r_t}\right)^{\beta}\right]^{-g/\beta}, \tag{5.13}$$

$$\rho_{\text{out}} = \bar{\rho}\left(\frac{r}{r_0}\right)^{-s_e}. \tag{5.14}$$

These expressions define a profile with two components: an inner halo and an infalling region. The term $\rho_{\text{Ein}}(r) f_{\text{trans}}(r)$ represents the collapsed halo through a truncated Einasto profile with shape parameter α and amplitude ρ_s (Einasto, 1965). The parameters g, β in the transition function determine the maximum steepness of the sharp drop between the two regions, and r_t determines its approximate location. Finally, the term $\rho_{\text{out}}(r)$ describes a power-law mass distribution with slope s_e and amplitude $\bar{\rho}$, parametrizing the outer region dominated by infalling material. For more information about the role of each parameter and its interpretation, we refer the reader to Diemer and Kravtsov (2014), and previous measurements presented in the introduction (see e.g. Contigiani et al., 2019, for more details about the role of the truncation radius r_t).

To extract the location of the splashback radius for our two LRG samples, we fitted this model profile to the correlation function data using the ensemble sampler EMCEE (Foreman-Mackey et al., 2013). The priors imposed on the various parameters are presented in Table 5.1, and we highlight in particular that the range for α is a generous scatter around the expectation from numerical simulations (Gao et al., 2008).

In clusters, it is possible for the location of the central galaxy to not correspond to

the barycenter of the satellite distribution. This discrepancy is usually accounted for in the modeling of the projected distribution in Equation (5.10), but we chose not to consider this effect in our primary analysis. This is justified because the miscentering term affects the profile within $R \sim 0.1$ Mpc, while we are interested in the measurement around $R \sim 1$ Mpc (Shin et al., 2021), and the data do not require a more flexible model to provide a good fit.

Finally, to transform the r_{sp} measurements into a value for M_{200m}, we used the relations from Diemer (2020b), evaluated at our median redshift of $\bar{z} = 0.44$. Because the splashback radius has a dependence on accretion rate, we used the median value of this quantity as a function of mass as a proxy for the effective accretion rate of our stacked sample. We note in particular that the additional scatter introduced by the accretion rate and redshift distributions is expected to be subdominant given the large number of clusters we have considered. We best fitting profiles and error intervals of the inferred M_{200m} are shown in Figure 5.2.

5.4.2 Lensing mass

To extract masses from the lensing signal, we performed a fit using an NFW profile (Navarro et al., 1996, 1997):

$$\rho(r) = \frac{1}{4\pi F(c_{\mathrm{200m}})} \frac{M_{\mathrm{200m}}}{r(r + r_{\mathrm{200m}}/c_{\mathrm{200m}})^2}, \tag{5.15}$$

where M_{200m} and r_{200m} are related by Equation (5.1), c_{200m} is the halo concentration, and the function appearing in the first term is defined as:

$$F(c) = \ln(1 + c) - c/(1 + c). \tag{5.16}$$

From this three-dimensional profile, the lensing signal can be derived using Equations (5.9) and (5.10) by replacing Σ_{m} with $\Sigma_{\mathrm{g}}/\Sigma_0$.

Because the mass and concentration of a halo sample are related, several mass-concentration relations calibrated against numerical simulations are available in the literature. We chose to fit an NFW profile because these mass-concentration relations are usually given in terms of its parameters, and imposing such constraint increases the precision of the measurement by forcing a strong prior on the shape of the profile. Notice that we could have used the complex model of Equation (5.11) also for the lensing measurement. However, the differences between the Einasto profile used there and the NFW profile presented above are not expected to induce systematic biases at the precision of our measurements (see e.g. Sereno et al., 2016). Although extra complexity might not be warranted, particular care should still be taken when measuring profiles at large scales, where the difference between the more flexible profile and a traditional NFW profile is more pronounced. Consequently, we reduce the bias in our measurement by fitting only projected distances $R < 1.5$ Mpc, where the upper limit is decided based on the r_{sp} inferred by our galaxy distribution measurement.

For the measurement presented in this section, we use the mass-concentration relation of Bhattacharya et al. (2013). However, because this relation is calibrated with numerical simulations based on a different cosmology, we also fit the lensing signal while keeping the concentration as a free parameter. This consistency check is particularly important because halo profiles are not perfectly self-similar (Diemer and Kravtsov, 2015) and moving between different cosmologies or halo mass definitions might require additional calibration. We perform the fit to the profiles in the right panel of Figure 5.2 using the median redshift of our samples, $\bar{z} = 0.44$. We find that statistical errors dominate the uncertainties, and we do not measure any systematic effect due to the assumed mass-concentration relation.

5.4.3   Supplementary mass measurements

In addition to the two mass measurements extracted from the galaxy and lensing profiles, we discuss the predictions we obtained from two additional methods. The first is based on an abundance matching argument, while the second is based on the clustering properties of our LRG sample. We focus on these two methods to estimate masses because, similarly to the main two methods, they can also be performed in the presence of photometric data alone.

For the abundance-matching mass, we used the mass function of Tinker et al. (2008) at the median redshift $\bar{z} = 0.44$ to convert the comoving densities from Figure 5.1 into lower limits on the halo mass $M_{200\mathrm{m}}$. To complete the process, we then extracted the mean mass of the sample using the same mass function.

For the clustering mass, we used the large-scale distribution of our sample as a proxy. Because the spatial correlation function of halos depends on their mass, we can estimate the average mass of our cluster sample by extracting the bias of this population with respect to the matter distribution of the Universe. To this end, we divided the LRG sample into three equally populated redshift bins and computed the angular autocorrelation functions within a range of scales. For the lower limit, we used $R = 10$ Mpc to make sure we considered only linear scales. For the upper limit, we used $\theta = 150$ arcmin to satisfy the flat-sky approximation and to accurately account for cosmic variance within the limited KiDS footprint. We converted between projected radii and angular distances using our assumed cosmology and measured the autocorrelation function using the same procedure presented in Section 5.3.1. However, we did take into account the off-diagonal terms of the covariance matrix in this case since the uncertainties at large scales are dominated by sample variance.

Using the Limber approximation (Limber, 1953), the measured angular autocorrelation function of the i-th LRG bin can be written as

$$\Theta_i(R|M) = \int dz \; \frac{n_i^2(z)}{d\chi/dz} b^2 \left(M_{200\mathrm{m}} \right) \int_{-\infty}^{+\infty} d\Delta \; \xi \left(\sqrt{R^2 + \Delta^2}, z \right), \qquad (5.17)$$

where $\xi(r, z)$ is the matter correlation function in terms of the comoving distance r and redshift z, $b(M_{200\mathrm{m}})$ is the bias as a function of mass from Tinker et al. (2010), $\chi(z)$ is the comoving distance to redshift z, and $n_i(z)$ is the normalized redshift distribution of the LRGs in the considered bin. This latter distribution was obtained by taking into account the redshift uncertainties of the red-sequence calibration (see Section 5.2.2). The clustering mass was measured by fitting this model to the three LRG bins assuming a constant value of $M_{200\mathrm{m}}$ throughout the entire redshift range.

We note that Vakili et al. (2020) has shown that the distribution of LRGs at the scales considered in this section can be strongly affected by survey systematics, and specific weights should be used when computing the clustering properties. We have verified that the autocorrelation signals of our samples are unaffected by the use of these weights. In general, fainter objects are more impacted by the varying depth introduced by survey systematics since they can scatter in or out of the detection threshold.
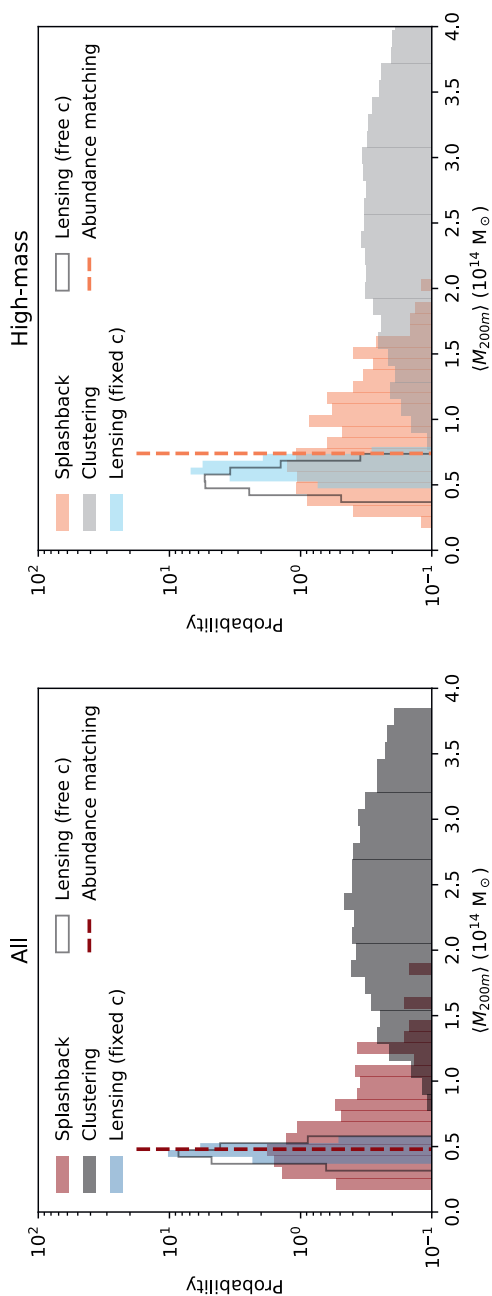
Figure 5.3: Comparison of the mass measurements performed in this chapter. Using four different techniques, we measured the mass of the halos hosting our LRG sample (*all*) and a high-luminosity subsample (*high-mass*). The remarkable consistency between the four methods for both samples is a testament to the robustness of our LRG selection and the power of the splashback feature in providing cluster masses. Table 5.2 reports the same results in textual form. See Section 5.5 for more details about this comparison.

Technique	M_{200m} (10^{14} M$_\odot$)		r_{sp} (Mpc)	
	All	High-mass	All	High-mass
Splashback	$0.57^{+0.73}_{-0.22}$	$0.77^{+0.64}_{-0.30}$	1.48 ± 0.28	1.6 ± 0.25
Lensing (fixed c)	0.46 ± 0.03	0.62 ± 0.05	1.40 ± 0.01	1.52 ± 0.02
Lensing (free c)	0.44 ± 0.05	0.54 ± 0.07	1.39 ± 0.03	1.6 ± 0.04
Abundance	0.48	0.74	1.42	1.6
Clustering	2.41 ± 0.94	2.62 ± 1.18	$-$	$-$

Table 5.2: The mass measurements performed in this chapter. This table summarizes the discussion of Section 5.5 and the measurements presented in Figure 5.3 for our LRG samples (*all* and *high-mass*). The quoted splashback radii are in comoving coordinates. The abundance-matching measurements are provided without error bars as we have not modeled the selection function of our LRGs. Since the clustering method is not informative, we do not present a splashback radius estimate based on it. Most measurements and conversions between M_{200m} and r_{sp} (see the end of Section 5.4.1 for details) are computed using a model at the median redshift $\bar{z} = 0.44$, identical for both samples. The bias measurements take into account a redshift-dependent clustering but assume a constant halo mass.

5.5 Discussion

In this section, we compare and validate the measurements presented in the previous one, see Figure 5.3 and Table 5.2 for a quick summary of our main conclusions. As an example of the power granted by multiple cluster mass measurements from the same survey, we also present an interpretation of these measurements in the context of modified theories of gravity.

In Figure 5.3 and Table 5.2, we present the results of our two main mass measurements combined with the two extra introduced in the previous subsection. All measurements are in agreement, providing evidence that there is no significant correlation between the selection criteria of our LRG sample and the measurements performed here.

The first striking result is the varying degree of precision among the different measurements. The lensing measurement is the most precise, even when the concentration parameter is allowed to vary. In particular, the fact that the inferred profiles do not exhaust the freedom allowed by error bars in the right-hand panel of Figure 5.2 implies that our model prior is responsible for the strength of our measurement and that a more flexible model will result in larger mass uncertainties. On the other hand, with splashback, we can produce a dynamical mass measurement without any knowledge of the shape of the average profile and, more importantly, without having to capture the exact nature of the measured scatter. In the end, the inferred average splashback mass of our high-mass LRG sample has an uncertainty of around 50 percent. This is significantly

higher than the lensing measurement but still considerably better than the clustering measurement, consistent with zero mass. Our results show that the sparsity of high-density peaks does not allow clustering to provide competitive mass constraints. This is despite the naive expectation that the clustering of massive halos should depend only on their overdensity, or, equivalently, that they are not affected by assembly bias (Sheth and Tormen, 2004).

As a final note on our results, we point out that the difference between the masses of the two samples (*all* and *high-mass*) is 2σ for the lensing measurement, but it is not even marginally significant for the splashback values (due to the large error bars). As already shown in Contigiani et al. (2019), splashback measurements are heavily weighted towards most massive objects. To produce a non-mass weighted measure of the splashback feature, it is necessary to rescale the individual profiles with a proxy of the halo mass. However, because the study of $r_{\rm sp}$ as a function of mass is not the focus of this work, we leave this line of study open for future research.

5.5.1   Gravitational constants

In this section, we present how the combination of the lensing masses and splashback radii measured in the section above can be used to constrain models of gravity. The principle behind this constraint is the fact that, while General Relativity (GR) predicts that the trajectories of light and massive particles are affected by the same metric perturbation, extended models generally predict a discrepancy between the two.

In extended models, the equations for the linearized-metric potentials (Φ and Ψ, see Bardeen, 1980) can be connected to the background-subtracted matter density $\rho(\boldsymbol{x})$ through the following equations (Amendola et al., 2008; Bertschinger and Zukin, 2008; Pogosian et al., 2010),

$$\nabla^2(\Phi + \Psi) = 8\pi G \Sigma(x)\rho(x), \tag{5.18}$$

$$\nabla^2\Phi = 4\pi G \mu(x)\rho(x). \tag{5.19}$$

In the expressions above, the functions μ and Σ, also known as $G_{\rm matter}/G$ and $G_{\rm light}/G$ can be in principle a function of space and time (collectively indicated by x). We stress that the symbol Σ, previously used to refer to projected three-dimensional distributions ($\Sigma_{\rm g}$, $\Sigma_{\rm m}$), has a different use in this context. These equations are expressed in terms of Φ and $\Phi + \Psi$ because the trajectories of particles are affected by the first, while the deflection of light is governed by the second. In the presence of only non-relativistic matter, Einstein's equations in GR reduce to $\Phi = \Psi$ and we have $\Sigma = \mu = 1$.

The same type of deviation from GR can also be captured in the post-Newtonian parametrization by a multiplicative factor γ between the two potentials: $\Psi = \gamma\Phi$. If μ, Σ, and γ are all constants, the three are trivially related:

$$\frac{\mu}{\Sigma} = \frac{1+\gamma}{2}. \tag{5.20}$$

Under this same assumption, the ratio between the masses measured through lensing and the mass measured through the dynamics of test particles (e.g. faint galaxies or stars) can be used to constrain these parameters and the literature contains multiple results concerning these extended models. Solar System experiments have constrained γ to be consistent with its GR value ($\gamma = 1$) up to 5 significant digits (Bertotti et al., 2003), but the current measurements at larger scales are substantially less precise. For kpc-sized objects (galaxy-scale), stellar kinematics have been combined with solid lensing measurements to obtain 10 percent constraints (Bolton et al., 2006; Collett et al., 2018), while large-scale measurements ($\sim 10 - 100$ Mpc) can be obtained by combining cosmic shear and redshift space distortion measurements to achieve a similar precision (see e.g. Simpson et al., 2013; Joudaki et al., 2018). As for the scales considered in this chapter, a precision of about 30 percent can be obtained by combining lensing masses with either the kinematics of galaxies inside fully collapsed cluster halos (Pizzuti et al., 2016) or the distribution of hot X-ray emitting gas (Wilcox et al., 2015). However, in this case, the effects of the required assumptions (e.g. spherical symmetry and hydrostatic equilibrium for the gas) are harder to capture. In all cases, no deviation from GR has been measured.

As an example of the power of the measurements presented in Section 5.4, we present here their implication for beyond-GR effects. On one hand, our lensing signal is a measurement of the amplitude $M_{200m,\,L}$ of the lensing matter density $\rho_L = \rho\Sigma$. On the other hand, the splashback radius r_{sp} depends on the amplitude of $\rho_L \times \mu/\Sigma$ and it is related to the splashback mass $M_{200m,\,sp}$. We, therefore, focus on the ratio of these two amplitudes measured in the high-mass sample:

$$\frac{\mu}{\Sigma} = \frac{M_{200m,\,L}}{M_{200m,\,sp}} = 0.8 \pm 0.4 \qquad \Leftrightarrow \qquad \gamma = 0.6 \pm 0.8. \qquad (5.21)$$

In high-density regions such as the Solar System, the expectation $\gamma = 1$ must the recovered with high precision. Hence, alternative theories of gravity commonly predict scale- and density-dependent effects, which cannot be captured through constant values of μ and Σ. Because r_{sp} marks a sharp density transition around massive objects, it is more suited to test these complicated dependencies. To provide an example of the constraints possible under this second interpretation, we followed Contigiani et al. (2019) to convert the effects of an additional scale-dependent force (also known as a fifth force) on the location of the splashback radius r_{sp}.

In the case of the symmetron gravity theory studied there (Hinterbichler et al., 2011), the change in r_{sp} introduced by the fifth force was obtained by integrating the trajectories of test particles in the presence or absence of this force. In total, the theory has three parameters: 1) the dimensionless vacuum Compton wavelength of the field $\lambda_0/R(t_0)$, that we fix to be 0.05 times the size of the collapsed object; 2) z_{SSB}, the redshift corresponding to the moment at which the fifth force is turned on in cosmic history, that we fix at $z_{SSB} = 1.25$; and 3) f, a dimensionless force-strength parameter

that is zero in GR. The choices of the fixed values that we imposed are based on physical considerations due to the connection of these gravity models to dark energy while maximizing the impact on splashback. See Contigiani et al. (2019) for more details.

To match the expectation of the model to observations, we first converted the M_{200m} lensing measurement into an expected splashback radius $r_{sp, L}$ by reversing the procedure explained at the end of Section 5.4.1 and then compared the measured r_{sp} to this value. From the high-mass data, we obtained the following 1σ constraints:

$$\frac{r_{sp, L} - r_{sp}}{r_{sp, L}} = 0.07 \pm 0.20 \qquad \Longrightarrow \qquad f < 1.8. \qquad (5.22)$$

The symmetron theories associated to $z_{SSB} \sim 1$ and cluster-sized objects correspond to a coupling mass scale of the order of 10^{-6} Planck masses, a region of the parameter space which is still allowed by the solar-system constraints (Hinterbichler et al., 2011) and which has not been explored by other tests (see e.g. O'Hare and Burrage, 2018; Burrage and Sakstein, 2018). In particular, the upper limit on f produced here directly translates into a constraint on the symmetron field potential of Contigiani et al. (2019).[1] Thus, our result shows that we can test the existence of scalar fields with quite weak couplings and directly project these measurements into a broader theory parameter space.

5.5.2   Future prospects

Our results show that the precision of the recovered splashback mass is not comparable to the low uncertainty of the lensing measurements. Because of this, every constraint based on comparing the two is currently limited by the uncertainty of the first. While this chapter's focus is not to provide accurate forecasts, we attempt to quantify how we expect these results to improve with larger samples. In particular, we focus our attention on wide stage-IV surveys such as *Euclid* (Laureijs et al., 2011) and LSST (LSST, LSST Science Collaboration et al., 2009).

First, we investigate how our results can be rescaled. In the process of inferring M_{200m} from r_{sp}, we find that the relative precision of the first is always a multiple $(3 - 4)$ of the second. This statement, which we have verified over a wide range of redshifts ($z \in [0, 1.5]$) and masses ($M_{200m} \in [10^{13}, 10^{15}]\,M_\odot$), is a simple consequence of the low slope of the $M_{200m} - r_{sp}$ relation. Second, we estimate the size of a cluster sample we can obtain and how that translates into an improved errorbar for r_{sp}. LSST is expected to reach 2.5 magnitudes deeper than KiDS and to cover an area of the sky 18 times larger (LSST Science Collaboration et al., 2009). Part of this region is covered by the galactic plane and will need to be masked, but the resulting LRG sample will reach up to $z \sim 1.2$ and cover a comoving volume about a factor 100 larger than what

---

[1]However, we stress here that this constraint does not have implications for dark energy, as the model considered there is not able to drive cosmic acceleration in the absence of a cosmological constant.

is considered in this work. Because the selected LRGs are designed to have a constant comoving density, we can use this estimate to scale the error bars of our galaxy profile measurement. A sample $N = 100$ times the size would result in a relative precision in $r_{\rm sp}$ of about 1 percent, which translates into a measured $M_{\rm 200m}$ with a few percentage point uncertainty. This result is obtained by simply rescaling the error bars by a factor $\sqrt{N} = 10$, but notice that the effects do not rescale linearly for $r_{\rm sp}$. This is still larger than what is allowed by lensing measurements but can easily apply to high-redshift clusters, for which fewer background sources are available.

We note that this simple rescaling sidesteps multiple issues. Here we consider three of them and discuss their implications and possible solutions. 1) At high redshift, color-identification requires additional bands, as the 4000 Å break moves out of the LSST $grizy$ filters. 2) Even if we assume that an LRG sample can be constructed, the population of orbiting satellites at high redshift might not necessarily be easy to identify as the read sequence is only beginning to form. 3) Finally, with more depth, we also expect fainter satellites to contribute to the galaxy profile signal, but the details of this population for large cluster samples at high-redshifts are not known. For example, a simple extrapolation of the observed satellite magnitude distribution implies that the number of satellites forming the galaxy distribution signal might be enhanced by a factor 10, but this does not consider, for example, the disruption of faint satellites.

In addition to the forecast for the galaxy profiles discussed above, we also expect a measurement of $r_{\rm sp}$ with a few percentage point uncertainty directly from the lensing profile (Xhakaj et al., 2020). This precision will only be available for relatively low redshifts ($z \sim 0.45$), allowing a precise comparison of the dark matter and galaxy profiles. This cross-check can also be used to understand the effects of galaxy evolution in shaping the galaxy phase-space structure (Shin et al., 2021) and help disentangle the effects of dynamical friction, feedback, and modified models of dark matter (Adhikari et al., 2016; Banerjee et al., 2020).

5.6 Conclusions

In this chapter, we have used the splashback feature to measure the average dynamical mass of halos hosting bright KiDS LRGs. We obtain a precision of 15 percent. To support our result, we have also validated this mass measurement using a simple abundance-matching argument and weak lensing masses (see Figure 5.3 and Table 5.2). We also presented a fourth validation technique based on the linear clustering of halos, but in this case, the low statistics of high-density peaks hindered the constraining power. Finally, as an application of the synergy between the strong lensing and splashback masses, we have provided constraints on models of modified gravity (see Equation 5.22).

The main achievement that we want to stress here is that these self-consistent measurements are exclusively based on and validated with photometric data. The bright

LRG samples employed here can be easily matched to simulations, offer a straightforward interpretation, and, in general, are found to be robust against systematic effects in the redshift calibration (Bilicki et al., 2021). This is in contrast to other dynamical masses presented in the literature: such measurements are based on expensive spectroscopic data (see e.g. Rines et al., 2016) and are found to produce masses higher than lensing estimates (Herbonnet et al., 2020), an effect which might be due to systematic selection biases afflicting these more precise measurements (Old et al., 2015).

Because the relation between $r_{\rm sp}$ and halo mass depends on cosmology, this measurement naturally provides a constraint on structure formation, although the precision is relatively low with current data. The predictions for splashback also have trends with redshift, mass, and galaxy properties that are expected to be informative (Xhakaj et al., 2020; Shin et al., 2021). By comparing splashback and lensing masses, we were able to constrain the effects on $r_{\rm sp}$ of deviations from GR in a relatively straightforward manner. In this case, the interpretation of the difference between dynamical mass and lensing mass is not a simple rescaling, but it is connected to the full trajectory of the infalling material. By performing this measurement as a function of redshift, it is in principle possible to track the effects as a function of cosmic time and disentangle the effects of the accretion rate from the effect of fifth forces.

Precise measurements of the outer edge of massive dark matter halos have become feasible only in the last decade, thanks to the introduction of large galaxy and cluster samples. These measurements allow the study of the interface between the nonlinear multi-stream region of collapsed structures and the mildly nonlinear scales of infalling material, and directly connect the environment of massive halos and their properties. As we have shown in this work, this new research direction offers a route to reliable dynamical mass measurements as well as a new way to probe gravitational theories.

As discussed in Section 5.5.2, future stage IV surveys will provide percentage level splashback measurements. Modeling the trends in redshift, mass, accretion rate, and satellite properties of this feature promises to provide a powerful probe of the physics behind galaxy formation (Adhikari et al., 2020), as well as the large-scale environment of massive halos and their anisotropy (Contigiani et al., 2021).

Bibliography

Susmita Adhikari, Neal Dalal, and Robert T. Chamberlain. Splashback in accreting dark matter halos. *Journal of Cosmology and Astroparticle Physics*, 2014(11):019–019, November 2014. ISSN 1475-7516. doi: 10.1088/1475-7516/2014/11/019.

Susmita Adhikari, Neal Dalal, and Joseph Clampitt. Observing dynamical friction in galaxy clusters. J. Cosmology Astropart. Phys., 2016(7):022, July 2016. doi: 10.1088/1475-7516/2016/07/022.

Susmita Adhikari, Tae-hyeon Shin, Bhuvnesh Jain, Matt Hilton, Eric Baxter, Chihway Chang, Risa H. Wechsler, Nick Battaglia, J. Richard Bond, Sebastian Bocquet, Joseph DeRose, Steve K. Choi, Mark Devlin, Jo Dunkley, August E. Evrard, Simone Ferraro, J. Colin Hill, John P. Hughes, Patricio A. Gallardo, Martine Lokken, Amanda MacInnis, Jeffrey McMahon, Mathew S. Madhavacheril, Frederico Nati, Laura B. Newburgh, Michael D. Niemack, Lyman A. Page, Antonella Palmese, Bruce Partridge, Eduardo Rozo, Eli Rykoff, Maria Salatino, Alessandro Schillaci, Neelima Sehgal, Cristóbal Sifón, Chun-Hao To, Ed Wollack, Hao-Yi Wu, Zhilei Xu, Michel Aguena, Sahar Allam, Alexandra Amon, James Annis, Santiago Avila, David Bacon, Emmanuel Bertin, Sunayana Bhargava, David Brooks, David L. Burke, Aurelio C. Rosell, Matias Carrasco Kind, Jorge Carretero, Francisco Javier Castander, Ami Choi, Matteo Costanzi, Luiz N. da Costa, Juan De Vicente, Shantanu Desai, Thomas H. Diehl, Peter Doel, Spencer Everett, Ismael Ferrero, Agnès Ferté, Brenna Flaugher, Pablo Fosalba, Josh Frieman, Juan García-Bellido, Enrique Gaztanaga, Daniel Gruen, Robert A. Gruendl, Julia Gschwend, Gaston Gutierrez, Will G. Hartley, Samuel R. Hinton, Devon L. Hollowood, Klaus Honscheid, David J. James, Tesla Jeltema, Kyler Kuehn, Nikolay Kuropatkin, Ofer Lahav, Marcos Lima, Marcio A. G. Maia, Jennifer L. Marshall, Paul Martini, Peter Melchior, Felipe Menanteau, Ramon Miquel, Robert Morgan, Ricardo L. C. Ogando, Francisco Paz-Chinchón, Andrés Plazas Malagón, Eusebio Sanchez, Basilio Santiago, Vic Scarpine, Santiago Serrano, Ignacio Sevilla-Noarbe, Mathew Smith, Marcelle Soares-Santos, Eric Suchyta, Molly E. C. Swanson, Tamas N. Varga, Reese D. Wilkinson, Yuanyuan Zhang, Jason E. Austermann, James A. Beall, Daniel T. Becker, Edward V. Denison, Shannon M. Duff, Gene C. Hilton, Johannes Hubmayr,

Joel N. Ullom, Jeff Van Lanen, Leila R. Vale, DES Collaboration, and ACT Collaboration. Probing galaxy evolution in massive clusters using ACT and DES: splashback as a cosmic clock. *arXiv e-prints*, art. arXiv:2008.11663, August 2020.

Andreas Albrecht, Gary Bernstein, Robert Cahn, Wendy L. Freedman, Jacqueline Hewitt, Wayne Hu, John Huth, Marc Kamionkowski, Edward W. Kolb, Lloyd Knox, John C. Mather, Suzanne Staggs, and Nicholas B. Suntzeff. Report of the Dark Energy Task Force. *arXiv e-prints*, art. astro-ph/0609591, September 2006.

Luca Amendola, Martin Kunz, and Domenico Sapone. Measuring the dark side (with weak lensing). J. Cosmology Astropart. Phys., 2008(4):013, April 2008. doi: 10.1088/1475-7516/2008/04/013.

S. Arnouts and O. Ilbert. LePHARE: Photometric Analysis for Redshift Estimate, August 2011.

Arka Banerjee, Susmita Adhikari, Neal Dalal, Surhud More, and Andrey Kravtsov. Signatures of self-interacting dark matter on cluster density profile and subhalo distributions. J. Cosmology Astropart. Phys., 2020(2):024, February 2020. doi: 10.1088/1475-7516/2020/02/024.

James M. Bardeen. Gauge-invariant cosmological perturbations. Phys. Rev. D, 22(8): 1882–1905, October 1980. doi: 10.1103/PhysRevD.22.1882.

Eric Baxter, Chihway Chang, Bhuvnesh Jain, Susmita Adhikari, Neal Dalal, Andrey Kravtsov, Surhud More, Eduardo Rozo, Eli Rykoff, and Ravi K. Sheth. The Halo Boundary of Galaxy Clusters in the SDSS. ApJ, 841(1):18, May 2017. doi: 10.3847/1538-4357/aa6ff0.

B. Bertotti, L. Iess, and P. Tortora. A test of general relativity using radio links with the Cassini spacecraft. Nature, 425(6956):374–376, September 2003. doi: 10.1038/nature01997.

Edmund Bertschinger and Phillip Zukin. Distinguishing modified gravity from dark energy. Phys. Rev. D, 78(2):024015, July 2008. doi: 10.1103/PhysRevD.78.024015.

Suman Bhattacharya, Salman Habib, Katrin Heitmann, and Alexey Vikhlinin. Dark Matter Halo Profiles of Massive Clusters: Theory versus Observations. ApJ, 766(1): 32, March 2013. doi: 10.1088/0004-637X/766/1/32.

M. Bilicki, A. Dvornik, H. Hoekstra, A. H. Wright, N. E. Chisari, M. Vakili, M. Asgari, B. Giblin, C. Heymans, H. Hildebrandt, B. W. Holwerda, A. Hopkins, H. Johnston, A. Kannawadi, K. Kuijken, S. J. Nakoneczny, H. Y. Shan, A. Sonnenfeld, and E. Valentijn. Bright galaxy sample in the Kilo-Degree Survey Data Release 4: selection, photometric redshifts, and physical properties. *arXiv e-prints*, art. arXiv:2101.06010, January 2021.

Adam S. Bolton, Saul Rappaport, and Scott Burles. Constraint on the Post-Newtonian Parameter gamma on Galactic Size Scales. *Phys. Rev. D*, 74:061501, 2006. doi: 10.1103/PhysRevD.74.061501.

Clare Burrage and Jeremy Sakstein. Tests of chameleon gravity. *Living Reviews in Relativity*, 21(1):1, March 2018. doi: 10.1007/s41114-018-0011-x.

Philipp Busch and Simon D. M. White. Assembly bias and splashback in galaxy clusters. *Monthly Notices of the Royal Astronomical Society*, 470(4):4767–4781, June 2017. ISSN 1365-2966. doi: 10.1093/mnras/stx1584.

DES Collaboration. The Splashback Feature around DES Galaxy Clusters: Galaxy Density and Weak Lensing Profiles. ApJ, 864(1):83, September 2018. doi: 10.3847/1538-4357/aad5e7.

Planck Collaboration. Planck 2015 results. *Astronomy & Astrophysics*, 594:A1, September 2016. ISSN 1432-0746. doi: 10.1051/0004-6361/201527101.

Thomas E. Collett, Lindsay J. Oldham, Russell J. Smith, Matthew W. Auger, Kyle B. Westfall, David Bacon, Robert C. Nichol, Karen L. Masters, Kazuya Koyama, and Remco van den Bosch. A precise extragalactic test of General Relativity. *Science*, 360 (6395):1342–1346, June 2018. doi: 10.1126/science.aao2469.

O. Contigiani, Y. M. Bahé, and H. Hoekstra. The mass-size relation of galaxy clusters. MNRAS, May 2021. doi: 10.1093/mnras/stab1463.

Omar Contigiani, Henk Hoekstra, and Yannick M. Bahé. Weak lensing constraints on splashback around massive clusters. MNRAS, 485(1):408–415, May 2019. doi: 10.1093/mnras/stz404.

Omar Contigiani, Valeri Vardanyan, and Alessandra Silvestri. Splashback radius in symmetron gravity. *Physical Review D*, 99(6), March 2019. ISSN 2470-0029. doi: 10.1103/physrevd.99.064030.

J. T. A. de Jong, G. A. Verdoes Kleijn, K. H. Kuijken, and E. A. Valentijn. The Kilo-Degree Survey. *Experimental Astronomy*, 35:25–44, January 2013. doi: 10.1007/s10686-012-9306-1.

Benedikt Diemer. The splashback radius of halos from particle dynamics. i. the sparta algorithm. *The Astrophysical Journal Supplement Series*, 231(1):5, July 2017. ISSN 1538-4365. doi: 10.3847/1538-4365/aa799c.

Benedikt Diemer. COLOSSUS: A python toolkit for cosmology, large-scale structure, and dark matter halos. *Astrophys. J. Suppl.*, 239(2):35, 2018. doi: 10.3847/1538-4365/aaee8c.

Benedikt Diemer. Universal at Last? The Splashback Mass Function of Dark Matter Halos. ApJ, 903(2):87, November 2020a. doi: 10.3847/1538-4357/abbf52.

Benedikt Diemer. The Splashback Radius of Halos from Particle Dynamics. III. Halo Catalogs, Merger Trees, and Host-Subhalo Relations. ApJS, 251(2):17, December 2020b. doi: 10.3847/1538-4365/abbf51.

Benedikt Diemer and Andrey V. Kravtsov. Dependence of the Outer Density Profiles of Halos on Their Mass Accretion Rate. ApJ, 789(1):1, July 2014. doi: 10.1088/0004-637X/789/1/1.

Benedikt Diemer and Andrey V. Kravtsov. A Universal Model for Halo Concentrations. ApJ, 799(1):108, January 2015. doi: 10.1088/0004-637X/799/1/108.

Benedikt Diemer, Surhud More, and Andrey V. Kravtsov. The Pseudo-evolution of Halo Mass. ApJ, 766(1):25, March 2013. doi: 10.1088/0004-637X/766/1/25.

Benedikt Diemer, Philip Mansfield, Andrey V. Kravtsov, and Surhud More. The splashback radius of halos from particle dynamics. ii. dependence on mass, accretion rate, redshift, and cosmology. *The Astrophysical Journal*, 843(2):140, July 2017. ISSN 1538-4357. doi: 10.3847/1538-4357/aa79ab.

Andrej Dvornik, Marcello Cacciato, Konrad Kuijken, Massimo Viola, Henk Hoekstra, Reiko Nakajima, Edo van Uitert, Margot Brouwer, Ami Choi, Thomas Erben, and et al. A kids weak lensing analysis of assembly bias in gama galaxy groups. *Monthly Notices of the Royal Astronomical Society*, 468(3):3251–3265, March 2017. ISSN 1365-2966. doi: 10.1093/mnras/stx705.

A. Edge, W. Sutherland, K. Kuijken, S. Driver, R. McMahon, S. Eales, and J. P. Emerson. The VISTA Kilo-degree Infrared Galaxy (VIKING) Survey: Bridging the Gap between Low and High Redshift. *The Messenger*, 154:32–34, December 2013.

J Einasto. On the Construction of a Composite Model for the Galaxy and on the Determination of the System of Galactic Parameters. *Trudy Astrofizicheskogo Instituta Alma-Ata*, 5:87–100, 1965.

T. Erben, M. Schirmer, J. P. Dietrich, O. Cordes, L. Haberzettl, M. Hetterscheidt, H. Hildebrandt, O. Schmithuesen, P. Schneider, P. Simon, E. Deul, R. N. Hook, N. Kaiser, M. Radovich, C. Benoist, M. Nonino, L. F. Olsen, I. Prandoni, R. Wichmann, S. Zaggia, D. Bomans, R. J. Dettmar, and J. M. Miralles. GaBoDS: The Garching-Bonn Deep Survey. IV. Methods for the image reduction of multi-chip cameras demonstrated on data from the ESO Wide-Field Imager. *Astronomische Nachrichten*, 326(6):432–464, July 2005. doi: 10.1002/asna.200510396.

I. Fenech Conti, Ricardo Herbonnet, Henk Hoekstra, Julian Merten, Lance Miller, and Massimo Viola. Calibration of weak-lensing shear in the Kilo-Degree Survey. *Mon. Not. Roy. Astron. Soc.*, 467(2):1627–1651, 2017. doi: 10.1093/mnras/stx200.

Daniel Foreman-Mackey, David W. Hogg, Dustin Lang, and Jonathan Goodman. emcee: The MCMC Hammer. *Publications of the Astronomical Society of the Pacific*, 125(925): 306–312, March 2013. ISSN 00046280. doi: 10.1086/670067.

Maria Cristina Fortuna, Henk Hoekstra, Harry Johnston, Mohammadjavad Vakili, Arun Kannawadi, Christos Georgiou, Benjamin Joachimi, Angus H. Wright, Marika Asgari, Maciej Bilicki, Catherine Heymans, Hendrik Hildebrandt, Konrad Kuijken, and Maximilian von Wietersheim-Kramsta. 2021.

Liang Gao, Julio F. Navarro, Shaun Cole, Carlos S. Frenk, Simon D. M. White, Volker Springel, Adrian Jenkins, and Angelo F. Neto. The redshift dependence of the structure of massive Λ cold dark matter haloes. *Monthly Notices of the Royal Astronomical Society*, 387(2):536–544, June 2008. ISSN 0035-8711. doi: 10.1111/j.1365-2966.2008. 13277.x.

Michael D. Gladders and H. K. C. Yee. A New Method For Galaxy Cluster Detection. I. The Algorithm. AJ, 120(4):2148–2162, October 2000. doi: 10.1086/301557.

Ricardo Herbonnet, Cristóbal Sifón, Henk Hoekstra, Yannick Bahé, Remco F. J. van der Burg, Jean-Baptiste Melin, Anja von der Linden, David Sand, Scott Kay, and David Barnes. CCCP and MENeaCS: (updated) weak-lensing masses for 100 galaxy clusters. MNRAS, 497(4):4684–4703, October 2020. doi: 10.1093/mnras/staa2303.

Kurt Hinterbichler, Justin Khoury, Aaron Levy, and Andrew Matas. Symmetron cosmology. Phys. Rev. D, 84(10):103521, November 2011. doi: 10.1103/PhysRevD.84. 103521.

M. Jarvis, G. Bernstein, and B. Jain. The skewness of the aperture mass statistic. MNRAS, 352(1):338–352, July 2004. doi: 10.1111/j.1365-2966.2004.07926.x.

Mike Jarvis. TreeCorr: Two-point correlation functions, August 2015.

Shahab Joudaki, Chris Blake, Andrew Johnson, Alexandra Amon, Marika Asgari, Ami Choi, Thomas Erben, Karl Glazebrook, Joachim Harnois-Déraps, Catherine Heymans, Hendrik Hildebrandt, Henk Hoekstra, Dominik Klaes, Konrad Kuijken, Chris Lidman, Alexander Mead, Lance Miller, David Parkinson, Gregory B. Poole, Peter Schneider, Massimo Viola, and Christian Wolf. KiDS-450 + 2dFLenS: Cosmological parameter constraints from weak gravitational lensing tomography and overlapping redshift-space galaxy clustering. MNRAS, 474(4):4894–4924, March 2018. doi: 10.1093/mnras/stx2820.

Arun Kannawadi, Henk Hoekstra, Lance Miller, Massimo Viola, Ian Fenech Conti, Ricardo Herbonnet, Thomas Erben, Catherine Heymans, Hendrik Hildebrandt, Konrad Kuijken, Mohammadjavad Vakili, and Angus H. Wright. Towards emulating cosmic shear data: revisiting the calibration of the shear measurements for the Kilo-Degree Survey. A&A, 624:A92, April 2019. doi: 10.1051/0004-6361/201834819.

K. Kuijken, C. Heymans, A. Dvornik, H. Hildebrandt, J. T. A. de Jong, A. H. Wright, T. Erben, M. Bilicki, B. Giblin, H. Y. Shan, F. Getman, A. Grado, H. Hoekstra, L. Miller, N. Napolitano, M. Paolilo, M. Radovich, P. Schneider, W. Sutherland , M. Tewes, C. Tortora, E. A. Valentijn, and G. A. Verdoes Kleijn. The fourth data release of the Kilo-Degree Survey: ugri imaging and nine-band optical-IR photometry over 1000 square degrees. A&A, 625:A2, May 2019. doi: 10.1051/0004-6361/201834918.

R. B. Larson, B. M. Tinsley, and C. N. Caldwell. The evolution of disk galaxies and the origin of S0 galaxies. ApJ, 237:692–707, May 1980. doi: 10.1086/157917.

R. Laureijs, J. Amiaux, S. Arduini, J. L. Auguères, J. Brinchmann, R. Cole, M. Cropper, C. Dabin, L. Duvet, A. Ealet, B. Garilli, P. Gondoin, L. Guzzo, J. Hoar, H. Hoekstra, R. Holmes, T. Kitching, T. Maciaszek, Y. Mellier, F. Pasian, W. Percival, J. Rhodes, G. Saavedra Criado, M. Sauvage, R. Scaramella, L. Valenziano, S. Warren, R. Bender, F. Castander, A. Cimatti, O. Le Fèvre, H. Kurki-Suonio, M. Levi, P. Lilje, G. Meylan, R. Nichol, K. Pedersen, V. Popa, R. Rebolo Lopez, H. W. Rix, H. Rottgering, W. Zeilinger, F. Grupp, P. Hudelot, R. Massey, M. Meneghetti, L. Miller, S. Paltani, S. Paulin-Henriksson, S. Pires, C. Saxton, T. Schrabback, G. Seidel, J. Walsh, N. Aghanim, L. Amendola, J. Bartlett, C. Baccigalupi, J. P. Beaulieu, K. Benabed, J. G. Cuby, D. Elbaz, P. Fosalba, G. Gavazzi, A. Helmi, I. Hook, M. Irwin, J. P. Kneib, M. Kunz, F. Mannucci, L. Moscardini, C. Tao, R. Teyssier, J. Weller, G. Zamorani, M. R. Zapatero Osorio, O. Boulade, J. J. Foumond, A. Di Giorgio, P. Guttridge, A. James, M. Kemp, J. Martignac, A. Spencer, D. Walton, T. Blümchen, C. Bonoli, F. Bortoletto, C. Cerna, L. Corcione, C. Fabron, K. Jahnke, S. Ligori, F. Madrid, L. Martin, G. Morgante, T. Pamplona, E. Prieto, M. Riva, R. Toledo, M. Trifoglio, F. Zerbi, F. Abdalla, M. Douspis, C. Grenet, S. Borgani, R. Bouwens, F. Courbin, J. M. Delouis, P. Dubath, A. Fontana, M. Frailis, A. Grazian, J. Koppenhöfer, O. Mansutti, M. Melchior, M. Mignoli, J. Mohr, C. Neissner, K. Noddle, M. Poncet, M. Scodeggio, S. Serrano, N. Shane, J. L. Starck, C. Surace, A. Taylor, G. Verdoes-Kleijn, C. Vuerli, O. R. Williams, A. Zacchei, B. Altieri, I. Escudero Sanz, R. Kohley, T. Oosterbroek, P. Astier, D. Bacon, S. Bardelli, C. Baugh, F. Bellagamba, C. Benoist, D. Bianchi, A. Biviano, E. Branchini, C. Carbone, V. Cardone, D. Clements, S. Colombi, C. Conselice, G. Cresci, N. Deacon, J. Dunlop, C. Fedeli, F. Fontanot, P. Franzetti, C. Giocoli, J. Garcia-Bellido, J. Gow, A. Heavens, P. Hewett, C. Heymans, A. Holland, Z. Huang, O. Ilbert, B. Joachimi, E. Jennins, E. Kerins, A. Kiessling, D. Kirk, R. Kotak, O. Krause, O. Lahav, F. van Leeuwen, J. Lesgourgues, M. Lombardi, M. Magliocchetti, K. Maguire, E. Majerotto, R. Maoli, F. Marulli, S. Maurogordato, H. McCracken,

R. McLure, A. Melchiorri, A. Merson, M. Moresco, M. Nonino, P. Norberg, J. Peacock, R. Pello, M. Penny, V. Pettorino, C. Di Porto, L. Pozzetti, C. Quercellini, M. Radovich, A. Rassat, N. Roche, S. Ronayette, E. Rossetti, B. Sartoris, P. Schneider, E. Semboloni, S. Serjeant, F. Simpson, C. Skordis, G. Smadja, S. Smartt, P. Spano, S. Spiro, M. Sullivan, A. Tilquin, R. Trotta, L. Verde, Y. Wang, G. Williger, G. Zhao, J. Zoubian, and E. Zucca. Euclid definition study report, 2011.

D. Nelson Limber. The Analysis of Counts of the Extragalactic Nebulae in Terms of a Fluctuating Density Field. ApJ, 117:134, January 1953. doi: 10.1086/145672.

LSST Science Collaboration, Paul A. Abell, Julius Allison, Scott F. Anderson, John R. Andrew, J. Roger P. Angel, Lee Armus, David Arnett, S. J. Asztalos, Tim S. Axelrod, and et al. LSST Science Book, Version 2.0. *arXiv e-prints*, art. arXiv:0912.0201, December 2009.

Conor L. Mancone and Anthony H. Gonzalez. EzGal: A Flexible Interface for Stellar Population Synthesis Models. PASP, 124(916):606, June 2012. doi: 10.1086/666502.

Rachel Mandelbaum, Uroš Seljak, Guinevere Kauffmann, Christopher M. Hirata, and Jonathan Brinkmann. Galaxy halo masses and satellite fractions from galaxy-galaxy lensing in the Sloan Digital Sky Survey: stellar mass, luminosity, morphology and environment dependencies. MNRAS, 368(2):715–731, May 2006. doi: 10.1111/j.1365-2966.2006.10156.x.

John P. McFarland, Gijs Verdoes-Kleijn, Gert Sikkema, Ewout M. Helmich, Danny R. Boxhoorn, and Edwin A. Valentijn. The Astro-WISE optical image pipeline. Development and implementation. *Experimental Astronomy*, 35(1-2):45–78, January 2013. doi: 10.1007/s10686-011-9266-x.

L. Miller, C. Heymans, T. D. Kitching, L. van Waerbeke, T. Erben, H. Hildebrandt, H. Hoekstra, Y. Mellier, B. T. P. Rowe, J. Coupon, J. P. Dietrich, L. Fu, J. Harnois-Déraps, M. J. Hudson, M. Kilbinger, K. Kuijken, T. Schrabback, E. Semboloni, S. Vafaei, and M. Velander. Bayesian galaxy shape measurement for weak lensing surveys - III. Application to the Canada-France-Hawaii Telescope Lensing Survey. MNRAS, 429(4):2858–2880, March 2013. doi: 10.1093/mnras/sts454.

Ben Moore, Neal Katz, George Lake, Alan Dressler, and Augustus Oemler. Galaxy harassment and the evolution of clusters of galaxies. Nature, 379(6566):613–616, February 1996. doi: 10.1038/379613a0.

Surhud More, Benedikt Diemer, and Andrey V. Kravtsov. The splashback radius as a physical halo boundary and the growth of halo mass. *The Astrophysical Journal*, 810 (1):36, August 2015. ISSN 1538-4357. doi: 10.1088/0004-637x/810/1/36.

Surhud More, Hironao Miyatake, Masahiro Takada, Benedikt Diemer, Andrey V. Kravtsov, Neal K. Dalal, Anupreeta More, Ryoma Murata, Rachel Mandelbaum, Eduardo Rozo, Eli S. Rykoff, Masamune Oguri, and David N. Spergel. Detection of the Splashback Radius and Halo Assembly Bias of Massive Galaxy Clusters. ApJ, 825(1): 39, July 2016. doi: 10.3847/0004-637X/825/1/39.

Julio F. Navarro, Carlos S. Frenk, and Simon D. M. White. The Structure of Cold Dark Matter Halos. *The Astrophysical Journal*, 462:563, May 1996. ISSN 0004-637X. doi: 10.1086/177173.

Julio F. Navarro, Carlos S. Frenk, and Simon D. M. White. A Universal Density Profile from Hierarchical Clustering. *The Astrophysical Journal*, 490(2):493–508, December 1997. ISSN 0004-637X. doi: 10.1086/304888.

Ciaran A. J. O'Hare and Clare Burrage. Stellar kinematics from the symmetron fifth force in the Milky Way disk. Phys. Rev. D, 98(6):064019, September 2018. doi: 10. 1103/PhysRevD.98.064019.

L. Old, R. Wojtak, G. A. Mamon, R. A. Skibba, F. R. Pearce, D. Croton, S. Bamford, P. Behroozi, R. de Carvalho, J. C. Muñoz-Cuartas, D. Gifford, M. E. Gray, A. von der Linden, M. R. Merrifield, S. I. Muldrew, V. Müller, R. J. Pearson, T. J. Ponman, E. Rozo, E. Rykoff, A. Saro, T. Sepp, C. Sifón, and E. Tempel. Galaxy Cluster Mass Reconstruction Project - II. Quantifying scatter and bias using contrasting mock catalogues. MNRAS, 449(2):1897–1920, May 2015. doi: 10.1093/mnras/stv421.

Stephanie O'Neil, David J. Barnes, Mark Vogelsberger, and Benedikt Diemer. The splashback boundary of haloes in hydrodynamic simulations. MNRAS, 504(3):4649–4666, July 2021. doi: 10.1093/mnras/stab1221.

L. Pizzuti, B. Sartoris, S. Borgani, L. Amendola, K. Umetsu, A. Biviano, M. Girardi, P. Rosati, I. Balestra, G. B. Caminha, B. Frye, A. Koekemoer, C. Grillo, M. Lombardi, A. Mercurio, and M. Nonino. CLASH-VLT: testing the nature of gravity with galaxy cluster mass profiles. J. Cosmology Astropart. Phys., 2016(4):023, April 2016. doi: 10.1088/1475-7516/2016/04/023.

Levon Pogosian, Alessandra Silvestri, Kazuya Koyama, and Gong-Bo Zhao. How to optimally parametrize deviations from general relativity in the evolution of cosmological perturbations. Phys. Rev. D, 81(10):104023, May 2010. doi: 10.1103/PhysRevD. 81.104023.

William H. Press and Paul Schechter. Formation of Galaxies and Clusters of Galaxies by Self-Similar Gravitational Condensation. ApJ, 187:425–438, February 1974. doi: 10.1086/152650.

A. M. Price-Whelan et al. The Astropy Project: Building an Open-science Project and Status of the v2.0 Core Package. *Astron. J.*, 156(3):123, 2018. doi: 10.3847/1538-3881/aabc4f.

Kenneth J. Rines, Margaret J. Geller, Antonaldo Diaferio, and Ho Seong Hwang. HeCS-SZ: The Hectospec Survey of Sunyaev-Zeldovich-selected Clusters. ApJ, 819(1):63, March 2016. doi: 10.3847/0004-637X/819/1/63.

E. Rozo, E. S. Rykoff, A. Abate, C. Bonnett, M. Crocce, C. Davis, B. Hoyle, B. Leistedt, H. V. Peiris, R. H. Wechsler, T. Abbott, F. B. Abdalla, M. Banerji, A. H. Bauer, A. Benoit-Lévy, G. M. Bernstein, E. Bertin, D. Brooks, E. Buckley-Geer, D. L. Burke, D. Capozzi, A. Carnero Rosell, D. Carollo, M. Carrasco Kind, J. Carretero, F. J. Castander, M. J. Childress, C. E. Cunha, C. B. D'Andrea, T. Davis, D. L. DePoy, S. Desai, H. T. Diehl, J. P. Dietrich, P. Doel, T. F. Eifler, A. E. Evrard, A. Fausti Neto, B. Flaugher, P. Fosalba, J. Frieman, E. Gaztanaga, D. W. Gerdes, K. Glazebrook, D. Gruen, R. A. Gruendl, K. Honscheid, D. J. James, M. Jarvis, A. G. Kim, K. Kuehn, N. Kuropatkin, O. Lahav, C. Lidman, M. Lima, M. A. G. Maia, M. March, P. Martini, P. Melchior, C. J. Miller, R. Miquel, J. J. Mohr, R. C. Nichol, B. Nord, C. R. O'Neill, R. Ogando, A. A. Plazas, A. K. Romer, A. Roodman, M. Sako, E. Sanchez, B. Santiago, M. Schubnell, I. Sevilla-Noarbe, R. C. Smith, M. Soares-Santos, F. Sobreira, E. Suchyta, M. E. C. Swanson, J. Thaler, D. Thomas, S. Uddin, V. Vikram, A. R. Walker, W. Wester, Y. Zhang, and L. N. da Costa. redMaGiC: selecting luminous red galaxies from the DES Science Verification data. MNRAS, 461(2):1431–1450, September 2016. doi: 10.1093/mnras/stw1281.

Joop Schaye, Claudio Dalla Vecchia, C. M. Booth, Robert P. C. Wiersma, Tom Theuns, Marcel R. Haas, Serena Bertone, Alan R. Duffy, I. G. McCarthy, and Freeke van de Voort. The physics driving the cosmic star formation history. MNRAS, 402(3):1536–1560, March 2010. doi: 10.1111/j.1365-2966.2009.16029.x.

Mauro Sereno, Cosimo Fedeli, and Lauro Moscardini. Comparison of weak lensing by NFW and Einasto halos and systematic errors. J. Cosmology Astropart. Phys., 2016 (1):042, January 2016. doi: 10.1088/1475-7516/2016/01/042.

Ravi K. Sheth and Giuseppe Tormen. On the environmental dependence of halo formation. MNRAS, 350(4):1385–1390, June 2004. doi: 10.1111/j.1365-2966.2004.07733.x.

T Shin, S Adhikari, E J Baxter, C Chang, B Jain, N Battaglia, L Bleem, S Bocquet, J DeRose, D Gruen, and et al. Measurement of the splashback feature around sz-selected galaxy clusters with des, spt, and act. *Monthly Notices of the Royal Astronomical Society*, 487(2):2900–2918, May 2019. ISSN 1365-2966. doi: 10.1093/mnras/stz1434.

T. Shin, B. Jain, S. Adhikari, E. J. Baxter, C. Chang, S. Pandey, A. Salcedo, D. H. Weinberg, A. Amsellem, N. Battaglia, M. Belyakov, T. Dacunha, S. Goldstein, A. V.

Kravtsov, T. N. Varga, T. M. C. Abbott, M. Aguena, A. Alarcon, S. Allam, A. Amon, F. Andrade-Oliveira, J. Annis, D. Bacon, K. Bechtol, M. R. Becker, G. M. Bernstein, E. Bertin, S. Bocquet, J. R. Bond, D. Brooks, E. Buckley-Geer, D. L. Burke, A. Campos, A. Carnero Rosell, M. Carrasco Kind, J. Carretero, R. Chen, A. Choi, M. Costanzi, L. N. da Costa, J. DeRose, S. Desai, J. De Vicente, M. J. Devlin, H. T. Diehl, J. P. Dietrich, S. Dodelson, P. Doel, C. Doux, A. Drlica-Wagner, K. Eckert, J. Elvin-Poole, S. Everett, S. Ferraro, I. Ferrero, A. Ferté, B. Flaugher, J. Frieman, P. A. Gallardo, M. Gatti, E. Gaztanaga, D. W. Gerdes, D. Gruen, R. A. Gruendl, G. Gutierrez, I. Harrison, W. G. Hartley, J. C. Hill, M. Hilton, S. R. Hinton, D. L. Hollowood, J. P. Hughes, D. J. James, M. Jarvis, T. Jeltema, B. J. Koopman, E. Krause, K. Kuehn, N. Kuropatkin, O. Lahav, M. Lima, M. Lokken, N. MacCrann, M. S. Madhavacheril, M. A. G. Maia, J. McCullough, J. McMahon, P. Melchior, F. Menanteau, R. Miquel, J. J. Mohr, K. Moodley, R. Morgan, J. Myles, F. Nati, A. Navarro-Alsina, M. D. Niemack, R. L. C. Ogando, L. A. Page, A. Palmese, B. Partridge, F. Paz-Chinchón, M. E. S. Pereira, A. Pieres, A. A. Plazas Malagón, J. Prat, M. Raveri, M. Rodriguez-Monroy, R. P. Rollins, A. K. Romer, E. S. Rykoff, M. Salatino, C. Sánchez, E. Sanchez, B. Santiago, V. Scarpine, A. Schillaci, L. F. Secco, S. Serrano, I. Sevilla-Noarbe, E. Sheldon, B. D. Sherwin, C. Sifón, M. Smith, M. Soares-Santos, S. T. Staggs, E. Suchyta, M. E. C. Swanson, G. Tarle, D. Thomas, C. To, M. A. Troxel, I. Tutusaus, E. M. Vavagiakis, J. Weller, E. J. Wollack, B. Yanny, B. Yin, and Y. Zhang. The mass and galaxy distribution around SZ-selected clusters. *Monthly Notices of the Royal Astronomical Society*, (4):5758–5779, September 2021.

Fergus Simpson, Catherine Heymans, David Parkinson, Chris Blake, Martin Kilbinger, Jonathan Benjamin, Thomas Erben, Hendrik Hildebrandt, Henk Hoekstra, Thomas D. Kitching, Yannick Mellier, Lance Miller, Ludovic Van Waerbeke, Jean Coupon, Liping Fu, Joachim Harnois-Déraps, Michael J. Hudson, Koenraad Kuijken, Barnaby Rowe, Tim Schrabback, Elisabetta Semboloni, Sanaz Vafaei, and Malin Velander. CFHTLenS: testing the laws of gravity with tomographic weak lensing and redshift-space distortions. MNRAS, 429(3):2249–2263, March 2013. doi: 10.1093/mnras/sts493.

Rachel S. Somerville, Philip F. Hopkins, Thomas J. Cox, Brant E. Robertson, and Lars Hernquist. A semi-analytic model for the co-evolution of galaxies, black holes and active galactic nuclei. MNRAS, 391(2):481–506, December 2008. doi: 10.1111/j.1365-2966.2008.13805.x.

Iskra Strateva, Željko Ivezić, Gillian R. Knapp, Vijay K. Narayanan, Michael A. Strauss, James E. Gunn, Robert H. Lupton, David Schlegel, Neta A. Bahcall, Jon Brinkmann, Robert J. Brunner, Tamás Budavári, István Csabai, Francisco Javier Castander, Mamoru Doi, Masataka Fukugita, Zsuzsanna Győry, Masaru Hamabe, Greg Hennessy, Takashi Ichikawa, Peter Z. Kunszt, Don Q. Lamb, Timothy A. McKay, Sadanori Okamura, Judith Racusin, Maki Sekiguchi, Donald P. Schneider, Kazuhiro Shimasaku, and Donald York. Color Separation of Galaxy Types in the Sloan Digital Sky Survey Imaging Data. AJ, 122(4):1861–1874, October 2001. doi: 10.1086/323301.

Jeremy Tinker, Andrey V. Kravtsov, Anatoly Klypin, Kevork Abazajian, Michael War-
    ren, Gustavo Yepes, Stefan Gottlöber, and Daniel E. Holz. Toward a Halo Mass Func-
    tion for Precision Cosmology: The Limits of Universality. ApJ, 688(2):709–728, De-
    cember 2008. doi: 10.1086/591439.

Jeremy L. Tinker, Brant E. Robertson, Andrey V. Kravtsov, Anatoly Klypin, Michael S.
    Warren, Gustavo Yepes, and Stefan Gottlöber. The Large-scale Bias of Dark Matter
    Halos: Numerical Calibration and Model Tests. ApJ, 724(2):878–886, December 2010.
    doi: 10.1088/0004-637X/724/2/878.

James W. Trayford, Tom Theuns, Richard G. Bower, Joop Schaye, Michelle Furlong,
    Matthieu Schaller, Carlos S. Frenk, Robert A. Crain, Claudio Dalla Vecchia, and Ian G.
    McCarthy. Colours and luminosities of z = 0.1 galaxies in the EAGLE simulation.
    MNRAS, 452(3):2879–2896, September 2015. doi: 10.1093/mnras/stv1461.

Keiichi Umetsu and Benedikt Diemer. Lensing Constraints on the Mass Profile Shape
    and the Splashback Radius of Galaxy Clusters. ApJ, 836(2):231, February 2017. doi:
    10.3847/1538-4357/aa5c90.

Mohammadjavad Vakili, Maciej Bilicki, Henk Hoekstra, Nora Elisa Chisari, Michael
    J. I. Brown, Christos Georgiou, Arun Kannawadi, Konrad Kuijken, and Angus H.
    Wright. Luminous red galaxies in the Kilo-Degree Survey: selection with broad-band
    photometry and weak lensing measurements. MNRAS, 487(3):3715–3733, August
    2019. doi: 10.1093/mnras/stz1249.

Mohammadjavad Vakili, Henk Hoekstra, Maciej Bilicki, Maria-Cristina Fortuna, Kon-
    rad Kuijken, Angus H. Wright, Marika Asgari, Michael Brown, Elisabeth Dom-
    brovskij, Thomas Erben, Benjamin Giblin, Catherine Heymans, Hendrik Hildebrandt,
    Harry Johnston, Shahab Joudaki, and Arun Kannawadi. Clustering of red-sequence
    galaxies in the fourth data release of the Kilo-Degree Survey. *arXiv e-prints*, art.
    arXiv:2008.13154, August 2020.

Frank C. van den Bosch, Daniel Aquino, Xiaohu Yang, H. J. Mo, Anna Pasquali,
    Daniel H. McIntosh, Simone M. Weinmann, and Xi Kang. The importance of satellite
    quenching for the build-up of the red sequence of present-day galaxies. MNRAS, 387
    (1):79–91, June 2008. doi: 10.1111/j.1365-2966.2008.13230.x.

Edo van Uitert, Marcello Cacciato, Henk Hoekstra, and Ricardo Herbonnet. Evolution
    of the luminosity-to-halo mass relation of LRGs from a combined analysis of SDSS-
    DR10+RCS2. A&A, 579:A26, July 2015. doi: 10.1051/0004-6361/201525834.

M. Viola, M. Cacciato, M. Brouwer, K. Kuijken, H. Hoekstra, P. Norberg, A. S. G.
    Robotham, E. van Uitert, M. Alpaslan, I. K. Baldry, A. Choi, J. T. A. de Jong, S. P.
    Driver, T. Erben, A. Grado, Alister W. Graham, C. Heymans, H. Hildebrandt, A. M.

Hopkins, N. Irisarri, B. Joachimi, J. Loveday, L. Miller, R. Nakajima, P. Schneider, C. Sifón, and G. Verdoes Kleijn. Dark matter halo properties of GAMA galaxy groups from 100 square degrees of KiDS weak lensing data. MNRAS, 452(4):3529–3550, October 2015. doi: 10.1093/mnras/stv1447.

Harry Wilcox, David Bacon, Robert C. Nichol, Philip J. Rooney, Ayumu Terukina, A. Kathy Romer, Kazuya Koyama, Gong-Bo Zhao, Ross Hood, Robert G. Mann, Matt Hilton, Maria Manolopoulou, Martin Sahlén, Chris A. Collins, Andrew R. Liddle, Julian A. Mayers, Nicola Mehrtens, Christopher J. Miller, John P. Stott, and Pedro T. P. Viana. The XMM Cluster Survey: testing chameleon gravity using the profiles of clusters. MNRAS, 452(2):1171–1183, September 2015. doi: 10.1093/mnras/stv1366.

Enia Xhakaj, Benedikt Diemer, Alexie Leauthaud, Asher Wasserman, Song Huang, Yifei Luo, Susmita Adhikari, and Sukhdeep Singh. How accurately can we detect the splashback radius of dark matter haloes and its correlation with accretion rate? MNRAS, 499(3):3534–3543, December 2020. doi: 10.1093/mnras/staa3046.

Chapter 6

Learning how to surf: studies in gravitational-wave cosmology

We investigate the relationship between the large-scale structure of the Universe and the gravitational wave (GW) signals emitted by merging binaries of astrophysical origin. We first study the effects of gravitational lensing on the observed population. By making minimal assumptions about the distribution of intrinsic properties, we show that lensing effects leave a recognizable signature on the observed rates and that they are prominent mainly at low inferred redshifts. We then consider the spatial cross-correlation of galaxy catalogs with either an unresolved GW background or catalogs of resolved GW sources. The first signal can constrain the evolution of the emitting population over cosmic time, while the second can be used to constrain the propagation of tensor metric perturbations. Our results suggest that galaxy surveys and GW signals will be powerful probes for both the astrophysical properties of the merging population and cosmology. Using mock data based on a simplified model, we show how our predictions can be re-scaled to multiple instrumental configurations. We find that a higher spatial resolution improves constraints across the board, but accurate distance measurements are essential for cosmological applications.

6.1   Introduction

Gravitational waves (GWs) are one of the most striking predictions of the General Theory of Relativity (Einstein, 1916, 1918) and their direct detection by the LIGO-Virgo collaboration (Abbott et al., 2016) triggered a rapidly increasing interest in exploiting this new field for cosmological information. In this chapter, we summarize three works pushing toward this objective.

In Section 6.2 we discuss the consequences of gravitational magnification, i.e., the enlargement of a source in the image plane of an observer due to the converging effect of one or more gravitational lenses along the line of sight. For point-like EM sources, this corresponds to an increase in brightness by a factor μ, which has been shown to affect the bright end of the luminosity functions of high redshift quasars and submillimeter galaxies (e.g. Negrello et al., 2010; Wyithe and Loeb, 2002). Similarly, the effects of magnification on the GW signals emitted by merging binary compact objects introduces a long and highly suppressed tail in the observed distribution (e.g. Dai et al., 2017; Oguri, 2018; Smith et al., 2018). Recently, Broadhurst et al. (2018) claimed that a considerable fraction of LIGO-Virgo events to date might belong to this tail and that another sign of strong lensing, i.e., multiple images originating from the same source, might have already been detected (Broadhurst et al., 2019). While this idea explains the present-day tension with binary evolution models (see e.g. Dominik et al., 2012) that predict lower masses than what is observed, the hypothesis is not favored by the data (Hannuksela et al., 2019; Singer et al., 2019). Furthermore, the tension it tries to explain might also be alleviated through tweaks to stellar evolution models (Abbott et al., 2016). The goal of Section 6.2 is to offer general quantitative insights into the effects of lensing on the expected rates of gravitational wave mergers and call attention to its general low likelihood in light of the aforementioned claims.[1]

GWs alone are not particularly useful for general cosmological applications because near future data will only provide rough estimates of the sky position and luminosity distance to the source. However, they can serve as powerful cosmological probes when combined with electromagnetic (EM) data, from which redshifts can be extracted. This idea dates back to Schutz (1986), and in Section 6.3 and 6.4, we discuss in detail how one can exploit the spatial correlation between the galaxies hosting GW events and the galaxies observed by wide surveys for cosmological applications.

First, we study the cross-correlation signal between an unresolved GW background (GWB) and galaxy catalogs, arguing why it represents the ideal observable to detect and measure said background. In the past, the anisotropies of the astrophysical GWB have been extensively studied (Thrane et al., 2009) and, more recently, two independent groups *Cusin et. al.* (Cusin et al., 2018, 2017) and *Jenkins et. al.* (Jenkins, Alexander C. and Sakellariadou, Mairi, 2018; Jenkins et al., 2018) obtained discrepant predictions for

---

[1]In the interest of reproducibility, a Jupyter notebook offering a guided version of this section is available at https://www.github.com/contigiani/lensingGW.

the scale-dependent signal (Cusin et al., 2018; Jenkins et al., 2019b). The main disagreements are related to the shape of the angular power spectrum as well as the overall amplitude of the signal. In this work, we explain how the difference in shape is related to the treatment of non-linear scales (see Section 6.3.1), whereas the difference in amplitude is simply due to the chosen normalization. Apart from this necessary clarification, we focus almost exclusively on the cross-correlation of the GWB with galaxies and quantify its constraining power. We choose to work with this observable for two main reasons. (1) the cross-correlation signal for diffuse backgrounds is expected to have a larger signal-to-noise ratio compared to the autocorrelation signal and is likely to be detected earlier (Ando et al., 2014), (2) the autocorrelation signal of the astrophysical GWB is susceptible to small scales and nearby structures, while the cross-correlation signal GW is free from this problem.

Second, in Section 6.4, we explore ways to reconstruct the difference between models of modified gravity and GR using resolved GW sources in combination with galaxy catalogs. An altered friction term for GWs arises in extended models displaying a redshift-dependent gravitational coupling (Amendola et al., 2018; Belgacem et al., 2018) and, as a result, the inferred luminosity distance to GW sources differs from the corresponding EM luminosity distance. It should be noted that this interesting phenomenon can already be loosely constrained today using multiple techniques, e.g. using the multimessenger detection of GW170817 (Arai and Nishizawa, 2018; Lagos et al., 2019) or features in the mass distribution of existing GW catalogs (María Ezquiaga, 2021). In addition to presenting our formalism, we also show how to jointly reconstruct the redshift evolution of modified gravity effects and the bias of GW sources. The reconstruction method we make use of is based on Gaussian processes (GPs), a well-known hyperparametric regression procedure (Rasmussen and Williams, 2005).

Unless stated otherwise, our fiducial cosmology is based on the best fit results from Planck 2018 (Aghanim et al., 2020). In our analysis, we use COLOSSUS (Diemer, 2018) and `Astropy` (Robitaille et al., 2013; Price-Whelan et al., 2018) for cosmological calculations, `sklearn` (Scikit-learn, 2018) for the GP implementation, `emcee` (Foreman-Mackey et al., 2013) as our posterior sampler and `GetDist` (Lewis, 2019) to plot the final contours.

6.2   Lensing boost

6.2.1   Formalism

The value of the magnification μ for cosmological sources at various redshifts z is modeled by a probability function $P(\mu, z)$ which can be obtained numerically by performing ray-tracing simulations (e.g. Hilbert et al., 2007; Takahashi et al., 2011). To simplify the notation, here we call $P(\mu)$ what is sometimes called $\frac{dP}{d\mu}$ in the literature. This quantity measures the distribution of magnification for all possible images of a given source and due to conservation of photons/gravitons on average we have null magnification,

$$\langle \mu \rangle = \int d\mu \; \mu P(\mu, z) = 1. \tag{6.1}$$

More details about how this distribution should be interpreted are available in appendix A of Oguri (2018).

For this section, we will use a simplified model of $P(\mu, z)$, calculated as the sum of two components: weak and strong lensing. For the first, we assume a log-normal distribution for the convergence κ (as in, e.g. Taruya et al., 2002; Hada and Futamase, 2018) and derive the corresponding magnification probability density function using the relation:

$$\mu \simeq \frac{1}{(1 - \kappa)^2}. \tag{6.2}$$

While this relation for μ and κ is valid only in the limit of null shear $|\gamma| = 0$, it has been shown to accurately reproduce the weak lensing component of the magnification distribution (Takahashi et al., 2011), where $\kappa \lesssim 1$. For the strong-lensing component, we do not assume any relation between $\mu, \kappa, |\gamma|$ and instead impose a power-law $P(\mu, z) \propto \mu^{-3}$ for $\mu > 1$, calibrated empirically using the lensing depths of Oguri (2018). Finally, to simulate the demagnification tail, we assume a constant value for $\mu < 1$. We point out that we do not consider sources with $z > 10$ in this work.

For EM sources, the source flux is amplified by a factor μ in the presence of magnification. If the redshift to the source is known and a cosmology is assumed, the result is a mismatch between the inferred luminosity ($\mathcal{L}$) and the intrinsic one ($\mathcal{L}_*$):

$$\frac{\mathcal{L}}{\mathcal{L}_*} = \mu. \tag{6.3}$$

If only the luminosity is known, then the result is a mismatch between the inferred and actual luminosity distance to the source:

$$D(z) = \frac{D(z_*)}{\sqrt{\mu}}, \tag{6.4}$$

where we call z and z_* the inferred redshift and the true one, respectively. We also refer to the corresponding luminosity distances as D and D_*. This case applies to

Supernovae type IA (SNIa), a category of transient events known as standard candles because they share the same intrinsic luminosity. The Jacobians of the transformations in Eqs. (6.3) and (6.4) are:

$$\frac{\partial \mathcal{L}_*}{\partial \mathcal{L}} = \frac{1}{\mu}, \tag{6.5}$$

and

$$\frac{\partial z_*}{\partial z} = \frac{D'(z)}{D'(z_*)} \sqrt{\mu}. \tag{6.6}$$

In the case of GWs, we limit ourselves to the inspiral phase of compact binary mergers. In this phase, the gravitational wave strain amplitude as a function of time, $h(t)$, carries information about the source's distance and the associated masses. The frequency evolution of the signal can be used to extract the redshifted chirp mass (an effective combination of the masses involved in the merger):

$$\dot{f} \propto \mathcal{M}(1 + z), \tag{6.7}$$

while the amplitude is connected to the inverse of the luminosity distance:

$$h(t) \propto \frac{A\left(\mathcal{M}(1 + z)\right)}{D(z)}, \tag{6.8}$$

where $A(-)$ is a function of the redshifted chirp mass alone. From this, it should be clear that both $\mathcal{M}$ and $D(z)$ can be extracted from the signal.

In the presence of magnification, the observed strain is multiplied by a factor $\sqrt{\mu}$, and the mismatch between the intrinsic properties $(z_*, \mathcal{M}_*)$ and the inferred ones $(z, \mathcal{M})$ is such that

$$D(z) = \frac{D(z_*)}{\sqrt{\mu}}, \tag{6.9}$$

and

$$\mathcal{M} = \mathcal{M}_* \frac{1 + z_*}{1 + z}. \tag{6.10}$$

For $\mu > 1$ this implies that distant events are assumed to be closer and more massive than they actually are, just like magnified electromagnetic sources are assumed brighter. An essential difference between the two, however, is that the dependence on magnification is significantly weaker for the GW merger parameter $\mathcal{M}$ compared to the luminosity $\mathcal{L}$,

$$\frac{\mathcal{M}}{\mathcal{M}_*} = \frac{1 + z_*}{1 + z} \propto \mu^{s(z)}, \tag{6.11}$$

with $s(z) < 0.5$ for any $z < z_*$ and $s(z) \to 0.5$ for increasing z. This can be easily shown by combining Eq. (6.9) and (6.10), together with the fact that the luminosity distance can be expressed, in a flat background, as the product of $(1 + z)$ and a strictly increasing function of z (comoving distance).

To conclude this section, it is useful to point out that the Jacobian of the transformation $(\mathcal{M}, z) \leftrightarrow (\mathcal{M}_*, z_*)$ can be written as

$$\frac{\partial \mathcal{M}_*}{\partial \mathcal{M}} \frac{\partial z_*}{\partial z} = \frac{D'(z)}{D'(z_*)} \frac{1+z}{1+z_*} \sqrt{\mu}. \tag{6.12}$$

Rates

We write the observed rate of merger events per unit redshift and unit chirp mass as:

$$r^{(GW)}(\mathcal{M}, z) = \frac{R(\mathcal{M}, z)}{1+z} \mathcal{E}_L^{(GW)}(\mathcal{M}, z), \tag{6.13}$$

where R is the intrinsic rate in the source frame, and $\mathcal{E}_L$ the lensing boost. Here, we separate the rate into two components:

$$R(\mathcal{M}, z) = R(\mathcal{M})R(z), \tag{6.14}$$

and, for the redshift-dependent part, we assume a rate which is proportional to the product of the comoving volume boosted by a factor $(1+z)^\beta$:

$$R(z) \propto \frac{dV_c}{dz}(1+z)^\beta \propto \frac{d_L^2(z)}{E(z)}(1+z)^{\beta-2}, \tag{6.15}$$

where we use a standard ΛCDM cosmology with $E(z) = \sqrt{0.3(1+z)^3 + 0.7}$. This power-law behavior is expected if the merger rate of compact binary objects traces the star formation history (Madau et al., 1998) at low redshift (Dominik et al., 2013). In this toy model, we also invert the sign of the power-law index $\beta = 2.3$ at $z = 2$, in order to simulate a peak in the star formation rate.

Similar expressions can also be written for the rates of SNIa and the number counts of quasars:

$$r^{(SN)}(z) = \frac{R(z)}{1+z} \mathcal{E}_L^{(SN)}(z), \tag{6.16}$$

$$n^{(Q)}(\mathcal{L}, z) = N(\mathcal{L})\mathcal{E}_L^{(Q)}(\mathcal{L}, z). \tag{6.17}$$

Even though we assume that the intrinsic luminosity function of quasars $N(\mathcal{L})$ is not redshift dependent, lensing effects introduce this dependence in the observed $n(\mathcal{L}, z)$. The lensing boost factors can then be written as:

$$\mathcal{E}_L^{(GW)} = \int d(\mathcal{M}_*/\mathcal{M}) \frac{R(\mathcal{M}_*)}{R(\mathcal{M})} W^{(GW)}(\mathcal{M}_*/\mathcal{M}, z), \tag{6.18}$$

$$\mathcal{E}_L^{(SN)} = \int dD_* \frac{R(z_*)}{R(z)} W^{(SN)}(D_*/D, z), \tag{6.19}$$

$$\mathcal{E}_L^{(Q)} = \int d\log_{10}\left(\mathcal{L}_*/\mathcal{L}\right) \; \frac{N(\mathcal{L}_*)}{N(\mathcal{L})} W^{(Q)}(\mathcal{L}_*/\mathcal{L}, z), \tag{6.20}$$

where we have introduced the weight functions W^X, quantifying the contribution to the observed rates at z, $\mathcal{M}$, $\mathcal{L}$ from lensed events. These weight functions can be written as the product of the following terms.

- A lensing term. For each z_*, $\mathcal{M}_*$ and $\mathcal{L}_*$, there is an associated lensing probability. For GW and SN, this is $P(\mu, z_*)$ because the measured redshift z, inferred from the luminosity distance, is different from the source redshift z_*. This probability is $P(\mu, z)$ for the Q case because it is measured directly. For $\mu > 3$, we have $P(\mu, z_*) > P(\mu, z)$, meaning that we expect strong lensing to be particularly efficient for standard candles/sirens. Furthermore, because the expressions above are not written as integrals in μ, this term also contains a probability volume, e.g. $d\mu/dz_*$ for the SN case.

- A comoving volume term for the GW and SN cases. This is due to our assumption that $R(z) \propto dV_c$. Because lensing introduces contributions from a redshift range different from the observed z, a term $dV_c(z_*)/dV_c(z)$ is present.

- A redshift evolution term for SN and GW. Similar to the previous case, except due to the assumed power-law dependence of $R(z)$. This term also accounts for the different redshifted rates and is equal to $\left(\frac{1+z_*}{1+z}\right)^{\beta-1}$.

- A Jacobian term. As introduced in the previous section, the lensing transformation from intrinsic to observed quantities introduces an additional Jacobian factor.

In the next section, we study the impact of lensing magnification on the inferred chirp mass and redshift values and compare these results to the EM cases. We will work with the arguments of the integrals written above and, for ease of readability, we will also normalize these functions w.r.t. their value at null magnification ($\mu = 1$). In particular, we chose not to focus extensively on the results of the integral $\mathcal{E}_L^{(GW)}$, since it strongly depends on the assumed mass function $R(\mathcal{M})$. For accurate rates, we refer the reader to previous works (e.g. Dai et al., 2017; Oguri, 2018; Broadhurst et al., 2018; Ng et al., 2018).
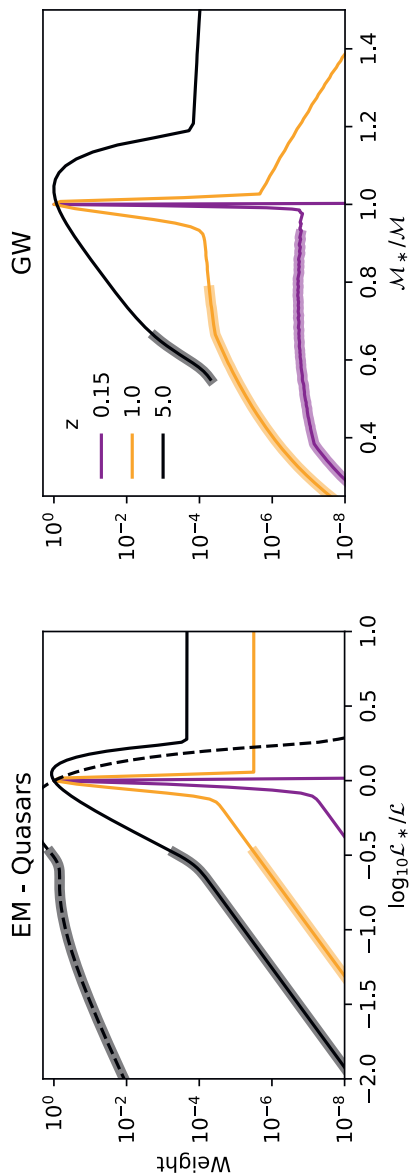
Figure 6.1: Relative contribution to the observed counts of transient GW events with chip-mass $\mathcal{M}$ or permanent EM sources with luminosity $\mathcal{L}$ by events with different intrinsic properties ($\mathcal{M}_*$ or $\mathcal{L}_*$). The observed redshift z is equal to the intrinsic one for the EM case. The filled lines assume a flat mass/luminosity function ($\mu > 3$ for the thick lines), while the dashed line corresponds to the weights for an observed luminosity located well past the knee of a Schechter luminosity function ($\mathcal{L}/\mathcal{L}_0 = 10$). For non-flat distributions, the relative contribution is the mass (or luminosity) function multiplied by these weights. see Eqs. (6.18) and (6.20).

6.2.2   Observational consequences

Weight functions

On the right side of Fig. 6.1, we plot the contribution of different intrinsic chirp masses to the integral in Eq. (6.18), while on the left-side we plot the equivalent result for light. These functions correspond to $W^{(GW)}$ and $W^{(Q)}$.

The first obvious conclusion is that magnification affects the inferred rates of GW mergers more efficiently than EM sources at both high and low redshift. This is mainly because GW lensing gives access to a broader volume at higher redshift, corresponding to a higher Jacobian factor and significantly stronger lensing probabilities. These effects are the main discriminant between the two cases and are dominant at low redshift.

We note, however, that the GW weights are still low. If we focus on a LIGO-like source ($z \sim 0.15$), we see that, to have rates at mass $\mathcal{M}$ dominated by events at $\mathcal{M}_* \sim \mathcal{M}/3$, the mass function $R(\mathcal{M})$ should span roughly 7 orders of magnitude between $\mathcal{M}_*$ and $\mathcal{M}$. While this is possible, we point out that this roughly corresponds to a doubly-exponential tail, with

$$R(M) \propto e^{-e^{\mathcal{M}/\mathcal{M}_0}} \tag{6.21}$$

and $\mathcal{M}_0 = \mathcal{M}_*$. This conclusion is mostly independent of our assumed mild redshift evolution.

Despite the lower lensing weights for the EM case, we also show that a typical Schechter function $N(\mathcal{L}) \propto \exp(-\mathcal{L}/\mathcal{L}_*)/\mathcal{L}$ (Schechter, 1976) is able to introduce a significant contribution from highly magnified sources at high z.

Lensing tail

In Fig. 6.2 we show the expected lensing tail of a truncated power-law distribution $R(\mathcal{M}) \propto \mathcal{M}^{-n}$ for a few choices of n. Events measured with a chirp-mass larger than the cut-off value $\mathcal{M} > \mathcal{M}_{\text{co}}$ must be magnified mergers with intrinsic redshift $z_* > z$ and intrinsic chirp-mass $\mathcal{M}_* < \mathcal{M}$.

The prominence of this tail for a steep mass function (large n) and low redshift z explains why a source distribution can be designed to produce a large number of lensed events (Broadhurst et al., 2018). It is useful to stress here that the main reason behind this is not the larger volume available to be lensed, but the fact that higher redshift events contributing to the low redshift rates are both more likely to be lensed and are also *necessarily* located on a more abundant portion of the mass function. This is because the mapping $(\mathcal{M}, z) \leftrightarrow (\mathcal{M}_*, z_*)$ depends only on μ. Despite the main advantage of amplifying the lensing tail compared to the naive expectation, this mechanism has the drawback of being efficient only for events with low z. For example, the shape of the $z = 5$ lensing tail is less sensitive to the details of the mass function.
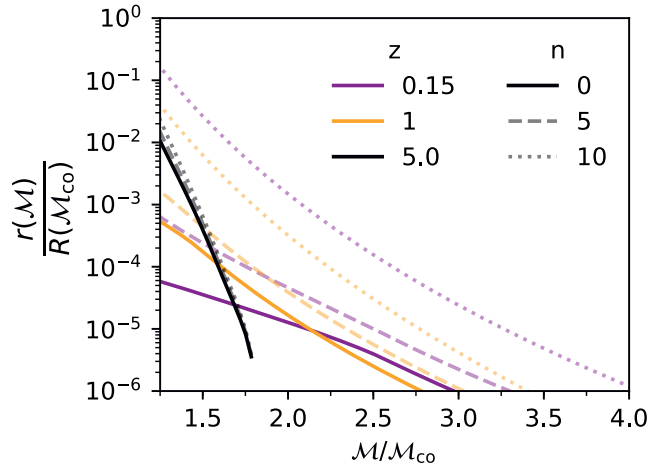
Figure 6.2: The shape of the lensing tail for truncated power-law distributions. The figure shows the observed rate $r(\mathcal{M})$ for an intrinsic chirp-mass function $R(\mathcal{M}) \propto \mathcal{M}^{-n}$ truncated at $\mathcal{M}_{\rm co}$. The observed rate for $\mathcal{M} > \mathcal{M}_{\rm co}$ must therefore be due to lensed events. The dependence on n is more striking for low inferred redshifts z due to how the intrinsic chip masses are distributed in the volume at $z_* > z$. See Section 6.2.2 for more details.

Here we do not assume a lower limit for the values $\mathcal{M}_*$, and the integrals are truncated because we impose $z_* < 10$. While this choice is unrealistic, it is possible to verify that setting a lower limit $\mathcal{M}_* > 5\,\mathrm{M}_\odot$ (1) does not affect the quantitative results of Fig. 6.2 for $n < 10$ and $\mathcal{M} > 20\,\mathrm{M}_\odot$, and (2) has no impact on the qualitative results discussed in this section for all values of n.

Luminosity distance

Another consequence of the dependence of the observed mass $\mathcal{M}$ on the magnification μ is the broadness of the peak in Fig. 6.1. The standard deviation of this distribution can be interpreted as an uncertainty in the measured $\mathcal{M}$, and, for an individual event, it can be pretty substantial: its value grows from 1 to about 7 percent between $z = 1$ and $z = 5$. The primary source of this scatter is the convergence distribution discussed in Section 6.2.1, and it is not particularly affected by our chosen source redshift dependence $R(z)$. For a flat mass function, no significant bias is observed in this redshift range, meaning that the contributors to an event of observed chirp mass $\mathcal{M}$ and redshift z are expected to have, on average, the same intrinsic properties.

This scatter also introduces an intrinsic error on the luminosity distance estimate to a source. For a flat mass function, we find a spread of 2.5 percent at $z = 0.15$ and 10 percent at redshift $z = 5$, which is consistent with results from previous works (e.g. Holz and Linder, 2005; Kocsis et al., 2006; Sathyaprakash et al., 2010; Oguri, 2016). However, this value should be compared to the present-day observational uncertainty in $D(z)$ of about 25 percent, dominated by the poorly constrained detector efficiency.

One can also find that in the presence of a steep mass function, the inferred $D(z)$ is substantially more biased compared to the inferred $\mathcal{M}$. This is because D_* and $\mathcal{M}_*$ scale differently with μ (Eq. 6.9 and 6.11).

6.2.3   Comparison to observations

LIGO-Virgo is expected to reach its design sensitivity in a few years. The expected statistical sample of mergers, made of hundreds or thousands of events, will allow a complete reconstruction of the chirp mass distribution of the underlying populations. If the intrinsic distribution is extremely peaked, the observed one might be contaminated by highly lensed events with biased luminosity distances and chirp masses. However, not only this scenario is in conflict with the expectation from current stellar evolution models (see e.g. Belczynski et al., 2016, 2017), but we have shown here that this would leave an easily recognizable signature in the LIGO rates due to (1) the wide range of probed masses at low redshift (Martynov et al., 2016) and (2) the flatness and low values of the lensing efficiency as a function of chirp mass (see Fig. 6.1).

As an example, the contribution to mergers with an observed $\mathcal{M} \sim 30\,M_\odot$ and $z \sim 0.15 - 1$ ($D \sim 700 - 1000$ Mpc) from events with lower $\mathcal{M}$ is suppressed by a factor $\sim 10^6 - 10^4$. No matter how these lensed events are distributed in intrinsic

chirp mass, the non-lensed events with similar properties should be both abundant and isolated from the highly suppressed lensing tail. Note that these properties roughly correspond to the 12 mergers detected during the first and second observing run of LIGO-Virgo (Abbott et al., 2019). This implies that the absence of a larger number of events at $\mathcal{M} < 10 \, \mathrm{M}_\odot$ (to which the detector is sensitive) suggests that the observed events are not lensed.

6.3   The astrophysical background

6.3.1   Formalism

Autocorrelation

In this section, we discuss the autocorrelation signal of the anisotropic GWB. This signal and the shot-noise contamination have been extensively studied in previous works (Jenkins, Alexander C. and Sakellariadou, Mairi, 2019; Jenkins et al., 2019a; Cusin et al., 2019). Here, we review the main modeling aspects and describe some particularities.

Our starting point is the definition of the dimensionless energy density of GWs per unit solid angle from a given direction of the sky $\hat{\mathbf{r}}$. We model this signal as

$$\Omega_{\mathrm{GW}}(\hat{\mathbf{r}}) \equiv \int dr \, r^2 \mathcal{K}(r) n(\vec{\mathbf{r}}), \qquad (6.22)$$

where $n(\vec{\mathbf{r}})$ is the galaxy density field in comoving coordinates $\vec{\mathbf{r}}$, and $\mathcal{K}$ is the GW kernel that encodes the average contribution of a galaxy to Ω_{GW} as a function of comoving distance r. In practice, this includes information about the star formation history of the Universe and the properties of the emitting binary population. It is instructive to rewrite Eq. (6.22) in terms of the galaxy overdensity $\delta_{\mathrm{g}}(\vec{\mathbf{r}}) \equiv n(\vec{\mathbf{r}})/\bar{n}(r) - 1$, with $\bar{n}(r)$ being the average number density of galaxies, defined as $\bar{n}(r) \equiv \int \mathrm{d}^2 \hat{\mathbf{r}} n(\vec{\mathbf{r}})/4\pi$. With this notation we have

$$\Omega_{\mathrm{GW}}(\hat{\mathbf{r}}) = \int dr \, r^2 \mathcal{K}(r) \bar{n}(r) \left(\delta_{\mathrm{g}}(\vec{\mathbf{r}}) + 1 \right). \qquad (6.23)$$

From this point, the angular power spectrum of the anisotropic GWB C_ℓ^{GW} can be calculated to be

$$C_\ell^{\mathrm{GW}} = 4\pi \int_{k_{\mathrm{min}}}^{k_{\mathrm{max}}} \frac{dk}{k} |\delta \Omega_\ell|^2 \mathcal{P}(k) + B_\ell^{\mathrm{GW}}. \qquad (6.24)$$

Here $\delta \Omega_\ell(k)$ is given by

$$\delta \Omega_\ell(k) = \int dr \, r^2 \mathcal{K}(r) \bar{n}(r) T_g(k, r) j_\ell(kr), \qquad (6.25)$$

where T_g is the synchronous gauge transfer function relating the galaxy power spectrum to the primordial one $\mathcal{P}(k) = A_s \, (k/k_*)^{n_s - 1}$, and j_ℓ is the spherical Bessel function of order ℓ. Note that the galaxy bias is implicitly absorbed in T_g. Note also that in Eq. (6.25) we neglect relativistic corrections, as they are generally found to be below cosmic variance (Bertacca et al., 2019).

The term B_ℓ^{GW} in the power spectrum is the shot-noise bias term introduced by the spatial and temporal shot-noise in the distribution of the individual events forming the GWB. Following Jenkins, Alexander C. and Sakellariadou, Mairi (2019), we write the shot-noise contribution in the kHz band as

$$B_\ell^{\mathrm{GW}} = \int dr \; \mathcal{K}^2(r)\bar{n}(r)r^2 \left[1 + \frac{1 + z(r)}{R(r)T_O}\right]. \tag{6.26}$$

Because of the low event rate in this frequency range, this noise contribution is inversely proportional to the average number of events per galaxy, written as the average redshifted event rate $R(r)/(1+z)$ multiplied by the observing time T_O. However, because the duration of the inspiral phase in the mHz band is much larger than any reasonable observing time, the contribution of the term $1/(R(r)T_0)$ is negligible in this case.

The GWB discussed here is an integrated signal. Because of this, the low-redshift objects might significantly contribute to the GWB. Indeed, the astrophysical models of Cusin et al. (2019) suggest that the combination

$$\tilde{\mathcal{K}}(r) = \mathcal{K}(r)\bar{n}(r)r^2 \tag{6.27}$$

is not decaying to negligible values close to redshifts $z \sim 0$. This introduces two complications in the modelling.

The first is connected to the shot noise. To highlight this, we rewrite Eq. (6.26) as

$$B_\ell^{\mathrm{GW}} = \int dr \; \frac{\tilde{\mathcal{K}}^2(r)}{\bar{n}(r)r^2} \left[1 + \frac{1 + z(r)}{R(r)T_O}\right]. \tag{6.28}$$

This expression shows that the shot-noise has a divergent expression due to low-redshift (low-r) contributions. This divergence can be suppressed if local events are excluded from the background to obtain a well-behaved prediction for the autocorrelation signal. This is equivalent to setting a lower limit in the integral above different from zero.

Second, there is a complication derived from the scale-dependent part of the angular power spectrum (the first term in Eq. (6.24)), which is expected to receive non-negligible contributions from small, highly non-linear scales. To get some intuition about this feature, let us simplify our expression for the GWB angular power spectrum by using the so-called Limber approximation

$$j_\ell(x) \to \sqrt{\frac{\pi}{2\alpha}}\delta_{\mathrm{D}}\left(\alpha - x\right), \tag{6.29}$$

where δ_{D} is the Dirac delta-function and $\alpha \equiv \ell + 1/2$. Using this in Eq. (6.25) and neglecting the bias term we obtain

$$C_\ell^{\mathrm{GW}} \approx \frac{2\pi^2}{\alpha} \int_{k_{\min}}^{k_{\max}} \frac{\mathrm{d}k}{k^3} \tilde{\mathcal{K}}^2 \left(\frac{\alpha}{k} \right) \mathcal{S}^2 \left(k, \frac{\alpha}{k} \right), \tag{6.30}$$

$$\mathcal{S}(k, r) \equiv T_g(k, r)\mathcal{P}(k)^{1/2}. \tag{6.31}$$

What Eq. (6.30) demonstrates is that $\tilde{\mathcal{K}}(r)$ acts as a modified kernel and selects a particular domain in the k-integral. This causes small scales to contribute significantly to C_ℓ^{GW}, unless $\tilde{\mathcal{K}}$ is vanishing at the lower end of its argument or $\tilde{\mathcal{S}}^2/k^3$ is falling fast enough at large values of k. As the modeling of the galaxy power spectrum at non-linear scales is highly uncertain, this feature signals a potential danger of using the autocorrelation signal as a probe of the GW merger history or cosmology.

Cross-correlation with galaxy clustering

This subsection introduces the main concepts necessary for modeling the cross-correlation signal and discusses its advantages. First of all, we define the observed overdensity of galaxies in the given direction $\hat{\mathbf{r}}$ per unit sold angle as

$$\Delta(\hat{\mathbf{r}}) = \int dr \; W_i(r)\delta_g(\vec{\mathbf{r}}), \tag{6.32}$$

where $W_i(r)$ is the probability density function of the galaxies' comoving distances (also referred to as the *window function*) and $\delta_g(\vec{\mathbf{r}})$ is the galaxy overdensity defined earlier. Using Eq. (6.32), the angular power spectrum of this field, C_ℓ^{GC}, can be shown to be

$$C_\ell^{\mathrm{GC}} = 4\pi \int \frac{dk}{k} |\Delta_\ell(k)|^2 \mathcal{P}(k) + \frac{1}{n_i}, \tag{6.33}$$

where $\Delta_\ell(k)$ is given by

$$\Delta_\ell(k) = \int dr \; W_i(r)T_i(k, r)j_\ell(kr). \tag{6.34}$$

$T_i(k, r)$ is the transfer function for the galaxy overdensity in the selected redshift range $W_i(r)$, $j_\ell(kr)$ is the spherical Bessel function of order ℓ and n_i is the average number of galaxies per steradian, also dependent on the specific redshift selection $W_i(r)$. This final quantity appears in the second term in Eq. (6.33) and dictates the size of the shot-noise component of the power spectrum. In total, the spectrum C_ℓ^{GC} as a function of scale ℓ is also sometimes referred to as the galaxy clustering (GC) angular power spectrum.

Using Eqs. (6.25) and (6.34), one can derive the angular power spectrum of the cross-correlation $C_\ell^\times$ of the GWB and the GC maps, given by Eq. (6.22) and (6.32). This is

$$C_\ell^\times = 4\pi \int \frac{dk}{k}\, \delta\Omega_\ell^*(k)\Delta_\ell(k)\mathcal{P}(k) + B_\ell, \tag{6.35}$$

where the shot-noise contribution B_ℓ, derived in Appendix 6A, can be shown to be

$$B_\ell = \int dr\, W_i(r)\mathcal{K}(r). \tag{6.36}$$

With these expressions in mind, we can now discuss how the cross-correlation signal can address the modeling challenges presented in the previous section.

To address the first one, we notice that, while the $1/r^2$ divergence is still present in the integral in Eq. (6.36), this integral is generally well behaved if the window function $W_i(r)$ decays fast enough at small redshifts. Notice that this is impossible to do in the equivalent expression for the autocorrelation in Eq. (6.26).

With respect to the second issue related to the small-scale dependence of the signal, we write the equivalent of Eq. (6.30) for the cross-correlation,

$$C_\ell^\times \approx \frac{2\pi^2}{\alpha} \int_{k_{\min}}^{k_{\max}} \frac{\mathrm{d}k}{k^3} W_i\left(\frac{\alpha}{k}\right) \tilde{\mathcal{K}}\left(\frac{\alpha}{k}\right) \mathcal{S}^2\left(k, \frac{\alpha}{k}\right). \tag{6.37}$$

Because GC surveys allow for redshift-selection of the sources, the GC window function $W_i(r)$ can be taken to be peaked at some non-zero redshift and quickly decaying for larger or smaller values of r. Eq. (6.37) proves that this behavior cuts off the contribution from very large and very small scales.

6.3.2 Forecast

Model set-up

In this section, our primary goal is to explore the sensitivity of the cross-correlation signal to various parameters and estimate its information content. To this end, we model the signal using simple but representative assumptions about the GW and GC maps. This allows us to derive an upper limit on the constraining power by assuming the minimum theoretical uncertainty due to cosmic variance.

We base our model for $\tilde{\mathcal{K}}(r)$ on the physically motivated one of Cusin et al. (2019), by noting that their function $\mathcal{A}(z)$ is the analogue of our $\tilde{\mathcal{K}}(r)$ in redshift space. In this reference, in particular, it is shown that $\mathcal{A}(r)$ is a slowly-evolving function of redshift and has a similar shape over a wide range of frequencies and assumptions about the source population (see their figures 19 and 13). Thus, we model the kernel as

$$\mathcal{K}(r) = \frac{\mathcal{K}_0}{2\bar{n}(r)r^2} \left\{\tanh\left[10(z_*(r) - z(r))\right] + 1\right\}, \tag{6.38}$$

where $\mathcal{K}_0$ is the amplitude of the kernel, z_* is a cut-off redshift, and $\bar{n}(r) \approx 10^{-1}$ Mpc^{-3} is the average comoving galaxy number density estimated using Figure 4 of Schaye et al. (2015). We do not implement a redshift dependence for this quantity because its value is relevant only for the shot-noise component of the cross-correlation, found to be negligible in the cases considered here. In our fiducial model, we assume $z_* = 1$ as the astrophysical kernel $\mathcal{K}(r)\bar{n}(r)r^2$ is expected to decay around that value in redshift. Notice that, while $\mathcal{K}_0$ should be dimensionful, its units are irrelevant to us because the cross-correlation signal is proportional to its value. For the rest of the section, we call $\mathcal{K}_0^{\mathrm{fid}}$ the fiducial value of this quantity.

In the next subsections, we study the cross-correlation between the GWB modeled above and two galaxy catalogs centered at different redshifts. The two window functions, W_1 and W_2, are assumed to be Gaussian distributions centered at $\bar{z} = \{0.5, 1.5\}$ and with widths of $\sigma_z = \{0.18, 0.6\}$. These values are picked so that the two selections overlap with the constant portions of $\tilde{\mathcal{K}}(r)$.

Moreover, we model the transfer functions in Eqs. (6.34) and (6.25) by using a linear bias approximation (valid for large scales):

$$T_i(k) = b_i T_{\mathrm{m}}(k, r), \tag{6.39}$$

and

$$T_g(k, r) = b_{\mathrm{GW}} T_{\mathrm{m}}(k, r), \tag{6.40}$$

where $T_{\mathrm{m}}(k, r)$ is the transfer function for cold dark matter, and the b_X are known as bias parameters. When varying our model, we freeze the bias of both galaxy catalogs since it can be extracted from their clustering autocorrelation signal alone. On the contrary, we treat the GW bias b_{GW} as a free parameter, and we assume it to be a constant over redshift. While this is not necessarily true, in the absence of shot-noise, only the combination $b_{\mathrm{GW}}\tilde{\mathcal{K}}(r)$ appears in the signal. This implies that a more complex model can always capture any redshift dependence through the function $\tilde{\mathcal{K}}(r)$. Note, however, that breaking the degeneracy between the linear bias of the GW population and the amplitude of the astrophysical kernel $\mathcal{K}(r)$ requires a full understanding of the GWB kernel and all ingredients (Scelfo et al., 2018b).

We focus on the mHz frequency band for the rest of the analysis and assume that low-redshift events (below $r = 150$ Mpc) can be filtered. As discussed in the previous sections, these assumptions are essential to obtain a well-behaved signal not overwhelmed by noise. For reference, under these assumptions, we get the following relative noise values at $\hat{\ell} = 10$:

$$\frac{B_{\hat{\ell}}^{\mathrm{GW}}}{C_{\hat{\ell}}^{\mathrm{GW}}} \approx \frac{B_{\hat{\ell}}}{C_{\hat{\ell}}^{\times}} \approx 10^{-4}. \tag{6.41}$$

This value is derived using the inspiral time of a solar mass black hole binary starting

from 1 mHz (Blanchet et al., 1995), an observing time of 1 year and a merger rate of 10^{-5} per year.

The codes used in this section are made publicly available on https://github.com/valerivardanyan/GW-GC-CrossCorr. To calculate the matter power-spectra we use the ΛCDM limit of EFTCAMB (Hu et al., 2014; Raveri et al., 2014).

Constraining $\mathcal{K}(r)$

The main goal of this section is to understand the constraining power of the cross-correlation signal by studying how precisely the astrophysical model can be inferred from a noisy C_ℓ measurement.

In our analysis, we focus on the best-case scenario of cosmic-variance limited uncertainties as derived in Appendix 6B and use a simple proxy for the overall signal-to-noise ratio of the cross-correlation, defined as

$$\left(\frac{S}{N}\right)^2 \equiv \sum_{\ell=\ell_{\min}}^{\ell_{\max}} \frac{\left(C_\ell^\times\right)^2}{\mathrm{Var}C_\ell^\times}. \tag{6.42}$$

Let us note that in our setup, the GC signal dominates over the GC shot noise, implying that Eq. (6.42) is indeed the theoretical limit for uncertainties. In the presence of multiple, independent window functions, we simply sum the relative signal-to-noise expressions in quadrature.

We compute the cross-correlation power spectra, given in Eq. (6.35), using the model presented in Section 6.3.2, and attempt to recover the model parameters from a noisy realization. To explore the inferred constraints as a function of angular resolution and S/N levels, we do this in several multipole ranges of ℓ with $\ell_{\min} = 2$ and varying $\ell_{\max}$.

The parameters of interest in our analysis are the amplitude of the GWB kernel $\mathcal{K}_0$ and the turnover redshift z_*. In addition to these, we also explore the bias b_{GW} and Ω_{m} to see if variations in $T_g(k, r)$ can affect the inferred $\mathcal{K}(r)$, and to explore the possible degeneracies between the GWB model and cosmology. To include the effects of varying Ω_{m} we have precomputed the dark matter transfer functions for a grid of Ω_{m} values and have inferred the results for the intermediate values through nearest-neighbor interpolation. We have employed a Gaussian likelihood function on C_ℓ with diagonal covariance matrix given through Eq. (6.77), and the prior ranges shown in Table 6.1. Note that since we expect $\mathcal{K}_0$ to be degenerate with b_{GW}, we do not vary $\mathcal{K}_0$ itself, but rather vary the combination $b_{\mathrm{GW}}\mathcal{K}_0$.

The main results of the analysis are summarised in Fig. 6.3, where we show the expected constraints on the parameters of interest as a function of the maximum multipole included in the analysis. We also offer the corresponding cosmic-variance-only signal-to-noise ratios.
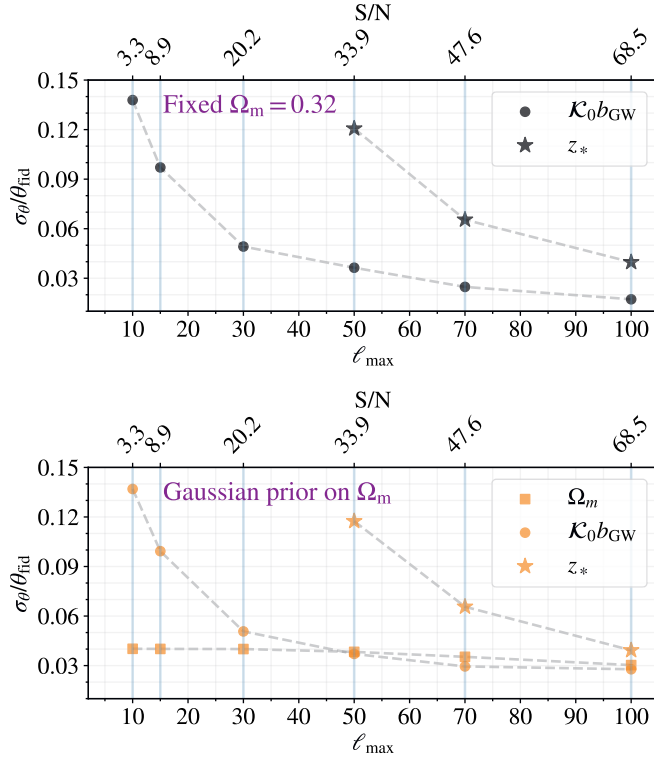
Figure 6.3: Constraints on the GWB parameters ($b_{GW}\mathcal{K}_0, z_*$) and cosmology (Ω_m) obtained using the cross-correlation signal with two window functions as a function of the maximum multipole included in the analysis. Cosmic-variance limited measurements are assumed for all the constraints, so these should be understood as the best-case scenario results. Larger values of the signal-to-noise ratio (S/N) correspond to better angular resolution (see Eq. 6.42). We have explored the effect of Ω_m on these constraints by either fixing its value (***top panel***), or setting a Planck-2018-like Gaussian prior (***bottom panel***). Remarkably, the combination $b_{GW}\mathcal{K}_0$ can be constrained even with very limited angular sensitivity. The turnover location z_* is practically unconstrained for $\ell_{max} \lesssim 50$, and Ω_m is prior dominated for these multipoles. In case of $\ell_{max} \gtrsim 50$ all the relevant parameters are tightly constrained, and for $\ell_{max} \sim 100$ the constraints are at the level of a few percent. Notably, the cosmology (mimicked by varying Ω_m in our analysis) can match and surpass the CMB results only in case of high angular resolution/signal-to-noise. For reference, $\ell_{max} = 100$ roughly corresponds to 2 degrees.

Parameter	Fiducial value	Prior
$b_{\mathrm{GW}}\mathcal{K}_0$	1	$[0.01, 100]$
b_{GW}	1	$[0.1, 10]$
z_*	1	$[0.5, 1.5]$
Ω_{m}	0.32	$\mathcal{G}(0.32, 0.013)$

Table 6.1: Prior ranges of the sampled parameters. For Ω_{m} we use a Planck-2018 inspired Gaussian prior.

Let us first have a look at the top panel of the figure, which corresponds to a fixed Ω_{m} value. As we see, $b_{\mathrm{GW}}\mathcal{K}_0$ is constrained and, notably, this is true even in the limited multipole range corresponding to $\ell_{\mathrm{max}} = 10$. This is expected, as a clear signal detection is associated with a measurement of its amplitude. On the other hand, less encouraging are the results for the turnover redshift z_*, which can be constrained only for $\ell_{\mathrm{max}} \gtrsim 50$ or, equivalently, an S/N of ~ 33. In the bottom panel of the figure, we now impose a Gaussian prior on Ω_{m}, with its variance being comparable to the Planck-2018 constraint on Ω_{m}. While the z_* results are not affected, the uncertainties on the amplitude are now slightly inflated due to a degeneracy between Ω_{m} and $b_{\mathrm{GW}}\mathcal{K}_0$.

Let us now fully concentrate on the two limiting angular sensitivities in our analysis. The turn-over redshift z_* is unconstrained for the low-resolution case, while it is tightly constrained for the case of $\ell_{\mathrm{max}} = 100$. The dark matter abundance Ω_{m} is prior dominated for the low-resolution case, while it beats the prior in the high-resolution scenario.

Before turning to the next section, we want to mention that the results presented in this section depend on the precise details of the GC window functions and GWB detection, and more accurate results can only be obtained by performing a realistic forecast with exact survey/detector specifications. While we leave a more detailed investigation for future research, our results suggest that a cosmic-variance limited measurement of the GWB anisotropies down to $\ell \sim 100$ can tightly constrain the redshift evolution of the GW kernel $\tilde{\mathcal{K}}$.

6.4   Resolved events

6.4.1   Formalism

Gravitational wave propagation

In GR, the amplitude of GWs on top of Friedmann-Lemaitre-Robertson-Walker (FLRW) background evolves according to

$$h''_\alpha + 2\mathcal{H}h'_\alpha - \vec{\nabla}^2 h_\alpha = 0, \tag{6.43}$$

where h_α denotes the amplitude of either polarization ($\alpha \in [\times, +]$), primes denote derivatives with respect to the conformal time, and $\mathcal{H}$ is the conformal Hubble function. In this equation, the prefactor of the Laplacian term controls the propagation speed, which we have set to coincide with the speed of light in $c = 1$ units.

The second term is the standard cosmic friction term and its impact, combined with conservation of gravitons, causes the strain amplitude to decay as $h_\alpha(z) \propto D_{\mathrm{L}}^{-1}(z)$, with D_L being the FLRW luminosity distance:

$$D_{\mathrm{L}}(z) = (1+z) \int_0^z \frac{\mathrm{d}\tilde{z}}{H(\tilde{z})}, \qquad (6.44)$$

where the Hubble function $H(z)$ is given in terms of the Hubble constant H_0, present-day dark matter abundance Ω_{m} and dark energy abundance $\Omega_{\mathrm{DE}}(z)$ as

$$H(z) = H_0 \left[\Omega_m (1+z)^3 + \Omega_{DE}(z) \right]. \qquad (6.45)$$

Throughout this section we assume a constant equation of state w_0 for dark energy, such that its energy density is given by

$$\Omega_{DE}(z) = (1 - \Omega_{\mathrm{m}})(1+z)^{3(1+w_0)}. \qquad (6.46)$$

The standard ΛCDM cosmology corresponds to $w_0 = -1$.

It is now established that modifications of GR can affect the propagation of GWs. The important effect for us is the modified friction term with respect to the GR expectation in Equation (6.43),

$$h_\alpha'' + [2 + \alpha_M(z)] \mathcal{H} h_\alpha' - \vec{\nabla}^2 h_\alpha = 0, \qquad (6.47)$$

where we have introduced an additional function α_M modelling this change. Once again, we imposed the GW speed to be unity as suggested by observations. The modified friction term introduces a new scaling $h_\alpha(z) \propto 1/D_{\mathrm{L,GW}}(z)$, with $D_{\mathrm{L,GW}}(z) \neq D_{\mathrm{L}}(z)$ for non-zero $\alpha_M(z)$. The luminosity distance to GW events can be written as:

$$\frac{D_{\mathrm{L,GW}}}{D_{\mathrm{L,EM}}}(z) = \exp \left\{ -\frac{1}{2} \int_0^z \mathrm{d}\tilde{z} \, \frac{\alpha_M(\tilde{z})}{(1+\tilde{z})} \right\}. \qquad (6.48)$$

In this work, we assume that the luminosity distance for EM sources $D_{\mathrm{L,EM}}$ is unaffected and is equal to the expression in Equation (6.44). The function α_M corresponds to the running of the effective Planck mass, i.e.,

$$\alpha_M = \frac{d \log(M_{\mathrm{eff}}/M_{\mathrm{P}})^2}{d \log a}, \qquad (6.49)$$

where M_{P} is the Planck mass and M_{eff} is its effective value at redshift $z = 1/a - 1$. This function encodes information about extensions of GR such as scalar-tensor theories

that predict the existence of a gravitational scalar degree of freedom non-minimally coupled to curvature (Horndeski, 1974; Bellini and Sawicki, 2014). This scalar degree of freedom can also propagate as a scalar wave. Still, its effects are expected to be suppressed on Earth, where local tests of gravity place tight constraints on deviations from GR (see e.g. Bertotti et al., 2003). However, notice that this restoration of the GR limit does not impact the effect discussed here, Eq. (6.48) is an integrated effect, and the impact of the local region of observation is minimal. More broadly, it should be noted that this modified friction term is also a natural prediction of quantum gravity (Calcagni et al., 2019) and non-local modifications of gravity (Dirian et al., 2016).

From an effective field theory point of view, $\alpha_M(z)$ is a free function of order unity. However, in practical studies of modified gravity and dark energy, α_M is often assumed to take simple parametric forms. The main guiding principle is the assumption that its effects should be negligible in the early universe, which prompts to choose $\alpha_M(z)$ to be proportional either to the dark energy abundance or simply to some power of the scale factor a.

Such parametrizations make it possible to find a closed form expression for the ratio in Equation (6.48) and have inspired a widely used parametrization of the ratio as a monotonic deviation which goes to 1 at present day (Belgacem et al., 2018)

$$\frac{D_{\mathrm{L,GW}}}{D_{\mathrm{L,EM}}}(z) = \Xi_0 + \frac{1 - \Xi_0}{(1 + z)^n}. \tag{6.50}$$

In this expression, Ξ_0 and n are two constant parameters typically ~ 1.

Angular power-spectra

We consider GW mergers with a distribution in redshift written as

$$n_{\mathrm{GW}}(z) = \frac{n_0}{1 + z}, \tag{6.51}$$

where n_0 corresponds to the comoving number density of observed events as a function of redshift, and the term $(1 + z)$ takes into account the cosmological time dilation. In our analysis for this section, we use a constant value of $n_0 \approx 3 \times 10^{-6}\ h^3\mathrm{Mpc}^{-3}$ (with h denoting here the usual normalized Hubble constant), motivated by current LIGO constraints (Abbott et al., 2020).

For a given selection of sources along the line of sight, the average number of projected sources can be written using the comoving distance $\chi(z)$:

$$\bar{n}_{\mathrm{gw}} = \int_0^\infty dz \frac{\chi^2(z)}{H(z)} S(z) n_{\mathrm{GW}}(z). \tag{6.52}$$

The function S encodes the selection, and the scatter due to observational errors. In this section, simple bins in a range $[D_{\mathrm{L,min}}, D_{\mathrm{L,max}}]$ are used and we assume a log-normal distribution with fixed scatter $\sigma_{\ln D}$ for the individual sources (Oguri, 2016). In

this case, S can be written as:

$$S(z) = \frac{1}{2} \left[x_{\min}(z) - x_{\max}(z) \right], \tag{6.53}$$

with

$$x_{\min}(z) = \mathrm{erfc} \left[\frac{\ln D_{\mathrm{L,min}} - \ln D_{\mathrm{L,GW}}(z)}{\sqrt{2}\sigma_{\ln D}} \right], \tag{6.54}$$

and similarly for $x_{\max}$. Including this effect makes S resemble a top-hat function with damping tails dictated by $\sigma_{\ln D}$.

The angular power spectrum of these sources can be written using the Limber approximation

$$C_{\mathrm{GW}}(\ell) = \int_0^\infty dz \, \frac{H(z)}{\chi^2(z)} W_{\mathrm{GW}}^2(z) b_{\mathrm{GW}}^2(z) P\left(\frac{\ell + 1/2}{\chi(z)}, z \right), \tag{6.55}$$

where $P(k, z)$ is the matter power-spectrum at redshift z and comoving scale k, b_{GW} is the bias of the GW sources, and the window function can be written as

$$W_{\mathrm{GW}}(z) = \frac{\chi^2(z)}{H(z)} \frac{n_{\mathrm{GW}}(z)}{\bar{n}_{\mathrm{GW}}} S(z). \tag{6.56}$$

For the purpose of illustration, we will make use of a few simple parametrization for the GW bias. We will consider either a constant bias b_{GW} with a value of order unity or a more complex form:

$$b_{\mathrm{GW}}(z) = b_0 \left(1 + \frac{1}{D(z)} \right), \tag{6.57}$$

where $D(z)$ represents the growth factor. The first model, with its low constant value, mimics a PBH origin for the mergers (Bird et al., 2016; Raccanelli et al., 2016), while the second mimics the stellar evolution case by tracking the galaxy linear bias (Oguri, 2016).

Similarly to the GW population, we again assume a constant comoving number density of galaxies. Throughout our analysis we fix

$$n_{\mathrm{gal}}(z) = 10^{-3} h^3 \mathrm{Mpc}^{-3}, \tag{6.58}$$

and we write the autocorrelation signal of galaxies under the Limber approximation as

$$C_{\mathrm{gal}}(\ell) = \int_0^\infty dz \, \frac{H(z)}{\chi(z)^2} W_{\mathrm{gal}}^2(z) b_{\mathrm{gal}}^2(z) P\left(\frac{\ell + 1/2}{\chi(z)}, z \right). \tag{6.59}$$

In this expression the definition of W_{gal} is the same as W_{GW} used in the previous section except for using $n_{\text{gal}}(z)$, a different selection function, and $b_{\text{gal}}(z)$ is the linear galaxy bias. In our analyses, we assume a known galaxy bias in the form of

$$b_{\text{gal}}(z) = 1 + \frac{1}{D(z)}. \tag{6.60}$$

In general, this function is expected to be accurately measured from the galaxy auto-correlation signal alone.

In this section, we employ a top-hat selection function for W_{gal}, which assumes no uncertainty in galaxy redshift estimates. This choice mimics a spectroscopic galaxy survey or a general redshift survey with negligible uncertainties. As an example, another choice commonly found in the literature is a Gaussian distribution $\mathcal{N}(z, \sigma_{\text{gal}})$, where σ_{gal} should be much larger than the expected redshift uncertainty for each galaxy.

By combining the distribution of GW sources and galaxies, one can construct a cross-correlation map. In our formalism, we write the cross-correlation between a GW bin i and a galaxy bin j (fully specified by their respective window functions) as:

$$C_\times^{ij}(\ell) = \int_0^\infty dz \frac{H(z)}{\chi^2(z)} W_{\text{GW}}^i(z) W_{\text{gal}}^j(z) \times b_{\text{GW}}(z) b_{\text{gal}}(z) P\left(\frac{\ell + 1/2}{\chi(z)}, z\right). \tag{6.61}$$

Note that this signal is different from the GWB cross-correlation of Eq. (6.35) from the previous section.

We conclude this subsection by pointing out that the power spectra in Equations (6.59), (6.55) and (6.61) do not include relativistic terms and do not capture the effects of evolution and lensing bias (see e.g. Scelfo et al., 2018a, 2020, for a detailed treatment). Specifically, while the lensing bias should be negligible compared to the luminosity distance uncertainties at the redshifts considered here (see Section 6.2), the same is not true for relativistic effects. Therefore, we choose not to consider small values of ℓ in the analysis of this section since the signal at these large angular scales is largely dictated by them.

Constraining the propagation

The primary goal of the subsection is to demonstrate how to reconstruct the properties of GW propagation and source clustering as a function of redshift. We show how to recover an assumed fiducial model using mock angular power spectra with cosmic-variance or shot-noise limited uncertainties.

Our methodology hinges on the fact that by cross-correlating a GW luminosity distance bin with multiple galaxy redshift bins, we can determine the redshift of the GW sources by matching the clustering properties of the two at the true redshift (Oguri, 2016; Bera et al., 2020).
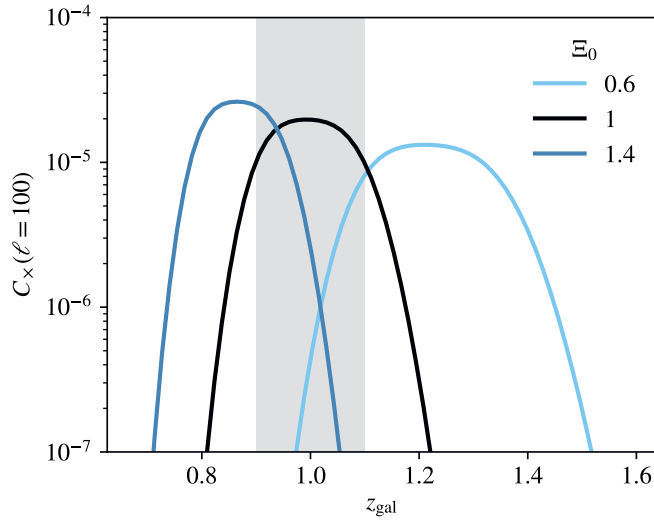
Figure 6.4: The cross-correlation signal between GW sources at $z = [0.9, 1.1]$ (shaded area) and galaxies at different redshifts (z_{gal}). If the luminosity distance ratio $D_{\mathrm{L,GW}}/D_{\mathrm{L,EM}}(z)$ in Equation (6.50) is different from its GR assumption ($\Xi_0 \neq 1$), the location of the predicted cross-correlation peak is also affected.

We demonstrate this idea in Figure 6.4, where we have considered GW sources located at redshift $[0.9, 1.1]$ in a GR cosmology where $D_{\mathrm{L,GW}}(z) = D_{\mathrm{L,EM}}(z)$. This figure shows the expected cross-correlation signal between the angular distribution of these sources and the angular distribution of galaxies located at various redshifts. As expected, in GR ($\Xi_0 = 1$), the signal peaks inside the correct redshift range (shaded area). However, as we depart from the GW luminosity distance relation, the location of this peak is affected.

6.4.2   Forecast

Model set-up

In this section, we describe the recipe used to generate the mock angular power spectra ($C_{\mathrm{gal}}, C_{\mathrm{GW}}$, and $C_{\times}$) that are fed into our reconstruction pipeline together with their error covariance matrix. These angular power-spectra are extracted from the autocorrelation and cross-correlation maps representing the sky distribution of galaxies and GW sources when describing actual data. The recipe has three main ingredients: the details of the fiducial model, a description of the instrumental configuration and a definition of the dominant source of error.

The first ingredient is the fiducial model. Our decision in this case is based on the results of Baker and Harrison (2021), where present-day constraints on the function α_M appearing in Equation (6.48) are presented. As shown in Belgacem et al. (2019), the results of the $\alpha_M \propto a$ parametrization found in that work can be mapped to the $\Xi(z)$ function in Equation (6.50). Using this transformation, we find that the 3σ upper limit roughly corresponds to

$$\Xi_0 \lesssim 1.4, \tag{6.62}$$

with $n = 1$. Thus, we assume a fiducial model with $\Xi_0^{\mathrm{fid}} = 1.4$ and $n^{\mathrm{fid}} = 1$, representing the limit of our present understanding.

The second ingredient of our forecast is the instrumental configurations. The size of our data vector is given by the number of multipoles ℓ and window functions that we include in our analysis. Since both are primarily dictated by observational considerations, in this work, we assume an optimistic combination of a network of three Einstein Telescopes (Maggiore et al., 2020b; Hall and Evans, 2019) capable of a log-scatter in measured $D_{\mathrm{L,GW}}$ of $\sigma_{\ln D} = 0.05$, and a high-z redshift survey with extensive sky coverage and negligible redshift uncertainties (such as, e.g., the Square Kilometer Array, Weltman et al., 2020).

The range of angular scales that we consider is limited by two factors. On small scales, large multipoles ($\ell > 100$) are excluded due to the angular resolution of about 1 degree expected for our GW detector configuration of choice (Hall and Evans, 2019). On large scales, we do not explore values of $\ell < 10$ because our modeling does not consider the relativistic effects dominating the signal at these scales. Nevertheless, we

Parameter	Prior
Node amplitudes	[0, 11] (Uniform)
Correlation length (L)	[1, 10] (Uniform)
Ω_m	1% (Gaussian)
h	1% (Gaussian)
w_0	5% (Gaussian)

Table 6.2: Summary of the priors imposed before reconstructing $b_{\mathrm{GW}}/b_{\mathrm{gal}}(z)$ and $D_{\mathrm{L,GW}}/D_{\mathrm{L,EM}}(z)$ using 4 nodes each. The GP hyper-parameters (i.e., the 2 correlation lengths and the 4×2 amplitudes) are explored independently. The fiducial model is given by $\Xi_0 = 1.4, n = 1, \Omega_{\mathrm{m}} = 0.31, h = 0.67, w_0 = -1$.

stress that these multipoles contribute relatively little information compared to larger multipoles since they are dominated by cosmic variance.

Our window functions are distributed in the redshift range $[0.1, 3]$. We assume $N_{\mathrm{gal}} = 12$ galaxy bins equally spaced in redshift, and $N_{\mathrm{GW}} = 8$ GW luminosity distance bins equally spaced in $D_{\mathrm{L,GW}}$. We mention in particular that this choice is not completely arbitrary. The number of GW bins is motivated by forcing well-defined bins such that their width is at least three times the luminosity distance uncertainty $\sigma_{\ln D}$ that we have assumed. Furthermore, we have also verified that the exact number of galaxy bins does not dominate our results as long as $N_{\mathrm{gal}} > N_{\mathrm{GW}}$.

As for the last ingredient, we assume cosmic-variance or shot-noise limited uncertainties. In this case, we can write the covariance matrix of the autocorrelation and cross-correlation signals defined in Equations (6.55), (6.59) and (6.61) as the following:

$$\mathrm{Cov}\left[C^{ij}(\ell)C^{mn}(\ell')\right] = \frac{\delta_{\ell\ell'}}{(2\ell + 1)f_{\mathrm{sky}}} \times \left(\tilde{C}^{im}\tilde{C}^{jn} + \tilde{C}^{in}\tilde{C}^{jm}\right), \qquad (6.63)$$

where the indices i, j, m, n can represent both galaxy or gravitational wave bins. The terms $\tilde{C}^{im}$ contain the shot-noise contribution when they represent the autocorrelations in the same bin:

$$\tilde{C}^{im}(\ell) = C^{im}(\ell) + \frac{\delta_{im}}{\bar{n}}, \qquad (6.64)$$

where $\bar{n}$ is the average density of projected objects from Equation (6.52). In this work, we assume a survey covering a sky fraction equal to $f_{\mathrm{sky}} = 0.5$.

Gaussian Processes

Similarly to what was done in subsection 6.3.2, we try to recover our assumed parameters. The main difference, in this case, is that we focus on the posteriors of $b_{\mathrm{GW}}(z)$

and $D_{\mathrm{L,GW}}/D_{\mathrm{L,EM}}(z)$ according to a Gaussian Process (GP) reconstruction. Our priors in Table 6.2 are imposed both on physical parameters (Ω_m, w_0, H_0) and also on the GP parameters. We consider a certain number of redshift nodes for the two functions, referred to as *training nodes* with a slight abuse of terminology. The amplitudes of the nodes are free and, given a node configuration, we consider GPs which pass through all of these nodes exactly. To render our scenario computationally feasible and not consider many functions for each node configuration, we use the GPs regressor of the python package sklearn to output the best fit and use this as our function.

Our use of GPs can be thought of as a binning of the functions of interest in redshift space, and imposing a certain prior correlations between the bins. These correlations are specified by the GP kernel function, which in our case is chosen to be

$$\kappa(z_i, z_j; L) \propto \exp\left\{-\frac{1}{2}\left(\frac{|z_i - z_j|}{L}\right)^2\right\}, \tag{6.65}$$

where L is the so-called correlation length. This kernel is flexible enough for our purposes, and we do not expect the detailed choice to have any significant impact on our results. For computational purposes, we generate the GPs using a baseline around $D_{\mathrm{L,GW}}/D_{\mathrm{L,EM}}(z) = 1$. This baseline makes the GPs reconstruction to efficiently return to $D_{\mathrm{L,GW}}/D_{\mathrm{L,EM}}(z) = 1$ when not pushed toward other values by the training nodes. For the function $D_{\mathrm{L,GW}}/D_{\mathrm{L,EM}}(z)$ we also artificially impose the physical constraint $D_{\mathrm{L,GW}}/D_{\mathrm{L,EM}}(z = 0) = 1$ (see Eq. 6.48).

For the setup described in this subsection, we find a total SNR of the GW-gal and GW-GW angular power-spectra of ~ 37. This value is dominated by the GW-gal cross-correlations since the GW-GW autocorrelations are not well measured (SNR$\lesssim 6$). To generalize our choices, in section 6.4.2 we expand on how different combinations of instrumental specifications can affect the precision of the reconstruction.

Results

The results of our Gaussian process reconstruction of the bias $b(z)$ and luminosity distance ratio $D_{\mathrm{L,GW}}/D_{\mathrm{L,EM}}(z)$ is presented in Figure 6.5. In the same figure, we also compare these constraints to different theoretical models. In the case of the luminosity distance ratio, we use the parametrization

$$\alpha_M(z) = \alpha_0 \left[\frac{H_0}{H(z)}\right]^2, \tag{6.66}$$

where we use the Equation (6.45) with $w_0 = -1$ to obtain the plotted lines (Belgacem et al., 2019). On the other hand, for $b_{\mathrm{GW}}/b_{\mathrm{gal}}(z)$ we plot the lines corresponding to constant values of $b_{\mathrm{GW}}(z)$, while keeping the galaxy bias fixed to the expression in Equation (6.60). As expected, we observe how the fiducial models for both

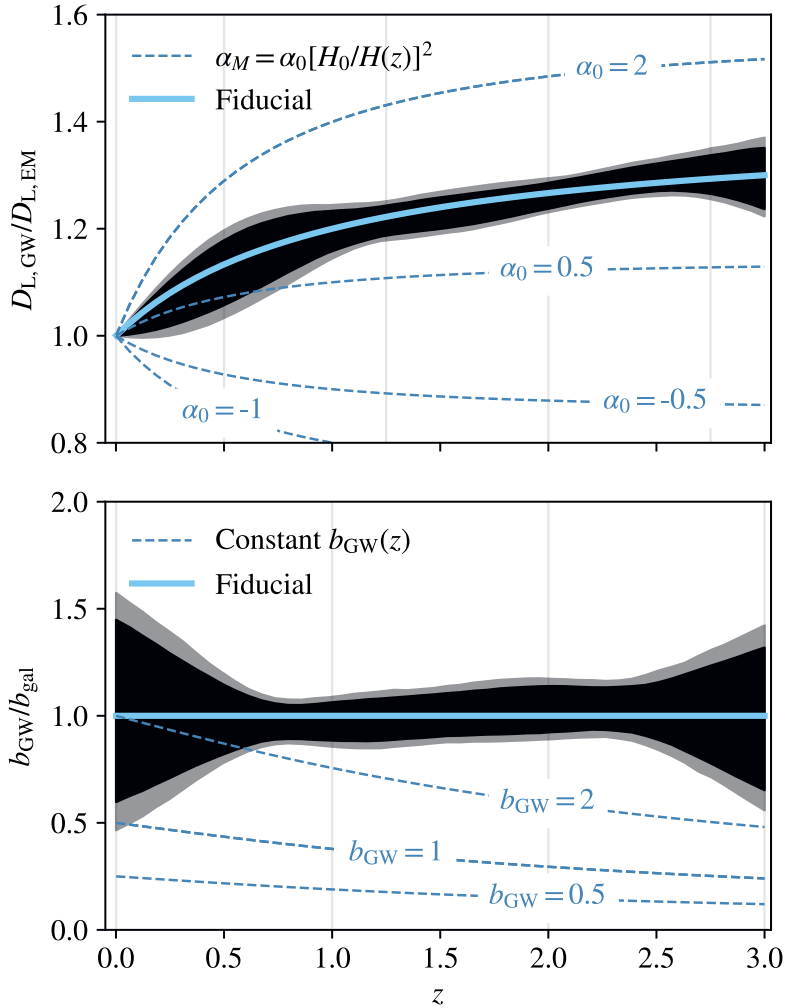Figure 6.5: Confidence intervals (68%, in black, and 95%, in lighter grey) of the jointly reconstructed functions $D_{\mathrm{L,GW}}/D_{\mathrm{L,EM}}\,(z)$ and $b_{\mathrm{GW}}/b_{\mathrm{gal}}\,(z)$. Together with the assumed fiducial model, we also plot the expectation for different models (see text for more details). The vertical lines mark the fixed location of the nodes used in the GP reconstruction.

$D_{\mathrm{L,GW}}/D_{\mathrm{L,EM}}(z)$ and $b_{\mathrm{GW}}/b_{\mathrm{gal}}(z)$ are well encoded within the reconstructed confidence contours in both panels of Figure 6.5. The constraints at higher redshift ($z \approx 3$) for both reconstructions are broader. This is an effect that could not be seen if a parametric function was used for $D_{\mathrm{L,GW}}/D_{\mathrm{L,EM}}(z)$, for instance, as the parametrization would have fixed the behavior similarly at low and higher redshifts.

In principle, the output of our sampling can also be used to reconstruct the function $\alpha_M(z)$ by calculating the numerical derivative of $D_{\mathrm{L,GW}}/D_{\mathrm{L,EM}}(z)$. For this paper, however, we chose not to do this. The kernel in Equation (6.65) can be interpreted as a smoothness prior, and the value of $\alpha_M(z)$ is directly affected by it. Because of this, if one is interested in inferring $\alpha_M(z)$, GPs should be used to sample this function directly.

The constraining power of our method crucially depends on several observational specifications. The most relevant parameters are (1) the angular sensitivity, specified by the maximum multipole $\ell_{\max}$ of the angular power spectra; (2) the number of GW sources, which is specified by the comoving number density n_{GW}; and (3) the precision of the GW luminosity distance measurements $\sigma_{\ln D}$. In the case of n_{GW}, we adjust the value of n_0 in Equation (6.51) as a way to explore different values of the total number of observed GW events, $N = 4\pi f_{\mathrm{sky}}\bar{n}_{\mathrm{GW}}$. This, in principle, should include selection effects not captured by our formalism. Obviously, for a given experimental configuration, the mentioned three variables are not independent, but it is still interesting to find the dependence of our results on each one of them separately. This allows us to reach conclusions without relying on specific experiments and to suggest potential design guidelines for future GW detectors.

To attain such insights, in this subsection, we consider constraints on the parametric expression in Equation (6.50), as well as the parametric GW bias given by Equation (6.57). For simplicity, we fix $n = 1$ and only constrain the parameter Ξ_0.

When varying $\ell_{\max}$ and N, we keep the rest of the configuration (including the luminosity distance binning) fixed. Each case of $\sigma_{\ln D}$, on the other hand, is accompanied by an adjustment in the number of luminosity distance bins. This is done to be consistent with our binning strategy, namely that the luminosity distance width of each bin is at least $\mathcal{O}(3)$ times wider than $\sigma_{\ln D}$.

Our results are summarized in Figure 6.6, where we plot the anticipated uncertainties in Ξ_0 (upper panel) and b_0 (lower panel) as a function of the SNR of the cross-correlation in Equation (6.61).

For a fixed $\sigma_{\ln D}$, the constraining power on Ξ_0 and b_0 is almost entirely determined by the cross-correlation SNR. This fact suggests that no matter how the given SNR is realized (either by increasing the number of sources or by improving the angular sensitivity), the expected constraints will be the same. This implies that the results presented in this section can be easily scaled to different configurations. Unsurprisingly, we find that the constraints scale as $1/\mathrm{SNR}$.

The situation is somewhat different for the case of varying $\sigma_{\ln D}$ (and the number of
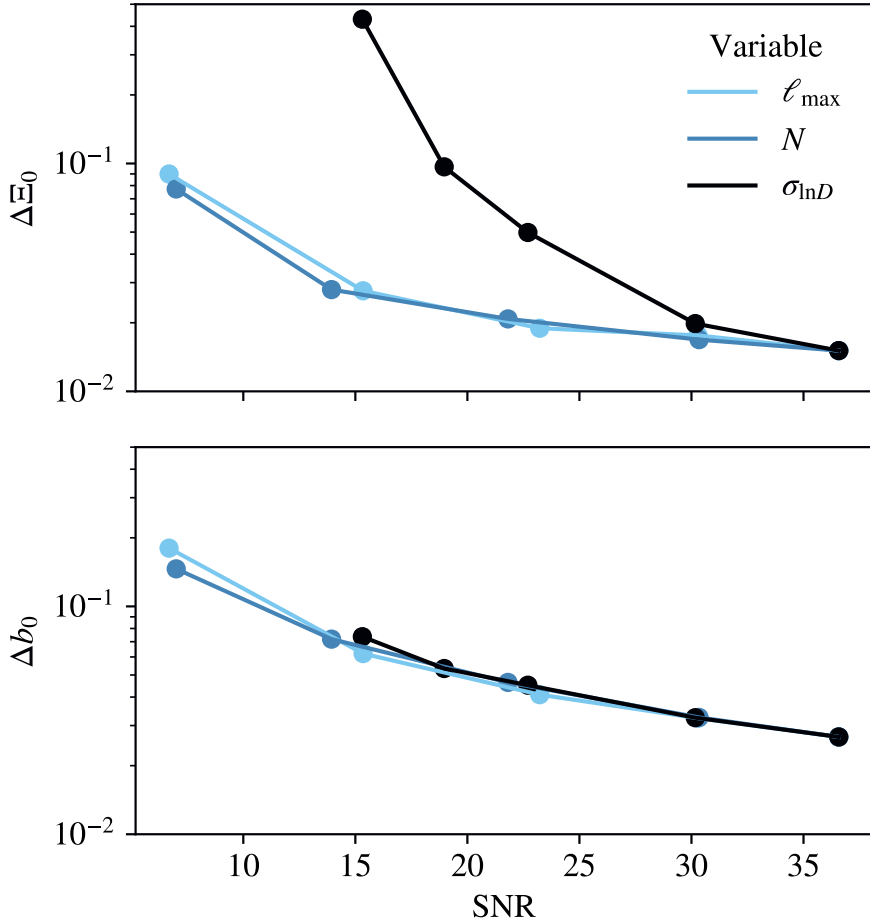
Figure 6.6: Scaling of the observed constraints with the cross-correlation SNR. Using a parametrized model for $b_{\mathrm{GW}}/b_{\mathrm{gal}}(z)$ and $D_{\mathrm{L,GW}}/D_{\mathrm{L,EM}}(z)$ we explore the constraining power of our method as a function of the number of observed GW sources $N = [0.7, 4, 7, 13, 20] \times 10^4$, angular resolution $\ell_{\mathrm{max}} = [20, 40, 60, 80, 100]$ and luminosity distance uncertainty $\sigma_{\ln D} = [0.5, 0.3, 0.2, 0.075, 0.05]$. As visible from the figure, the data SNR completely captures the effect on the observed uncertainties Δb_0 and $\Delta \Xi_0$ in the first two cases. In the case of $\sigma_{\ln D}$, we observe that the increase in constraining power for $D_{\mathrm{L,GW}}/D_{\mathrm{L,EM}}(z)$ is steeper due to the larger number of window functions that we can build to sample $D_{\mathrm{L,GW}}(z)$.

luminosity distance bins). The constraints on the bias still follow the same form (see the lower panel), but the scaling of the Ξ_0 constraints, on the other hand, is much steeper than in the cases of varying $\ell_{\max}$ and n_{GW}, roughly $1/\mathrm{SNR}^3$. This fact can be qualitatively understood by remembering the importance of the relative positions of GW and galaxy window functions demonstrated in Figure 6.4. Sampling this relation with a higher number of window functions increases the precision of our reconstruction.

The results presented in this section quantify the importance of accurate luminosity distance measurements and demonstrate the benefit that smaller values of $\sigma_{\ln D}$ can bring to a binned approach.

6.4.3   Comparison with previous works

Our formalism, based on binned angular power-spectra and sky maps, is optimal for many sources with no known counterpart. Its main advantages are related to the simple modeling of the theoretical signals and their data covariance matrix. Because no reconstruction of the underlying density field is necessary, the predictions display a clear separation of scales. For example, the angular scales that we have considered hare are all within the linear regime ($k \lesssim 0.1\,\mathrm{Mpc}^{-1}$). Furthermore, because this formalism is well established, our shot-noise limited covariance matrix can be easily generalized to include additional sources of (co-)variance.

Although a comprehensive comparison between multiple approaches is outside the scope of this work, it is worth discussing how our results compare to others found in the literature. However, we preface this by saying that one-to-one comparisons are often complicated either by significantly different assumptions or the impossibility of directly translating these assumptions from one prescription to another. Despite this, here, we draw a parallel between our method and two other methods.

The first method is the one used in Mukherjee et al. (2020), which has also been shown to be extremely successful in measuring both $b_{\mathrm{GW}}(z)$ and $D_{\mathrm{L,GW}}(z)$ using parametric models. Similarly to this work, the information is also extracted from the cross-correlation with redshift sources, but no binning of the GW data is performed. In this case, we have verified that such methods perform significantly better than our map-based approach in the case of a low number density of GW sources and large uncertainty in the measured $D_{\mathrm{L,EM}}(z)$. These features, in particular, make it especially useful for near-future samples of a few tens of objects.

The second promising method to measure $D_{\mathrm{L,GW}}(z)$ proposed in the literature is offered by GW sources with known counterparts. Such observations give direct access to $D_{\mathrm{L,GW}}$ as a function of redshift and can be combined with similar measurements in the EM spectrum to obtain $D_{\mathrm{L,GW}}/D_{\mathrm{L,EM}}(z)$. The analysis of Belgacem et al. (2020) is based on this methodology and, similarly to ours, also employs GPs to reconstruct this ratio from an Einstein Telescope sample with $\sim 10^2$ sources. Ultimately, we expect this counterpart-based formalism and the one described in this work to be complementary:

a direct measure of $D_{\mathrm{L,GW}}(z)$ can be used to break the degeneracy between the bias and luminosity distance reconstruction. However, we do not attempt to combine the two methods here because the fraction of events with known counterparts that will be observed is heavily dependent on both the GW source distribution and multiple instrumental setups.

6.5   Conclusions

In Section 6.2 we have explored the impact of gravitational lensing on the soon to be measured merger rates of GW mergers. These results offer guidance when interpreting magnification effects and are intentionally agnostic regarding detector or source population. The main result is that the presence of a lensed population in an observed sample is easily recognizable. This conclusion hinges only on the weak dependence of the inferred binary properties on the factor μ and provides a general explanation for the established result that lensing contamination for luminosity-limited GW events are low for a wide range of detectors and source populations (e.g. Sereno et al., 2010; Ding et al., 2015; Ng et al., 2018; Oguri, 2018).

In Section 6.3 we have quantified for the first time the need for high-resolution GW detectors to extract the total information content of the GWB of astrophysical origin. In particular, we have shown that both a high angular resolution and a high signal-to-noise ratio ($\ell \sim 100$, S/N ~ 70) are required to recover both the matter abundance Ω_{m} and features of the kernel $\mathcal{K}(r)$ as a function of redshift. Note, in particular, that these requirements exceed the angular resolution of present-day and near-future detectors (roughly $\ell \lesssim 10$, and even $\ell \lesssim 4$ for LISA (Ungarelli and Vecchio, 2001; LIGO Scientific collaboration and VIRGO collaboration, 2019)). While this is not the priority of currently proposed third-generation detectors (Maggiore et al., 2020a), it is worth noting that the advantages of high-resolution gravitational-wave astronomy are numerous and not limited to the study of this anisotropic background (Baker et al., 2019). Furthermore, the case for studying the cross-correlation is strengthened by noticing that the anisotropies of the GWB in the kHz band will most probably first be measured through cross-correlation with galaxy surveys. The galaxy map provides a guiding pattern look into the noisy GW data and therefore enhances the SNR.

Finally, the work presented in Section 6.4 shows that the combination of GW resolved events and the clustering of galaxies is expected to improve our current knowledge of the physics of GW mergers and GW propagation. We have discussed how to reconstruct these properties as a function of redshift in a generic way and highlighted the need for accurate and precise measurements of $D_{\mathrm{L,GW}}$. This will require control over the instrument calibration uncertainties (Cahillane et al., 2017), but also the degeneracy between the inclination of the source and its luminosity distance (Ghosh et al., 2016). In the future, we aim to apply our current analysis pipeline to the next generation of large-scale structure surveys and incoming GW observations.

Given the promising nature of our results, we believe that the cross-correlation between GW and galaxy catalogs has the potential to be a robust observational probe in the era of multimessenger cosmology.

Appendices

6A   Shot-noise for the background cross-correlation signal

We follow (Jenkins, Alexander C. and Sakellariadou, Mairi, 2019) and evaluate the shot-noise contribution to the observed cross-correlation signal $C_\ell^\times$ in terms of the shot-noise contribution to the covariance between the observed maps $\Omega(\hat{\mathbf{r}})$ and $\Delta(\hat{\mathbf{r}}')$. Our starting point is

$$B_\ell = \int d^2\hat{\mathbf{r}} P_\ell(\hat{\mathbf{r}} \cdot \hat{\mathbf{r}}') \text{Cov}[\Omega(\hat{\mathbf{r}}), \Delta(\hat{\mathbf{r}}')]_{\text{SN}}. \tag{6.67}$$

By keeping in mind that $\tilde{\mathcal{K}}(r) = r^2 \mathcal{K}(r) \bar{n}(r)$ and that $\delta_g(\vec{\mathbf{r}}) = (n(\vec{\mathbf{r}}) - \bar{n}(r))/\bar{n}$ we use the definitions in Eqs. (6.22), (6.32) to write:

$$\text{Cov}[\Omega(\hat{\mathbf{r}}), \Delta(\hat{\mathbf{r}}')]_{\text{SN}} = \int dr \int dr' \frac{r^2}{\bar{n}} \times \text{Cov}[\mathcal{K}(r)n(\vec{\mathbf{r}}), W_i(r')n(\vec{\mathbf{r}}')]_{\text{SN}}. \tag{6.68}$$

As a side note, we point out that this expression is a stretch of notation since, formally, the quantities $\mathcal{K}(r)n(\vec{\mathbf{r}})$ and $W(r)n(\vec{\mathbf{r}})$ represent the mean values of the variables that we are trying to correlate. To proceed, we notice that $W(r)n(\vec{\mathbf{r}})$ is proportional to the number density of galaxies visible in the galaxy survey and that $\mathcal{K}(r)n(\vec{\mathbf{r}})$ is proportional to the number density of GW events around an infinitesimal volume centered in $\vec{\mathbf{r}}$. This is confirmed by the formalism used in the references mentioned above, (Jenkins, Alexander C. and Sakellariadou, Mairi, 2019) and (Cusin et al., 2018), to predict a realistic $\mathcal{K}(r)$.

In a finite volume δV_i we write down the number of GW mergers as

$$\Lambda_i = \sum_k^{N_i} \lambda_k, \tag{6.69}$$

where N is the number of galaxies present in this volume and the λ_j-s are the number of events for each galaxy. If we assume that N and λ_k are Poisson distributed, Λ_i follows a compound Poisson distribution with variance

$$\text{Var}[\Lambda_i] = \langle \Lambda_i^2 \rangle - \langle \Lambda_i \rangle^2 = \langle N_i \rangle \left(\langle \lambda \rangle + \langle \lambda \rangle^2 \right). \tag{6.70}$$

If we call f the fraction of galaxies in the volume δV_j visible in the galaxy survey we also derive:

$$\mathrm{Cov}[fN_j, \Lambda_i] = f\langle N\rangle\langle\lambda\rangle\delta_{ij}, \tag{6.71}$$

where δ_{ij} is the Kronecker delta. By going back to the continuous case, we obtain the following result:

$$\mathrm{Cov}[\mathcal{K}(r)n(\vec{\mathbf{r}}), W_i(r')n(\vec{\mathbf{r}}')]_{\mathrm{SN}} = \bar{n}(r)W_i(r)\mathcal{K}(r)\delta^3(\vec{\mathbf{r}} - \vec{\mathbf{r}}'). \tag{6.72}$$

Finally, by plugging everything into Eq. (6.67), we obtain the result shown in the main text:

$$B_\ell = \int dr\, W_i(r)\mathcal{K}(r). \tag{6.73}$$

6B Cosmic variance of the background cross-correlation signal

Assume we have two maps on the sky, corresponding to the GWB and GC anisotropies. The angular decomposition coefficients $a_{\ell m}^{\mathrm{GW}}$ and $a_{\ell m}^{\mathrm{GC}}$ are assumed to be Gaussian random variables with zero mean, and each m-mode is drawn from the same distribution. The relevant angular power spectra are defined as

$$C_\ell^\times \equiv \mathrm{Cov}\left[a_{\ell m}^{\mathrm{GW}}, a_{\ell m}^{\mathrm{GC}}\right], \quad C_\ell^{\mathrm{GW}} \equiv \mathrm{Var}\left[a_{\ell m}^{\mathrm{GW}}\right], \quad C_\ell^{\mathrm{GC}} \equiv \mathrm{Var}\left[a_{\ell m}^{\mathrm{GC}}\right]. \tag{6.74}$$

It is then trivial to construct an unbiased estimator of the cross-correlation power spectrum as

$$\widehat{C_\ell^\times} = \frac{1}{2\ell+1}\sum_{m=-\ell}^{+\ell} a_{\ell m}^{\mathrm{GW}}a_{\ell m}^{\mathrm{GC}}. \tag{6.75}$$

The variance of this estimator can then be shown to be

$$\mathrm{Var}C_\ell^\times = \frac{1}{(2\ell+1)^2}\sum_{m=-\ell}^{+\ell} \mathrm{Var}\left[a_{\ell m}^{\mathrm{GW}}a_{\ell m}^{\mathrm{GC}}\right] = \frac{1}{(2\ell+1)^2}\sum_{m=-\ell}^{+\ell} C_\ell^{\mathrm{GW}}C_\ell^{\mathrm{GC}} +$$
$$\mathrm{Cov}\left[\left(a_{\ell m}^{\mathrm{GW}}\right)^2, \left(a_{\ell m}^{\mathrm{GC}}\right)^2\right] - \mathrm{Cov}\left[a_{\ell m}^{\mathrm{GW}}, a_{\ell m}^{\mathrm{GC}}\right]^2. \tag{6.76}$$

In summary, we have

$$\mathrm{Var}C_\ell^\times = \frac{C_\ell^{\mathrm{GW}}C_\ell^{\mathrm{GC}} + \left(C_\ell^\times\right)^2}{2\ell+1}, \tag{6.77}$$

where we have used the Gaussianity of $a_{\ell m}$'s. Making the $a_{\ell m}^{\mathrm{GC}} \to a_{\ell m}^{\mathrm{GW}}$ replacement turns this expression into

$$\mathrm{Var} C_\ell^{\mathrm{GW}} = \frac{2 \left(C_\ell^{\mathrm{GW}} \right)^2}{2\ell + 1}, \tag{6.78}$$

which, of course, recovers the usual cosmic variance result.

Bibliography

B. P. Abbott, R. Abbott, T. D. Abbott, S. Abraham, F. Acernese, K. Ackley, C. Adams, R. X. Adhikari, V.B. Adya, C. Affeldt, and et al. Gwtc-1: A gravitational-wave transient catalog of compact binary mergers observed by ligo and virgo during the first and second observing runs. *Physical Review X*, 9(3), Sep 2019. ISSN 2160-3308. doi: 10.1103/physrevx.9.031040.

B. P. Abbott et al. Astrophysical Implications of the Binary Black-hole Merger GW150914. ApJ, 818:L22, February 2016. doi: 10.3847/2041-8205/818/2/L22.

B. P. Abbott et al. Observation of Gravitational Waves from a Binary Black Hole Merger. *Phys. Rev. Lett.*, 116(6):061102, 2016. doi: 10.1103/PhysRevLett.116.061102.

R. Abbott, T. D. Abbott, S. Abraham, F. Acernese, K. Ackley, A. Adams, C. Adams, R. X. Adhikari, V. B. Adya, C. Affeldt, and et al. Population Properties of Compact Objects from the Second LIGO-Virgo Gravitational-Wave Transient Catalog. 10 2020.

N. Aghanim et al. Planck 2018 results. I. Overview and the cosmological legacy of Planck. *Astron. Astrophys.*, 641:A1, 2020. doi: 10.1051/0004-6361/201833880.

Luca Amendola, Ignacy Sawicki, Martin Kunz, and Ippocratis D. Saltas. Direct detection of gravitational waves can measure the time variation of the planck mass. *Journal of Cosmology and Astroparticle Physics*, 2018(08):030–030, Aug 2018. ISSN 1475-7516. doi: 10.1088/1475-7516/2018/08/030.

Shin'ichiro Ando, Aurélien Benoit-Lévy, and Eiichiro Komatsu. Mapping dark matter in the gamma-ray sky with galaxy catalogs. Phys. Rev. D, 90(2):023514, July 2014. doi: 10.1103/PhysRevD.90.023514.

Shun Arai and Atsushi Nishizawa. Generalized framework for testing gravity with gravitational-wave propagation. II. Constraints on Horndeski theory. Phys. Rev. D, 97(10):104038, May 2018. doi: 10.1103/PhysRevD.97.104038.

John Baker et al. High angular resolution gravitational wave astronomy. 8 2019.

Tessa Baker and Ian Harrison. Constraining Scalar-Tensor Modified Gravity with Gravitational Waves and Large Scale Structure Surveys. *JCAP*, 01:068, 2021. doi: 10.1088/1475-7516/2021/01/068.

Krzysztof Belczynski, Daniel E. Holz, Tomasz Bulik, and Richard O'Shaughnessy. The first gravitational-wave source from the isolated evolution of two stars in the 40-100 solar mass range. Nature, 534(7608):512–515, Jun 2016. doi: 10.1038/nature18322.

Krzysztof Belczynski, Taeho Ryu, Rosalba Perna, Emanuele Berti, Takamitsu L. Tanaka, and Tomasz Bulik. On the likelihood of detecting gravitational waves from Population III compact object binaries. MNRAS, 471(4):4702–4721, Nov 2017. doi: 10.1093/mnras/stx1759.

Enis Belgacem, Yves Dirian, Stefano Foffa, and Michele Maggiore. Modified gravitational-wave propagation and standard sirens. *Phys. Rev. D*, 98(2):023510, 2018. doi: 10.1103/PhysRevD.98.023510.

Enis Belgacem, Stefano Foffa, Michele Maggiore, and Tao Yang. Gaussian processes reconstruction of modified gravitational wave propagation. *Phys. Rev. D*, 101(6):063505, 2020. doi: 10.1103/PhysRevD.101.063505.

Enis Belgacem et al. Testing modified gravity at cosmological distances with LISA standard sirens. *JCAP*, 07:024, 2019. doi: 10.1088/1475-7516/2019/07/024.

Emilio Bellini and Ignacy Sawicki. Maximal freedom at minimum cost: linear large-scale structure in general modifications of gravity. *JCAP*, 07:050, 2014. doi: 10.1088/1475-7516/2014/07/050.

Sayantani Bera, Divya Rana, Surhud More, and Sukanta Bose. Incompleteness Matters Not: Inference of H_0 from Binary Black Hole–Galaxy Cross-correlations. *Astrophys. J.*, 902(1):79, 2020. doi: 10.3847/1538-4357/abb4e0.

Daniele Bertacca, Angelo Ricciardone, Nicola Bellomo, Alexander C. Jenkins, Sabino Matarrese, Alvise Raccanelli, Tania Regimbau, and Mairi Sakellariadou. Projection effects on the observed angular spectrum of the astrophysical stochastic gravitational wave background. *arXiv e-prints*, art. arXiv:1909.11627, September 2019.

B. Bertotti, L. Iess, and P. Tortora. A test of general relativity using radio links with the Cassini spacecraft. Nature, 425(6956):374–376, September 2003. doi: 10.1038/nature01997.

Simeon Bird, Ilias Cholis, Julian B. Muñoz, Yacine Ali-Haïmoud, Marc Kamionkowski, Ely D. Kovetz, Alvise Raccanelli, and Adam G. Riess. Did LIGO detect dark matter? *Phys. Rev. Lett.*, 116(20):201301, 2016. doi: 10.1103/PhysRevLett.116.201301.

Luc Blanchet, Thibault Damour, Bala R. Iyer, Clifford M. Will, and Alan G. Wiseman. Gravitational-Radiation Damping of Compact Binary Systems to Second Post-Newtonian Order. Phys. Rev. Lett., 74(18):3515–3518, May 1995. doi: 10.1103/PhysRevLett.74.3515.

Tom Broadhurst, Jose M. Diego, and III Smoot, George. Reinterpreting Low Frequency LIGO/Virgo Events as Magnified Stellar-Mass Black Holes at Cosmological Distances. arXiv e-prints, art. arXiv:1802.05273, Feb 2018.

Tom Broadhurst, Jose M. Diego, and III Smoot, George F. Twin LIGO/Virgo Detections of a Viable Gravitationally-Lensed Black Hole Merger. arXiv e-prints, art. arXiv:1901.03190, Jan 2019.

Craig Cahillane, Joe Betzwieser, Duncan A. Brown, Evan Goetz, Evan D. Hall, Kiwamu Izumi, Shivaraj Kandhasamy, Sudarshan Karki, Jeff S. Kissel, Greg Mendell, Richard L. Savage, Darkhan Tuyenbayev, Alex Urban, Aaron Viets, Madeline Wade, and Alan J. Weinstein. Calibration uncertainty for Advanced LIGO's first and second observing runs. Phys. Rev. D, 96(10):102001, November 2017. doi: 10.1103/PhysRevD.96.102001.

Gianluca Calcagni, Sachiko Kuroyanagi, Sylvain Marsat, Mairi Sakellariadou, Nicola Tamanini, and Gianmassimo Tasinato. Quantum gravity and gravitational-wave astronomy. JCAP, 10:012, 2019. doi: 10.1088/1475-7516/2019/10/012.

Giulia Cusin, Cyril Pitrou, and Jean-Philippe Uzan. Anisotropy of the astrophysical gravitational wave background: Analytic expression of the angular power spectrum and correlation with cosmological observations. Phys. Rev. D, 96(10):103019, Nov 2017. doi: 10.1103/PhysRevD.96.103019.

Giulia Cusin, Irina Dvorkin, Cyril Pitrou, and Jean-Philippe Uzan. First Predictions of the Angular Power Spectrum of the Astrophysical Gravitational Wave Background. Phys. Rev. Lett., 120(23):231101, Jun 2018. doi: 10.1103/PhysRevLett.120.231101.

Giulia Cusin, Irina Dvorkin, Cyril Pitrou, and Jean-Philippe Uzan. Comment on the article "Anisotropies in the astrophysical gravitational-wave background: The impact of black hole distributions" by A.C. Jenkins et al. [arXiv:1810.13435]. 2018.

Giulia Cusin, Irina Dvorkin, Cyril Pitrou, and Jean-Philippe Uzan. Properties of the stochastic astrophysical gravitational wave background: astrophysical sources dependencies. 2019.

Liang Dai, Tejaswi Venumadhav, and Kris Sigurdson. Effect of lensing magnification on the apparent distribution of black hole mergers. Phys. Rev. D, 95(4):044011, Feb 2017. doi: 10.1103/PhysRevD.95.044011.

Benedikt Diemer. COLOSSUS: A python toolkit for cosmology, large-scale structure, and dark matter halos. *Astrophys. J. Suppl.*, 239(2):35, 2018. doi: 10.3847/1538-4365/aaee8c.

Xuheng Ding, Marek Biesiada, and Zong-Hong Zhu. Strongly lensed gravitational waves from intrinsically faint double compact binaries—prediction for the Einstein Telescope. *Journal of Cosmology and Astro-Particle Physics*, 2015(12):006, Dec 2015. doi: 10.1088/1475-7516/2015/12/006.

Yves Dirian, Stefano Foffa, Martin Kunz, Michele Maggiore, and Valeria Pettorino. Non-local gravity and comparison with observational datasets. ii. updated results and bayesian model comparison with λcdm. *Journal of Cosmology and Astroparticle Physics*, 2016(05):068–068, May 2016. ISSN 1475-7516. doi: 10.1088/1475-7516/2016/05/068.

Michal Dominik, Krzysztof Belczynski, Christopher Fryer, Daniel E. Holz, Emanuele Berti, Tomasz Bulik, Ilya Mand el, and Richard O'Shaughnessy. Double Compact Objects. I. The Significance of the Common Envelope on Merger Rates. ApJ, 759(1):52, Nov 2012. doi: 10.1088/0004-637X/759/1/52.

Michal Dominik, Krzysztof Belczynski, Christopher Fryer, Daniel E. Holz, Emanuele Berti, Tomasz Bulik, Ilya Mandel, and Richard O'Shaughnessy. Double Compact Objects. II. Cosmological Merger Rates. ApJ, 779(1):72, Dec 2013. doi: 10.1088/0004-637X/779/1/72.

Albert Einstein. Näherungsweise Integration der Feldgleichungen der Gravitation. *Sitzungsberichte der Königlich Preußischen Akademie der Wissenschaften (Berlin*, pages 688–696, Jan 1916.

Albert Einstein. Über Gravitationswellen. *Sitzungsberichte der Königlich Preußischen Akademie der Wissenschaften (Berlin), Seite 154-167.*, 1918.

Daniel Foreman-Mackey, David W. Hogg, Dustin Lang, and Jonathan Goodman. emcee: The MCMC Hammer. *Publ. Astron. Soc. Pac.*, 125:306–312, 2013. doi: 10.1086/670067.

Archisman Ghosh, Walter Del Pozzo, and Parameswaran Ajith. Estimating parameters of binary black holes from gravitational-wave observations of their inspiral, merger and ringdown. *Phys. Rev. D*, 94(10):104070, 2016. doi: 10.1103/PhysRevD.94.104070.

R. Hada and T. Futamase. Forecasts of cosmological constraints from Type Ia supernovae including the weak-lensing convergence. *arXiv e-prints*, October 2018.

Evan D. Hall and Matthew Evans. Metrics for next-generation gravitational-wave detectors. *Classical and Quantum Gravity*, 36(22):225002, November 2019. doi: 10.1088/1361-6382/ab41d6.

O. A. Hannuksela, K. Haris, K. K. Y. Ng, S. Kumar, A. K. Mehta, D. Keitel, T. G. F. Li, and P. Ajith. Search for Gravitational Lensing Signatures in LIGO-Virgo Binary Black Hole Events. ApJ, 874(1):L2, Mar 2019. doi: 10.3847/2041-8213/ab0c0f.

Stefan Hilbert, Simon D. M. White, Jan Hartlap, and Peter Schneider. Strong lensing optical depths in a ΛCDM universe. MNRAS, 382(1):121–132, Nov 2007. doi: 10.1111/j.1365-2966.2007.12391.x.

Daniel E. Holz and Eric V. Linder. Safety in numbers: Gravitational lensing degradation of the luminosity distance–redshift relation. *The Astrophysical Journal*, 631(2):678–688, oct 2005. doi: 10.1086/432085.

Gregory Walter Horndeski. Second-order scalar-tensor field equations in a four-dimensional space. *Int. J. Theor. Phys.*, 10:363–384, 1974. doi: 10.1007/BF01807638.

Bin Hu, Marco Raveri, Noemi Frusciante, and Alessandra Silvestri. Effective Field Theory of Cosmic Acceleration: an implementation in CAMB. *Phys. Rev.*, D89(10):103530, 2014. doi: 10.1103/PhysRevD.89.103530.

Alexander C. Jenkins, Mairi Sakellariadou, Tania Regimbau, and Eric Slezak. Anisotropies in the astrophysical gravitational-wave background: Predictions for the detection of compact binaries by LIGO and Virgo. *Phys. Rev.*, D98(6):063501, 2018. doi: 10.1103/PhysRevD.98.063501.

Alexander C. Jenkins, Joseph D. Romano, and Mairi Sakellariadou. Estimating the angular power spectrum of the gravitational-wave background in the presence of shot noise. 2019a.

Alexander C. Jenkins, Mairi Sakellariadou, Tania Regimbau, Eric Slezak, Richard O'Shaughnessy, and Daniel Wysocki. Response to Cusin et al's comment on arXiv:1810.13435. 2019b.

Jenkins, Alexander C. and Sakellariadou, Mairi. Anisotropies in the stochastic gravitational-wave background: Formalism and the cosmic string case. *Phys. Rev*, D98(6):063509, 2018. doi: 10.1103/PhysRevD.98.063509.

Jenkins, Alexander C. and Sakellariadou, Mairi. Shot noise in the astrophysical gravitational-wave background. 2019.

Bence Kocsis, Zsolt Frei, Zoltan Haiman, and Kristen Menou. Finding the electromagnetic counterparts of cosmological standard sirens. *The Astrophysical Journal*, 637(1): 27–37, jan 2006. doi: 10.1086/498236.

Macarena Lagos, Maya Fishbach, Philippe Landry, and Daniel E. Holz. Standard sirens with a running Planck mass. Phys. Rev. D, 99(8):083504, April 2019. doi: 10.1103/PhysRevD.99.083504.

Antony Lewis. GetDist: a Python package for analysing Monte Carlo samples. 2019.

LIGO Scientific collaboration and VIRGO collaboration. Directional limits on persistent gravitational waves using data from Advanced LIGO's first two observing runs. Phys. Rev. D, 100(6):062001, September 2019. doi: 10.1103/PhysRevD.100.062001.

P. Madau, L. Pozzetti, and M. Dickinson. The Star Formation History of Field Galaxies. ApJ, 498:106–116, May 1998. doi: 10.1086/305523.

Michele Maggiore, Chris Van Den Broeck, Nicola Bartolo, Enis Belgacem, Daniele Bertacca, Marie Anne Bizouard, Marica Branchesi, Sebastien Clesse, Stefano Foffa, Juan García-Bellido, Stefan Grimm, Jan Harms, Tanja Hinderer, Sabino Matarrese, Cristiano Palomba, Marco Peloso, Angelo Ricciardone, and Mairi Sakellariadou. Science case for the einstein telescope. *Journal of Cosmology and Astroparticle Physics*, 2020(03):050–050, mar 2020a. doi: 10.1088/1475-7516/2020/03/050. URL https://doi.org/10.1088%2F1475-7516%2F2020%2F03%2F050.

Michele Maggiore et al. Science Case for the Einstein Telescope. *JCAP*, 03:050, 2020b. doi: 10.1088/1475-7516/2020/03/050.

Jose María Ezquiaga. Hearing gravity from the cosmos: GWTC-2 probes general relativity at cosmological scales. *arXiv e-prints*, art. arXiv:2104.05139, April 2021.

D. V. Martynov, E. D. Hall, B. P. Abbott, R. Abbott, T. D. Abbott, C. Adams, R. X. Adhikari, R. A. Anderson, S. B. Anderson, K. Arai, and et al. Sensitivity of the Advanced LIGO detectors at the beginning of gravitational wave astronomy. Phys. Rev. D, 93 (11):112004, Jun 2016. doi: 10.1103/PhysRevD.93.112004.

Suvodip Mukherjee, Benjamin D. Wandelt, and Joseph Silk. Testing the general theory of relativity using gravitational wave propagation from dark standard sirens. 12 2020. doi: 10.1093/mnras/stab001.

Mattia Negrello, R. Hopwood, G. De Zotti, and et al. The Detection of a Population of Submillimeter-Bright, Strongly Lensed Galaxies. *Science*, 330(6005):800, Nov 2010. doi: 10.1126/science.1193420.

K. K. Y. Ng, K. W. K. Wong, T. Broadhurst, and T. G. F. Li. Precise LIGO lensing rate predictions for binary black holes. Phys. Rev. D, 97(2):023012, January 2018. doi: 10.1103/PhysRevD.97.023012.

Masamune Oguri. Measuring the distance-redshift relation with the cross-correlation of gravitational wave standard sirens and galaxies. Phys. Rev. D, 93(8):083511, Apr 2016. doi: 10.1103/PhysRevD.93.083511.

Masamune Oguri. Measuring the distance-redshift relation with the cross-correlation of gravitational wave standard sirens and galaxies. *Phys. Rev. D*, 93(8):083511, 2016. doi: 10.1103/PhysRevD.93.083511.

Masamune Oguri. Effect of gravitational lensing on the distribution of gravitational waves from distant binary black hole mergers. MNRAS, 480(3):3842–3855, Nov 2018. doi: 10.1093/mnras/sty2145.

A. M. Price-Whelan et al. The Astropy Project: Building an Open-science Project and Status of the v2.0 Core Package. *Astron. J.*, 156(3):123, 2018. doi: 10.3847/1538-3881/aabc4f.

Alvise Raccanelli, Ely D. Kovetz, Simeon Bird, Ilias Cholis, and Julian B. Munoz. Determining the progenitors of merging black-hole binaries. *Phys. Rev. D*, 94(2):023516, 2016. doi: 10.1103/PhysRevD.94.023516.

Carl Edward Rasmussen and Christopher K. I. Williams. *Gaussian Processes for Machine Learning (Adaptive Computation and Machine Learning)*. The MIT Press, 2005. ISBN 026218253X.

Marco Raveri, Bin Hu, Noemi Frusciante, and Alessandro Silvestri. Effective Field Theory of Cosmic Acceleration: constraining dark energy with CMB data. *Phys. Rev.*, D90(4):043513, 2014. doi: 10.1103/PhysRevD.90.043513.

Thomas P. Robitaille et al. Astropy: A Community Python Package for Astronomy. *Astron. Astrophys.*, 558:A33, 2013. doi: 10.1051/0004-6361/201322068.

B. S. Sathyaprakash, B. F. Schutz, and C. Van Den Broeck. Cosmography with the Einstein Telescope. *Classical and Quantum Gravity*, 27(21):215006, Nov 2010. doi: 10.1088/0264-9381/27/21/215006.

Giulio Scelfo, Nicola Bellomo, Alvise Raccanelli, Sabino Matarrese, and Licia Verde. GW\times$LSS: chasing the progenitors of merging binary black holes. *JCAP*, 09:039, 2018a. doi: 10.1088/1475-7516/2018/09/039.

Giulio Scelfo, Nicola Bellomo, Alvise Raccanelli, Sabino Matarrese, and Licia Verde. Gwxlss: chasing the progenitors of merging binary black holes. *Journal of Cosmology and Astroparticle Physics*, 2018(09):039–039, sep 2018b. doi: 10.1088/1475-7516/2018/09/039.

Giulio Scelfo, Lumen Boco, Andrea Lapi, and Matteo Viel. Exploring galaxies-gravitational waves cross-correlations as an astrophysical probe. *JCAP*, 10:045, 2020. doi: 10.1088/1475-7516/2020/10/045.

Joop Schaye et al. The EAGLE project: Simulating the evolution and assembly of galaxies and their environments. *Mon. Not. Roy. Astron. Soc.*, 446:521–554, 2015. doi: 10.1093/mnras/stu2058.

P. Schechter. An analytic expression for the luminosity function for galaxies. ApJ, 203: 297–306, January 1976. doi: 10.1086/154079.

Bernard F. Schutz. Determining the Hubble Constant from Gravitational Wave Observations. *Nature*, 323:310–311, 1986. doi: 10.1038/323310a0.

Scikit-learn. Scikit-learn 0.19.1 documentation: Gaussian Processes. http://scikit-learn.org/stable/modules/gaussian_process.html, 2018. Accessed: 10-06-2019.

M. Sereno, A. Sesana, A. Bleuler, P. Jetzer, M. Volonteri, and M. C. Begelman. Strong Lensing of Gravitational Waves as Seen by LISA. *Physical Review Letters*, 105(25): 251101, December 2010. doi: 10.1103/PhysRevLett.105.251101.

L. P. Singer, D. A. Goldstein, and J. S. Bloom. The Two LIGO/Virgo Binary Black Hole Mergers on 2019 August 28 Were Not Strongly Lensed. *arXiv e-prints*, October 2019.

Graham P. Smith, Mathilde Jauzac, John Veitch, Will M. Farr, Richard Massey, and Johan Richard. What if LIGO's gravitational wave detections are strongly lensed by massive galaxy clusters? MNRAS, 475(3):3823–3828, Apr 2018. doi: 10.1093/mnras/sty031.

R. Takahashi, M. Oguri, M. Sato, and T. Hamana. Probability Distribution Functions of Cosmological Lensing: Convergence, Shear, and Magnification. ApJ, 742:15, November 2011. doi: 10.1088/0004-637X/742/1/15.

A. Taruya, M. Takada, T. Hamana, I. Kayo, and T. Futamase. Lognormal Property of Weak-Lensing Fields. ApJ, 571:638–653, June 2002. doi: 10.1086/340048.

Eric Thrane, Stefan Ballmer, Joseph D. Romano, Sanjit Mitra, Dipongkar Talukder, Sukanta Bose, and Vuk Mand ic. Probing the anisotropies of a stochastic gravitational-wave background using a network of ground-based laser interferometers. Phys. Rev. D, 80(12):122002, December 2009. doi: 10.1103/PhysRevD.80.122002.

Carlo Ungarelli and Alberto Vecchio. Studying the anisotropy of the gravitational wave stochastic background with lisa. *Phys. Rev. D*, 64:121501, Nov 2001. doi: 10.1103/PhysRevD.64.121501. URL https://link.aps.org/doi/10.1103/PhysRevD.64.121501.

A. Weltman et al. Fundamental physics with the Square Kilometre Array. *Publ. Astron. Soc. Austral.*, 37:e002, 2020. doi: 10.1017/pasa.2019.42.

J. S. B. Wyithe and A. Loeb. Magnification of light from many distant quasars by gravitational lenses. Nature, 417:923–925, June 2002. doi: 10.1038/nature00794.

Samenvatting

6.8   Moderne kosmologie

De fascinatie van de mensheid voor de kosmos is een alomtegenwoordig thema in onze gemeenschappelijke geschiedenis. De eerste scheppingsmythen vertegenwoordigen de eenvoudigste kosmogonie, d.w.z. modellen over de oorsprong van het heelal, en de meeste hebben de mensheid in een fundamenteel bevoorrechte rol, soms als het natuurlijke eindpunt van de kosmische geschiedenis. De ontwikkeling van de kosmologie, d.w.z. de wetenschappelijke studie van de oorsprong en de evolutie van het heelal, is daarentegen een proces geweest van voortdurende abstractie van onze persoonlijke ervaring en is een duidelijke verwerping gebleken van onze unieke positie. Wat wij hebben ontworpen is een onverschillig Universum, waarin wij opzettelijk geen bevoorrechte waarnemer zijn. Voor het grootste deel is deze onderneming een verootmoedigend en pijnlijk proces geweest. Toch is de moderne kosmologie ook een uiting van onze overmoed. Het gaat ons er niet om uitspraken te doen over ons, hier en nu, maar we streven ernaar alles te verklaren wat was en ooit zal zijn, om wetten af te leiden die we echt universeel kunnen noemen. Een perfect voorbeeld hiervan is de Algemene Relativiteitstheorie van Albert Einstein, die we vandaag de dag zien als de gravitatiewet van het heelal. Zij kan vrijwel elk fenomeen in haar toepassingsgebied beschrijven en kan een groot aantal waarnemingen nauwkeurig voorspellen: de aantrekkingskracht van de zwaartekracht tussen atomen, de structuur van de dichtste objecten in het heelal (zwarte gaten), en de evolutie van het heelal zelf.

Ondanks haar relatieve zwakte is de zwaartekracht de meest relevante kracht op grote schalen, omdat zij niet kan worden afgeschermd en haar bereik formeel oneindig is. Het is dan ook niet verwonderlijk dat het belangrijkste kader dat in de kosmologie wordt gebruikt, gebaseerd is op de Algemene Relativiteit. Volgens de huidige leidende opvatting is deze theorie het toneel van een touwtrekkerij tussen twee componenten: donkere materie en donkere energie. Deze twee componenten hebben tegengestelde effecten: de eerste vormt structuren die bijeen worden gehouden door gravitatiekrachten, terwijl de andere de dingen uit elkaar trekt en de structuur vernietigt. Ondanks hun essentiële rol is er zeer weinig bekend over de donkere sector, afgezien van deze zeer

basiseigenschappen en het feit dat beide componenten geen licht uitzenden. Vandaar het bijvoeglijk naamwoord "donker". De "normale" materie, die alles vormt wat we zien en aanraken, is daarentegen een subdominante component die geen belangrijke rol speelt in de vorming van de geschiedenis van het heelal.

6.9   De rand en donkere energie

De Melkweg is een spiraalvormig sterrenstelsel waarin het zonnestelsel en de aarde zich bevinden. Door onze positie lijken de sterren waaruit het bestaat als een melkweg-streep zichtbaar aan de nachtelijke hemel van afgelegen gebieden. Deze grote kosmi-sche structuren zijn bij de meesten wel bekend, maar in werkelijkheid bevat het heelal nog veel grotere objecten. In het bijzonder gaat de aandacht in dit proefschrift uit naar donkere materie halo's, dichte klonters donkere materie die 1.000 keer groter zijn dan ons melkwegstelsel. Deze objecten zijn omgeven door een web-achtige verdeling die gewoonlijk wordt aangeduid als de grootschalige structuur van het heelal. In de afge-lopen decennia is het mogelijk geworden om het ontstaan van dit complexe netwerk te bestuderen door middel van numerieke simulaties. Gesimuleerde heelallen worden gemaakt en geanalyseerd om de effecten van de donkere sector op de structuurvor-ming in te schatten. Dit begrip wordt echter bemoeilijkt door het feit dat structuren van donkere materie in het echte heelal niet kunnen worden gefotografeerd, omdat zij geen licht uitstralen. Gelukkig kunnen de sterrenstelsels die binnen de halo's ontstaan en evolueren, worden gebruikt om de structuren waarin zij leven te onderzoeken. Als je van veraf naar de sterrenstelsels kijkt, zie je ze als heldere punten die ingebed zijn in de stellage van donkere materie, die de grootschalige structuur van het heelal vormt.

Het vroege heelal bestond uit een homogene verdeling van materie, maar na ver-loop van tijd leidden zwaartekrachten tot de vorming van dichte kluiten die dankzij hun zwaartekracht nog meer materie aantrekken. Dit zijn de donkere materie halo's die centraal staan in dit proefschrift. Wanneer men hun gesimuleerde versie in detail bekijkt, kan men een dichte binnenkern herkennen, omgeven door een buitengebied dat bestaat uit materie die langzaam naar het binnengebied stroomt. Het overgangs-gebied tussen deze twee zones is relatief klein en gaat gepaard met een abrupte ver-andering van dichtheid: omdat het binnenste gebied in de loop van de kosmische tijd is gegroeid, is het aanzienlijk dichter dan het buitenste gebied. Deze scherpe daling in massadichtheid staat bekend als de splashback en vormt de titulaire rand van dit proefschrift.

Laten we, om te begrijpen hoe donkere energie van invloed is op structuurvorming en spatten, een eenvoudig model daarvoor beschouwen. De minimale verklaring voor donkere energie is de zogenaamde kosmologische constante, een numerieke parameter die voorkomt in de vergelijkingen van de Algemene Relativiteit en die resulteert in een drukkracht die tegengesteld is aan de aantrekkingskracht van de zwaartekracht. Dit vertraagt effectief de hierboven beschreven groei en belemmert de vorming van kos-

mische structuren. Er wordt echter getwijfeld aan deze verklaring omdat, indien waar, de numerieke waarde van deze constante aanzienlijk kleiner zou zijn dan die van andere natuurconstanten. Om deze discrepantie aan te pakken, wordt donkere energie in alternatieve modellen beschreven als een kwintessens: een vorm van energie die in de loop van de tijd kan evolueren. Met name vanwege het exclusieve verband met gravitatieverschijnselen kunnen modellen van quintessentie ook worden geïnterpreteerd als een uitgebreide versie van de Algemene Relativiteit in plaats van een nieuwe generieke component. Omdat zij evolueren, is de druk die door deze gewijzigde zwaartekracht-modellen wordt uitgeoefend anders dan in het geval van de kosmologische constante en kan hun invloed op de structuur van het heelal worden gebruikt om ze te bestuderen.

6.10   Dit proefschrift

De grenzen van de grootste structuren bieden een laboratorium om de relatie tussen donkere materie halo's en kosmologie te onderzoeken. Het kenmerk dat deze randen definieert is een eenvoudige voorspelling, maar het potentieel ervan om de fysica van de structuurvorming te bestuderen is pas onlangs erkend. In het bijzonder is dit gebied de afgelopen vijftig jaar tot bloei gekomen dankzij recente grootschalige onderzoeken van de hemel, waarmee miljoenen melkwegstelsels kunnen worden waargenomen, verdeeld over een aanzienlijk deel van het waarneembare heelal. Ondanks de toegenomen belangstelling staat het vakgebied nog in de kinderschoenen, en er is meer kennis nodig voordat het ware potentieel kan worden gerealiseerd. Deze dissertatie presenteert vier hoofdstukken die erop gericht zijn deze wetenschap tot een volwassen vakgebied te maken en te laten zien hoe de dynamische aard van de grootschalige structuur van het heelal kan worden gemodelleerd en gemeten.

Hoofdstuk 2 van dit proefschrift presenteert de eerste meting van de splashback rond massieve halo's. Deze meting maakt gebruik van gravitatielensing, een bijzonder geavanceerde manier om de verdeling van donkere materie in het heelal waar te nemen. In de Algemene Relativiteit wordt de zwaartekracht van zware objecten opgevat als een vervorming van het weefsel van de ruimtetijd. Daarom worden lichtstralen die door verre objecten worden uitgezonden, beïnvloed door de kromming van structuren van donkere materie langs de gezichtslijn. De vervorming van beelden die het gevolg is van dit effect kan vervolgens worden gebruikt om de massaverdeling in het heelal te meten.

Hoofdstuk 3 presenteert de eerste kwantitatieve voorspellingen van hoe de rand van halo's wordt beïnvloed in de aanwezigheid van quintessence. Het hoofdstuk concentreert zich op een specifiek model, het symmetron, en maakt gebruik van een eenvoudig semi-analytisch model om greep te krijgen op de meest kritische parameters van deze theorie. Het resultaat is een consistent beeld van deze eigenschap als functie van deze parameters in de context van het bekende paradigma van structuurvorming.

Hoofdstuk 4 brengt twee nieuwe waarneembare groatheden naar voren. De eerste

is de relatie tussen de vorm van de rand van een halo en zijn verbinding met het hem omringende kosmische web. De tweede is het bestaan van een duidelijke relatie tussen de grootte van een halo, gedefinieerd door zijn rand, en zijn massa. Het meten van deze relatie is informatief omdat uitgebreide modellen van de zwaartekracht wel invloed blijken te hebben op de eerste, maar niet op de tweede.

Hoofdstuk 5 is het hoogtepunt van de vorige twee. De belangrijkste resultaten zijn de meting van de massa-grootte relatie in de gegevens verkregen door de Kilo-Degree Survey, en de studie van de implicaties daarvan voor het symmetron model.

Hoofdstuk 6 is een samenvatting van drie aanvullende projecten die tijdens het schrijven van dit proefschrift zijn uitgevoerd. Zij richten zich op de studie van de groot-schalige structuur van het heelal door middel van een nieuwe probe, gravitatiegolven. Door de grote kromming die met zwarte gaten samenhangt, veroorzaken de samen-smeltingen van twee van zulke objecten rimpelingen in de ruimtetijd die vanuit de hele kosmos kunnen worden waargenomen. Dit hoofdstuk onderzoekt deze nieuwe klasse van signalen in alternatieve zwaartekrachttheorieën en in de aanwezigheid van gravitatielensing.

Summary

6.11   Modern cosmology

Humanity's fascination with the cosmos is a pervasive theme of our shared history. The first creation myths represent the simplest cosmogonies, i.e., models concerning the origin of the Universe, and most have humanity in a fundamentally privileged role, sometimes as the natural endpoint of cosmic history. In contrast, the development of cosmology, i.e., the scientific study of the origin and evolution of the Universe, has been a process of continuous abstraction from our personal experience and has proved to be a clear rejection of our unique position. What we have designed is an indifferent Universe, in which we deliberately do not represent a privileged observer. Nonetheless, modern cosmology is also a display of our hubris. We are not concerned with making statements about *us, here and now*, but we aspire to explain *everything* that was and will ever be, to derive laws which we can genuinely call Universal. A perfect example of this is Albert Einstein's theory of general relativity, which we see today as the Universe's law of gravitation. It is able to describe virtually every phenomenon in its purview and can accurately predict a plethora of observations: the gravitational attraction between atoms, the structure of the densest objects in the Universe (black holes), and the evolution of the Universe itself.

Despite its relative weakness, gravity is the most relevant force at large scales because it cannot be screened away and its range is formally infinite. Therefore, it is not surprising that the leading framework used in cosmology is based on general relativity. According to the current leading view, this theory represents the playground hosting a tug of war between two ingredients: dark matter and dark energy. These two components have opposite effects, the first forms structures held together by gravitational forces, while the other pulls things apart and destroys structure. Despite their essential role, very little is known about the dark sector apart from these very basic properties and the fact that both components do not emit light. Hence the "dark" adjective. In contrast, the "normal" matter, which forms everything we see and touch, is a subdominant component that does not play an important role in shaping the history of the Universe.

6.12 The edge and dark energy

The Milky Way is a spiral galaxy hosting the Solar System and Earth. Because of our position, the stars that comprise it appear as a streak spilled of milk visible in the night skies of remote areas. These large cosmic structures are familiar to most, but in reality, the Universe contains even larger objects. In particular, the main focus of this thesis is dark matter halos, dense clumps of dark matter that are $1,000$ times larger than our galaxy. These objects are surrounded by a web-like distribution commonly referred to as the large-scale structure of the Universe. In the past few decades, it became possible to study the emergence of this complex network through numerical simulations. Simulated universes are created and analyzed to estimate the effects of the dark sector on structure formation. This understanding, however, is complicated by the fact that dark matter structures cannot be photographed in the real Universe, since they do not emit light. Fortunately, the galaxies that form and evolve inside the halos can be used to probe the structures they live in. When looking at them from far away, galaxies appear as bright points embedded in the dark matter scaffolding that is the large-scale structure of the Universe.

The early Universe consisted of a homogeneous distribution of matter, but over time gravitational forces led to the formation of dense clumps that attract even more matter thanks to their gravitational pull. These are the dark matter halos at the center of this thesis. When looking at their simulated version in detail, one can recognize a dense inner core surrounded by an outer region made of material slowly flowing towards the inner region. The transition area between these two zones is relatively small and it is associated with an abrupt change of density: because the inner region has been growing over cosmic time it is significantly denser than the outer region. This sharp drop in mass density is known as the splashback feature and it represents the titular edge of this thesis.

To understand how dark energy affects structure formation and splashback, let us consider a simple model for it. The minimal explanation for dark energy is the so-called cosmological constant, a numerical parameter appearing in the equations of general relativity that results in a pressure force opposing the attractive pull of gravity. This effectively slows down the growth described above and hinders the formation of cosmic structures. However, doubts are cast on this explanation because, if true, the numerical value of this constant would be significantly smaller than other constants of Nature. To address this discrepancy, alternative models of dark energy describe it as a quintessence: a form of energy that can evolve over time. In particular, due to its exclusive connection to gravitational phenomena, models of quintessence can also be interpreted as an extended version of general relativity instead of a new generic component. Because they evolve, the pressure exerted by these modified gravity models is different from the cosmological constant case and their impact on the Universe's structure can be used to study them.

6.13 This thesis

The boundaries of the largest structures offer a laboratory to examine the relationship between dark matter halos and cosmology. The feature that defines these edges is a straightforward prediction, but its potential to study the physics of structure formation has only been being recently recognized. In particular, this field thrived in the past half-decade thanks to recent wide surveys of the sky, capable of observing millions of galaxies distributed in a sizable portion of the observable Universe. Despite a surge in interest, the field is still in its infancy, and additional knowledge is required before its true potential can be realized. This thesis presents four chapters aimed at transforming this science into a mature field and showcasing how the dynamical nature of the large-scale structure of the Universe can be modeled and measured.

Chapter 2 of this thesis presents the first measurement of the splashback feature around massive halos. This measurement makes use of gravitational lensing, a particularly sophisticated way to observe the distribution of dark matter in the Universe. In general relativity, the gravitational pull of massive objects is understood as a deformation of the fabric of space-time. Therefore light rays emitted by distant objects are affected by the curvature of dark matter structures along the line of sight. The deformation of images resulting from this effect can then be used to measure the mass distributions in the Universe.

Chapter 3 presents the first quantitative predictions of how the edge of halos is affected in the presence of quintessence. The chapter focuses on a specific model, the symmetron, and makes use of a straightforward semi-analytical model to get a handle on the most critical parameters of this theory. The result is a consistent view of this feature as a function of these parameters in the context of the known paradigm of structure formation.

Chapter 4 brings forward two new observable quantities. The first one is the relationship between the shape of a halo's edge and its connection to the cosmic web surrounding it. The second one is the existence of a clear relationship between the size of a halo, defined by its boundary, and its mass. Measuring this relation is informative because extended models of gravity are found to affect the first but not the second.

Chapter 5 is the culmination of the previous two. Its main results are the measurement of the mass-size relation in the data obtained by the Kilo-Degree Survey, and the study of its implication for the symmetron model.

Chapter 6 is a summary of three additional projects that were performed during the writing of this thesis. Their focus is the study of the large-scale structure of the Universe through a new probe, gravitational waves. Due to the large curvature associated with black holes, the mergers of two such objects create space-time ripples that can be observed from across the cosmos. This chapter explores this new class of signals in alternative theories of gravity and in the presence of gravitational lensing.

184

List of publications

Dynamical cluster masses from photometric surveys
Omar Contigiani and the KiDS collaboration
2021, Astronomy & Astrophysics (to be submitted, **Chapter 5**)

Unifying gravitational waves and dark energy
Alice Garoffolo and Omar Contigiani
2021, Physical Review D (submitted)

Early warning for healthcare acquired infections in neonatal care units in a low resource setting using routinely collected hospital data: the experience from Haiti, 2014-2018.
Annick Lenglet, Omar Contigiani, Cono Ariti *et al.*
2021, PLOS Global Public Health (submitted)

Learning how to surf: Reconstructing the propagation and origin of gravitational waves with Gaussian Processes
Guadalupe Cañas-Herrera, Omar Contigiani, and Valeri Vardanyan
2021, The Astrophysical Journal, 918, 20 (**Chapter 6**)

The mass-size relation of galaxy clusters
Omar Contigiani, Yannick M. Bahé, and Henk Hoekstra
2021, Monthly Notices of the Royal Astronomical Society, 505, 2932 **(Chapter 4)**

Cross-correlation of the astrophysical gravitational-wave background with galaxy clustering
Guadalupe Cañas-Herrera, Omar Contigiani, and Valeri Vardanyan
2020, Physical Review D, 102, 043513 **(Chapter 6)**

Lensing efficiency for gravitational wave mergers
Omar Contigiani
2020, Monthly Notices of the Royal Astronomical Society, 492, 3359 **(Chapter 6)**

On measuring the Galactic dark matter halo with hypervelocity stars
Omar Contigiani, Elena Maria Rossi, and Tommaso Marchetti
2019, Monthly Notices of the Royal Astronomical Society, 487, 4025

Weak lensing constraints on splashback around massive clusters
Omar Contigiani, Henk Hoekstra, and Yannick Bahé
2019, Monthly Notices of the Royal Astronomical Society, 485, 408 **(Chapter 2)**

Splashback radius in symmetron gravity
Omar Contigiani, Valeri Vardanyan, and Alessandra Silvestri
2019, Physical Review D, 99, 064030 **(Chapter 3)**

Predicting the hypervelocity star population in Gaia
Tommaso Marchetti, Omar Contigiani, Elena Maria Rossi *et al.*
2018, Monthly Notices of the Royal Astronomical Society, 476, 4697

Radio Galaxy Zoo: cosmological alignment of radio sources
Omar Contigiani, Francesco de Gasperin, George Miley *et al.*
2017, Monthly Notices of the Royal Astronomical Society, 472, 636

Curriculum vitae

I was born on the 14$^{\text{th}}$ of October 1992 to Vittorio Contigiani and Hend Achouri in Montevarchi, Italy. As a child, I spent my time climbing trees in the hills surrounding the Arno Valley and, perhaps unsurprisingly, I started considering an academic career only later in life. My passion for science began during the final years of my high-school education, when I learned to appreciate the elegance of mathematics and the pleasure of discovering something new. In retrospect, I now realize that I owe my enthusiasm to my biology teacher, Elio Barbuti. He was the first who showed me the stunning complexity of science and focused my attention towards one of the greatest examples of it, Charles Darwin's On the Origin of Species. True to my inquisitive nature and bookworm inclinations, I kept reading and enjoyed other similar works, including the Dialogue Concerning the Two Chief World Systems by Galileo and Six Not-So-Easy Pieces by Feynman. The beauty of the descriptions and the powerful subtlety of the arguments presented in these books are what cemented my interest, and eventually led to me obtaining a bachelor's degree in physics at the University of Florence in 2015. Despite following only two astronomy-related courses, I later ended up specializing in cosmology.

When asked about my University career, I like to mention that I attended "graduate school" in Leiden, since I stayed there for both a master's degree and a doctorate. In particular, for my PhD I was offered a de Sitter fellowship. This joint program between the Leiden Observatory and the Lorentz Institute for Theoretical Physics gave me the opportunity to independently develop my science goals and learn from experts in multiple fields. During these six years, I was mentored by numerous advisors: a radio astronomer (Francesco de Gasperin), a theoretical astrophysicist (Elena Rossi), and, last but not least, the supervisors of this thesis: a theoretical (Alessandra Silvestri) and an observational (Henk Hoekstra) cosmologist. During my time in Leiden, I also had the opportunity of supervising students both as a master thesis co-supervisor and as a teaching assistant. For my work in this second role, I was awarded a Teaching Assistant Award by the educational board of the physics department. In my research activities, I had the pleasure of collaborating with people from four continents and I presented my work at numerous conferences. The first of these, the 11$^{\text{th}}$ Kosmologietag at the Univer-

sity of Bielefeld, was during my master's and, in the subsequent years, I have presented (sometimes virtually) in Canada, France, Germany, Italy, Spain, United Kingdom, and United States.

Guided by a desire for new challenges, I spent some of my time volunteering for the Amsterdam operational center of Médecins Sans Frontières (Doctors Without Borders). Starting from January 2020, I helped epidemiologists and doctors in analysing and modeling data concerning the onset of antimicrobial resistance in low-resource hospital settings. Motivated by a similar curiosity, I was also involved in outreach and projects at the intersection between science and art. I participated in a theater performance centered on the concept of time (60 in real time) as an expert guest, and I was part of a Nederlands Dans Theater workshop where scientists, coreaographers, dancers and composers worked together to combine their creative processes (Open Space 2021). Collaborating with world-class experts has given me a new appreciation for the versatility of the skill set I have acquired and the ability to participate in such diverse activities. Dedication and sacrifice are sometimes mistaken as exclusive properties of an academic life, but in my experience this could not be further from the truth.

In the fall of 2021, I began a postdoctoral fellowship at the Canadian Institute for Theoretical Astrophysics in Toronto. In the next few years, I plan to continue there my work on of the growth of the largest structures and gravitational wave cosmology.

Acknowledgments

After two degrees and many other adventures, I am happy to say that I have changed a great deal during my time in the Netherlands. I probably would not even recognize the young man who first came to Leiden six years ago, and I am grateful for every interaction that has contributed to this growth: prolonged, short, negative, positive, and everything in between.

I am indebted to the administrative staff, the many mentors, and a multitude of colleagues who have supported me throughout this period. You have pushed me to do more and do better. Your dedication has inspired me, and I was lucky to have had the opportunity to work in the vibrant environment you have created. I am also thankful for the many experiences I shared with acquaintances, friends, and more outside of the workplace. The good times we have spent together have made me a happier, more confident person, and they should not be left unrecognized. Some of you come and go, and some of you might now be far, but hopefully, never *too* faraway.

If you are reading these acknowledgments, there is a good chance that you were one of the catalysts behind these changes. It might not be easy, but I hope to pay it forward and give as much as I have received – Thank you.